Università degli Studi di Salerno

DIPARTIMENTO DI CHIMICA E BIOLOGIA

"A. Zambelli"

Dottorato in Chimica - XXXVIII ciclo

Ph.D. Thesis

Stereoselective (Co)Polymerization of Bio-Based Conjugated Dienes Derived from Natural Aldehydes Using [OSSO]- Titanium Catalysts

2022-2025

Tutor:	**Candidate**:
Prof. Carmine Capacchione	Ilaria Grimaldi
PhD Coordinator:	8860400007
Prof. Alessandra Lattanzi	

Table of Contents

Abstract

The transition toward a sustainable polymer industry requires the design of new materials derived from renewable resources that can match the performance of their fossil-based counterparts. In this context, this work focuses on the synthesis and stereoselective (co)polymerization of bio-based conjugated dienes obtained from natural aldehydes. Three key monomers were prepared and studied: *trans*-1-phenyl-1,3-butadiene (1PB), derived from cinnamaldehyde; *S*-4-isopropenyl-1-vinyl-1-cyclohexene (IVC), obtained from perillaldehyde and incorporating a rigid cyclic scaffold with a pendant isopropenyl group; and (E)-4,8-dimethyl-1,3,7-nonatriene (DMNT), synthesized from citral. Alongside these, 1-vinylcyclohexene (VCH) was included as a non-renewable but scarcely investigated benchmark sharing the same cyclohexene backbone as IVC, and two linear terpenes, β-myrcene and β-ocimene, were employed as flexible comonomers.

All homopolymerizations conducted with titanium [OSSO]-type complexes activated by MAO afforded highly regio- and stereoregular polymers with remarkable isotacticity (typically *mmmm* > 99%), high yields and significant molecular weights. The sterically more demanding cumyl-substituted complex **2** consistently outperformed the tert-butyl analogue, promoting 3,4-regioselective and isotactic polymerization of 1PB, VCH and IVC, and 1,2-selective, isotactic polymerization of DMNT. The resulting polymers were comprehensively characterized by NMR spectroscopy, thermal analysis and mechanical testing, allowing clear correlations to be established between microstructure and properties. PVCH and PIVC emerged as rigid, high-T_g thermoplastic materials that remain fully amorphous despite their perfect regularity, while poly(1PB) could be converted, via post-polymerization hydrogenation, from a glassy thermoplastic ($T_g \approx 80$ °C) into a much softer material ($T_g \approx 17$ °C). Poly(DMNT), in contrast, displayed a single T_g (-34 to -40 °C), establishing DMNT as a renewable building block for high-molecular-weight elastomers.

The monomers were then copolymerized among themselves and with β-myrcene and β-ocimene under conditions optimized in the homopolymerization studies, yielding fully or largely renewable copolymers with compositions and architectures tailored to cover a broad spectrum of behaviour from rigid thermoplastics to soft elastomers and thermoplastic elastomers. Copolymers of 1PB with terpenes provided amorphous materials whose T_g and mechanical properties could be continuously tuned by varying the terpene content. Copolymers of IVC and VCH with terpenes and with 1PB offered access to rigid and mixed hard-soft

systems, while DMNT-based copolymers with terpenes, IVC and 1PB bridged the gap between soft rubbers and materials with more complex, TPE-like responses. In particular, an 80:20 DMNT:1PB copolymer functioned as a renewable analogue of SBR, and a sequential 1PB-DMNT-1PB triblock copolymer reproduced the dual glass transitions typical of SBS-type thermoplastic elastomers.

Owing to the presence of residual carbon-carbon double bonds in the backbone, PIVC was further used as a model system to investigate both irreversible and reversible thiol-ene cross-linking aimed at improving or modulating mechanical performance. Permanent networks were obtained with simple dithiols, while ester-containing dithiols enabled the formation of hydrolytically cleavable cross-links. A first hydrolysis study demonstrated partial network breakdown and a marked decrease in T_g, providing direct proof of the feasibility of controlled reversible cross-linking in this bio-based system.

Finally, kinetic studies based on in situ ^{1}H NMR spectroscopy were carried out on homo- and copolymerization systems to extract reactivity ratios and establish the relative reactivity order of the monomers. The kinetic data were analyzed using the Jaacks model, which allows the determination of apparent reactivity ratios from the instantaneous copolymer composition under differential conversion conditions, and the nonterminal Beckingham-Sanoja-Lynd (BSL) model, which accounts for penultimate-unit effects by considering the influence of the second-to-last inserted monomer on chain-end reactivity. The analysis revealed that, despite the occurrence of chain-transfer and termination events, the titanium [OSSO] catalysts operate under pseudo-living, nonterminal conditions on the time scale of monomer consumption, enabling reliable reconstruction of compositional drift and predictive microstructure design.

Overall, this research demonstrates that titanium [OSSO]-catalyzed stereoselective polymerization is a powerful strategy for converting monomers from natural building blocks such as cinnamaldehyde, perillaldehyde and citral into high-performance, renewable polymers. The resulting materials significantly expand the accessible space of bio-based polymers, from rigid thermoplastics to soft elastomers and SBS-like thermoplastic elastomers and show that renewable conjugated dienes can realistically compete with fossil-derived analogues in terms of structure, properties and potential applications.

Chapter 1

Introduction

Plastics have revolutionized modern life, offering unmatched versatility, durability, and low production costs. These materials are an integral part to numerous sectors, including packaging, automotive, construction, electronics, and medicine. However, their widespread use has come at a significant environmental cost. Since their commercial expansion in the 1940s, global plastic production has grown exponentially, exceeding 400 million tons annually in recent years. Alarmingly, a substantial fraction of this plastic becomes waste shortly after use, particularly in the case of single-use items, and is often mismanaged, leading to its accumulation in both terrestrial and aquatic ecosystems.

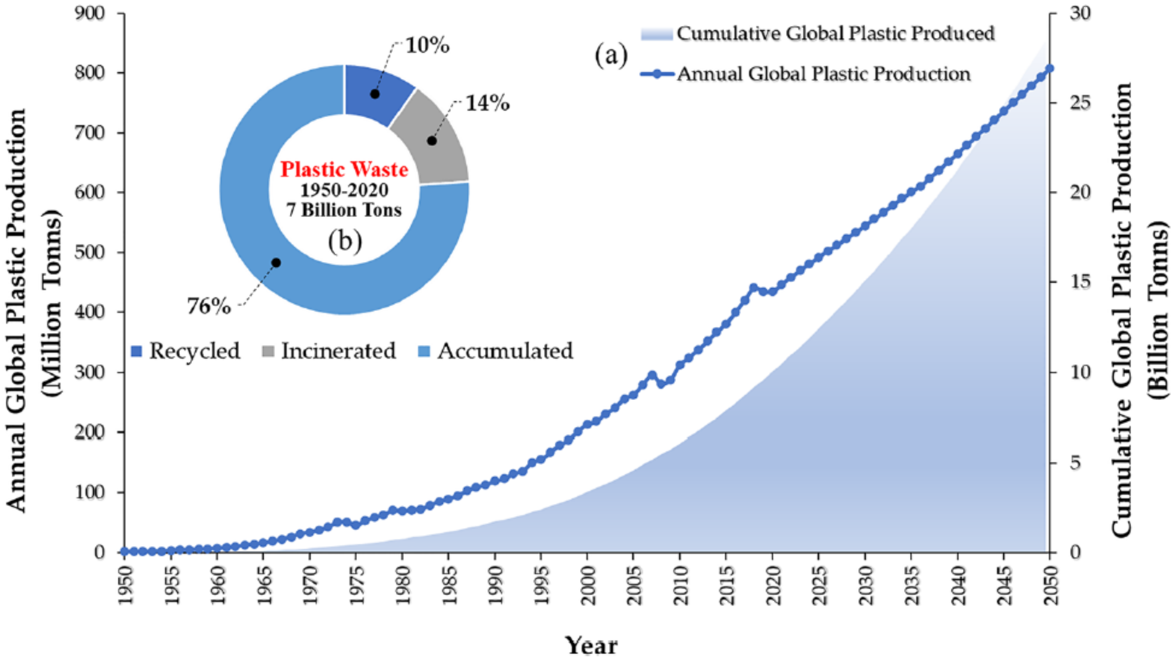

Figure 1.1. Annual Global Plastic Production and Cumulative Distribution of Global Plastic Produced.[1]

The scale of plastic waste mismanagement underscores the gravity of the issue. To date, more than 8 billion tons of waste plastics remain unused, unutilized, and largely unrecyclable, creating significant environmental, health, economic, and social challenges. Of the total plastic produced globally, only about 10% (~1.1 billion tons) has been recycled, while 14% (~1.6 billion tons) has been incinerated. The overwhelming majority, approximately 76% (~8.6

billion tons), has accumulated in landfills or leaked into aquatic ecosystems, where it persists and poses long-term ecological risks.[1]

Degradation times of plastic waste range from hundreds to thousands of years, depending on polymer type and environmental conditions. Fragmentation processes, such as photooxidation and mechanical abrasion, transform macroplastics into micro- and nanoplastics, which are widely dispersed across air, soil, and water. These small particles have been detected in diverse environments, from oceanic gyres to mountain soils, and are increasingly found within biological systems. The consequences are severe: ingestion and entanglement threaten wildlife, while plastic-associated chemicals such as bisphenol A (BPA), phthalates, and flame retardants pose risks to human health, including endocrine disruption, carcinogenicity, and developmental disorders.[2]

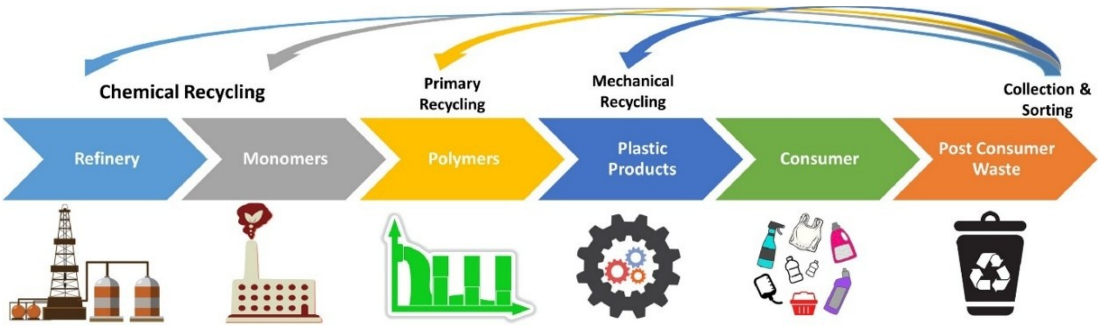

Figure 1.2. Schematic Representation of the Plastic Life Cycle and Recycling Pathways.

The persistence of plastic waste and the challenges associated with its degradation have underscored the urgent need for effective recycling and recovery strategies. Mechanical recycling is currently the dominant industrial method due to its scalability and relatively low cost; however, it faces major limitations when applied to post-consumer waste streams, which often consist of mixed or multi-material plastics (e.g. PE, PP, PS, PET). Such materials are typically inseparable and thermodynamically incompatible, leading to phase separation and a loss of mechanical performance during reprocessing. Contamination from additives and progressive chain degradation further compromise recycling efficiency. To overcome these barriers, research has explored compatibilization strategies, including the use of block or graft copolymers, in situ reactive techniques, and dynamic cross-linking approaches, aimed at improving the compatibility of polymer blends and restoring their properties. While these methods have shown promise, they are often restricted to specific systems and remain costly to scale, highlighting the need for more universal and economically viable solutions.[3]

Alongside mechanical approaches, chemical recycling and thermo-chemical processes, such as pyrolysis and gasification, have gained attention as alternative pathways for converting waste plastics into valuable products. In particular, integrated systems that combine pyrolysis with gasification and reforming offer the possibility of efficiently processing heterogeneous plastic feedstocks into liquid fuels and useful gases, while simultaneously enabling the utilization of captured CO_2 to reduce greenhouse gas emissions. Nevertheless, the development and scale-up of such integrated processes remain technically challenging, requiring a careful balance between environmental sustainability, economic feasibility, and product yield.[1]

This growing crisis has also underscored the urgent need to transition from a fossil-based linear economy to a more sustainable and circular model.

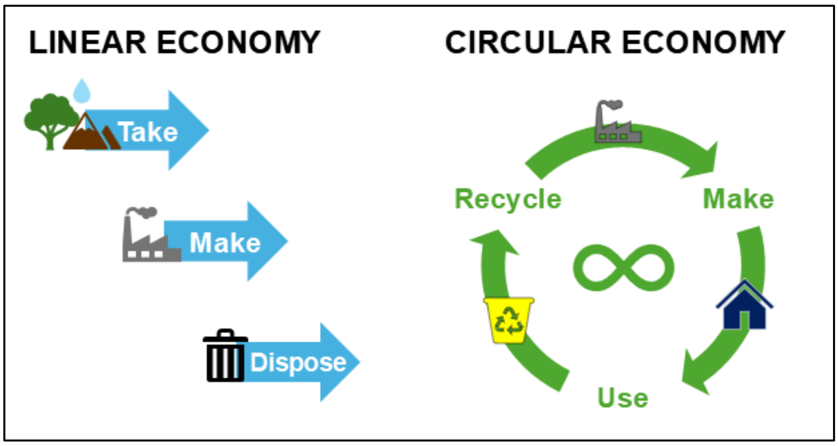

Figure 1.3. Transition From a Linear to a Circular Economy.

One key avenue of innovation lies in the development of polymers derived from renewable resources. Bioplastics, and particularly bio-based polyolefins, have emerged as promising candidates due to their potential to reduce carbon footprint, mitigate pollution, and decrease reliance on non-renewable petrochemical feedstocks. While current bioplastics represent only a small fraction of total plastic production, technological advancements and market growth forecasts point to a significant expansion in the coming decades.

Nevertheless, producing renewable polyolefins that match the performance characteristics, such as mechanical strength, thermal stability, and processability, of conventional polyethylene and polypropylene remains a scientific and engineering challenge. The design of novel catalytic systems, the valorization of bio-based monomers, and the optimization of polymerization processes are all critical steps toward achieving scalable, economically viable solutions.[2]

1.1 Polyolefins: From Rigid Plastics to Elastomers

Polyolefins represent one of the most important classes of synthetic polymers, widely employed in applications ranging from rigid plastics to flexible elastomers. They are produced by the polymerization of α-olefins. Polyethylene (PE) and polypropylene (PP) are the most representative members of the polyolefin family, which constitutes the largest class of synthetic polymers produced worldwide (Figure 1.4). Their predominance in the plastics industry is mainly due to their versatility, as they are employed in a remarkably wide spectrum of applications. While packaging remains the dominant sector of use, polyolefins are also found in consumer goods such as toys, in construction materials such as pipes and cable sheathing, in the automotive sector for both interior and exterior components, as well as in specialized products including ship ropes and high-performance protective equipment.[4]

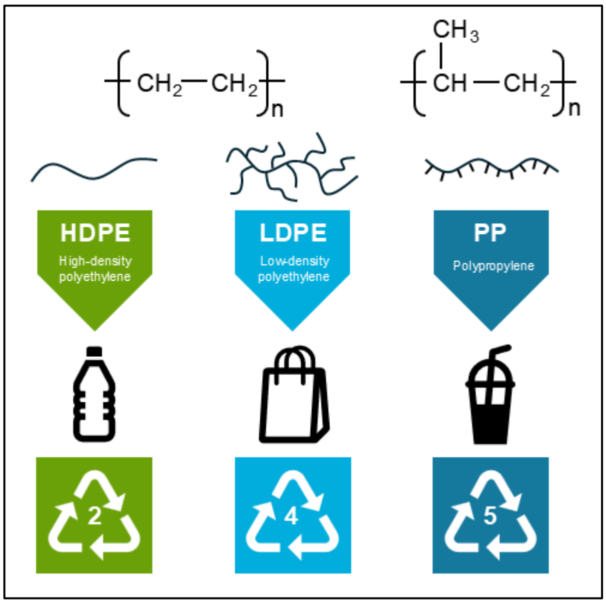

Figure 1.4. Structures Of Polyethylene and Polypropylene.

The properties of polyolefins are strongly influenced by their microstructural features, particularly chain regularity (tacticity), molecular weight, and branching. Low-density polyethylene (LDPE) is characterized by a high degree of branching, which accounts for its relatively low density and flexibility, whereas high-density polyethylene (HDPE) exhibits a more linear backbone with very limited branching, resulting in higher stiffness and crystallinity. Linear low-density polyethylene (LLDPE) represents an intermediate case, being synthesized through the copolymerization of ethylene with longer α-olefins, such as 1-butene, 1-hexene, or 1-octene, which generate short and uniformly distributed branches along the main chain. Early polyolefins like LDPE were synthesized under high-pressure free-radical conditions, resulting in highly branched, amorphous materials. In contrast, the discovery of Ziegler-Natta catalysts in the 1950s enabled the production of linear HDPE and isotactic polypropylene (*i*PP) under low-pressure conditions. These coordination catalysts allowed for precise control over polymer chain growth, enabling the production of polymers with well-defined stereochemistry and crystallinity.[5,6]

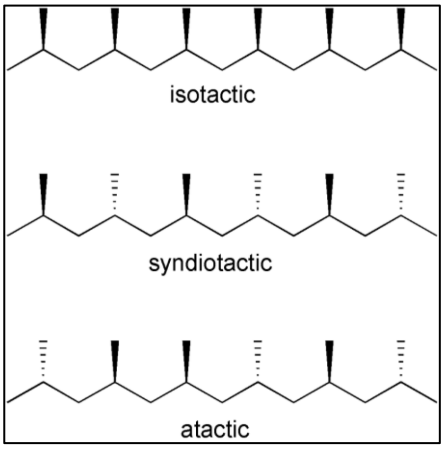

Figure 1.5. Possible Tacticities of Polypropylene.

The stereoregularity of polyolefins, whether isotactic, syndiotactic, or atactic (Figure 1.5), has profound effects on their mechanical and thermal properties. Isotactic and syndiotactic polypropylene, for instance, are semicrystalline materials with high tensile strength and melting points, suitable for rigid applications. Atactic polypropylene, by contrast, lacks regularity, resulting in an amorphous, rubber-like material of limited structural utility. The development of single-site catalysts, such as metallocenes, further advanced the control over polyolefin microstructure, enabling the synthesis of highly stereoregular polymers with narrow molecular weight distributions and tunable comonomer incorporation.[7]

As mentioned before, a notable distinction arises between stereoregular polyolefins and amorphous or partially crystalline polyolefins that serve as elastomers. For example, natural rubber (*cis*-1,4-polyisoprene) and synthetic rubbers such as *cis*-1,4-polybutadiene (BR), styrene-butadiene rubber (SBR), and styrene-butadiene-styrene (SBS) block copolymers (Figure 1.6), while structurally related to polyolefins, are typically produced via radically different polymerization mechanisms rather than coordination catalysis.

Natural rubber (NR) is obtained from latex, an aqueous colloidal dispersion of rubber particles, which after coagulation and processing is available in different commercial forms such as ribbed smoked sheets (RSS), technically specified rubber (TSR), and crepe grades. Natural rubber exhibits strain-induced crystallization, which gives it excellent tensile strength, tear resistance, and wear properties. It also shows good dynamic performance with low heat build-up and effective electrical insulation. However, its disadvantages include poor resistance to weathering, ozone, oil, and elevated temperatures. Because of its superior mechanical properties, natural rubber remains indispensable in tire manufacturing (tread, sidewall, carcass), conveyor belts, footwear, adhesives, and coated fabrics.

The synthetic analogue of natural rubber is *cis*-1,4-polybutadiene (BR), which closely reproduces the structural and elastic features of *cis*-1,4-polyisoprene. Industrially, BR is obtained through coordination polymerization of 1,3-butadiene using neodymium-based catalytic systems, which allow precise control over the polymer microstructure. These catalysts promote a highly stereospecific insertion of butadiene into the metal-carbon bond, yielding polymers with an exceptionally high *cis*-1,4 content and very low 1,2-vinyl fraction. The resulting material exhibits outstanding resilience, low heat build-up, and excellent low-temperature performance, making it particularly suitable for high-performance tire treads and sidewalls, golf balls, and impact-modification applications.

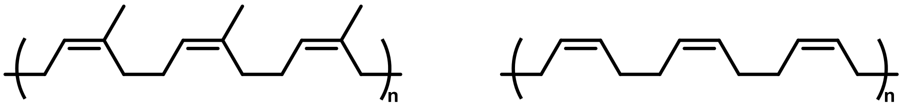

Natural Rubber (NR)
cis-1,4-polyisoprene

Synthetic Rubber (BR)
cis-1,4-polybutadiene

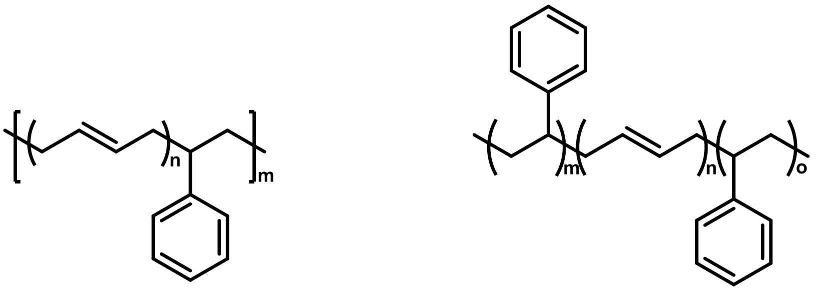

Styrene-Butadiene Rubber (SBR)

Styrene-Butadiene-Styrene (SBS)
Block Copolymers

Figure 1.6. Structures of Natural Rubber (NR) and Synthetic Rubbers (BR, SBR and SBS).

Among synthetic rubbers, SBR is the most widely produced elastomer globally, synthesized by emulsion or solution radical polymerization of styrene and butadiene. This copolymer offers good abrasion resistance, flex fatigue resistance, and processability, it has lower intrinsic mechanical strength than natural rubber and displays poor oil and ozone resistance. Its applications include car and motorcycle tire treads, light truck tires, conveyor belts, shoe soles, adhesives, and waterproof materials.

SBS, on the other hand, belongs to the class of thermoplastic elastomers, combining the elasticity of rubber with the processing advantages of thermoplastics. It is a triblock copolymer consisting of polystyrene end-blocks and a polybutadiene mid-block, typically obtained through anionic polymerization, forming microphase-separated domains that act as physical crosslinks. This morphology imparts SBS with high elasticity, flexibility, and ease of processing without the need for chemical vulcanization. SBS exhibits excellent abrasion resistance and resilience, though it has limited thermal and weather resistance compared to chemically crosslinked rubbers. Due to its balance of performance and processability, SBS is used in shoe soles, adhesives, bitumen modification for road pavements, sealants, and impact-resistant plastics.[8]

These materials are designed to be amorphous or lightly cross-linked to achieve elasticity and resilience rather than stiffness and strength. In this regard, the synthetic approach and desired properties sharply contrast with those of crystalline polyolefins. The development of tailor-made polyolefins, ranging from semicrystalline plastics to soft, processable elastomers, highlights the versatility of olefin polymerization chemistry. Through careful selection of catalysts and polymerization conditions, it is possible to fine-tune polymer properties for a wide range of applications, bridging the gap between rigid materials and synthetic rubbers.

1.2 Catalyst Design for Stereoregular Polyolefins

The synthesis of stereoregular polyolefins relies largely on the rational design of catalysts capable of controlling the spatial orientation of monomer insertion during polymerization. It has been profoundly influenced by the progressive evolution of catalytic technologies, starting with the pioneering discoveries of Karl Ziegler and Giulio Natta in the 1950s. At that time, the industrial production of polyethylene was limited to high-pressure radical processes, which yielded low-density materials characterized by extensive branching and suboptimal properties. Ziegler’s breakthrough came with the discovery that mixtures of titanium halides and aluminium alkyls could catalyse the polymerization of ethylene at low pressure, affording linear high-density polyethylene. This unexpected finding revolutionized the field of polymer science, enabling the production of a new class of materials with superior crystallinity, strength, and thermal resistance, and ultimately earned Ziegler, together with Natta, the Nobel Prize in Chemistry in 1963.[9]

Giulio Natta extended Ziegler's discovery to α-olefins, most famously propylene, where he was able to isolate a crystalline polymer with all methyl substituents aligned in the same configuration along the chain. The early heterogeneous Ziegler-Natta catalysts were nevertheless complex, containing multiple types of active sites with different stereoselectivities and propagation rates. This intrinsic heterogeneity produced polymers with broad molecular weight distributions and mixtures of stereoregular and atactic fractions. Subsequent developments, such as the introduction of $MgCl_2$ supports and the use of internal and external donors, allowed an increase in catalyst activity and stereoselectivity, laying the groundwork for the industrial dominance of isotactic polypropylene, which grew from laboratory in 1954 to one of the most widely produced polymers worldwide within just a few decades.[9,10]

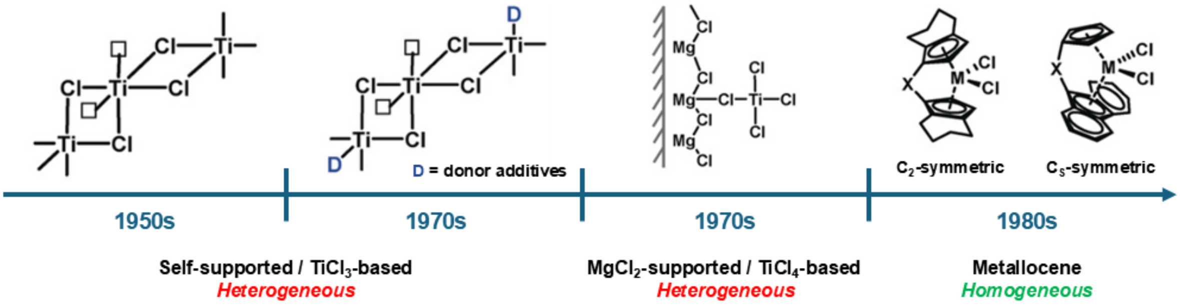

Figure 1.7. Progression of Ziegler-Natta Catalysts.

However, despite their success, heterogeneous Ziegler-Natta systems posed a fundamental limitation: their poorly defined active sites made it impossible to establish clear structure-activity relationships. This challenge stimulated intense academic research into homogeneous model systems that could replicate the essential features of Ziegler-Natta catalysis while offering molecular-level definition. Early attempts with soluble metallocenes such as $Cp_2TiCl_2/AlEt_3$ demonstrated only modest activity, and propylene polymerization remained unselective.[7] The decisive breakthrough arrived in the late 1970s and early 1980s, when methylaluminoxane (MAO) was discovered, formed by partial hydrolysis of trimethylaluminum, could act as a highly effective cocatalyst. MAO not only activated group 4 metallocenes for ethylene polymerization, but also enabled the stereoselective polymerization of propylene, marking the beginning of the "metallocene era".[6,10]

Metallocenes consist of a group 4 metal (typically Ti, Zr, or Hf) sandwiched between cyclopentadienyl ligands, and their activity and stereoselectivity can be finely tuned by modifying ligand symmetry, steric hindrance, and electronic properties. The homogeneous, single-site nature of metallocenes provided a true molecular analogue of Ziegler-Natta catalysis and allowed for rational tuning of polymer microstructure. With the ability to correlate ligand architecture to polymer properties, clear rules for stereocontrol were established: C_2-symmetric *ansa*-metallocenes were shown to yield isotactic polypropylene, while C_S-symmetric complexes favored syndiotactic chains (Figure 1.8A).[7] Moreover, the precise control afforded by single-site systems extended beyond tacticity, enabling unprecedented control over molecular weight distribution, comonomer incorporation, and branching.

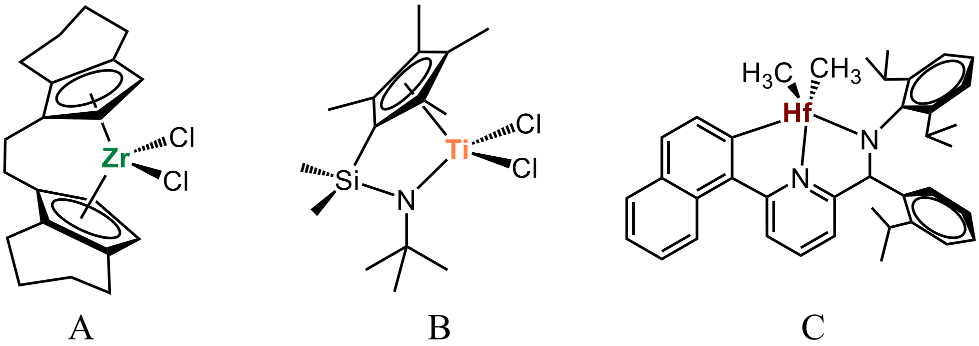

Figure 1.8. Structures of Homogeneous Catalysts: (A) *Ansa*-Bridged Metallocene; (B) Constrained Geometry Catalyst; (C) Post-Metallocene Catalyst.

The framework established by metallocenes was further expanded through the development of constrained geometry catalysts (CGCs), in which a cyclopentadienyl fragment is covalently tethered to an amido donor (Figure 1.8B). These systems offered enhanced comonomer incorporation and facilitated the synthesis of materials with novel microstructures, including long-chain branched polyethylenes and elastomeric copolymers. Beyond group 4 metals, late transition metal catalysts based on nickel and palladium (Figure 1.9) have also been explored for their ability to copolymerize ethylene with polar monomers, although achieving high stereoregularity with such systems remains a significant challenge.[6,11]

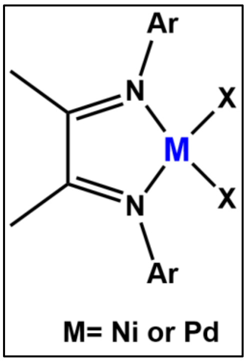

Figure 1.9. Structure of nickel- and palladium-based late transition metal catalysts.

In parallel, post-metallocene catalysts with alternative ligand frameworks (such as pyridine-diimines or phenoxy-imines, figure 1.8C) demonstrated that stereoregular polymerization could be achieved beyond the confines of metallocene chemistry, further broadening the design space for tailored polyolefins.

Thus, the trajectory from heterogeneous Ziegler-Natta systems to homogeneous metallocenes represents not only a technological evolution but also a scientific revolution. This historical progression underscores the central role of catalyst innovation in polyolefin chemistry and highlights how advances in fundamental organometallic chemistry continue to shape one of the most important classes of materials in modern society. As the demand for sustainable, high-performance materials grows, catalyst innovation continues to be at the heart of polyolefin chemistry.

1.3 [OSSO]-Bis(phenolate) Complexes in Polymerization Catalysis

The introduction of [OSSO]-type bis(phenolate) ligands has opened a new frontier in post-metallocene catalysis. These ligands are tetradentate scaffolds containing typically two hard phenolate oxygen donors and two soft thioether sulfur donors in an *O-S-S-O* arrangement, connected by a carbon bridge of different nature between the sulfur atoms.[12]

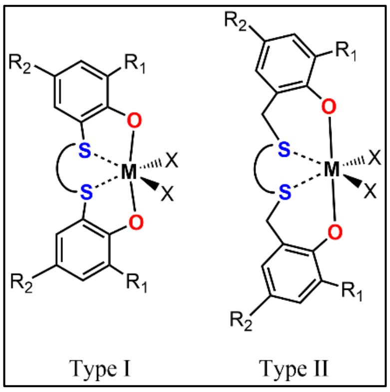

Figure 1.10. Type I and Type II [OSSO] Complexes.

This architecture creates a hemilabile and electronically flexible coordination environment around the metal center, where the hard O donors enforce stability and the softer, more polarizable S donors enable dynamic binding and release during catalysis. Structurally, two principal families are recognized: **type I complexes**, in which the sulfur atoms are directly bonded to the aromatic rings adopting a more rigid chelating arrangement enforcing C_2 symmetry, and **type II complexes**, in which methylene spacers between the aromatic ring and the sulfur atoms impart greater flexibility and fluxionality, leading to reduced stereorigidity (Figure 1.10). This structural distinction has profound consequences on catalytic performance, as the balance between rigidity and hemilability governs both activity and stereoselectivity in olefin polymerization.[13]

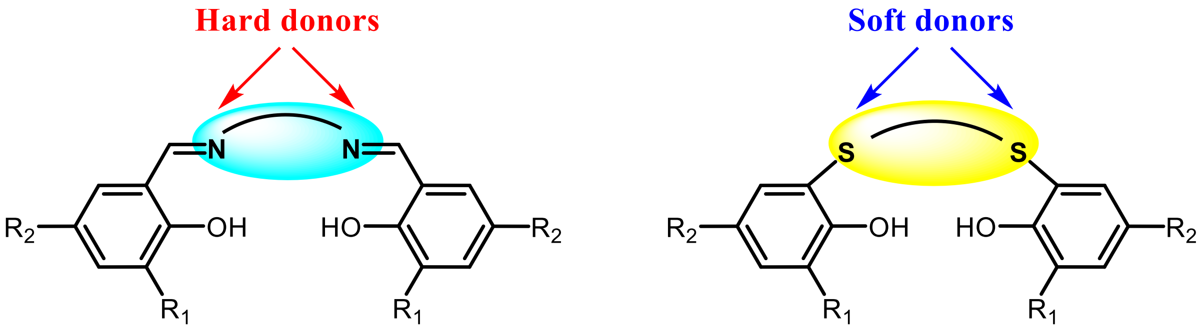

Figure 1.11. General Structures of Salen-Ligand (left) And [OSSO]-Ligand (right).

Compared to the more established Salen-type ligands (*O-N-N-O* donor tetradentates), the difference in donor atoms is crucial (Figure 1.11). In Salen systems, imine nitrogen atoms act as hard, directional donors, imparting rigidity and enforcing a defined geometry at the metal center, which favors highly stereoregular polymerizations of olefins and conjugated dienes (e.g., isotactic polypropylene or *cis*-1,4-polybutadiene).[13,14] In contrast, sulfur donors in [OSSO] frameworks are softer and more polarizable, providing weaker and more hemilabile interactions that allow dynamic rearrangements. This flexibility facilitates chain transfer and branching pathways typically inaccessible to Salen complexes. As a result, while Salen complexes usually promote the formation of strictly stereoregular polymers, [OSSO] complexes broaden the accessible architectures, enabling isotactic or syndiotactic polystyrene, branched polyethylene, alternating ethylene-styrene copolymers, and even stereoblock materials.[12,13,15]

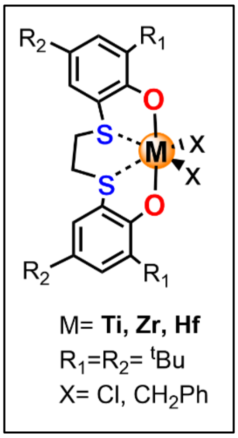

Figure 1.12. Structures of Titanium, Zirconium and Hafnium [OSSO]-Complexes.

Since their emergence in the early 2000s, [OSSO]-type complexes have been widely investigated with group 4 metals (Ti, Zr, Hf). The first examples were reported by Capacchione *et al.*, who synthesized a family of titanium, zirconium, and hafnium dichloride or dibenzyl complexes supported by 1,4- and 1,5-dithiaalkanediyl-bridged bis(phenolate) ligands (Figure 1.12).[16] Upon activation with methylaluminoxane (MAO), these complexes displayed remarkable activity in styrene polymerization. Later, Lian *et al.* synthesized and characterized zirconium and hafnium complexes supported by analogous [OSSO] frameworks. These catalysts displayed polymerization behavior comparable to their titanium analogues, maintaining excellent isospecificity in styrene polymerization and high thermal stability, though with lower overall activity consistent with slower insertion kinetics for the heavier group 4 metals. Notably, these [OSSO]-Zr and -Hf complexes also catalyzed the regioselective oligomerization of 1-hexene, yielding predominantly linear internal olefins and demonstrating that the [OSSO] scaffold can direct regioselectivity through its asymmetric donor environment.[17] Moreover, systematic ligand modification enabled control over stereochemistry in α-olefin polymerization, allowing the switch between isotactic and syndiotactic polypropylene and, in some cases, the formation of stereoblock architectures. Group 4 [OSSO] complexes were subsequently applied to the stereoselective polymerization of conjugated dienes and styrene-butadiene copolymerizations, achieving fine control over elastomer microstructure and composition.[13] These results underline the ability of [OSSO] ligands to act as stereorigid, single-site catalysts, competing with metallocenes but offering broader electronic flexibility through O/S donor combinations.

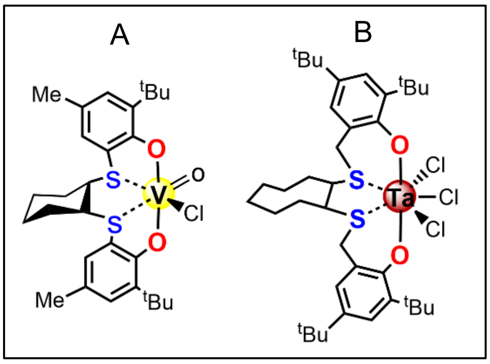

Figure 1.13. Structures of (A) Vanadium and (B) Tantalum [OSSO]-Complexes.

The versatility of the [OSSO] platform has since extended to other metals. Group 5 complexes, particularly those of vanadium and tantalum, have been synthesized and tested in olefin polymerization. Vanadium-[OSSO] complexes, such as the oxovanadium(V) species reported by Meppelder *et al.*, catalyze the polymerization of ethylene upon activation with methylaluminoxane (MAO), producing polyethylene with high molecular weight (Figure 1.13A). Although inactive toward propylene and styrene, these systems highlight the ability of [OSSO] ligands to stabilize high-valent vanadium centers and maintain catalytic activity under polymerization conditions typically unfavorable for such species.[18] Toda *et al.* synthesized a series of Group 5 [OSSO]-type complexes with V, Nb, and Ta precursors, expanding the platform across the 3d-5d metals. Among these, the tantalum(V) complex catalyzed the polymerization of 1-hexene to yield completely isotactic poly(1-hexene) with *mmmm* > 95% (Figure 1.13B). This represents the first Group 5 catalyst for α-olefin polymerization to afford a highly isospecific polymer.[19]

Beyond early transition metals, the scope of [OSSO] catalysis has expanded to include late transition metals, particularly iron, and chromium, which exploit the hemilabile sulfur donors to stabilize redox-active cycles in the coupling of CO_2 with epoxides.

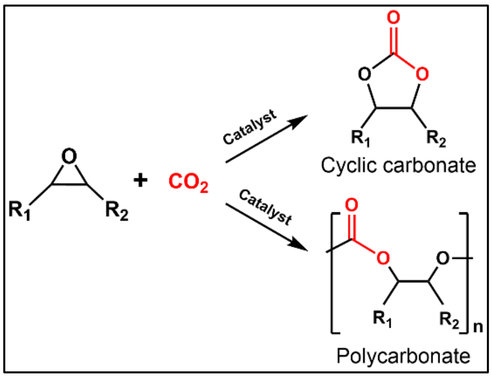

Scheme 1.1. Generic Ring-Opening Copolymerization (ROCOP) Reaction of Epoxides and CO_2.

Mononuclear [OSSO]-Fe(III) complexes (Figure 1.14A) have proven to be efficient and selective catalysts for the Ring Opening Copolymerization (ROCOP) of CO_2 with epoxides (Scheme 1.1), operating under mild conditions. Della Monica *et al.* demonstrated that the product selectivity strongly depends on the epoxide substrate: propylene oxide affords cyclic carbonates, while cyclohexene oxide leads to poly(cyclohexene carbonate) formation. Mechanistic studies suggested that the Fe-S coordination environment favors distinct mono- or bimetallic pathways, stabilizing the active species and preventing catalyst deactivation.[20] Similarly, mononuclear [OSSO]-Cr(III) complexes (Figure 1.14C) have shown excellent performance in the copolymerization of CO_2 with various terminal and internal epoxides. Complexes developed by Della Monica and Niknam displayed turnover frequencies up to 35 h^{-1} and polymer selectivity approaching 99%, while the nature and rigidity of the [OSSO] ligand framework were found to control polymer molecular weight and microstructure. The hemilabile sulfur donors play a key role in tuning both the electronic and steric environment around the Cr center, thereby determining the balance between polycarbonate and cyclic carbonate formation.[21,22]

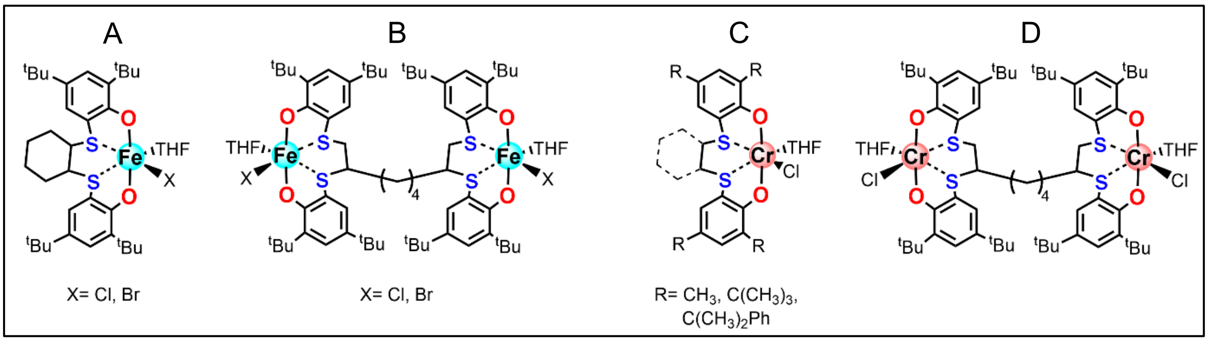

Figure 1.14. Structures Of (A) Monometallic And (B) Bimetallic Iron [OSSO]-Complexes And (C) Monometallic And (D) Bimetallic Chromium [OSSO]-Complexes.

Building on these studies, Paradiso *et al.* reported the first dinuclear [OSSO]-Fe(III) complexes for CO_2/epoxide coupling, revealing cooperative bimetallic mechanisms (Figure 1.14B). The alkyl-bridged bis-[OSSO] Fe system achieved turnover frequencies up to 1680 h^{-1} in the formation of propylene carbonate and enabled the synthesis of poly(cyclohexene carbonate) with molecular weights up to 26 kDa. Kinetic analysis supported an intramolecular bimetallic pathway in which one Fe center activates the epoxide while the other promotes nucleophilic attack, in contrast to the monometallic pathways previously observed.[23] Analogously, Niknam *et al.* reported a new series of dinuclear Cr(III) complexes supported by [OSSO]-type bis-thioether-diphenolate ligands (Figure 1.14D), which demonstrated outstanding performance in the copolymerization of CO_2 with epoxides and in the terpolymerization of CO_2, epoxides, and phthalic anhydride.[24] In combination with bis(triphenylphosphine)iminium chloride (PPNCl) as co-catalyst, this systems showed the highest activity and selectivity, achieving up to 91% conversion and 95% selectivity toward polypropylene carbonate (PPC) under mild conditions. Moreover, the system proved highly effective in the terpolymerization reactions, affording poly(ester-*block*-carbonate) copolymers with >99% selectivity toward polycarbonate segments and TOF values up to 41 h^{-1} for cyclohexene oxide and vinylcyclohexene oxide.

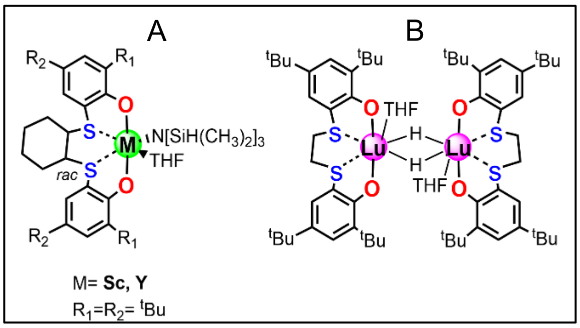

Figure 1.15. Structures of (A) Scandium, Yttrium and (B) Lutetium [OSSO]-Complexes.

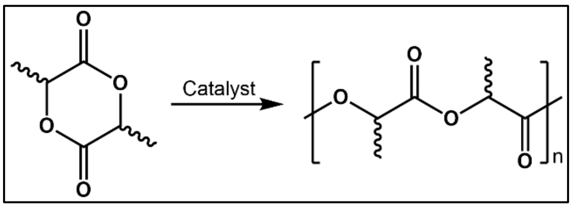

Scheme 1.2. Generic Ring-Opening Polymerization (ROP) Reaction of Lactide.

The framework's adaptability has also facilitated its application with rare-earth metals (Sc, Y, Lu) and main-group elements such as Al. These [OSSO] complexes proved effective in the ring-opening polymerization (ROP) of cyclic esters such as lactide and ε-caprolactone, delivering aliphatic polyesters with controlled molar mass and narrow dispersity (Scheme 1.2). Rare-earth [OSSO] complexes of scandium and yttrium, reported by Ma *et al.*, exhibited high activity in the ROP of L-lactide, affording poly(L-lactide) with high molecular weight under mild conditions (Figure 1.15A). Their monomeric structures feature distorted octahedral or trigonal-prismatic coordination geometries, where the tetradentate [OSSO] ligand stabilizes the active metal center through a combination of hard oxygen and hemilabile sulfur donors.[25] Analogously, lutetium alkyl and hydride complexes supported by [OSSO]-type ligands were synthesized by Konkol *et al.*, revealing both monomeric alkyl and dimeric hydride species active in the ROP of L-lactide (Figure 1.15B). The hydride complexes displayed cooperative reactivity between the two metal centers, while the monomeric alkoxide precursors allowed for efficient initiation, yielding poly(L-lactide) with controlled molecular weight and narrow dispersity.[26]

Main-group analogues were developed by Ma *et al.*, who reported aluminium alkyl complexes capable of living ROP of *rac*-lactide in the presence of isopropanol (Figure 1.16). These catalysts produced polylactides with PDI = 1.03-1.06, with the ligand framework governing both propagation rate and stereoselectivity. The hemilabile sulfur donors modulated the coordination geometry around the Al center, allowing control over tacticity.[27]

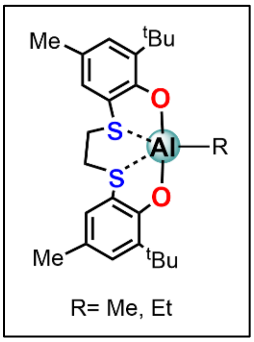

Figure 1.16. Structure of Aluminium [OSSO]-Complexes.

Overall, the catalytic behavior of [OSSO] systems strongly depends on the nature of the coordinated metal: early transition metals typically promote coordination-insertion mechanisms in olefin and diene polymerization, while rare-earth metals and main-group [OSSO] complexes are particularly efficient in ester ring-opening (co)polymerization. [OSSO]-type ligands have introduced a remarkable degree of versatility in coordination chemistry. Their unique balance of hard and soft donors, together with the tunable geometry of the tetradentate framework, allows for the stabilization of a wide range of metals. This adaptability has enabled the design of catalysts that combine high stereoselectivity in polyolefin production with excellent performance in the synthesis of cyclic carbonates and polycarbonates. Compared to classical ligand platforms, [OSSO] complexes uniquely bridge traditional polyolefin catalysis with modern green and sustainable chemistry.[13]

1.4 Polymerization of Fossil-Based Monomers With [OSSO]-Titanium Catalysts

1.4.1. Styrene Polymerization

The first decisive breakthrough in the field of titanium [OSSO]-type catalysis concerned the stereoregular polymerization of styrene, a monomer whose controlled coordination-insertion had long represented a formidable challenge. Early contributions demonstrated that dichloro titanium complexes supported by a 1,4-dithiabutanediyl-bridged bis(phenolate) ligand, upon activation with methylaluminoxane (MAO), afforded isotactic polystyrene under mild conditions and with significant activities.[14]

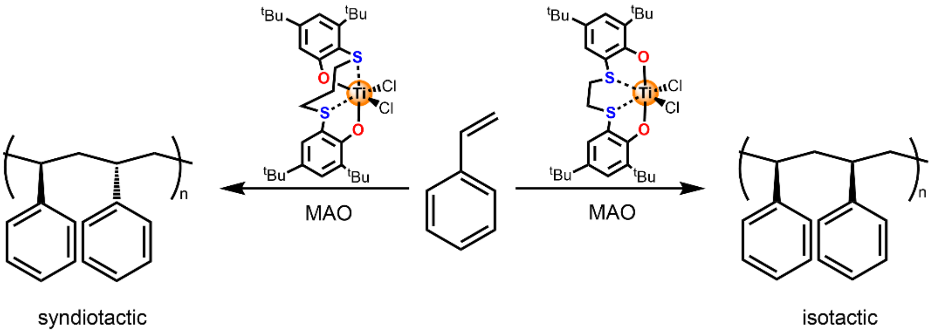

Scheme 1.3. Stereospecific Styrene Polymerization by Chiral Titanium Complexes.

Crystallographic and spectroscopic analyses revealed that the steric hindrance introduced by bulky ortho-substituents stabilized a C_2-symmetric helical configuration, which was directly responsible for enantiomorphic site control and, ultimately, isotacticity.[28] Conversely, extension of the sulfur bridge to a 1,5-dithiapentanediyl moiety resulted in conformational flexibility, leading to syndiospecific polymerization with markedly reduced activity (Scheme 1.3). This clear structure-activity relationship provided an unprecedented demonstration that stereoregularity in styrene polymerization could be finely dictated by ligand topology in post-metallocene systems, thereby extending stereocontrol beyond the realm of classical *ansa*-metallocenes. Subsequent investigations established that electron-donating para-substituents on the styrene monomer further enhanced catalytic activity, while mechanistic studies confirmed secondary insertion pathways. The incorporation of isolated ethylene units into isotactic polystyrene chains represented an additional conceptual advance, as it revealed the possibility of incorporating controlled defects into stereoregular crystalline matrices, with direct implications for the regulation of crystallization behavior.[29]

1.4.2. Conjugated Diene Polymerization

The catalytic scope of [OSSO]-type titanium complexes was rapidly extended to conjugated dienes, whose polymerization typically poses severe challenges due to competing regio- and stereochemical pathways. In 2007, Milione *et al.* shown that these complexes promote the highly stereoselective homopolymerization of 1,3-butadiene and isoprene, preferentially yielding *trans*-1,4 microstructures and, in the case of isoprene, tunable proportions of 1,4- and 3,4-units depending on the reaction conditions (Scheme 1.4).[30]

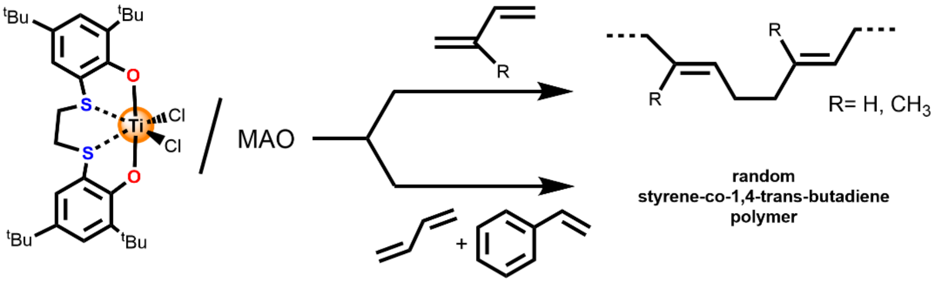

Scheme 1.4. Stereoselective Polymerization of Conjugated Dienes and Styrene-Butadiene Copolymerization.

Even more significantly, the same catalytic system enabled the synthesis of isotactic polystyrene-co-*trans*-1,4-polybutadiene copolymers over a broad compositional window, a result unattainable with either anionic or conventional coordination catalysis.[30]

The mechanistic foundations of these processes were clarified in 2012, when systematic investigations revealed that diene insertion proceeded predominantly via an allylic coordination pathway, with distinct behaviors for E- and Z-isomers: E-1,3-pentadiene underwent insertion with temperature-dependent selectivity for 1,2- versus *trans*-1,4-units, whereas Z-1,3-pentadiene was essentially unreactive.[31]

This fine differentiation underscored the extraordinary sensitivity of [OSSO]-based catalysts to substrate geometry, highlighting the central role of ligand-imposed steric constraints.

1.4.3. Ethylene Polymerization and its Copolymerizations

In parallel, major advances were achieved in the polymerization of ethylene and its copolymerization with styrene. In 2004, Capacchione *et al.* reported that titanium [OSSO] complexes were shown to convert pure ethylene into branched polyethylene, with activities up to 6200 kg·mol^{-1}·h^{-1}·bar^{-1} and a microstructure enriched in long-chain branches arising from in situ oligomer incorporation.[32]

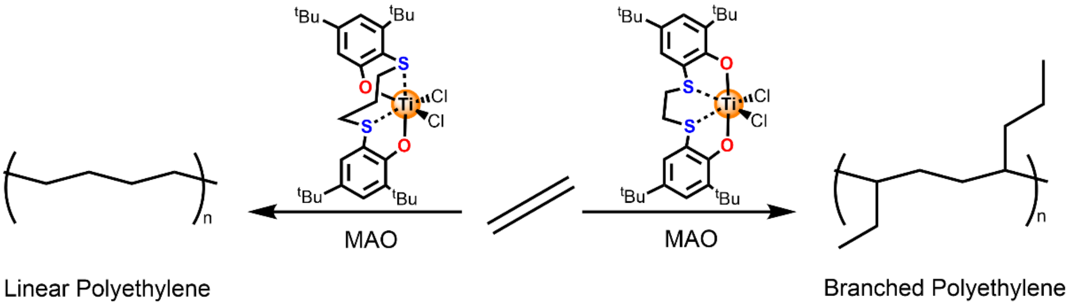

Scheme 1.5. Synthesis of Linear and Branched Polyethylene Using Titanium Catalysts.

The branching density and distribution were demonstrated to be directly modulated by the length of the sulfur bridge in the ligand: the 1,4-dithiabutanediyl system promoted extensive long-chain branching, whereas the 1,5-dithiapentanediyl analogue afforded predominantly linear polyethylene (Scheme 1.5). This represented a novel pathway to branched polyethylene from single-monomer feed, bypassing the need for external comonomers.

Subsequently, the introduction of phenylene-bridged [OSSO] ligands (Figure 1.17) afforded new titanium complexes exhibiting fluxional equilibria between C_2 and C_1 geometries in solution. Lapenta *et al.* reported that, when activated with borate cocatalysts, these systems displayed activities as high as 238 kg·mol^{-1}·h^{-1}·bar^{-1} in ethylene polymerization, producing high molecular weight, semicrystalline polyethylene.[33] The extension to propylene revealed the formation of atactic oligomers, underscoring the delicate interplay between ligand rigidity and stereocontrol.

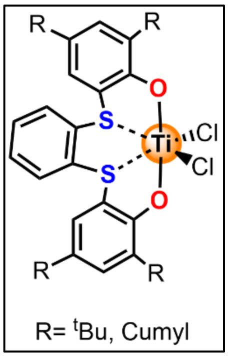

Figure 1.17. Phenylene-Bridged OSSO-Type Titanium Complexes.

Furthermore, the copolymerization of ethylene with styrene was successfully realized, yielding alternating copolymers whose microstructure could be finely tuned by the feed composition. Styrene incorporation reached up to 68%, and ^{13}C NMR analyses confirmed the presence of both alternating sequences and styrene homosequences depending on the monomer ratio.[34] This ability to control comonomer distribution represented a substantial improvement over constrained-geometry catalysts, which were limited to less than 50% styrene incorporation.

Building on this achievement, a wide range of copolymerizations have been explored. Ethylene-butadiene (2008)[35] and ethylene-4-methyl-1,3-pentadiene (2009)[36] copolymerizations proceeded with unexpectedly high activities, producing materials with alternating or highly diene-rich microstructures.

1.4.4. Block Copolymers and Other Binary Systems

The culmination of these developments was the demonstration, in 2010, of living isospecific styrene polymerization at room temperature, enabled by the strategic introduction of ortho-cumyl substituents that suppressed chain-transfer pathways. This innovation not only produced isotactic polystyrene with narrow dispersities but also allowed the sequential synthesis of *i*PS-block-*trans*-1,4-polybutadiene, thereby establishing titanium [OSSO] systems as powerful tools for block copolymer design (Scheme 1.6).[37]

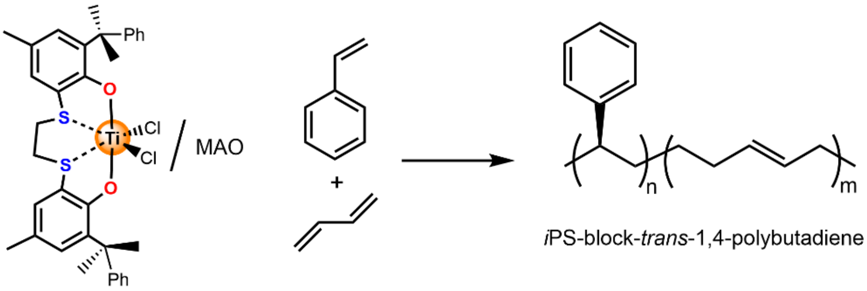

Scheme 1.6. Stereoregular Copolymerization of Styrene and Butadiene.

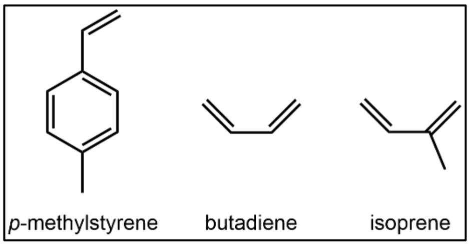

Figure 1.18. Structures of Monomers in the Binary Copolymerization.

In 2013, further sophistication was achieved with the binary copolymerization of *p*-methylstyrene with butadiene and isoprene (Figure 1.18).[38] Depending on the catalyst employed, either syndiotactic poly(*p*-methylstyrene)-co-*cis*-1,4-poly(diene) block copolymers or isotactic poly(*p*-methylstyrene)-co-*trans*-1,4-poly(diene) random copolymers were obtained, demonstrating that stereoselectivity and sequence distribution could be inverted by careful catalyst selection.

That works not only underscored the versatility of titanium [OSSO]-type complexes but also highlighted their unique position among post-metallocene catalysts like their ability to achieve living behavior, stereoregularity, and comonomer tolerance in systems where classical metallocenes had consistently failed.

1.5 Synthesis of Sustainable Polymers from Terpenes

The transition from a fossil-dependent chemical industry to a sustainable, bio-based economy has placed increasing emphasis on the development of renewable feedstocks capable of replacing petroleum-derived monomers. A wide range of natural resources have been explored for this purpose, including carbohydrates, fatty acids and vegetable oils, lignin derivatives, and terpenes (Figure 1.19). Each class offers specific advantages: carbohydrates are oxygen-rich precursors easily converted into lactones or cyclic esters for polyester synthesis; fatty acids provide long hydrophobic chains suited for the preparation of polyamides, polyurethanes, and polyesters; lignin derivatives supply aromatic units for bio-based analogues of polystyrene or epoxy resins. Terpenes, however, stand out as particularly attractive candidates because they are hydrocarbon-rich, structurally diverse, and available from non-food biomass streams in large quantities. Their exploitation allows for the synthesis of renewable polyolefin-like polymers as well as functionalized polyesters and polycarbonates, addressing both the need for drop-in replacements of commodity plastics and the design of novel degradable or specialty materials.[39,40]

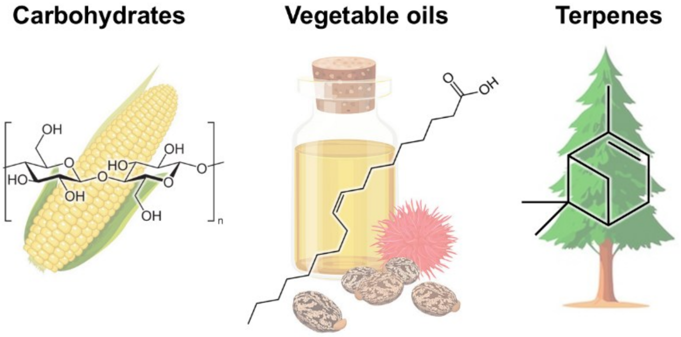

Figure 1.19. Options for Replacing Petrochemicals as Raw Materials in the Manufacture of Polymers.

Terpenes represent a vast family of more than 80 thousand known compounds, biosynthesized in plants, fungi, and microorganisms via the mevalonate and methylerythritol phosphate (MEP) pathways from acetyl-CoA.[41] They are composed of repeating isoprene (C_5H_8) units arranged in head-to-tail or head-to-head fashion, and they are classified according to the number of units (Figure 1.20): *monoterpenes* (C_{10}, such as α-pinene, β-pinene, limonene, and myrcene), *sesquiterpenes* (C_{15}, such as farnesene), *diterpenes* (C_{20}), *triterpenes* (C_{30}), and *polyterpenes*, including natural rubber.[42]

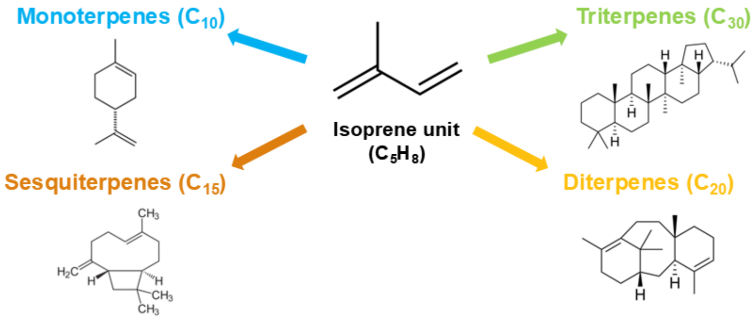

Figure 1.20. Classification of Terpenes.

Industrially, the largest natural source is turpentine, a volatile fraction of pine resin, with an annual global production of over 300 thousand tons. Turpentine contains up to 97% α-pinene and 28% β-pinene, which can be thermally cracked to yield myrcene and ocimene (Figure 1.21). Farnesene is accessible both from plant extracts and via fermentation of sugar feedstocks. Thus, terpenes are renewable, non-food-competitive, and available at scales that are compatible with industrial polymer production.[43] The structural features of terpenes (multiple carbon-carbon double bonds, stereogenic centers, and rigid hydrocarbon backbones) make them ideal candidates for polymer chemistry.

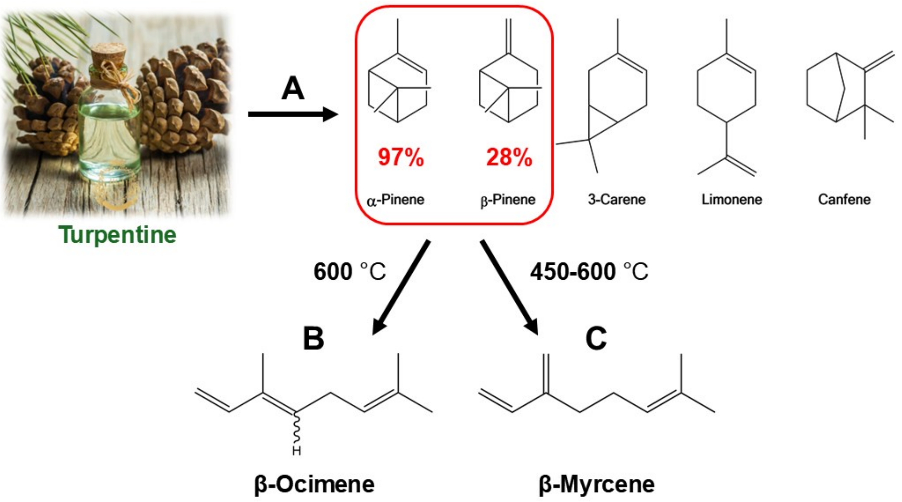

Figure 1.21. Major Components of Turpentine (A); Thermal Cracking of α-pinene (B); Pyrolysis of β-pinene (C).

Early studies dating back to the mid-20th century demonstrated the feasibility of terpene polymerization using cationic or radical initiators. For example, β-pinene underwent cationic polymerization with Friedel-Crafts catalysts such as $AlCl_3$, leading to exothermic reactions and polymers of low to moderate molecular weight.[44] However, the lack of stereochemical and molecular weight control limited their technological relevance, and terpenes remained underexploited for several decades.

Beyond direct polymerization into polyolefin-like materials, terpenes also serve as precursors for oxygenated monomers. Among them, limonene oxide (LO), obtained by selective epoxidation of limonene, has been widely exploited in ROCOP with CO_2 to yield renewable polycarbonates with tunable crystallinity and thermal properties. Zinc, cobalt, and aluminum complexes have been developed as catalysts for these transformations, enabling efficient incorporation of CO_2 under mild conditions.[39,40,45] In particular, Coates and Kleij demonstrated that zinc β-diiminate and aluminum aminotriphenolate complexes promote highly stereoselective copolymerization of *trans*-(*R*)-limonene oxide, affording poly(limonene carbonate) (PLC) with >98% trans content and high optical and thermal stability (Scheme 1.7).[46,47] Stereocomplexed PLCs formed from (*R*)- and (*S*)-limonene oxide enantiomers display elevated glass transition temperatures ($T_g \approx 120$ °C) and improved thermal degradation resistance compared to amorphous counterparts, confirming the role of stereoregularity in enhancing thermal performance.

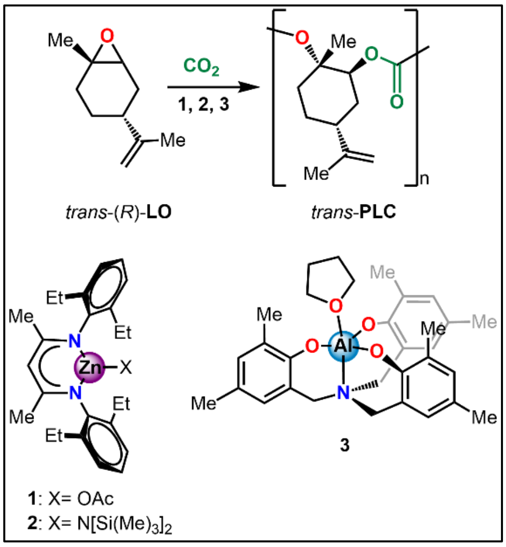

Scheme 1.7. Copolymerization of *trans*-(*R*)-LO by zinc β-diiminate and aluminum aminotriphenolate complexes.

In addition, terpenes have been explored as renewable precursors for the synthesis of bio-based polyamides.[48] In this case, cyclic terpenes such as pinene, limonene, menthone, and carene can be selectively transformed into nitrogen-containing monomers through oxidation to ketones, oxime formation, and subsequent Beckmann rearrangement, affording chiral lactams suitable for ring-opening polymerization in close analogy to the industrial synthesis of polyamide 6. Alternatively, terpene-derived diamines have been employed in step-growth polycondensation routes, enabling the incorporation of rigid cyclic units directly into the polymer backbone. These strategies provide access to terpene-based polyamides with tunable crystallinity and thermal properties, ranging from amorphous transparent materials to semi-crystalline, high-performance polymers, while preserving opportunities for further functionalization inherited from the terpene scaffold.

Other terpene-derived cyclic anhydrides and esters have been employed as monomers for ROP, enabling the synthesis of biodegradable polyesters and polycarbonates with tailored properties. Examples include the conversion of borneol, camphor, and menthol derivatives into cyclic monomers, producing aliphatic polyesters with moderate to high glass transition temperatures and hydrolytic degradability.[49–51] These strategies extend the utility of terpenes to classes of polymers beyond elastomers, enabling the design of biodegradable materials and specialty polymers for biomedical or packaging applications.

1.5.1. Stereoselective Polymerization of Acyclic Terpenes

In recent years, there has been a renewed interest, supported by the urgency to develop renewable elastomers and polyolefinic materials, leading to the application of modern coordination-insertion catalysts to achieve stereoregular polymerization of terpenes.[52] Acyclic terpenes such as *myrcene*, *ocimene*, and *farnesene* have emerged as the most promising candidates due to their conjugated diene structures, which closely resemble those of butadiene and isoprene. Their stereoselective polymerization has been extensively investigated using rare-earth, titanium and group 3 metal catalysts, which are particularly effective in controlling both the regio- and stereochemistry of conjugated diene polymerizations. These systems have provided access to a wide range of microstructures, including *cis-1,4*, *trans-1,4*, and *3,4* configurations (Scheme 1.8), depending on the catalyst structure and reaction conditions.[42]

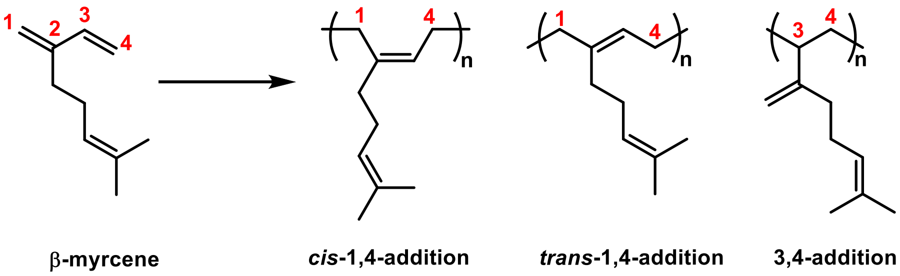

Scheme 1.8. Possible Microstructures of Poly(Myrcene) Depending on the Polymerization Regioselectivity.

The stereoselective polymerization of myrcene has been the subject of extensive investigation owing to its structural similarity to isoprene and its potential as a renewable monomer for synthetic rubbers. A wide range of rare-earth and group 3 metal complexes has been employed to achieve control over both the regio- and stereochemistry of the polymerization.

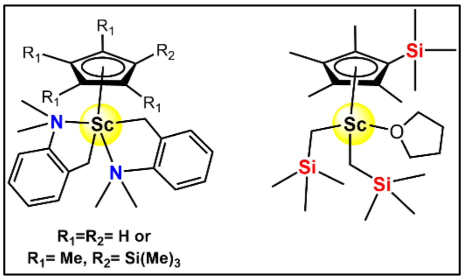

Figure 1.22. Half-Sandwich Scandium Complexes.

Early work by Hou *et al.* demonstrated that half-sandwich scandium complexes (Figure 1.22), in combination with the borate activator $[Ph_3C][B(C_6F_5)_4]$, were highly active in the homopolymerization and copolymerization of myrcene with ethylene and propylene under mild conditions (typically in toluene, at 25 °C).[53] These catalytic systems afforded both block and random copolymers, depending on the feed composition, with tunable glass transition and melting temperatures associated with the respective poly(myrcene) and poly(olefin) segments.

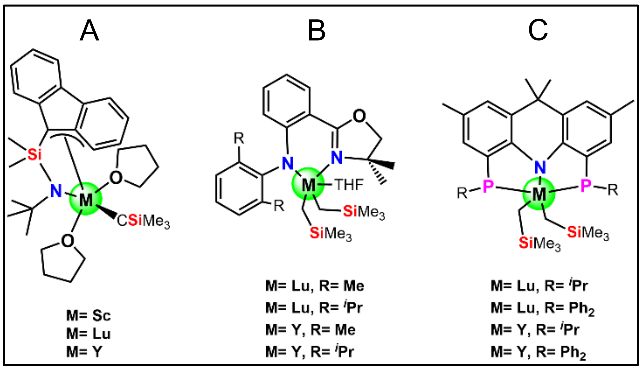

Figure 1.23. Fluorenyl-Amide Rare Earth Metal Complexes (A); Anilido-Oxazoline Supported Lu and Y Complexes (B); PNP Ligated Rare-Earth Complexes (C).

Further studies expanded the scope of myrcene polymerization using various lanthanide-based complexes such as fluorenyl-amide, amidinate, anilido-oxazoline, and PNP-pincer ligands, coordinated to metals including yttrium, lutetium, and lanthanum (Figure 1.23). Under typical reaction conditions (0-70 °C, in toluene or chlorobenzene, with AlR_3 cocatalysts), these systems produced highly *cis*-1,4-selective poly(myrcene) with relatively narrow dispersities (Đ ≈ 1.3-2.0). In several cases, the reactions proceeded in a living or quasi-living fashion, allowing excellent molecular weight control and the synthesis of well-defined block copolymers.[54] In particular, binuclear yttrium amidinate complexes exhibited exceptional 3,4-selectivity and stereocontrol, furnishing isotactic or syndiotactic 3,4-poly(myrcene) with narrow molecular weight distributions and high catalytic efficiency.[55]

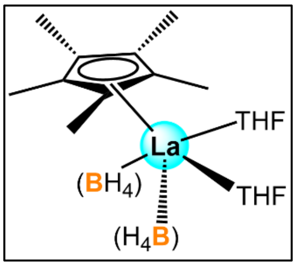

Figure 1.24. Lanthanum complex $Cp^*La(BH_4)_2(THF)_2$.

An alternative approach to myrcene polymerization involved coordinative chain-transfer polymerization (CCTP), developed using lanthanum or neodymium catalysts in combination with alkylmagnesium or alkylaluminum reagents acting as chain-transfer agents. Lanthanum complex $Cp^*La(BH_4)_2(THF)_2$ (Cp*=pentamethylcyclopentadienyl) (Figure 1.24) enabled the synthesis of highly *trans*-1,4-selective poly(myrcene) as well as their copolymers with isoprene or styrene, combining good stereoregularity with improved catalyst economy.[56] Neodymium-based complexes, including borohydride, phosphate, and alkoxide derivatives, also exhibited high *cis*-1,4 selectivity and pseudo-living behavior, enabling the preparation of block copolymers and end-functionalized trans-1,4-poly(myrcenes) through controlled termination reactions.[57,58]

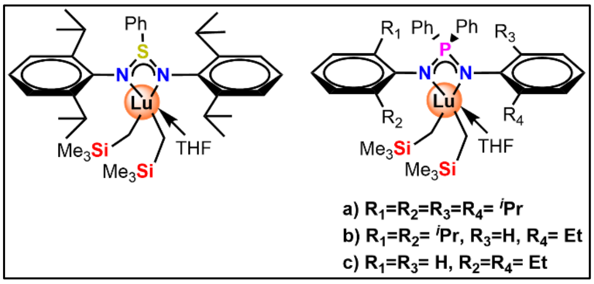

Figure 1.25. Lutetium Complexes with NSN (left) and NPN (right) Ligand.

More recently, the development of lutetium complexes bearing NSN or NPN ligands (Figure 1.25) has led to a new class of catalysts capable of promoting the 3,4-regioselective polymerization of myrcene.[59,60] When activated by $[Ph_3C][B(C_6F_5)_4]$ and trialkylaluminum reagents, these systems exhibited remarkable stereocontrol, providing either isotactic or syndiotactic 3,4-poly(myrcene) depending on the ligand steric environment and the solvent polarity. Typical reactions were conducted between -30 and 60 °C in chlorobenzene, yielding polymers with narrow molecular weight distributions (Đ ≈ 1.4-2.4).

The stereoregular polymerization of ocimene was first reported by Li and Zhang in 2016, representing a significant advancement in the polymerization of substituted conjugated dienes.[61,62] Using half-sandwich rare-earth metal dialkyl complexes bearing either chiral or achiral cyclopentadienyl ligands, in combination with the activator $[Ph_3C][B(C_6F_5)_4]$ and triisobutylaluminum, the authors achieved unprecedented levels of regio- and stereocontrol. Under mild reaction conditions, scandium complexes bearing chiral ligands afforded syndiotactic *cis*-1,4-poly(ocimene) with up to 100% selectivity, whereas the corresponding achiral analogues produced isotactic *trans*-1,2-poly(ocimene) with selectivities up to 78% (Scheme 1.9). The reaction temperature was found to be crucial: decreasing the temperature significantly enhanced both *cis*-1,4 and syndiotactic selectivity.

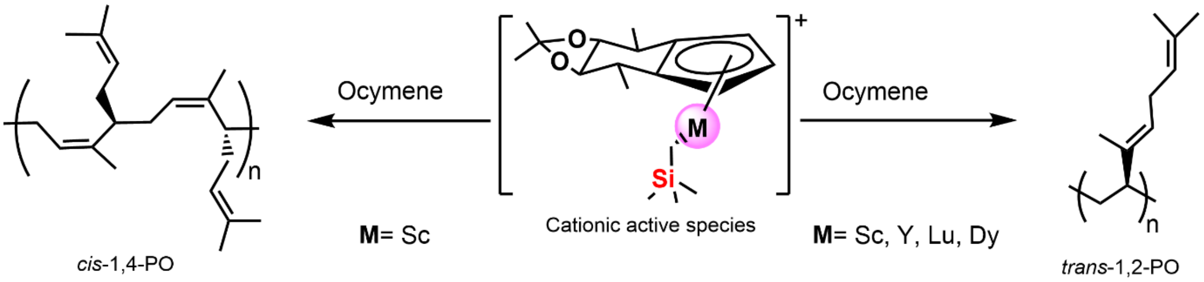

Scheme 1.9. Regio and stereocontrolled polymerization of Ocymene by Sc, Y, Lu and Dy complexes.

Analogous complexes of lutetium, yttrium, and dysprosium displayed similar selectivity trends, albeit with lower catalytic activities, producing polymers with molecular weights in the range of 30-250 kg·mol^{-1}. These studies collectively demonstrated the ability of rare-earth catalysts to achieve precise stereo- and regiocontrol in ocimene polymerization, providing the first examples of stereoregular poly(ocimene) under mild and controllable conditions.

The polymerization of farnesene has been comparatively less explored. The most effective catalytic systems have been based on neodymium complexes, particularly the neodymium versatate (NdV_3) system, activated by alkylaluminum reagents such as Al^iBu_2H or $AlEt_2Cl$.[63] Reactions typically conducted in cyclohexane at 50-60 °C yielded *cis*-1,4-poly(farnesene) with high molecular weights (up to 200-250 kg·mol^{-1}) and moderate dispersities (Đ ≈ 3-4). The resulting polymers exhibited low glass transition temperatures (-30 to -25 °C) and mechanical properties reminiscent of natural rubber, confirming their potential as renewable elastomeric materials.

Moreover, *ansa*-neodymocene catalysts (Figure 1.26) were later employed for the copolymerization of farnesene and myrcene with styrene, under relatively mild conditions.[64] These systems afforded random copolymers and terpolymers in which the terpene units were homogeneously distributed along the polystyrene backbone, as confirmed by the observation of a single, composition-dependent glass transition temperature. The resulting materials combined the flexibility of poly(terpene) segments with the rigidity of polystyrene domains, providing a new family of hybrid, partially bio-based elastomers.

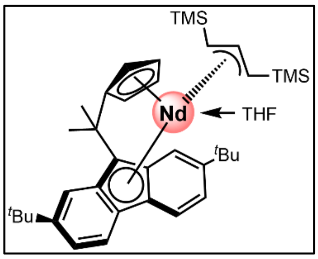

Figure 1.26. Ansa-Neodymocene Catalyst.

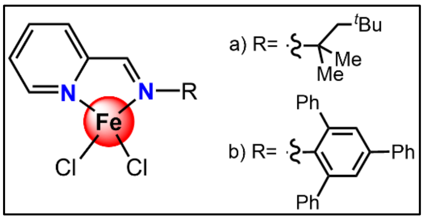

Figure 1.27. Fe(II) Iminopyridine Complexes.

Base metals such as iron and cobalt have also been exploited for terpene polymerization. Fe(II) iminopyridine complexes activated by $[Ph_3C][B(C_6F_5)_4]$ and MAO polymerized myrcene and farnesene at ambient temperature, yielding high molecular weight polymers (M_n > 100 kg·mol^{-1}) with *trans*-1,4 selectivity for myrcene and *cis*-1,4 selectivity for farnesene, depending on the ligand electronics.[65]

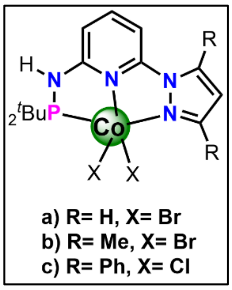

Figure 1.28. Structures of Co(II)-based complexes.

Co(II) complexes bearing PN_3 pincer ligands (Figure 1.28), activated with $AlEt_2Cl$, afforded *cis*-1,4-poly(myrcene) with selectivity up to 98% and M_n up to 289 kg·mol^{-1} when run at 30-80 °C in toluene.[66] Copolymerizations of myrcene with isoprene under these conditions produced elastomeric copolymers with controlled architectures and thermal properties. Later, cobalt complexes supported by phenoxy-imine ligands or oxazoline-pyridine ligands were reported by Gong *et al.* and have enabled the incorporation of functionalized terpenes, such as hydroxylated myrcene, into copolymers, enhancing hydrophilicity and compatibility with silica fillers for elastomer applications.[67]

In conclusion, terpenes are promising candidates in polymer science. Their hydrocarbon skeletons allow the synthesis of stereoregular polyolefinic materials (polymyrcene, polyocimene, polyfarnesene, and their copolymers) that can replace or complement fossil-derived elastomers. The broad spectrum of catalytic systems already explored, including rare-earth (Nd, La, Sc, Y, Lu) and base metal (Fe, Co), demonstrates that terpene polymerization can be conducted under relatively mild conditions, yielding high molecular weight polymers with precise stereocontrol. The combination of abundant industrial availability, structural diversity, and compatibility with modern polymerization methodologies confirms that terpenes are destined to play a central role in the development of next-generation sustainable polymers.

1.6 The Second Life of [OSSO]-Titanium Catalysts: Stereoregular Polymerization of Terpene-Based Monomers

The exploration of titanium-based catalysts for the polymerization of terpenes represents one of the most significant advances toward the development of renewable elastomers with controlled microstructure. The earliest studies in this field date back to the 1960s, when heterogeneous Ziegler-Natta systems, such as $TiCl_4$ combined with trialkylaluminum cocatalysts, were applied to the polymerization of β-myrcene, yielding polymers with predominant 1,4-insertion but relatively low molecular weights and limited stereochemical control.[68]

After several decades of limited progress, the introduction of homogeneous titanium complexes bearing [OSSO]-type bis(phenolate) ligands marked a renaissance in the catalytic polymerization of terpenes. In recent years, Capacchione and co-workers have developed a systematic series of studies on the stereoselective polymerization and copolymerization of renewable linear terpenes, including β-myrcene (**M**), β-ocimene (**O**), and β-farnesene (**F**).

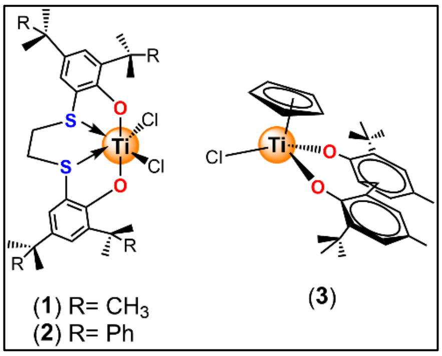

Figure 1.29. Titanium complexes with [OSSO]-type ligands (complexes **1** and **2**) and Ti(η^5-C_5H_5)(η^2-MBMP)Cl_2 (complex **3**).

In the first of these contributions, Naddeo *et al.* investigated both the homopolymerization of **M** and **O** and their copolymerizations with styrene using titanium complexes with tetradentate [OSSO]-type bis(phenolate) ligands (complexes **1-2**, figure 1.29) and Ti(η^5-C_5H_5)(η^2-MBMP)Cl_2 where MBMP= 2,2'-methylenebis(6-*tert*-butyl-4-methylphenoxo) (complex **3**, figure 1.28), activated by methylalumoxane (MAO).[69] The reactions were performed under mild conditions in toluene at temperatures between 0 and 70 °C, allowing the systematic evaluation of the influence of temperature and ligand environment on the regio- and stereochemical outcome of the polymerization.

In the homopolymerization of β-myrcene, the catalysts displayed a temperature-dependent behavior, with activity being negligible below 70 °C but, above this threshold all systems promoted the formation of poly(myrcene) with well-defined microstructures. Both [OSSO]-type complexes (**1** and **2**) provided polymers characterized predominantly by a *trans*-1,4 microstructure ($\mathbf{M^T}$). Interestingly, the more sterically congested complex **2** exhibited lower stereoselectivity compared to complex **1**, yielding polymers that contained up to 40 % of 3,4-vinyl units ($\mathbf{M^V}$) along the backbone. This behavior was attributed to the increased steric hindrance around the titanium center in complex **2**. Conversely, the related titanium complex **3** produced a polymer with a predominantly *cis*-1,4 microstructure ($\mathbf{M^C}$), essentially unaffected by variations in the polymerization temperature. In this case, increasing the reaction temperature resulted primarily in a decrease of the polymer's molecular weight rather than any significant change in microstructure. The resulting materials displayed glass transition temperatures around -65 °C, consistent with the formation of flexible, elastomeric polymers.

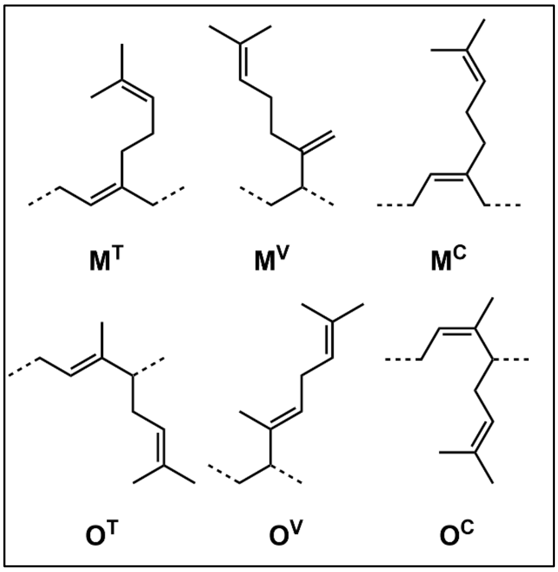

Figure 1.30. The possible *trans*-1,4, 3,4-, and *cis*-1,4 microstructures of β-myrcene (top) and β-ocimene (bottom).

The homopolymerization of β-ocimene was also investigated under conditions analogous to those employed for myrcene, using titanium complexes **1-3**, activated by methylalumoxane (MAO). At room temperature, complex **1** produced a polymer composed of approximately 50% *trans*-1,4-units **(O^T)** and 50% 1,2-vinyl-units **(O^V)**, while the more sterically congested complex **2** exhibited higher activity and selectivity, yielding a polymer with up to 92 mol% 1,2-vinyl units. The influence of temperature was found to be significant. When the reaction temperature was increased (from 0 °C to 70 °C), complex **1** progressively shifted its selectivity toward *trans*-1,4-insertion. Conversely, decreasing the temperature to 0 °C in the case of complex **2** promoted the formation of an almost only 1,2-poly(ocimene), with negligible amounts of 1,4-linkages. The polymer obtained under these conditions displayed a highly isotactic 1,2-trans tacticity. In analogy with the behavior observed in myrcene polymerization, the titanium complex **3** generated less stereoregular polymers, characterized mainly by a *cis*-1,4 microstructure **(O^C)**, independent of the polymerization temperature.

These systems have also been extended to copolymerization with styrene. The authors demonstrated that the same [OSSO]-Ti catalysts could copolymerize M and O with **styrene**, giving rise to poly(terpene-co-styrene) materials with high terpene incorporation (up to 96 mol%). The microstructure of the resulting copolymers depended on both the reaction temperature and the steric environment of the catalyst. In most cases, random copolymers were obtained at moderate temperatures (25-50 °C), whereas under specific conditions, the system enabled the formation of short isotactic polystyrene sequences incorporated within *trans*-1,4-polyterpene segments, resulting in materials with multiblock-like architectures. Structural analyses performed through high-resolution NMR spectroscopy confirmed the presence of well-defined junctions between styrene and terpene units. The resulting copolymers displayed tunable glass transition temperatures and viscoelastic properties that could be modulated by varying the styrene content, demonstrating the ability of titanium [OSSO]-type complexes to control both stereoregularity and sequence distribution within the polymer chain.

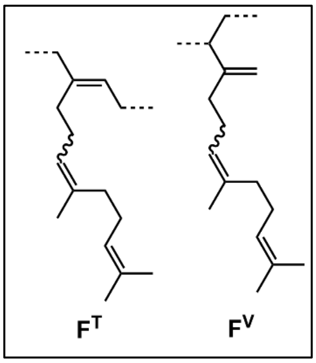

Figure 1.31. The possible *trans*-1,4 and 3,4-microstructures of β-farnesene.

Building upon these results, Lamparelli *et al.* further expanded the catalytic scope by exploring both the homopolymerization of β-farnesene and the copolymerization of M, O, and F with 1,3-butadiene, employing the same titanium-based catalytic system (complex **2**, figure 1.29) activated by modified methylalumoxane (m-MAO).[70] The homopolymerization of **F** was initially attempted at 30 °C but proved unsuccessful, likely due to the lower intrinsic reactivity of farnesene compared to its congeners **M** and **O**. However, by increasing the reaction temperature to 50 °C, poly(farnesene) was successfully obtained. The resulting polymer exhibited a molecular weight of approximately 9 kg·mol^{-1} with a narrow polydispersity, and NMR analyses revealed a predominantly 1,4-insertion **(F^{T})**. Under mild reaction conditions (in toluene, 30-50 °C, [Al]/[Ti] = 800), complex **2** yielded terpene-butadiene copolymers, poly(ocimene-butadiene) (**POB**), poly(myrcene-butadiene) (**PMB**), and poly(farnesene-butadiene) (**PFB**), with high terpene incorporation (up to 92%, 71%, and 86% for O, M, and F, respectively) and excellent stereocontrol, reaching up to 95% *trans*-1,4 selectivity in the butadiene units. The obtained copolymers exhibited multiblock microstructures, and their glass transition temperatures varied from -24 °C to -71 °C depending on the terpene content. Remarkably, when incorporated into model tire tread formulations, POB-based materials demonstrated improved mechanical and dynamic properties relative to commercial *cis*-polybutadiene, confirming the potential of these partially bio-based copolymers for industrial applications.

These studies collectively demonstrate that titanium catalysts, particularly those supported by [OSSO]-type bis(phenolate) ligands, enable an unprecedented level of control in the stereoselective polymerization of renewable conjugated dienes, including the homopolymerization and copolymerization of terpenes with styrene and butadiene. Their ability to modulate *cis/trans* and *1,2/1,4* selectivity through variations in the ligand environment, reaction temperature, and cocatalyst composition allows for the synthesis of well-defined homo-, co-, and terpolymers with finely tuned microstructures and tailored physical properties. Such tunability places these systems among the most versatile and effective catalytic platforms available for transforming bio-based terpenes into sustainable elastomeric materials.

1.7 Aim of the Project

The [OSSO]-titanium catalytic systems described so far have shown promising reactivity toward conjugated monomers derived from biobased feedstocks, thus extending their potential beyond terpenes. The study of these systems and their (co)polymerization behavior is the focus of this doctoral research and will be detailed in subsequent chapters. The objective of this thesis is to demonstrate that conjugated dienes derived from natural aldehydes can be efficiently transformed, through stereoselective (co)polymerization catalyzed by titanium [OSSO], into a coherent family of polymers that includes rigid thermoplastics, soft elastomers, and thermoplastic elastomers, materials capable of competing with their petrochemical counterparts.

To achieve this goal, the work focuses on three conjugated dienes of biological origin that are structurally related but span significantly different topologies and degrees of rigidity. *Trans*-1-phenyl-1,3-butadiene (1PB) is synthesized from cinnamaldehyde, a key component of cinnamon essential oil, and represents a renewable aromatic diene capable of playing a role analogous to styrenic units. The cyclic diene *S*-4-isopropenyl-1-vinyl-1-cyclohexene (IVC), obtained from perillaldehyde present in *Perilla* herb, combines a constrained cyclohexene backbone with a pendant isopropenyl group that provides both rigidity and functional handles for post-polymerization modification. Linear (E)-4,8-dimethyl-1,3,7-nonatriene (DMNT), synthesized from citral, the major constituent of lemongrass oil, is conceived as an ideal renewable monomer for the construction of elastomeric segments. The non-renewable cyclic diene 1-vinylcyclohexene (VCH) is included as a structurally simplified analogue of IVC, allowing the influence of the isopropenyl substituent on polymerization and material properties to be investigated. Finally, β-myrcene and β-ocimene, two linear terpenes of natural origin, are used as flexible comonomers to modulate the thermal and mechanical behaviour of the resulting copolymers.

Within this molecular framework, the first part of the work is devoted to establishing how titanium [OSSO]-type catalysts, activated with MAO, control the homopolymerization of these monomers. Particular emphasis is placed on comparing complexes containing tert-butyl and cumyl substituents on the aromatic rings of the ligand backbone, in order to understand how the steric properties of the ligand influence activity, regioselectivity, and stereocontrol. Homopolymerizations of 1PB, VCH, IVC, and DMNT are systematically studied as a function of temperature and reaction time. The objective is to identify the conditions under which high yields, high isotacticity, and well-defined insertion patterns are achieved (3,4- for 1PB, VCH, and IVC; 1,2 for DMNT), and to determine the resulting molecular weights and dispersities. The resulting polymers are characterized in detail by NMR, DSC, TGA, and, where appropriate, mechanical testing, in order to map how differences in monomer structure translate into differences in morphology and glass transition behavior. In this way, the work positions each homopolymer along a spectrum from rigid high-T_g thermoplastics (PVCH, PIVC) to glassy aromatic materials (poly(1PB)) to soft low-T_g elastomers (poly(DMNT)).

Based on this homopolymerization study, the second main part of the thesis uses copolymerization as a tool to extend the accessible property space and to approach target architectures relevant for real-world applications. Copolymers of 1PB with β-myrcene and β-ocimene are prepared using the same catalytic systems and conditions optimized for the homopolymerizations, with the goal of combining a cinnamaldehyde-derived aromatic segment with flexible terpene units to generate amorphous materials whose T_g and mechanical response can be tuned. Copolymers of VCH with styrene and with terpenes are explored to benchmark how the cyclic backbone and comonomer selection affect T_g, phase behaviour and the degree of microphase separation in hard-soft systems. IVC is then used in copolymerizations with β-myrcene, β-ocimene and 1PB to build fully or largely renewable materials where perillaldehyde-derived cyclic motifs serve both as rigid segments and as crosslinkable units, thus enriching the structural and functional diversity of the bio-based polymer library. Finally, special attention is paid to DMNT-based copolymers. DMNT is combined with β-myrcene and β-ocimene to adjust T_g and elasticity within purely renewable elastomeric matrices. More importantly, DMNT is copolymerized with IVC and 1PB to cover a range from soft rubbers to materials that emulate the architecture and behavior of industrial SBR and SBS. One-pot one-step DMNT:1PB copolymers are synthesized in compositions chosen to mimic SBR formulations, while One-pot two-step 1PB-DMNT-1PB polymerizations produce triblock copolymers designed as renewable counterparts to SBS.

The third pillar of the thesis is the development of a kinetic and mechanistic understanding of these polymerization processes through *in situ* ^{1}H NMR spectroscopy. Homo- and copolymerizations are monitored directly in sealed NMR tubes that closely emulate those employed in conventional Schlenk-tube experiments. For 1PB, IVC and DMNT homopolymerizations, the goal is to verify that the high regio- and stereocontrol observed on larger scale is preserved, to determine conversion profiles and molecular-weight growth as a function of time, and to identify optimal polymerization temperatures and Al/Ti ratios. For copolymerizations, the consumption of each monomer is followed in real time and analysed using Jaacks and nonterminal BSL models. By extracting reactivity ratios and reconstructing compositional drifts along the chains, the work seeks to classify each system as effectively homopolymeric, gradient, tapered or random and to establish a hierarchy of monomer reactivities as a function of structure and temperature. A key question addressed here is whether these [OSSO]-Ti-catalysed systems can be treated, on the timescale of monomer consumption, as pseudo-living, nonterminal processes, such that kinetic parameters can be used predictively in the design of future copolymer architectures.

In summary, the scope of the project is to show that bio-based conjugated dienes derived from cinnamaldehyde, perillaldehyde and citral, in combination with terpenes such as β-myrcene and β-ocimene and catalysed by titanium [OSSO]-type complexes, can be converted into a broad, structurally well-defined family of polymers whose properties extend from rigid thermoplastics to soft elastomers and thermoplastic elastomers. By integrating stereoselective synthesis, copolymer design, and quantitative kinetic analysis, the thesis aims to demonstrate that these materials can be good candidates to complement and potentially compete with fossil-derived polymers.

Chapter 2

Stereoselective (Co)Polymerization of a Biobased Aromatic Diene Catalyzed by [OSSO]-Titanium Complexes

2.1 1-Phenyl-1,3-Butadiene: state of art

1-Phenyl-1,3-butadiene (1PB) is an aromatic-substituted conjugated diene whose polymerization behavior has long attracted attention as a model system to study the influence of phenyl substitution on conjugated diene coordination and insertion mechanisms. The monomer is typically synthesized via Wittig olefination of *trans*-cinnamaldehyde, providing the *E*-isomer with high selectivity and purity (Scheme 2.1).

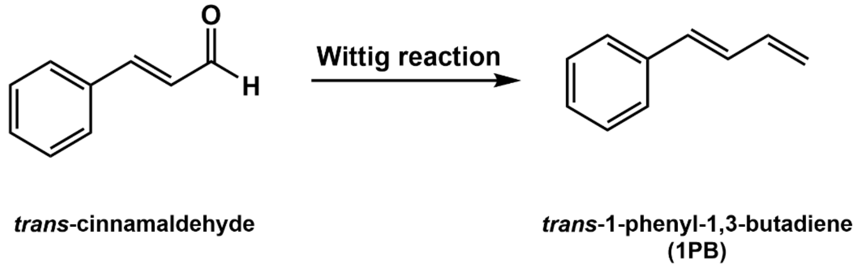

Scheme 2.1. Generic Scheme of the Wittig Reaction of *trans*-cinnamaldehyde.

The first systematic studies on its polymerization were reported by Pragliola *et al.*[71] the polymerization of (*E*)-1-phenyl-1,3-butadiene was investigated using three catalytic systems: $CpTiCl_3$/MAO, Cp^*TiCl_3/MAO, and $Ni(acac)_2$/MAO (Figure 2.1). Among them, Cp^*TiCl_3/MAO was almost inactive, while $CpTiCl_3$/MAO and $Ni(acac)_2$/MAO exhibited moderate activity, leading predominantly to 3,4-polymer structures with minor amounts of 1,4-units. Specifically, the $Ni(acac)_2$/MAO system afforded polymers with about 84% of 3,4-units, whereas $CpTiCl_3$/MAO produced polymers containing approximately 76% of 3,4-units, together with small fractions of 1,4-*cis* and 1,4-*trans* configurations. These results highlight the influence of the catalyst nature on the regioselectivity of (*E*)-1-phenyl-1,3-butadiene polymerization and

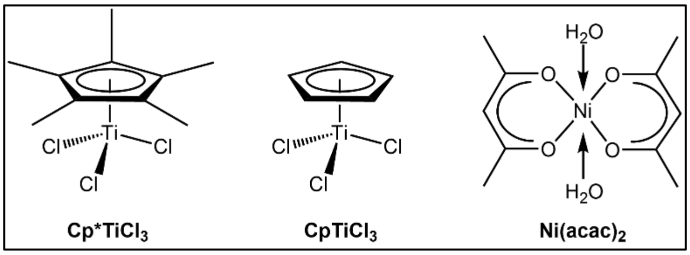

Figure 2.1. Structures of Cp^*TiCl_3, $CpTiCl_3$, and $Ni(acac)_2$.

confirm the strong preference of these systems for 3,4-insertion in aryl-substituted conjugated dienes.

Subsequent work by Lin *et al*. extended this approach to coordination copolymerization of 1PB and its analogues with 1,3-butadiene using $CpTiCl_3$/MAO.[72] In this work, the half-titanocene complex exhibited high activity and strong *cis*-1,4-selectivity, allowing the copolymerization of 1PB with 1,3-butadiene over a wide range of comonomer feed ratios. The incorporation of 1PB increased with the comonomer feed, reaching up to 44.6 mol%, and produced materials with higher glass transition temperatures (from -93.7 °C to -22.4 °C) due to the rigidity of the pendant phenyl groups. These results demonstrated the effectiveness of the $CpTiCl_3$/MAO system in promoting highly regio- and stereoselective copolymerization of phenyl-substituted 1,3-butadienes, enabling the synthesis of phenyl-functionalized polydienes with tunable microstructure and thermal properties.

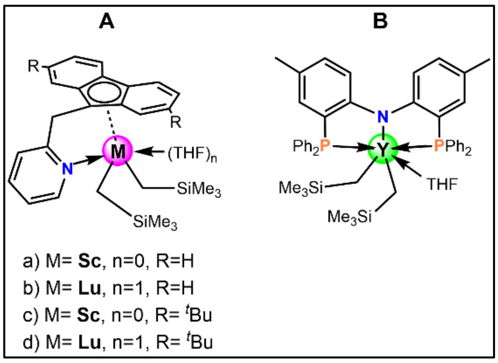

Figure 2.2. Structures of Scandium, Lutetium and Yttrium Complexes.

A major advancement was then achieved with rare-earth metal catalytic systems, which enabled both homo- and copolymerization of 1PB and its polar derivatives with a high degree of stereorecontrol. In particular, Jiang *et al.* reported the polymerization of 1PB using a series of rare-earth metal complexes.[73] The most effective catalysts were pyridyl-methylene-fluorenyl scandium and lutetium complexes (Figure 2.2A) and a bis(phosphinophenyl)amido yttrium complex (Figure 2.2B), all activated with $[Ph_3C][B(C_6F_5)_4]$ and Al^iBu_3. These systems exhibited very high activity and exceptional 3,4-regioselectivity (> 99%) combined with syndiotactic control (≥ 95% *rrrr*). The resulting syndiotactic 3,4-poly(1PB) could be hydrogenated to yield a syndiotactic poly(4-phenyl-1-butene) elastomer with T_g = 17 °C, or converted via cationic cyclization into a rigid cyclic polymer with T_g up to 327 °C. Overall, the study demonstrates that rare-earth complexes with finely balanced steric and electronic environments enable the first highly active and syndioselective 3,4-polymerization of 1PB, producing well-defined stereoregular polymers with tunable mechanical properties.

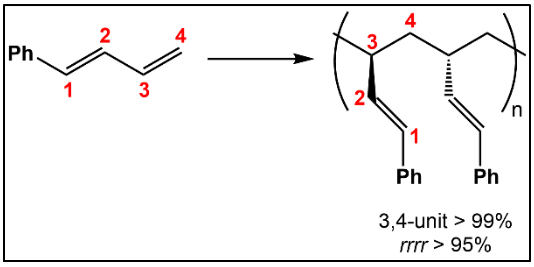

Scheme 2.2. 3,4- insertion of Syndiotactic Poly(1PB).

Building upon this, You *et al.* synthesized a family of halo-, amino-, methoxy-, and thio-substituted 1PB derivatives and polymerized them with unsymmetrical diarylamido rare-earth complexes (Sc, Y, Gd).[74] These catalysts exhibited excellent activity and 3,4-regioselectivity (> 99%), producing polymers with high molecular weights and tunable *Tg* values between 120 °C and 190 °C. Moreover, the copolymerization of *p*-fluorophenyl-1,3-butadiene with 1PB gave random copolymers while fully retaining 3,4-regularity.

Overall, the evolution of 1PB polymerization ranges from early Ziegler-Natta systems producing mixed 1,4/3,4 poly(phenyl-butadiene) to rare-earth-catalyzed processes affording highly 3,4-regular and syndiotactic polymers, marking a transition from semi-random elastomeric materials to well-defined, thermally stable, and potentially functional high-performance polymers.

In this context, the following sections will explore the coordination polymerization of *trans*-1-phenyl-1,3-butadiene promoted by titanium [OSSO] complexes, with the aim of obtaining a highly isotactic polymer, a microstructure that has not been achieved for this monomer so far. Moreover, the copolymerization of 1PB with the linear terpenes β-myrcene and β-ocimene will be investigated to develop fully renewable elastomeric materials that combine the rigidity of the phenyl-substituted diene with the flexibility of terpene-based monomers.

2.2 Isospecific Polymerization of 1-Phenyl-1,3-Butadiene (1PB)

The stereospecific polymerization of 1-phenyl-1,3-butadiene (1PB) was investigated using two titanium complexes bearing [OSSO]-type ligands with different substituents on the aromatic rings: complex **1**, featuring *tert*-butyl groups, and complex **2**, featuring cumyl groups (Figure 2.3). When activated by methylaluminoxane (MAO), complex **1** produced a polymer with not complete regioselectivity and no stereoregularity, while complex **2** showed high regioselectivity toward the 3,4-insertion and remarkable isoselectivity (Scheme 2.3). The results are summarized in Table 2.1.

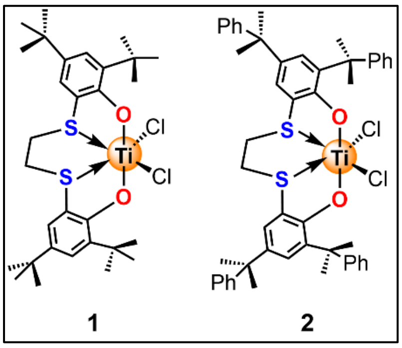

Figure 2.3. Structures of the titanium-[OSSO] complexes **1** and **2**.

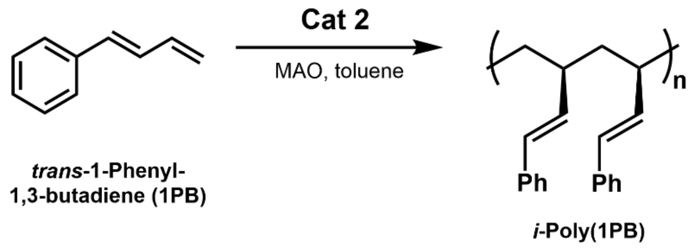

Scheme 2.3. Isospecific polymerization of 1PB promoted by [OSSO]-titanium complex **2**.

Table 2.1. Homopolymerization of 1PB in presence of catalysts **1-2** activated with MAO.

Run[a]	Cat	*T* (°C)	Time (h)	Yield (%)	3,4-unit (%)[b]	*mmmm* (%)[b]	M_n (Kg/mol)[c]	Đ[c]	T_g (°C)[d]
1	**1**	25	15	7	83	*n.d.*	263.0/1.7	3.2/2.3	78.4
2	**1**	40	15	16	83	*n.d.*	111.1/1.5	2.2/2.6	72.7
3	**1**	80	15	17	74	*n.d.*	2.6	8.9	68.7
4	**2**	25	15	12	> 99	> 99	28.8	1.5	85.0
5	**2**	40	15	35	> 99	> 99	37.8	1.9	94.8
6	**2**	80	15	58	> 99	> 99	31.0	2.1	83.7
7	**2**	80	5	54	> 99	> 99	22.4	2.1	80.4
8	**2**	80	24	65	> 99	> 99	21.0	2.3	84.0
9	**2**	80	48	63	> 99	> 99	22.5	2.1	88.9

[a] Reaction conditions: Catalyst **1** or **2** ($1.0 \cdot 10^{-5}$ mol), [Al]/[Ti] = 500, 1PB (2.3 mmol, 0.3 g), toluene (5 mL). [b] Determined by ^{1}H and ^{13}C NMR spectroscopy. [c] Determined by GPC. [d] Determined by DSC in the 2nd heating scan.

Catalyst **1** and **2** were employed in the synthesis of poly(1-phenyl-1,3-butadiene) (poly(1PB)) at various temperatures in toluene. Preliminary polymerizations were carried out using catalyst **1**, which exhibited lower regioselectivity respect to 3,4-insertion and afforded polymers with poor yields and bimodal molecular weight distributions (runs 1-3, Table 2.1). Subsequently, the more sterically hindered catalyst **2** was used and revealed that polymer yield increases with temperature, reaching a maximum of 58% at 80°C after 15 hours (runs 4-6, Table 2.1). In all cases, the obtained polymer exhibited high isotacticity and regioselectivity for 3,4-insertion (> 99%), as confirmed by ^{1}H and ^{13}C NMR analyses (Figure 2.4). The ^{13}C NMR spectrum shows a peak at 40.39 ppm, which is unambiguously assigned to the methylene carbon of the polymer backbone. The absence of other peaks, as reported for the syndiotactic polymer,[73] indicates that the polymer is highly isotactic, with a pentad distribution of *mmmm* > 99%. At a fixed temperature of 80°C, the reaction was monitored at different time intervals - 5, 24, and 48 hours. The results indicate that the maximum yield (65%) was achieved after 24 hours, without further variations. The so-reached quasi-plateau could be attributed to catalyst deactivation over time or the establishment of a dynamic equilibrium where monomer consumption is balanced by chain termination or transfer processes.

The ability to control molecular weights aligns well with the characteristic behavior of [OSSO]-type complexes functioning as single-site catalysts in the polymerization of diene monomers.[31,37,70,75,76] This is particularly evident from the dispersity (Đ) values obtained through gel permeation chromatography (GPC) analyses (see Appendix 2), which highlight the uniformity of the produced polymer chains. The observed dispersity values are indicative of a well-regulated polymerization process where each active site operates independently and uniformly.

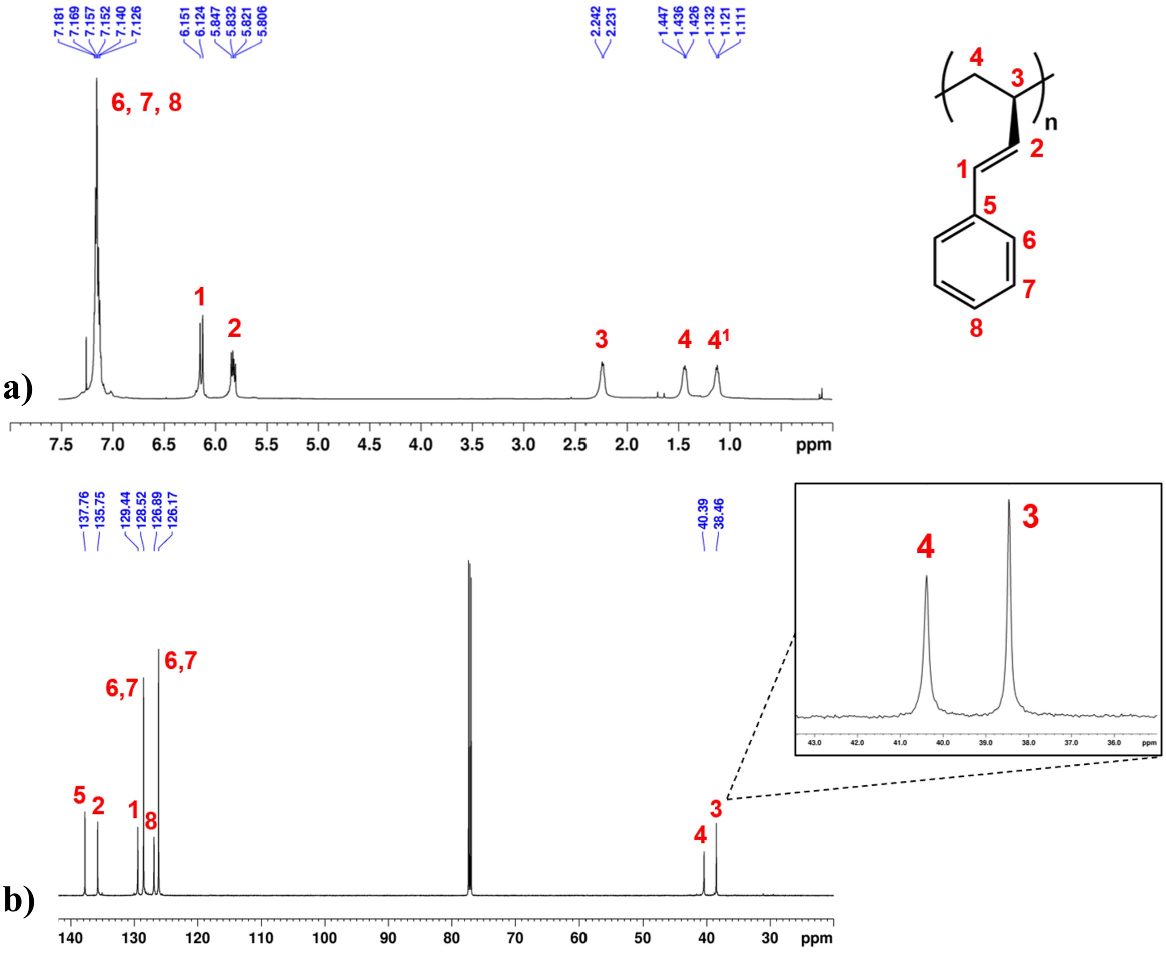

Figure 2.4. a) ^{1}H NMR (600 MHz, $CDCl_3$, 298 K) and b) ^{13}C NMR (150 MHz, $CDCl_3$, 298 K) of 3,4-isotactic poly(1PB) from run **6**, Table 2.1.

The glass transition temperature (T_g) values are slightly lower compared to the T_g of the highly syndiotactic polymer (104°C) produced using rare-earth-based catalysts.[73] This difference can be attributed to the distinct stereoregularity of the polymer chains. Highly isotactic chains, despite their regularity, tend to pack less efficiently in the amorphous phase due to the uniform orientation of bulky substituents along the backbone. The steric congestion generated by this arrangement restricts the ability of chains to approach closely and form strong intermolecular interactions, ultimately resulting in increased free volume and enhanced segmental mobility. In contrast, syndiotactic polymers, where substituents alternate regularly along the chain, often achieve a more favourable spatial distribution that reduces steric hindrances and promotes more compact packing in the amorphous domains. This more efficient packing increases cohesive energy density and limits local motion, thereby leading to a higher T_g than that of their isotactic counterparts.

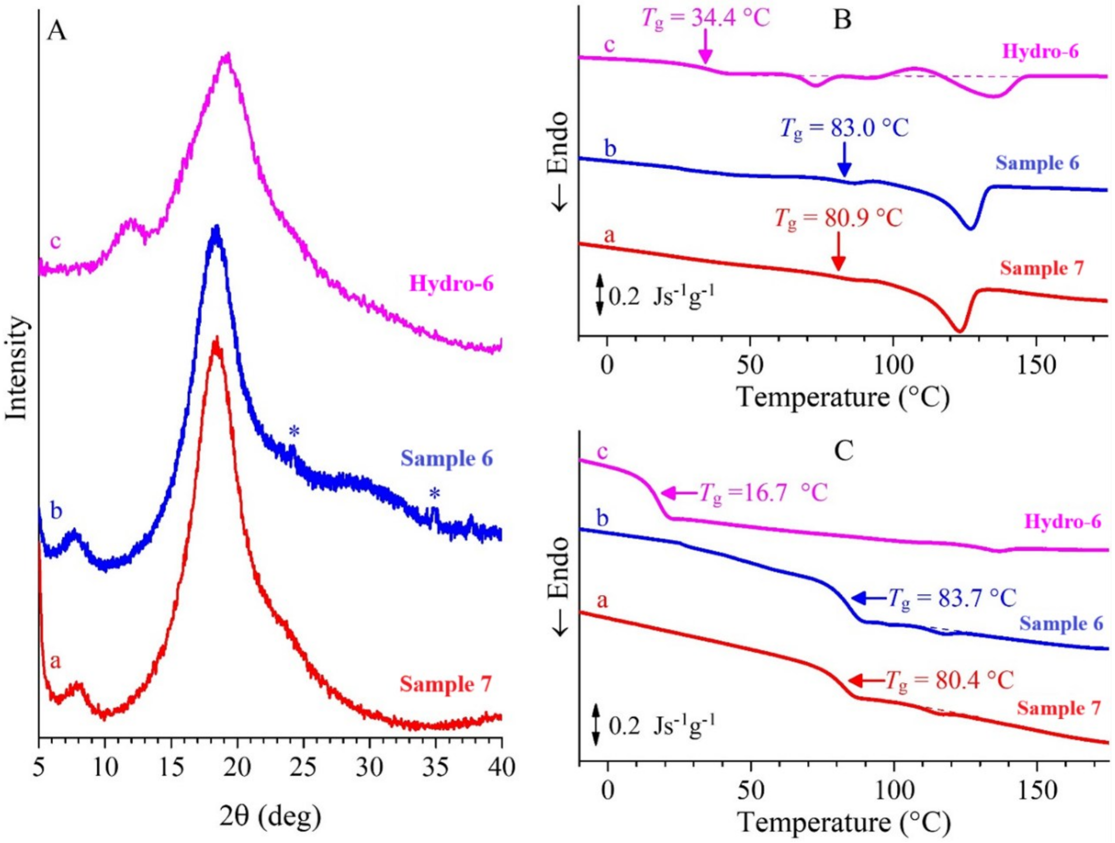

Figure 2.5. X-ray powder diffraction profiles of as synthesized samples **7** (a), **6** (b) and of the sample **6** after hydrogenation Hydro-6 (c) (A), and corresponding DSC curves recorded in the 1st (B) and 2nd heating (C). The stars in A (curve b) mark weak peaks tracing back the presence of a small fraction of a crystalline phase.

As an example, the X-ray powder diffraction (XRD) profiles of the as synthesized samples of runs **6** and **7** (Table 2.1) are shown in Figure 2.5A. It is apparent that the XRD profiles of the samples **6** and **7** were dominated by a main halo centered at $2\theta \approx 18°$, preceded by a weak broad peak centered at 2θ ≈ 8°, corresponding to intra and interchain correlation distances of ≈0.5 and 1 nm, respectively. The absence of relevant Bragg's peaks indicates that the samples were essentially amorphous. Moreover, while the sample **6** showed two faint diffraction peaks at 2θ ≈ 24 and 35 °, possibly due to the presence of a small crystalline fraction, for the sample **7** these peaks were not observed, probably because the crystals had very small size.

The DSC curves of the samples **6** and **7** showed, in the first heating scan, a glass transition temperature at ≈80°C and an endothermic peak around 125 °C (Figure 2.5B) with area corresponding to ≈18 J/g. The endotherm peak at ≈125 °C indicates the presence of a small crystalline fraction, even though the presence of these crystals could not be readily recognized through XRD analysis because they were of very small size (cryptocristallinity).[77] In the successive cooling scan, the DSC curves did not show any relevant exothermic peak, but only the glass transition. However, the DSC curves recorded in the second heating scan showed, beside the glass transition at ≈80°C (Figure 2.5C), a faint endothermic peak at to ≈118 °C (ΔH ≈ 2 J/g), due to the melting of the cryptocrystals.

A sample of 3,4-isotactic(poly1PB) (run 6, Table 2.1) with a T_g of approximately 84 °C was hydrogenated using *p*-toluenesulfonylhydrazine under reflux in *o*-xylene (Scheme 2.4).

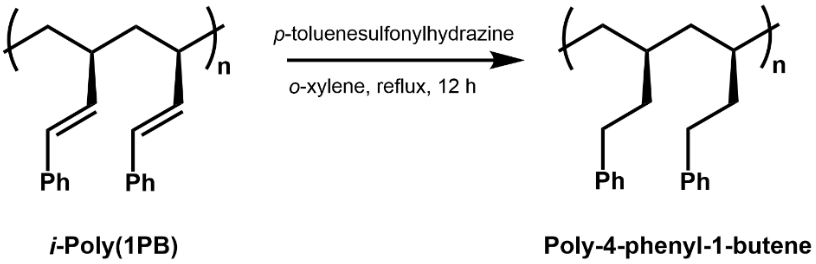

Scheme 2.4. Hydrogenation of 3,4-isotactic(poly1PB).

Complete reduction of the double bonds was confirmed by ^{1}H and ^{13}C NMR spectra (Figure 2.6).

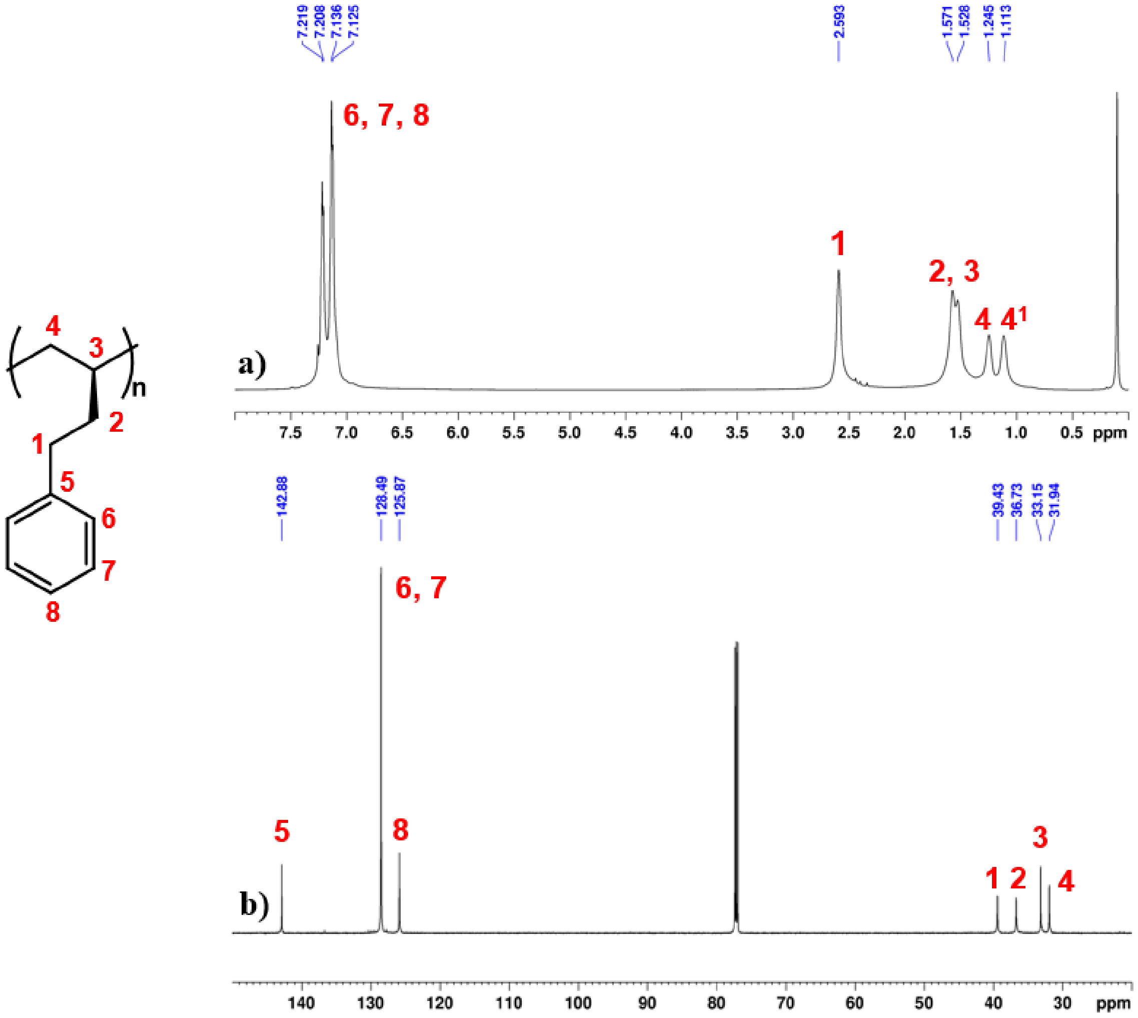

Figure 2.6. a) ^{1}H NMR (400 MHz, $CDCl_3$, 298 K) and b) ^{13}C NMR (100 MHz, $CDCl_3$, 298 K) of 3,4-isotactic poly(1PB) after hydrogenation.

The resulting polymer, poly-4-phenyl-1-butene (**Hydro-6**), retained its stereoregularity but exhibited a significantly lower T_g (approximately 17 °C), as observed by DSC analysis (curve c of Figure 2.5C). The drastic reduction in T_g after the hydrogenation of the polymer double bonds could be attributed to the increased flexibility of the polymer backbone. Indeed, the dumped rotational dynamics of the side chains, in which the -C=C- double bonds are conjugated to phenyl rings, induces a high glass transition temperature of the initial polymer species. The reduction of the double bonds to single bonds eliminates rotational restriction, enhancing chain mobility and thereby lowering the T_g. Besides, the DSC curve recorded in the first heating scan (curve c of Figure 2.5B) showed a first endotherm at ≈76 °C ($\Delta H \approx 3$ J/g) due to the melting of a small crystalline fraction, followed by an exotherm at ≈109 °C ($\Delta H \approx 3$ J/g) due to re-crystallization and a successive endotherm at ≈138 °C ($\Delta H \approx 13$ J/g), marking complete melting of the crystals. The sample did not crystallize from the melt, as indicated by the DSC curve recorded in the cooling step but tended to crystallize in part during the 2nd heating scan, as indicated by the weak melting peak at ≈126 °C ($\Delta H \approx 2$ J/g) (curve c of Figure 2.5C). The lack of any exothermic peak in the cooling and/or 2nd heating DSC scans indicate that crystallization from the melt and/or the amorphous phase (cold crystallization) occurred over a broad range of temperatures above the T_g, so that it could not be observed. It is worth noting that the presence of the crystals in the as-synthesized Hydro-6 samples were not detected in the corresponding XRD profile (curve c of Figure 2.5A). The hydrogenated sample, indeed, did not show Bragg's peaks, probably because the size of the crystals is too low (cryptocrystallinity), but only two haloes centered at $2\theta \approx 12$ and 19° were present, corresponding to inter- and intra-chain correlation distances of 0.7 and 0.5 nm, respectively. The increase of chain flexibility achieved by hydrogenated 3,4-isotactic poly(1PB), indeed, led to approach lower inter and intrachain correlation distances than those achieved by the non-hydrogenated counterpart.

Isotactic poly-4-phenyl-1-butene was early synthesized from 4-phenyl-1-butene through $TiCl_4$ in presence of triethylaluminum as catalyst system.[78] The resulting polymer showed DSC curves similar to those of hydrogentated poly(1PB) of Figure 2.5B (Hydro-6, curve c), with a melting temperature of ≈158 °C. Specimens, stretched up to 2-3 times the initial length and then annealed under vacuum for 1 week at 120 °C, suitable for X-ray fiber diffraction analysis, were then obtained. It is shown that the polymer crystallized with chain in 3/1 helical conformation, packed in a monoclinic unit cell with orthorhombic parameters ($a = 1.04$ nm, $b = 1.80$ nm., $c = 0.661$ nm), according to the space group symmetry *Pa.* The results achieved in the present investigation demonstrate that isotactic poly(4-phenyl-1-butene) may be obtained also by hydrogenation of isotactic poly(1PB) and highlights the impact of backbone structure on the thermal and mechanical behavior of polymers.

2.3 Copolymerization of 1PB with Linear Terpenes

To further explore the synthesis of polymers derived from renewable sources, catalysts **1-2** were subsequently employed in the copolymerization of 1PB with two natural terpenes: β-ocimene (O), mainly found in the essential oils of aromatic plants such as basil, mint, and lavender, and β-myrcene (M), abundantly present in bay, hops, lemongrass, and other plant resins (Scheme 2.5).

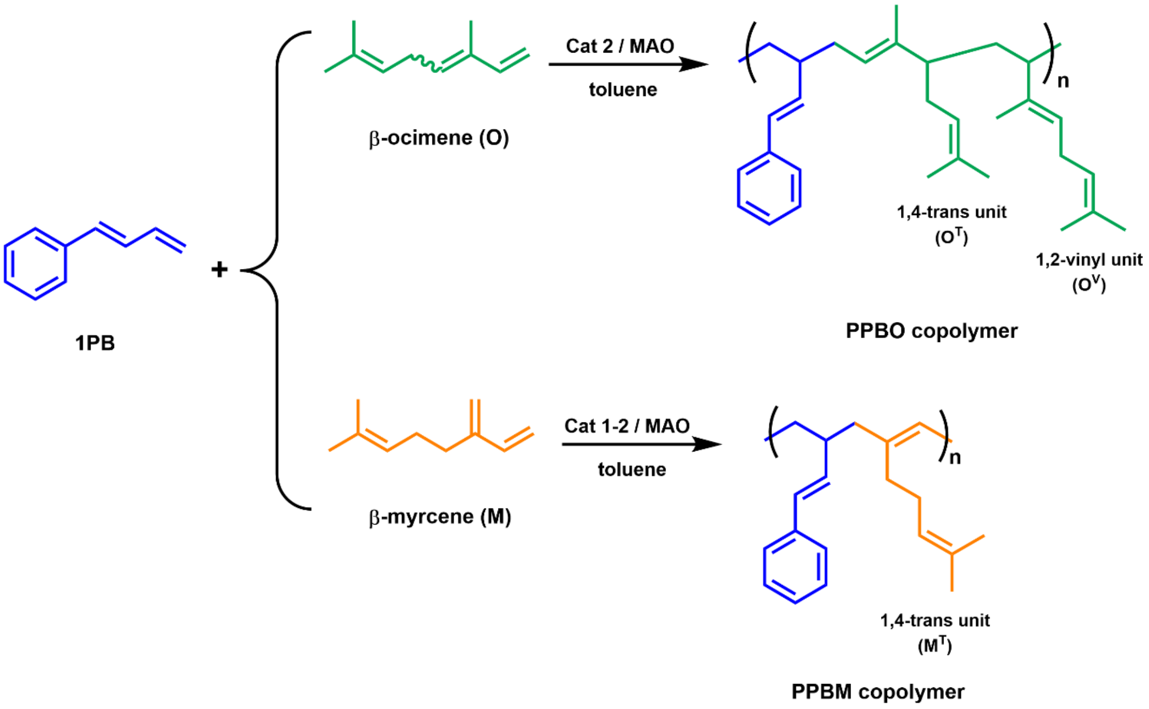

Scheme 2.5. Copolymerization of 1PB and terpenes promoted by [OSSO]-titanium complexes (**1** and **2**) activated with MAO.

Several experiments were conducted by varying the composition of the two monomers to investigate how their ratio influences the chemical, thermal, and mechanical properties of the resulting copolymers, with the aim of obtaining fully bio-based elastomeric materials featuring tunable performance. O/1PB (PPBO) and M/1PB (PPBM) copolymers were hence obtained, as summarized in Table 2.2.

Table 2.2. Copolymerization of 1PB and terpenes in presence of catalysts **1-2**/MAO.

Run [a]	Cat.	Terp. / mol%	Yield (%)	M_n (Kg/mol) [c]	Đ [c]	Polymer composition (%) [b]		T_g (°C) [d]
						Terp. (mol%)	1PB (mol%)	
1	**2**	**O** / 50	56	40.4	2.3	46	54	61.8
2	**2**	**O** / 70	45	29.6	2.0	64	36	43.7 / 133.4
3	**2**	**O** / 80	56	37.8	2.1	81	19	-20.4
4	**2**	**M** / 50	39	45.0	2.3	18	82	53.7
5	**2**	**M** / 80	18	20.2	2.1	46	54	68.7
6	**1**	**M** / 50	9	3.3	4.1	40	60	58.4
7	**1**	**M** / 80	9	1.9	6.6	72	28	11.2

[a] Reaction conditions: Catalyst ($5.0 \cdot 10^{-6}$ mol), ([1PB]+[Terp])/[Ti] = 1000, [Al]/[Ti] = 500, toluene (5 mL), 80°C, 24 h. [b] Determined by ^{1}H and ^{13}C NMR spectroscopy. [c] Determined by GPC. [d] Determined by DSC in the 2nd heating scan.

In the copolymerizations of 1PB with *β*-ocimene with catalyst **2**, the final polymer composition aligns with the molar ratio used between the two comonomers. The maximum conversion of 1PB is consistent with the conversion observed in homopolymerizations (approximately 60%), resulting in a polymer with lower yield in all three cases (runs 1-3, Table 2.2). The microstructure of all copolymers was thoroughly characterized using a combination of analytical techniques, including NMR spectroscopy, gel permeation chromatography (GPC), and differential scanning calorimetry (DSC). The ^{1}H and ^{13}C NMR spectra (Figure 2.7) of the PPBO copolymers suggest a possible multiblock structure, where short homosequences of both comonomers alternate along the polymer chain. Indeed, both types of insertions of *β*-ocimene, 1,4-*trans* (O^T) and 1,2-vinyl (O^V), are observed, as expected.

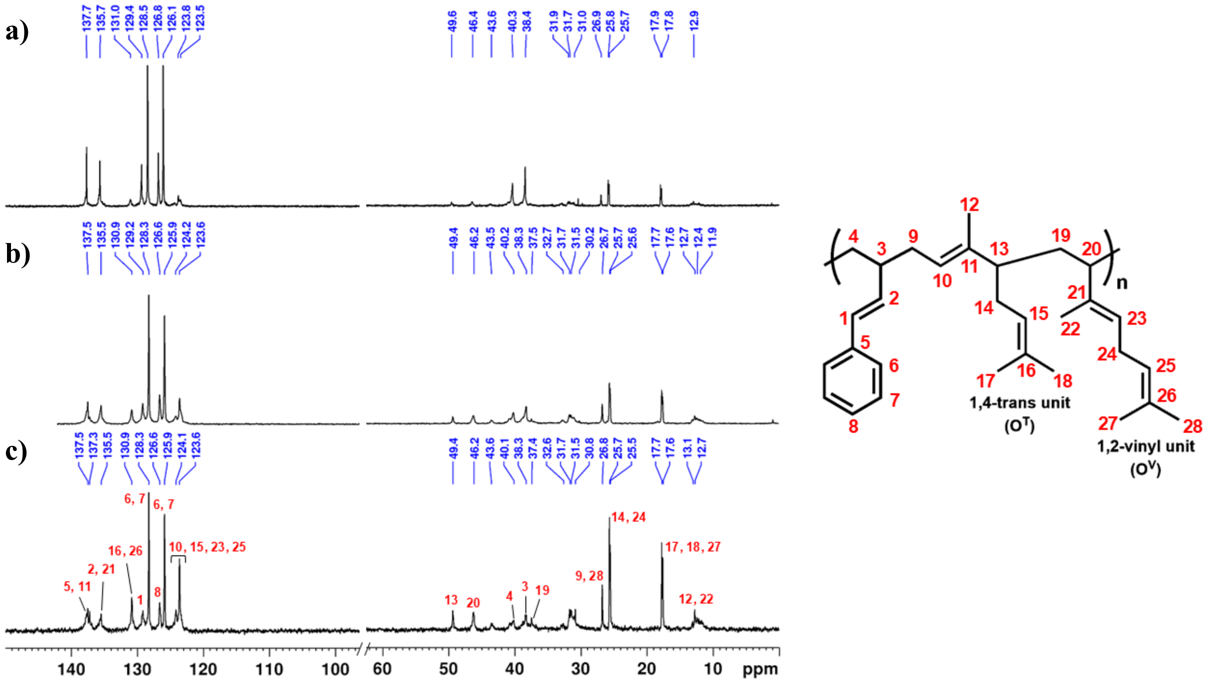

Figure 2.7. ^{13}C NMR spectra (100 MHz, $CDCl_3$, 25°C) of PPBO copolymers from: a) run **1**, b) run **2** and c) run **3** of Table 2.2.

In all cases, the GPC analyses revealed monomodal profiles (see Appendix 2), and the Đ values confirmed the copolymeric nature of the samples, whereas the XRD profiles (Figure 2.8, left) indicate that all the samples are amorphous. Additionally, the DSC curves (Figure 2.8, right) recorded in the 1st heating scan showed, at temperatures greater than ≈100 °C, the presence of spurious exothermic and/or endothermic peaks. These peaks are especially evident for the samples **2** and **3**. They are due to a portion of chain segments undergoing cross-link reactions, and also, in part, to slight degradation. In particular, a slight degradation is indicated by the small weight loss occurring at temperatures lower than 200 °C in the thermogravimetric (TGA) traces (see Appendix 2). Moreover, the occurrence of cross-linking reactions was indicated by the presence of a glass transition in the 2nd DSC heating traces of the sample **2** with terpene content of 64 mol%, at temperatures of ≈133 °C, that is at temperatures significantly greater than those of the homopolymers polyocimene,[69] and poly(1PB). These samples showed a second glass transition at temperatures lower or similar to those of the corresponding homopolymers, indicating phase separation of cross-linked and non-cross-linked segments in different domains. The samples **1** and **3**, with terpene unit content of 46 and 81 mol%, respectively, instead, showed a single glass transition temperature, due to the good miscibility of terpene and 1PB sequences. Interestingly, for the uncross-linked fraction of the PPBO copolymers the T_g values showed a marked decrease as the terpene content increased, suggesting a pronounced influence of the terpene incorporation on the thermal properties of the resulting polymers.

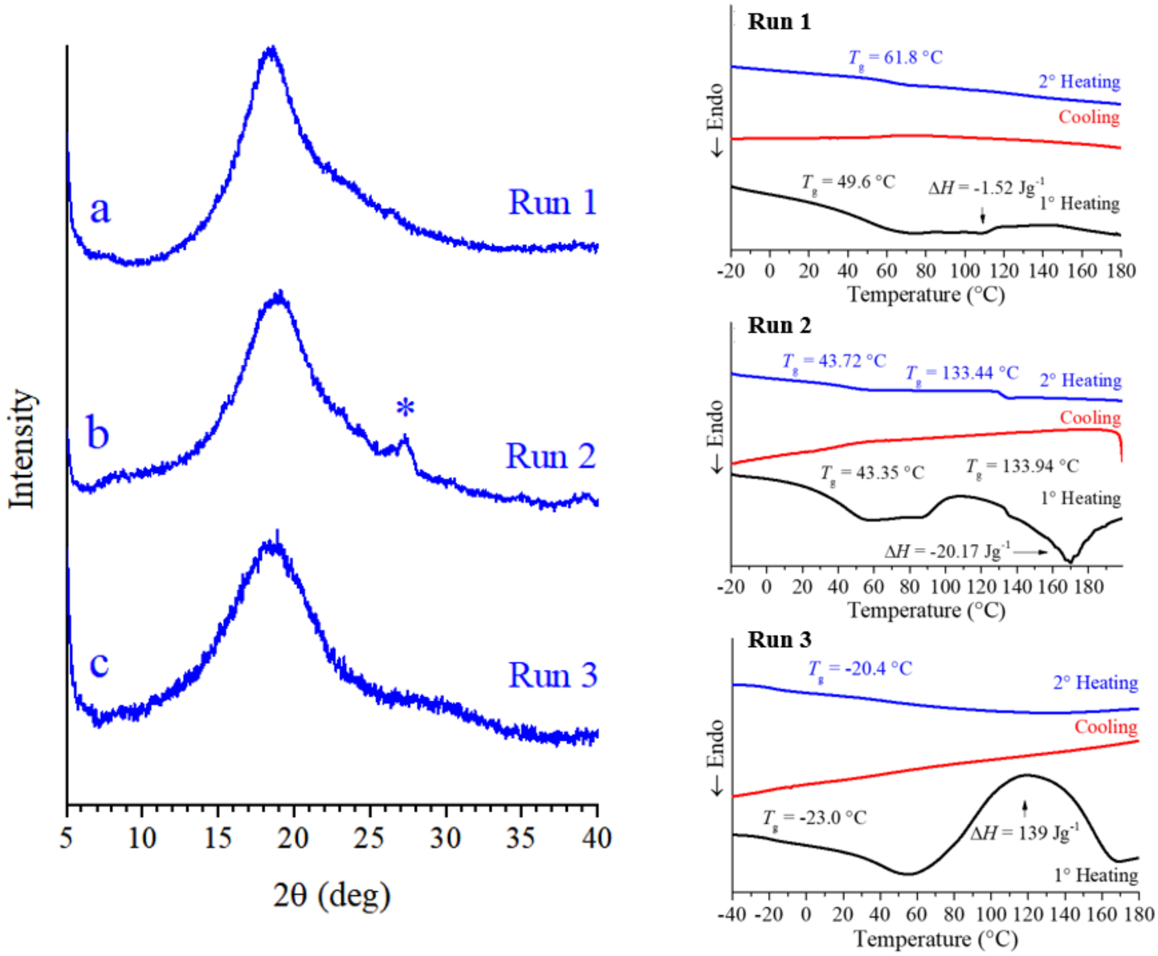

Figure 2.8. X-ray powder diffraction profiles (left) of as synthesized samples **1** (a), **2** (b) and **3** (c) and corresponding DSC curves (right). The star at 2θ ≈ 27 ° (curve b, left) indicate the presence of a small amount of some crystalline impurity (e.g. catalyst remnant).

Preliminary measurements of the mechanical properties of selected PPBO sample (see Appendix 2), measured at room temperature, exhibits a very low stiffness (E = 37 MPa), corresponding to less than 10 % of the Young's modulus typically observed for rigid polymers such as PS or PMMA. This indicates a soft, elastomer-like behavior, consistent with a highly amorphous structure and limited intermolecular interactions.

After the promising results obtained in the copolymerization of 1PB with O, catalyst **2** was also employed in the copolymerization of 1PB with β-myrcene, with the aim of further expanding the scope of renewable terpenic comonomers. A series of experiments was performed by varying the feed composition of the two monomers. Interestingly, unlike what was observed for the β-ocimene system, the copolymer composition did not correspond to the initial monomer feed ratio (runs 4-5, Table 2.2). The ^{1}H and ^{13}C NMR spectra (Figure 2.9A) revealed in both cases a predominant incorporation of 1PB units along the polymer backbone. This unbalanced incorporation can reasonably be attributed to the lower reactivity of β-myrcene toward complex **2**, which bears cumyl substituents on the aromatic rings, and had already proven to be less efficient in the homopolymerization of β-myrcene.[69] The polymer yields, molecular weights, and glass transition temperatures (T_g) are consistent with a higher proportion of 1PB units.

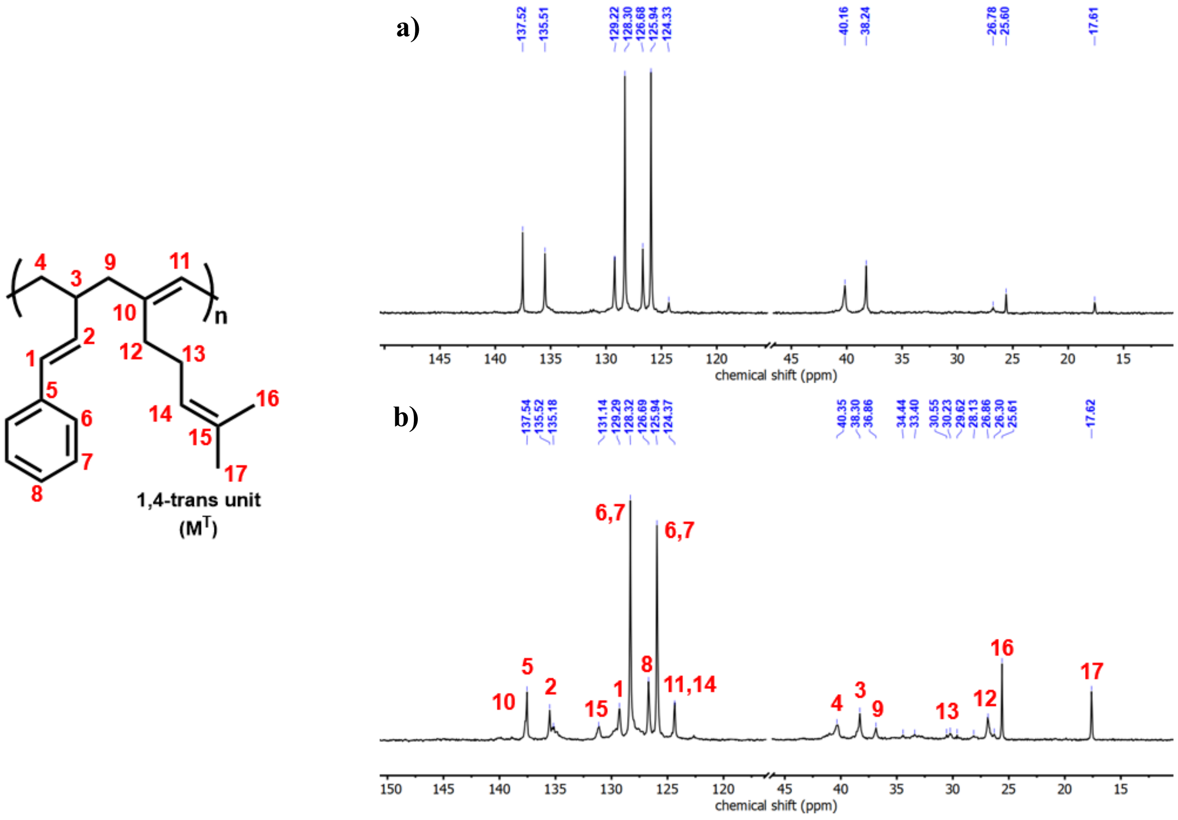

Figure 2.9. ^{13}C NMR spectra (100 MHz, $CDCl_3$, 25°C) of PPBM copolymers from: a) run **4** and b) run **6** of Table 2.2.

To better assess the role of the catalyst structure on the comonomer incorporation, the copolymerization of 1PB and β-myrcene was subsequently carried out in the presence of catalyst 1 (runs 5-6, Table 2.2). As expected, the ^{1}H and ^{13}C NMR analyses (Figure 2.9B) evidenced a higher incorporation of the terpene units into the copolymer chains, confirming the enhanced reactivity of β-myrcene toward the *tert*-butyl-substituted titanium complex. However, this improved incorporation occurred at the expense of both polymer yield and molecular weight, which decreased drastically under the same reaction conditions. Furthermore, as already observed in the homopolymerization of β-myrcene catalyzed by complex **1**, the insertion of the terpene units took place mainly in 1,4-*trans* units, indicating that the steric environment of the OSSO ligand strongly directs the polymerization pathway.

2.4 Conclusion

The stereospecific polymerization of 1PB carried out with the two [OSSO]-type titanium complexes highlighted the decisive role of ligand sterics on both regio- and stereocontrol. Catalyst **1**, bearing tert-butyl substituents, proved less efficient, affording polymers with incomplete regioselectivity, low yields, and bimodal molecular-weight distributions. In contrast, catalyst **2**, featuring cumyl substituents, when activated by methylaluminoxane (MAO), proved highly effective in promoting 3,4-regioselective and isotactic polymerization of 1PB, achieving high stereocontrol (*mmmm* > 99%) and regioselectivity (> 99%) under optimized conditions. The polymerizations showed a clear temperature dependence, with yields increasing up to 80 °C and reaching a plateau after prolonged times due to catalyst deactivation or competitive chain-transfer processes. The microstructural and thermal characterization revealed that the obtained 3,4-isotactic poly(1PB) samples are essentially amorphous, presenting only traces of cryptocrystallinity detectable in DSC but not in XRD. Their glass transition temperatures are slightly lower than those reported for the syndiotactic analogue, emphasizing the impact of tacticity on packing efficiency in the amorphous phase.

Post-polymerization hydrogenation of isotactic poly(1PB) led to a drastic reduction in the glass transition temperature (T_g) from ≈80 °C to 17°C, underscoring the critical role of backbone structure in determining thermal properties. The hydrogenation of the double bonds enhanced chain flexibility, transforming the polymer into a material with a high potential to show elastomeric properties suitable for applications requiring elasticity and impact resistance at lower temperatures.

The subsequent copolymerization studies with renewable terpenes further demonstrated how the interplay between monomer structure and catalyst design governs comonomer incorporation and the resulting polymer properties. In the copolymerization of 1PB with β-ocimene catalyzed by complex **2**, the final polymer composition closely reflected the initial monomer feed ratio, and the maximum 1PB conversion was comparable to that of its homopolymerization. NMR, GPC, and DSC analyses revealed the formation of amorphous copolymers with a possible multiblock microstructure in which short homosequences of both comonomers alternate along the chain. The presence of both 1,4-*trans* and 1,2-vinyl insertions of β-ocimene was confirmed, and DSC/TGA analyses indicated partial cross-linking above 100 °C and phase-separated domains displaying distinct glass-transition behaviors depending on the terpene content. Mechanical measurements confirmed a soft, elastomer-like character for representative PPBO samples.

In the case of β-myrcene, catalyst **2** promoted an unbalanced incorporation of comonomers, with a predominant presence of 1PB units along the polymer backbone, consistent with the lower reactivity of β-myrcene toward the cumyl-substituted complex; conversely, when using catalyst **1**, a higher incorporation of terpene units was observed, although at the expense of polymer yield and molecular weight.

2.5 Experimental Section

2.5.1. Materials and methods. Reagents and solvents were purchased from Sigma-Aldrich, Merck or TCI chemicals. Solvents were dried and distilled before use. All air- and/or water-sensitive compound manipulations were carried out using a glovebox or standard Schlenk techniques under an N_2 atmosphere. Commercial grade toluene (Sigma-Aldrich) was dried over calcium chloride, refluxed 48 h under a nitrogen atmosphere over sodium and distilled before use. Methylaluminoxane (MAO; 10 wt% solution in toluene; Sigma-Aldrich) was used as received. Titanium complex **1** and **2** were synthesized according to the literature procedure.[28] NMR spectra were recorded on a Bruker AM 300 spectrometer (300 MHz for ^{1}H; 75 MHz for ^{13}C), a Bruker AVANCE 400 spectrometer (400 MHz for ^{1}H; 100 MHz for ^{13}C) and a Bruker AVANCE III 600 spectrometer (600 MHz for ^{1}H; 150 MHz for ^{13}C). ^{1}H and ^{13}C chemical shifts are listed in parts per million (ppm) referenced to tetramethylsilane (TMS) using the protio residual signal of the deuterated solvent. Spectra are reported as chemical shift (δ ppm), multiplicity and integration. Multiplicity is abbreviated as follows: singlet (*s*), doublet (*d*), triplet (*t*), multiplet (*m*), broad (*br*), overlapped (*o*). The number-average molecular weights (M_n) and molecular weight distributions of polymers (dispersity, Đ) were evaluated by gel permeation chromatography (GPC) using an Agilent 1260 Infinity Series GPC chromatograph equipped with an RI, PLGPC 220 refractive index detector. All measurements were performed with THF as the eluent at a 1.0 mL/min flow rate at 35°C. Monodisperse poly(styrene) polymers were used as calibration standards. Differential scanning calorimetry (DSC) analyses were carried out with a Mettler Toledo DSC-822 apparatus in a flowing N_2 atmosphere at a rate of 10°C/min. X-ray powder diffraction (XRD) profiles were collected in reflection mode using a multipurpose PANalytical Empyrean diffractometer with the Cu Kα radiation ($\lambda = 0.15418$ nm). Melt pressed films (thickness = 340 μm) were prepared by melting selected as polymerized samples at ≈150 °C under pressure lower than 5 bar, to avoid preferred orientations of the chains, and cooling to room temperature at rate of about 20 °C/min, by circulation of cold water in press plates. Mechanical tests were carried out at room temperature by stretching specimens cut from the melt pressed films (gauge length = 10 mm, width 3 mm), using a universal testing machine (Instron 5566H1543), according to the ASTM D 412−87. The reported stress−strain curves and the values of the mechanical parameters are averaged over at least five independent experiments.

2.5.2. Monomer synthesis. *Trans*-1-phenyl-1,3-butadiene was synthesized according to the literature.[73] Under a nitrogen atmosphere, *n*-butyllithium (40.0 mmol, 16 mL, 2.5 M in hexane) was added dropwise over 30 minutes to a suspension of methyltriphenylphosphonium bromide (14.3 g, 40.0 mmol) in anhydrous THF (250 mL) at 0 °C. The mixture was stirred at 0 °C for an additional 2 hours. Subsequently, cinnamaldehyde (4.2 g, 32.0 mmol) was added dropwise, and the reaction was allowed to proceed at room temperature for 22 hours. Once the reaction was complete, the reaction mixture was neutralized with saturated NH_4Cl, extracted with hexane, dried over Na_2SO_4, filtered, and concentrated under reduced pressure. The pure product was obtained in a 72% yield via column chromatography on silica gel using hexane as the eluent. ^1H NMR (300 MHz, $CDCl_3$): δ 7.34 (d, J = 8.0 Hz, 1H), 7.25 (t, J = 7.5 Hz, 1H), 7.19 – 7.10 (m, 1H), 6.73 (dd, J = 15.6, 10.5 Hz, 1H), 6.55 – 6.34 (m, 1H), 5.27 (d, J = 16.8 Hz, 1H), 5.11 (d, J = 9.7 Hz, 1H).

2.5.3. Polymerization of 1-phenyl-1,3-butadiene (runs 1-9, Table 2.1). Complex **1** or **2** (10 μmol) was added into a 10 mL Schlenk tube equipped with a magnetic stirrer and dissolved in 3 mL of dry toluene. MAO was added, and the solution was left stirring for 30 minutes to pre-activate the metal complex. Then 1PB (2.3 mmol, 0.3 g) was added, and the system was placed in an oil bath thermostated to the desired temperature (25, 40 or 80 °C) and stirred for the required time. The polymers were coagulated in an excess of acidified methanol and containing 2,6-di-tert-butyl-4-methylphenol (BHT) as antioxidant, washed several times with methanol, recovered by filtration and dried in the vacuum oven overnight.

2.5.4. Hydrogenation of poly(1PB). The hydrogenation of poly(1PB) was carried out in accordance with a literature procedure[73]. A 100 mg sample of 3,4-isotactic poly(1PB) (run 6, Table 2.1) was dissolved in 5 mL of o-xylene. An excess of *p*-toluenesulfonylhydrazine was added, and the mixture was stirred under reflux for 12 hours. The fully reduced polymer was subsequently precipitated in methanol, filtered, and dried under vacuum overnight.

2.5.5. Copolymerization of 1PB and *β*-ocimene/ *β*-myrcene (runs 1-7, Table 2.2). Complex **1** or **2** (5 μmol) was added into a 10 mL Schlenk tube equipped with a magnetic stirrer and dissolved in 4 mL of dry toluene. MAO was added, and the solution was left stirring for 30 minutes to pre-activate the metal complex. Then both comonomers (1PB and O/M) were dissolved in 1 mL of dry toluene and added, and the system was placed in a thermostated oil bath at 80°C and stirred for 24 h. The polymers were coagulated in an excess of acidified methanol containing 2,6-di-tert-butyl-4-methylphenol (BHT), washed several times with methanol, recovered by filtration and dried in the vacuum oven overnight.

Chapter 3

Stereoselective (Co)Polymerization of a (Biobased) Cyclic Dienes Catalyzed by [OSSO]-Titanium Complexes

3.1 1-Vinylcyclohexene and 4-isopropenyl-1-vinyl-1-cyclohexene: state of art

1-Vinylcyclohexene (VCH) is a cyclic conjugated diene that structurally combines features of styrene and linear 1,3-dienes, bearing both a vinyl and an endocyclic double bond within a six-membered ring. The monomer can be synthesized by the partial hydrogenation of 1-ethynylcyclohexene using a Pd/$CaCO_3$ catalyst contaminated with $Pb(OAc)_2$ (Scheme 3.1).

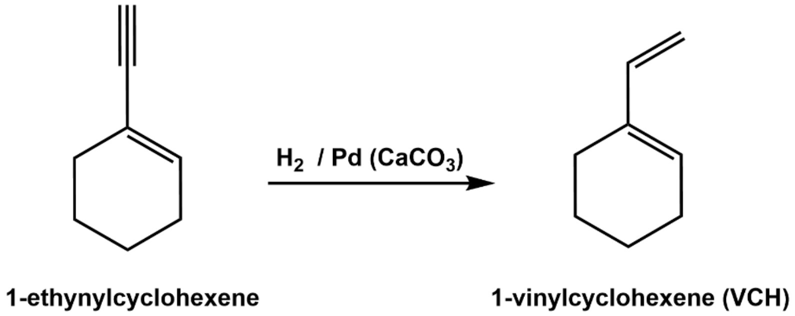

Scheme 3.1. Generic Scheme of the Synyhesis of 1-vinylcyclohexene (VCH).

The first detailed investigation was carried out by Longo *et al.*, who examined the polymerization of VCH using group 4 metallocene catalysts activated by methylaluminoxane (MAO).[79] Their results demonstrated a dependence of the polymer structure on the catalyst employed: $CpTiCl_3$ promoted the formation of a 1,4-*cis* polymer, (Flu)(Cp)iPr$ZrCl_2$ yielded a 1,4-*trans* polymer, and *rac*-[ethylenebis(1-indenyl)]$ZrCl_2$ produced a 3,4-isotactic polymer, even if in very low yield. These findings revealed the ambivalent behavior of VCH, which can act either as a conjugated diene or as a vinylic monomer, depending on the electronic environment of the active site. Moreover, the study suggested that the endocyclic double bond of the cyclohexene ring is only marginally involved in coordination, indicating that VCH behaves similarly to α-olefins during the propagation step. Overall, this work represented an important milestone in understanding how transition metal catalysts can direct regio- and stereoselectivity in cyclic dienes.

More recently, Hahn *et al.* revisited the polymerization of VCH from a different perspective, reporting the first example of living anionic polymerization of this monomer.[80] Using *sec*-butyllithium as an initiator in cyclohexane at 25 °C, they achieved complete monomer conversion and excellent control over molecular weight (Đ = 1.07-1.20), obtaining polymers that contained both 1,4- and 3,4-units (in a 64:36 ratio). The addition of small amounts of tetrahydrofuran as a polar modifier enabled fine tuning of the microstructure toward a higher 3,4 content, resulting in polymers with increased rigidity and glass-transition temperatures up to 89 °C. Upon catalytic hydrogenation, the resulting poly(1-vinylcyclohexene) was converted into poly(vinylcyclohexane) exhibiting even higher thermal stability ($T_g \approx 114$ °C), bridging the gap between flexible polydienes and rigid styrenic polymers. This work demonstrated that VCH can undergo living chain growth with precise structural control, behaving as a conjugated diene in the anionic mechanism but giving rise to materials whose properties closely resemble those of polystyrene.

A structurally related compound, 4-isopropenyl-1-vinyl-1-cyclohexene (IVC), has recently gained attention as a renewable analogue of VCH. It differs by the presence of an isopropenyl substituent attached to the ring, which increases steric bulk and provides an additional unsaturation site. Importantly, IVC can be synthesized from renewable sources, as it is derived from perillaldehyde, a natural monoterpenoid, through a Wittig reaction (Scheme 3.2).

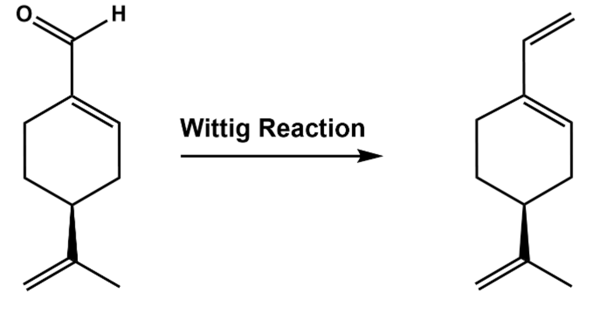

Scheme 3.2. Generic Scheme of the Wittig Reaction of Perillaldehyde.

In a recent study, Liu *et al.* reported the rare-earth-metal-catalyzed polymerization of IVC and other terpene-derived conjugated dienes, achieving 3,4- and isotactic selectivity using a yttrium-based catalytic system (Figure 3.1) combined with $[\mathrm{Ph_3C}][\mathrm{B(C_6F5)_4}]$ and triisobutylaluminium (TIBA).[81] The polymerization proceeded rapidly at room temperature, yielding high-molecular-weight poly(IVC) with T_g values around 87 °C. The study also demonstrated the controlled polymerization of modified IVC derivatives bearing hydrogenated or polar substituents, highlighting the system's versatility and thermal robustness. These results underscore the potential of terpene-derived cyclic dienes like IVC as renewable building blocks for stereoregular polymers, bridging sustainability with advanced material performance.

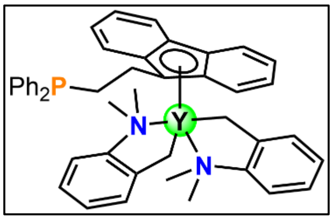

Figure 3.1. Yttrium-based catalyst.

Taken together, the limited number of studies on VCH and IVC underscores how minor structural differences and distinct catalytic environments can drastically influence their polymerization behavior and the microstructure of the resulting materials. The contrasting outcomes observed under coordination, anionic, and rare-earth catalysis highlight the dual nature of these cyclic dienes, bridging the flexibility typical of poly(conjugated dienes) with the rigidity of styrenic polymers.

In the following sections of this thesis, the stereoselective polymerization of both VCH and IVC will be investigated using [OSSO]-titanium catalysts, with the goal of using a new catalytic systems capable of precisely controlling regio- and stereochemistry. Moreover, the copolymerization of these monomers with styrene and with linear terpenes such as β-myrcene and β-ocimene will be explored to obtain fully hydrocarbon polymers with tunable mechanical and thermal behavior. Finally, the copolymerization of IVC with 1PB will be studied to generate new polymeric materials that combine the rigidity of cyclic monomers with the conjugated character of aromatic dienes, expanding the structural and functional diversity of bio-based systems.

3.2 Isospecific Polymerization of 1-Vinylcyclohexene (VCH)

The performance in the stereoselective polymerization of VCH of the two titanium complexes **1** and **2** (Figure 2.3), bearing [OSSO]-type ligand, activated by MAO, were compared and the results are reported in Table 3.1. Both these [OSSO]-type Ti catalysts were found to be active in producing polymers with predominantly 3,4-insertion of VCH along the polymer chain (Scheme 3.3).

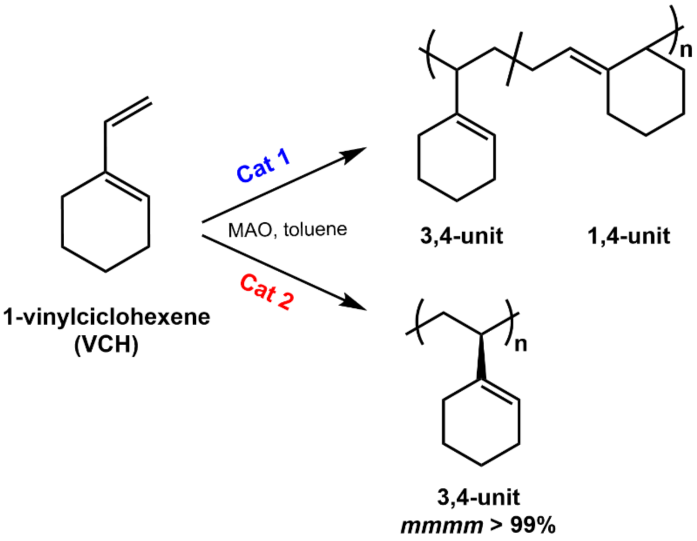

Scheme 3.3. Polymerization of VCH promoted by [OSSO]-titanium complexes **1** and **2**.

Table 3.1. Homopolymerization of VCH in presence of catalysts **1-2** activated with MAO.

Run[a]	Cat	*T* (°C)	Time (h)	Yield (%)	3,4- (%)[b]	*mmmm* (%)[b]	M_n (Kg/mol)[c]	Đ[c]	T_g (°C)[d]
1	**1**	25	18	17	80	*n.d.*	15.7	1.5	79.9
2	**1**	40	18	39	75	*n.d.*	28.2	1.7	80.8
3	**2**	0	18	4	>99	>99	13.5	1.9	86.6
4	**2**	25	18	54	>99	>99	104.2	2.2	96.0
5	**2**	40	18	59	>99	>99	125.7	2.0	95.7
6	**2**	80	18	57	>99	>99	84.8	2.0	92.1
7	**2**	40	5	53	>99	>99	134.4	1.9	96.7
8[e]	**2**	40	18	82	>99	>99	103.8	1.9	98.9

[a] Reaction conditions: Catalyst ($1.0\cdot10^{-5}$ mol), [Al]/[Ti] = 500, VCH (3 mmol, 0.3 g), toluene (3 mL). [b] Determined by ^{1}H and ^{13}C NMR spectroscopy. [c] Determined by GPC. [d] Determined by DSC. [e] Catalyst ($5.0\cdot10^{-5}$ mol), [Al]/[Ti] = 500, VCH (14 mmol, 1.5 g), toluene (15 mL).

Catalyst **2**, due to its greater steric hindrance, exhibited significantly higher regio- and stereo-selectivity when compared to catalyst **1** (runs 2 and 5, Table 3.1). Specifically, at a temperature of 40°C, poly(vinylcyclohexene) (PVCH) was obtained with a higher yield, showing 99% of 3,4-insertion and high isotacticity with *mmmm* >99%, as evidenced by ^{1}H and ^{13}C NMR (Figure 3.3b). The ^{13}C NMR signals of the PVCH indicate the formation of a highly isotactic polymer. The diagnostic chemical shifts of carbon 1 (35.5 ppm) and carbon 2 (41.29 ppm), highly sensitive to the tacticity of the polymer, are compatible with the previously reported chemical shifts for isotactic PVCH.[79] Considering the presence of a single ^{13}C signal for the carbon 2 of the PVCH, it can be concluded that the polymer has high isotacticity (*i.e. mmmm*> 99%).

The control of molecular weights is consistent with the behavior shown by [OSSO]-type complexes as single-site catalyst in the polymerization of diene monomers as evidenced by the value of the dispersity (*Đ*) obtained from GPC analyses.[31,37,76]

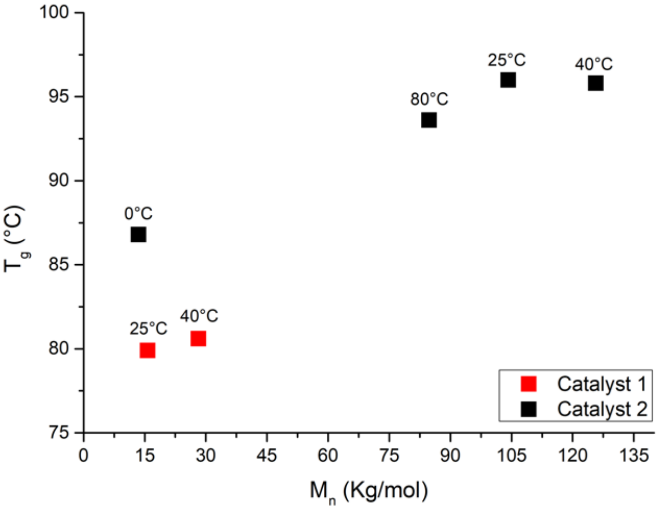

Figure 3.2. Diagram showing the correlation between molecular weight (M_n) and glass transition temperature (T_g): comparison of PVCH samples synthesized using catalysts **1** and **2**. The polymerization temperatures are indicated.

In Figure 3.2, the diagram relating molecular weights to glass transition temperatures for PVCH samples is reported. From the comparison between the two catalysts, it is evident that under identical conditions, the molecular weights are significantly different. Higher regioselectivity correlates with a higher T_g value of the polymer. Catalyst **1**, with lower regioselectivity and stereoselectivity, results in lower molecular weights and, consequently, lower T_g values. For instance, at 40°C, the T_g value increases from 80.8°C to 95.8°C as the 3,4-selectivity of the polymer obtained from catalyst **2** increased from 75% to over 99% (runs 2 and 5, Table 3.1).

The glass transition (T_g) values were sensibly higher than those reported for the polymer obtained from anionic polymerization (80-99 °C),[80] but despite the high degree of stereoregularity, no melting point was observed in the thermal analysis. As further proof of the high stereoregularity of the obtained polymer, the exhaustive hydrogenation of the sample obtained in run **8** led to the formation of semicrystalline isotactic poly(vinylcyclohexane) as confirmed by NMR and WAXS analyses (Figures 3.3a and 3.4). It is worth noting that isotactic PVCH, being the "missing link" between two semicrystalline isotactic polymers such as isotactic polystyrene and isotactic poly(vinylcyclohexane), is amorphous in nature. The ^{13}C NMR signals of hydrogenated PVCH (Figure 3.3a), *i.e.* for the resulting poly(vinylcyclohexane), are fully in agreement with those of hydrogenated isotactic polystyrene.[82]

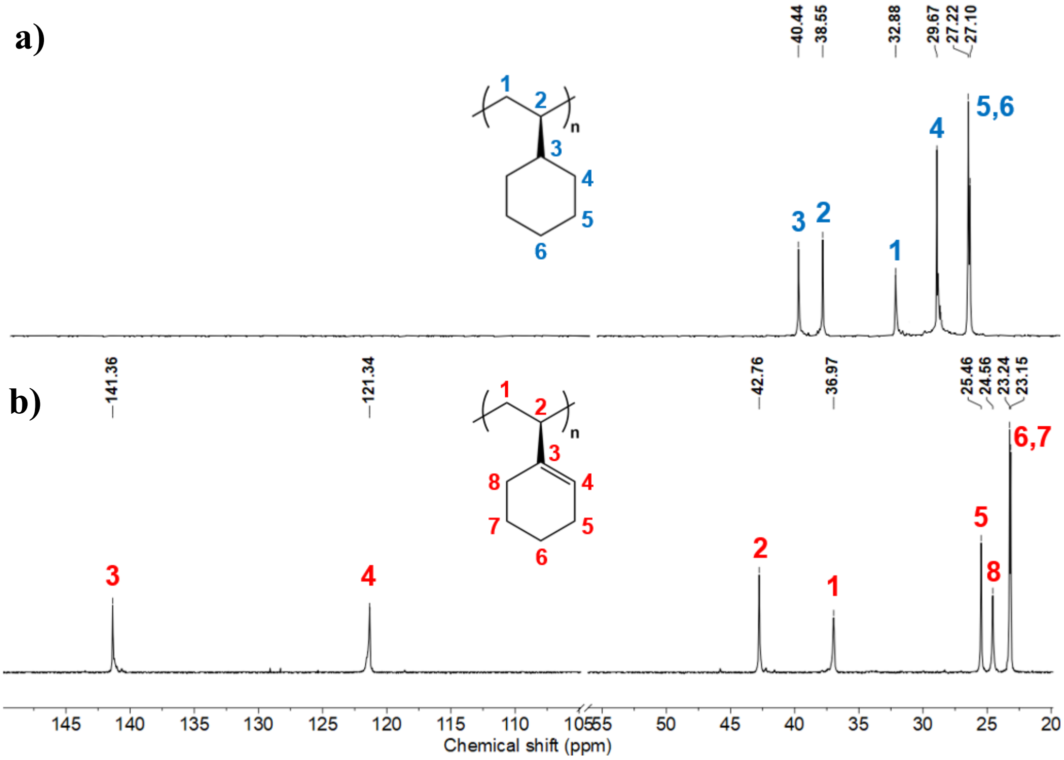

Figure 3.3. ^{13}C NMR spectra (150 MHz, $CDCl_3$, 298 K) of isotactic poly(vinylcyclohexene) (run **8**, Table 3.1) before (**a**) and after hydrogenation to isotactic poly(vinylcyclohexane) (**b**).

Despite the high stereoregularity, the as-synthesized PVCH samples are not crystalline (Figure 3.4, curve a), and it is unable to crystallize from the melt, even after prolonged (at least 2 h) annealing at temperatures above the glass transition neither by solution using solvents such as toluene or chloroform. Possible reasons for the lack of crystallinity of PVCH may be envisaged in a too-slow crystallization kinetics, in the adopted trial conditions. Therefore, isotactic PVCH represents a non-common example of polymer not able to crystallize despite its regular constitution and configuration. Similar behavior is shown by enantiomerically pure species of isotactic poly(limonene carbonate), derived from citrus oil and CO_2.[83,84]

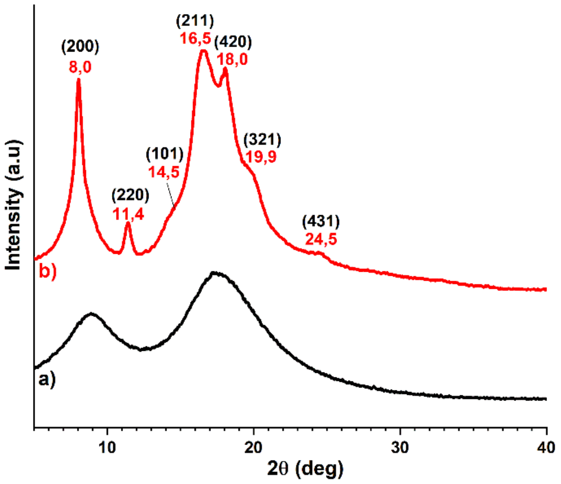

Figure 3.4. WAXS profiles of isotactic poly(vinylcyclohexene) before (black curve) and after hydrogenation to isotactic poly(vinylcyclohexane) (red curve).

3.3 Copolymerization of VCH with Styrene and Linear Terpenes

The copolymerization of 1-vinylcyclohexene (VCH) with styrene (S), β-myrcene (M), and β-ocimene (O) was carried out under the same experimental conditions optimized for the homopolymerization of VCH, using catalyst **2** activated with methylaluminoxane (MAO) at 40 °C (Scheme 3.4).

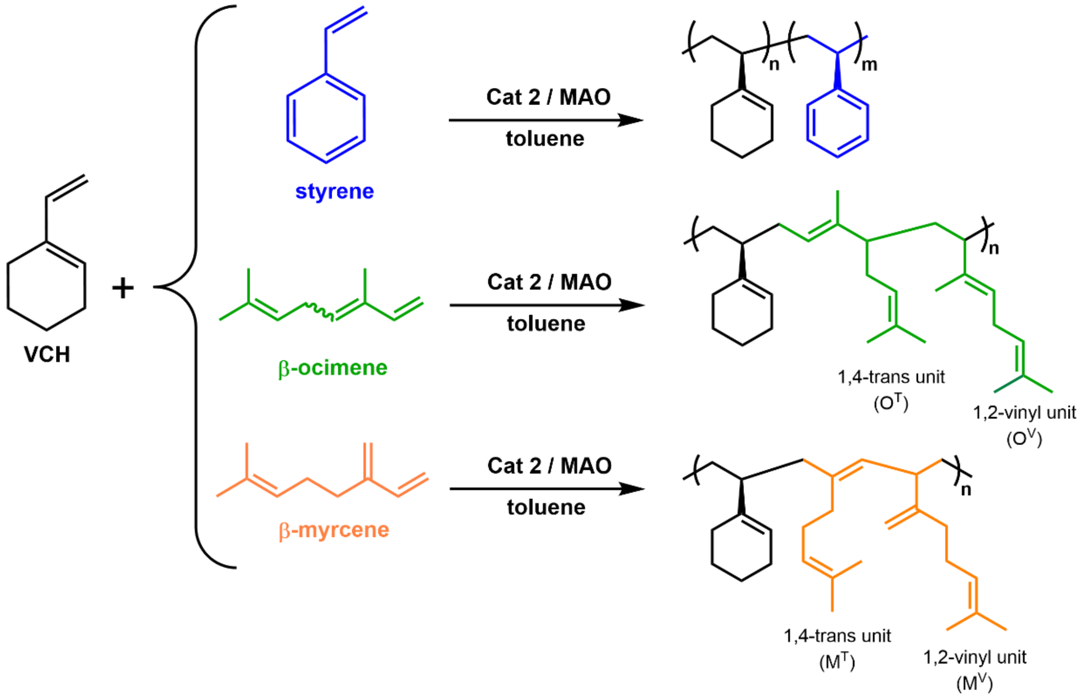

Scheme 3.4. Copolymerization of VCH with styrene and terpenes promoted by [OSSO]-titanium complex **2**.

The results in Table 3.2 clearly show how both the copolymerization strategy and the nature of the comonomer significantly affect the catalytic activity, molecular weights, and microstructure of the resulting copolymers.

Table 3.2. Copolymerization of VCH with S, M and O in presence of catalyst **2**/MAO.

Run[a]	**C / mol%**	**Yield (%)**	**M_n (Kg/mol)**[c]	**Đ**[c]	**Polymer composition (%)**[b]		**T_g (°C)**[d]
					VCH (mol%)	**C (mol%)**	
1[e]	**S** / 20	95	94.8	2.7	52	48	94.7
2[e]	**S** / 50	90	119.0	2.0	36	64	97.2
3	**S** / 50	95	56.0	2.1	25	75	91.1
4	**M** / 50	14	25.0	1.9	77	23	56.1
5	**O** / 50	28	31.0	4.0	72	28	40.6

[a] Reaction conditions: Catalyst **2** ($5.0\cdot10^{-6}$ mol), ([VCH]+[C])/[Ti] = 1000, [Al]/[Ti] = 500, toluene (5 mL), 40°C, 18 h. [b] Determined by ^{1}H and ^{13}C NMR spectroscopy. [c] Determined by GPC. [d] Determined by DSC. [e] Performed by sequential addition (one-pot two-step). **C**= comonomer.

In the one-pot two-step copolymerizations (runs 1 and 2, Table 3.2), styrene was added after 5 hours of VCH polymerization, maintaining the same catalytic and solvent conditions. These systems exhibited high activity and excellent overall yields (90-95%), producing copolymers with high molecular weights ($M_n \approx$ 95-120 kg mol^{-1}) and moderate dispersities (Đ ≈ 2-2.7), indicative of efficient chain propagation and limited chain transfer. The monomer conversion and copolymer composition were determined by ^{1}H and ^{13}C NMR spectroscopy (Figure 3.5a). As expected, styrene reached almost quantitative conversion (96% and 99%), while the conversion of VCH after 5 hours was consistent with that observed in its homopolymerization, confirming the comparably lower reactivity of VCH under these conditions. Consequently, even when the feed ratio was shifted toward VCH, the copolymers obtained showed a dominant polystyrene composition, reflecting the preferential incorporation of the more reactive styrene. The resulting materials displayed high glass-transition temperatures (T_g = 94.7-97.2 °C), which increased with the styrene content. These results indicate that the sequential monomer addition strategy favors the formation of high-molecular-weight diblock copolymers with well-defined composition and enhanced rigidity, consistent with the incorporation of polystyrene-rich segments.

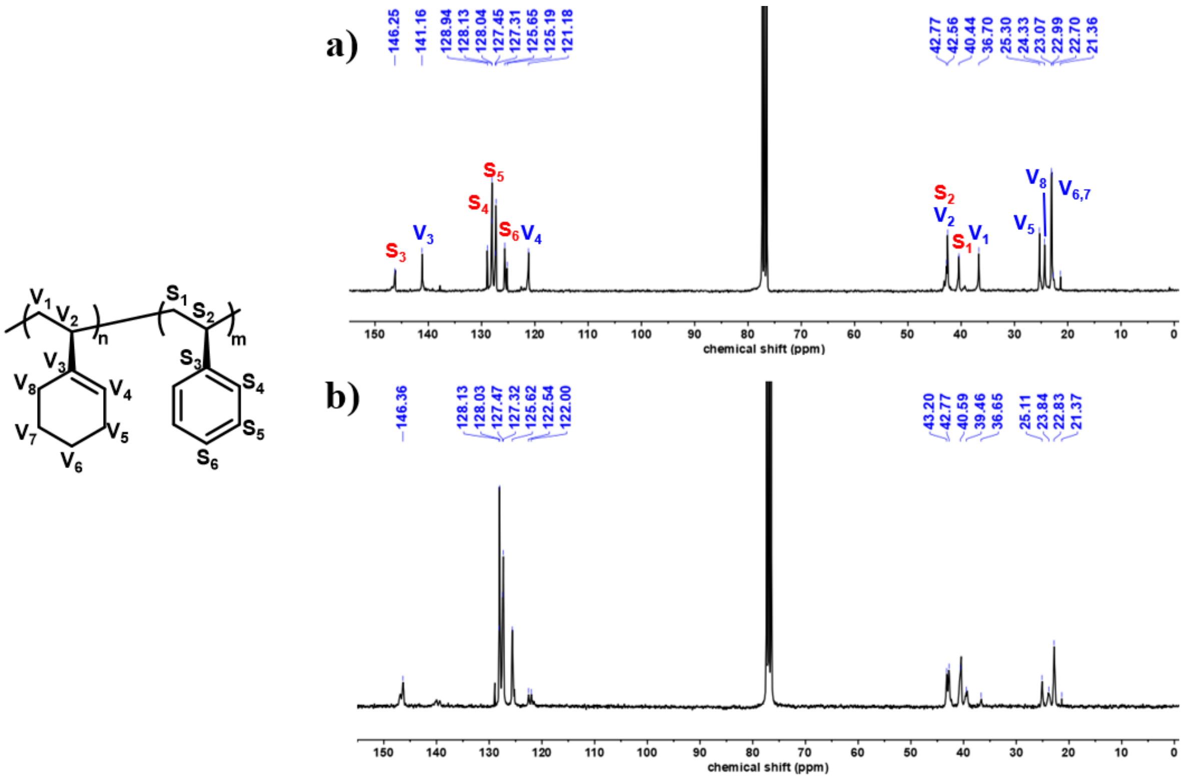

Figure 3.5. ^{13}C NMR spectra (150 MHz, $CDCl_3$, 298 K) of VCH-S copolymers from run **2** (a) and run **3** (b) of Table 3.2.

In contrast, the one-pot one-step one-step copolymerizations (runs 3-5, Table 3.2) gave lower yields and molecular weights, reflecting the competitive coordination and propagation behavior of the two monomers when present simultaneously. For the VCH/S one-pot one-step one-step system (run 3), the M_n decreased to 56 kg mol^{-1} with slightly higher dispersity, suggesting partial chain transfer and compositional drift toward styrene incorporation (75 mol%). The corresponding T_g (91 °C) was reduced compared to the sequential systems, indicating a less stereoregular microstructure and more random copolymer chain distribution (Figure 3.5b). For the copolymerizations involving β-myrcene (run 4) and β-ocimene (run 5), the catalyst remained active but with considerably reduced efficiency, leading to lower yields (14-28%) and molecular weights. The NMR analysis confirmed that the copolymers contained a higher proportion of VCH (72-77 mol%), consistent with the lower reactivity of the conjugated terpenes under these conditions. ^{1}H and ^{13}C NMR spectra also revealed the coexistence of both 1,4-*trans* and 1,2-vinyl insertions, as expected for this type of titanium-based catalytic system operating at 40 °C (see Appendix 3). The copolymer with β-myrcene exhibited the lowest T_g (56 °C), consistent with the flexible diene backbone and reduced microstructural order. The β-ocimene copolymer also reached a significantly lower T_g (41 °C), indicating that this comonomer further decreases chain rigidity.

3.4 Isospecific Polymerization of (*S*)-4-isopropenyl-1-vinyl-1-cyclohexene (IVC)

Owing to the isospecific polymerization of VCH using catalyst **2**, the polymerization of *S*-4-isopropenyl-1-vinyl-1-cyclohexene (IVC), a bio-based monomer obtained from perillaldehyde, was also performed (Scheme 3.5).

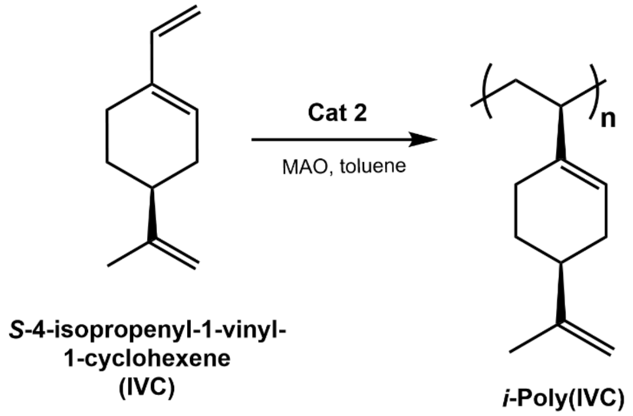

Scheme 3.5. Isospecific polymerization of IVC promoted by [OSSO]-titanium complex **2**.

Polymerizations were carried out at varying temperatures, and a notable increase in yield was observed as the temperature increased. The most favorable outcome was achieved at 80 °C even after 5 hours (run 4, Table 3.3).

Table 3.3. Homopolymerization of IVC in presence of catalyst **2** activated with MAO.

Run [a]	*T* (°C)	Time (h)	Yield (%)	3,4- (%) [b]	*mmmm* (%) [b]	M_n (Kg/mol) [c]	Đ [c]	T_g (°C) [d]
1	25	18	32	>99	>99	34.3	2.1	81.8
2	40	18	80	>99	>99	158.4	1.4	74.9
3	80	18	90	>99	>99	124.0	1.6	78.2
4	80	5	93	>99	>99	124.2	1.7	74.9

[a] Reaction conditions: Catalyst **2** ($1.0 \cdot 10^{-5}$ mol), [Al]/[Ti] = 500, IVC (2 mmol, 0.3 g), toluene (3 mL). [b] Determined by ^{1}H and ^{13}C NMR spectroscopy. [c] Determined by GPC. [d] Determined by DSC.

Also in this case, a highly isotactic polymer was obtained, as confirmed by the ^{13}C and ^{1}H NMR spectra (Figure 3.6), consistent with the highly isotactic microstructure reported for polymers obtained using lanthanide catalysts.[81]

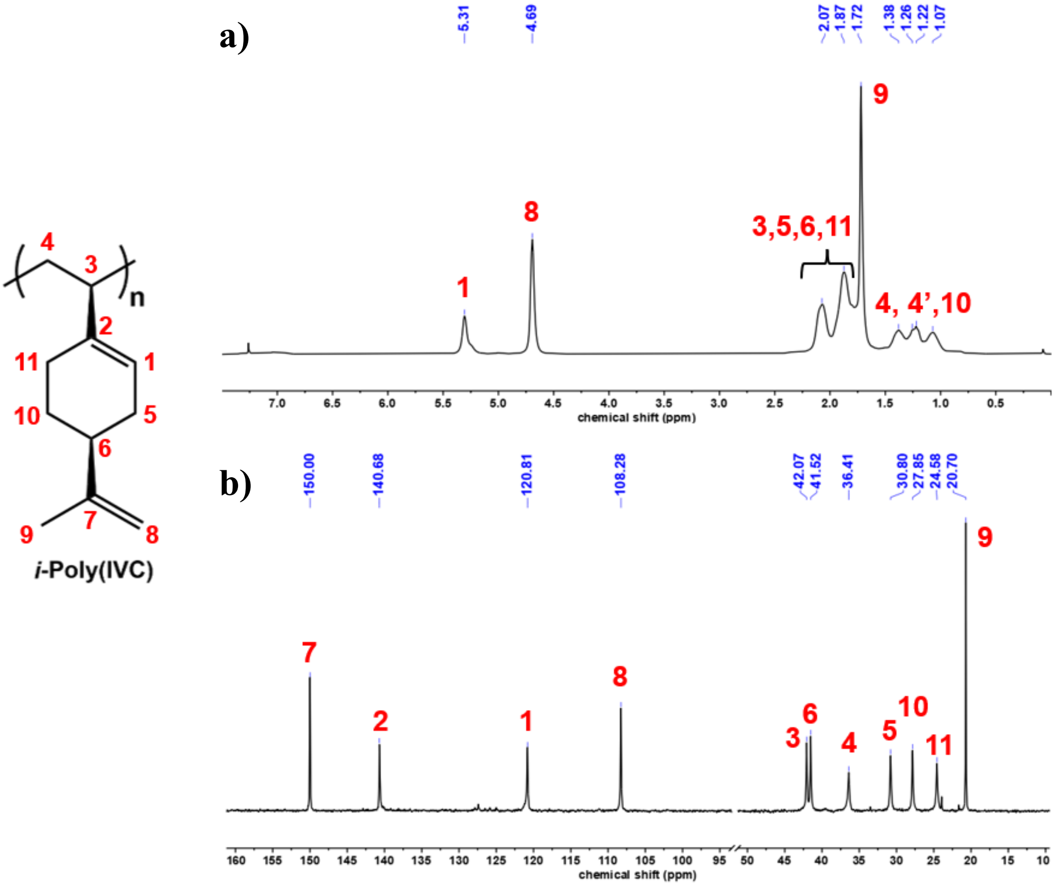

Figure 3.6. a) ^{1}H NMR (600 MHz, $CDCl_3$, 298 K) and b) ^{13}C NMR (150 MHz, $CDCl_3$, 298 K) of 3,4-isotactic poly(IVC) from run **4**, Table 3.3.

The polymerization of IVC to poly(*S*-4-isopropenyl-1-vinyl-1-cyclohexene) (PIVC) was undertaken to explore the potential of creating novel materials with unique properties that could complement or enhance those of PVCH. By examining both IVC and VCH, the study aimed to understand the influence of structural variations on polymer properties, particularly in relation to thermal behavior and crystallinity. Additionally, it is important to note that PIVC is a polymer derived from renewable sources, which makes it a sustainable alternative in polymer chemistry. Isotactic PIVC exhibits distinct glass transition temperatures (T_g) compared to PVCH. Reasonably, the presence of the isopropenyl group in PIVC results in different chain dynamics and packing efficiency, influencing T_g. However, as shown by WAXS analysis (Figure 3.7), like PVCH, PIVC is amorphous and unable to crystallize under the common crystallization conditions, even after prolonged annealing at temperatures close to T_g.

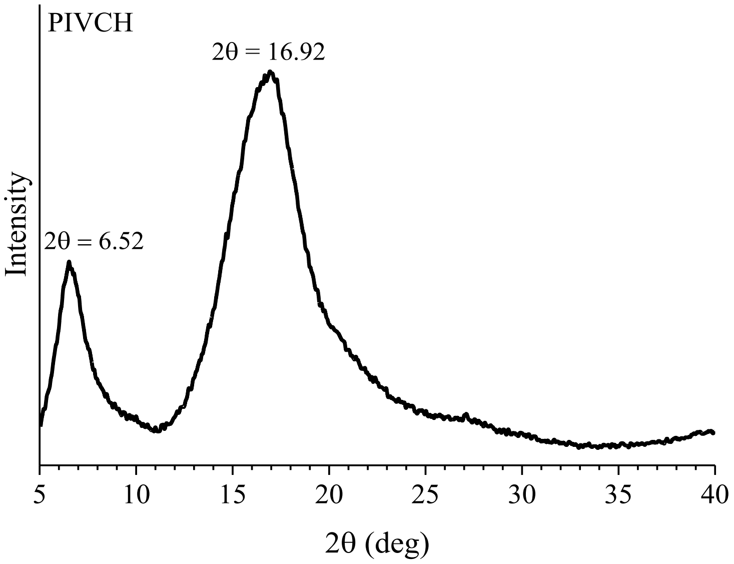

Figure 3.7. WAXS profile of as prepared isotactic poly(S-4-isopropenyl-1-vinyl-1-cyclohexene) sample.

While it is generally expected that T_g increases with molecular weight due to reduced chain mobility, this relationship is not always straightforward.[85] Several factors can influence T_g beyond just molecular weight like architecture of the polymer, intermolecular interactions, polymer crystallinity etc. Given these complexities, it is not surprising that some high molecular weight samples exhibit lower T_g values.[86,87]

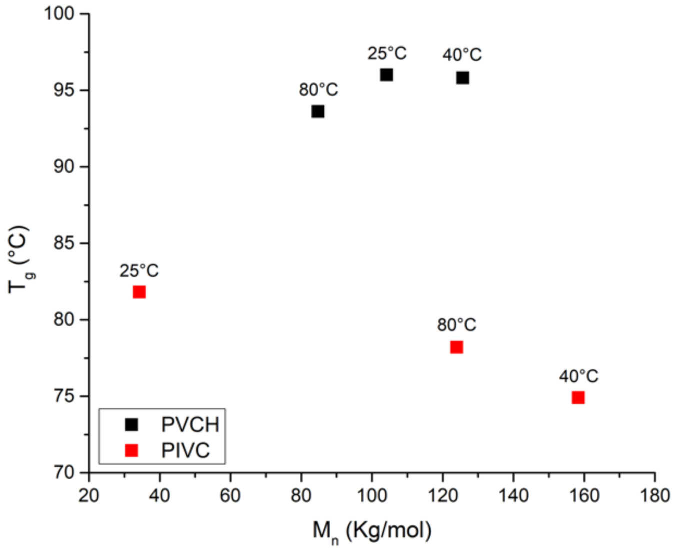

Figure 3.8. Diagram showing the correlation between molecular weight (M_n) and glass transition temperature (T_g): comparison between PVCH and PIVC samples synthesized with catalyst **2**. The polymerization temperatures are indicated.

In Figure 3.8, a comparison between PVCH and PIVC samples synthesized with catalyst **2** at various temperatures is reported. For PVCH, T_g increases as molecular weight rises, whereas for PIVC, the opposite trend is observed. This study found that the T_g of isotactic PIVC is lower than that of PVCH, indicating a more flexible polymer structure due to the bulkier side groups disrupting efficient chain packing.

PVCH and PIVC are both fragile. As an example, the stress-strain curves of films cast from toluene solutions of PVCH (Entry **8** of Table 3.1) and PIVC (Entry **3** of Table 3.3) are shown in Figure 3.9. Both samples are fragile, with values of deformation at break ε_b less than 8 and 2, respectively, and rigid, with values of Young's modulus of ≈25 and 1090 MPa, respectively.

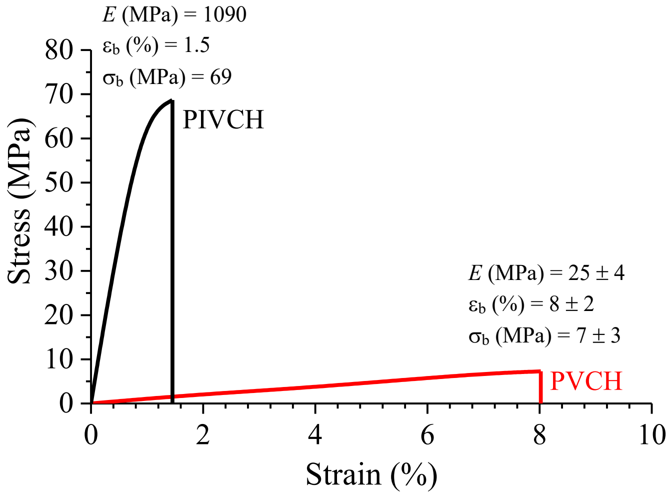

Figure 3.9. Stress-strain curves of isotactic PVCH and PIVC samples.

3.5 Study of Cross-Linking Reactions on PIVC

The synthesis and structural design of crosslinked polymers represent a central focus in modern polymer chemistry, as they enable the transformation of flexible, thermoplastic materials into robust, dimensionally stable, and functionally adaptive systems. In their linear form, polymer chains are held together by weak van der Waals interactions or hydrogen bonds, which confer flexibility but also limit mechanical strength, solvent resistance, and thermal stability. The introduction of covalent crosslinks between polymer chains forms a three-dimensional network that restricts molecular mobility, drastically modifying the viscoelastic behavior and transforming a polymer from a meltable material into an insoluble thermoset (Figure 3.10). This structural evolution enhances properties such as elasticity, chemical resistance, and environmental stability, which are crucial for applications in coatings, adhesives, elastomers, membranes, and biomedical materials.[88]

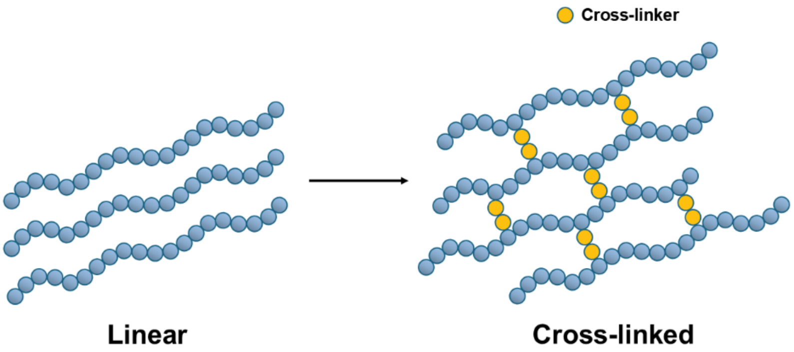

Figure 3.10. Representation of a Linear Polymer Being Cross-Linked.

Crosslinkable polymers often rely on the presence of reactive functionalities either along the backbone or as pendant groups. Among these, carbon-carbon double bonds (-C=C-) constitute one of the most versatile chemical handles, as they can engage in a variety of addition and radical reactions that enable the formation of controlled network structures. Conventional crosslinking approaches, such as vulcanization or peroxide-induced coupling, are effective but often require harsh conditions, lead to heterogeneous networks, and offer limited opportunities for recyclability or reprocessability. For these reasons, increasing attention has shifted toward milder, more selective, and potentially reversible chemistries able to deliver homogeneous networks with improved control over crosslinking density and topology.[88,89]

Within this framework, thiol-ene click chemistry has emerged as a highly attractive platform for polymer functionalization and crosslinking. The radical-mediated addition of thiols to olefinic double bonds proceeds rapidly, with high efficiency and minimal sensitivity to oxygen, making it compatible with both thermal and photochemical activation. The reaction typically leads to uniform network structures characterized by delayed gelation and reduced shrinkage and offers a degree of control often superior to that of classical acrylate-based systems. Moreover, the use of thiols or crosslinkers containing disulfide bonds provides an opportunity to incorporate dynamic or stimuli-responsive linkages, enabling reversible network rearrangements and offering pathways toward recyclable, reprocessable, or self-healing materials.[89,90]

In this context, PIVC represents a particularly interesting substrate for thiol-ene crosslinking. Owing to the presence of a pendant exocyclic double bond, PIVC intrinsically contains reactive sites suitable for thiol-ene coupling without requiring any post-functionalization. This structural advantage provides access to well-defined crosslinked networks under mild conditions, allowing the polymer to retain its backbone integrity while achieving substantial enhancements in mechanical robustness, thermal stability, and chemical resistance. At the same time, the availability of these unsaturated sites facilitates the design of advanced network architectures in which the density, flexibility, and reversibility of crosslinks can be finely tuned by appropriate selection of the thiol-based crosslinker.

Building upon these considerations, the crosslinking of PIVC was explored using two approaches: an *irreversible* thiol-ene reaction employing different dithiols to produce permanently crosslinked networks, and a potentially *reversible* crosslinking strategy using dithiols containing internal ester groups capable of undergoing hydrolysis. This second approach enables the incorporation of cleavable linkages into the network, opening the possibility for controlled degradation, recyclability, or post-processing of the crosslinked materials.

3.5.1. Irreversible Crosslinking Via the Thiol-Ene "Click" Reaction

The irreversible cross-linking of PIVC was carried out by reacting the polymer with a series of dithiols through a thiol-ene process involving the pendant exocyclic double bond (Scheme 3.6).

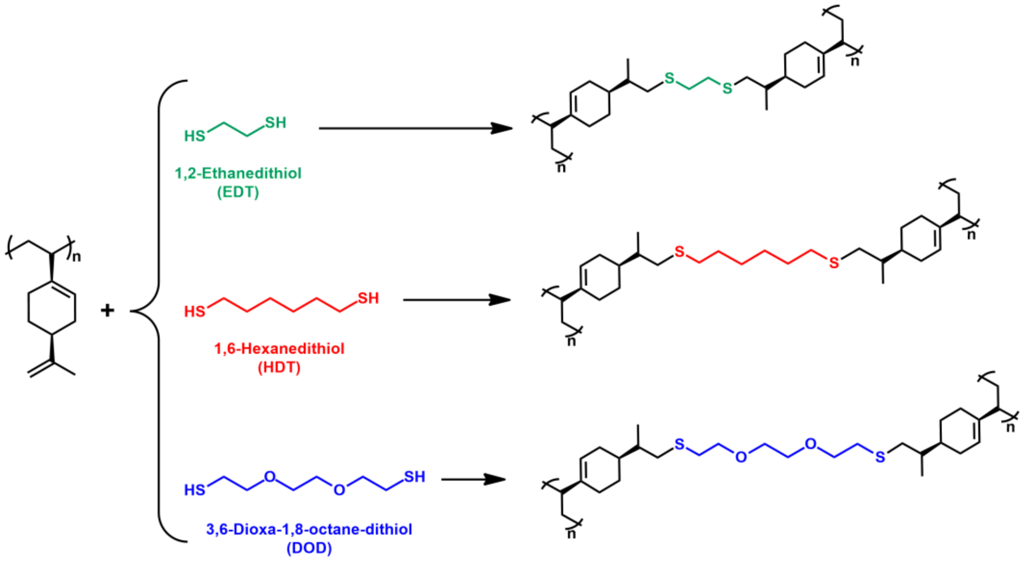

Scheme 3.6. Thiol-ene reaction of PIVC with different aliphatic dithiols.

Several PIVC samples were reacted in the presence of 2,2′-Azobis(2-methylpropionitril) (AIBN) as an initiator at 80°C for 24 hours and the results are summarized in Table 3.4.

Table 3.4. Thiol-ene reaction of PIVC with aliphatic dithiols.

Sample	Dithiol	Yield (g)	Notes
CL1	**EDT**	0.246	Insoluble
CL2	**HDT**	0.280	Insoluble
CL3	**DOD**	0.278	Insoluble

Reaction conditions: PIVC (0.200 g, 2 eq); Dithiol ($6.65x10^{-4}$ mol, 1 eq); AIBN ($6.65x10^{-4}$ mol, 1 eq); pyridine dry (3 mL); T = 80°C; 24 h.

In all cases, the reaction led to the formation of a permanently cross-linked network, as evidenced by the complete loss of solubility of the resulting materials in common organic solvents.

The shift of the glass transition temperature to temperatures above 250 °C in the DSC thermograms further confirmed the formation of a rigid three-dimensional structure that limits segmental mobility (Figure 3.11). For all three cases, the cross-linked polymer no longer exhibited a glass transition temperature (T_g), which was initially around 80°C before cross-linking.

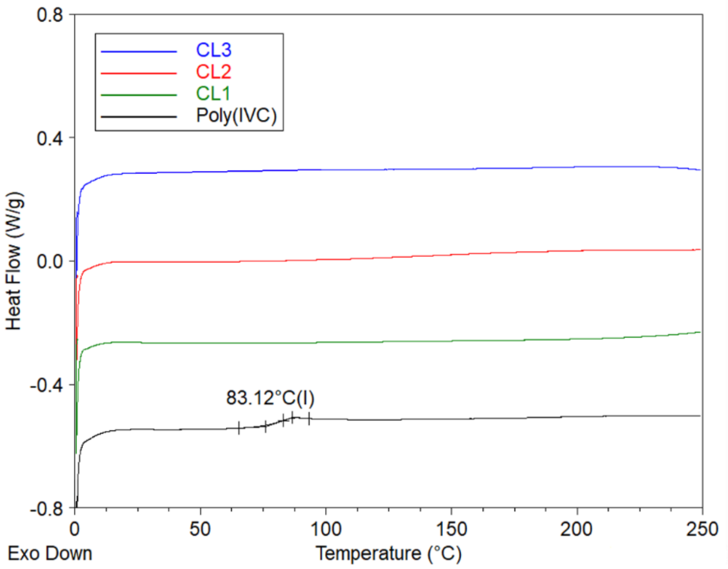

Figure 3.11. DSC thermograms of PIVC before and after crosslinking.

Interestingly, while the T_g increased in all samples, thermogravimetric analysis (TGA) showed that the thermal decomposition temperature (T_d) remained largely unchanged, indicating that the cross-linking primarily affects chain mobility rather than the intrinsic thermal stability of the polymer backbone (see Appendix 3).

Additional analytical techniques provided complementary evidence of successful cross-linking: elemental analysis (Figure 3.12a) confirmed the incorporation of sulfur into the network, while Raman spectroscopy (Figure 3.12b) revealed the appearance of a characteristic C-S stretching vibration around 500 cm^{-1}, a feature absent in the uncross-linked polymer.

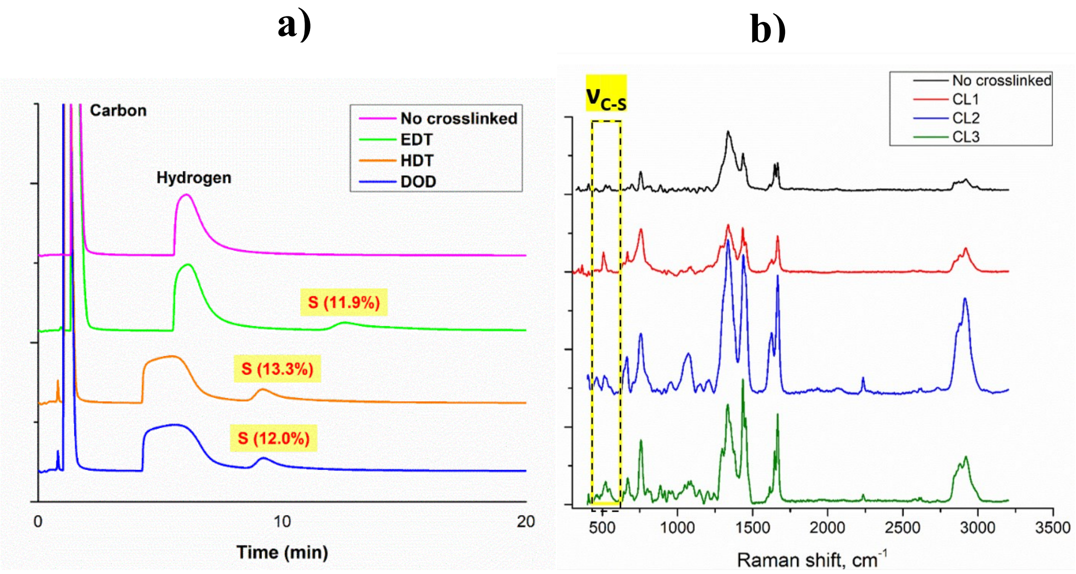

Figure 3.12. a) CHNS chromatograms and b) Raman spectra of the PIVC samples before and after crosslinking.

Altogether, these results demonstrate that thiol-ene chemistry enables efficient and irreversible cross-linking of PIVC, yielding insoluble and thermally robust materials with significantly reduced chain mobility.

3.5.2. Reversible Crosslinking Via the Thiol-Ene "Click" Reaction

For the reversible cross-linking strategy, two dithiols with an internal ester functionality, such as the methyl ester-containing dithiol (MEtAc) and its propyl analogue (MPrAc), were synthesized following a procedure reported in the literature (Scheme 3.7).[91] These reagents were selected because the ester group incorporated into the cross-link junction is susceptible to hydrolysis, offering a potential pathway to partially or fully reverse the network structure under appropriate conditions.

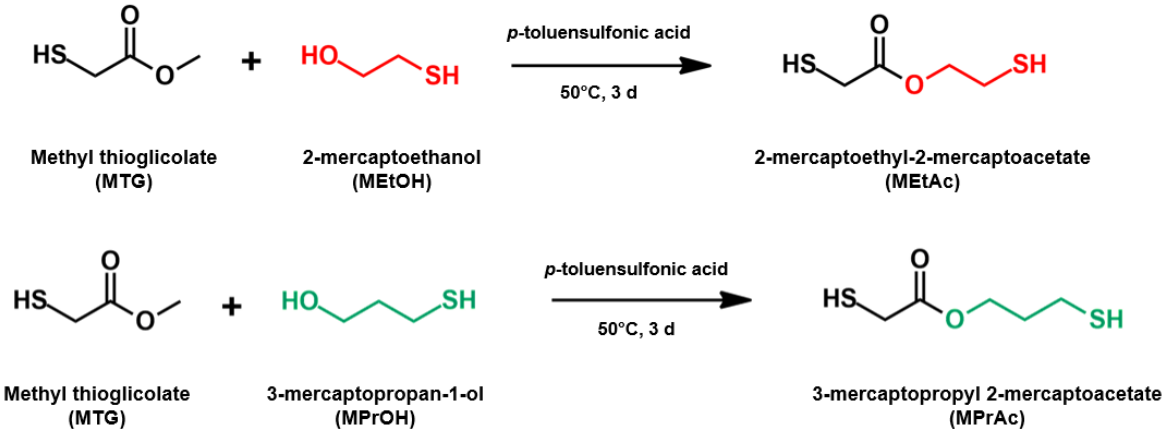

Scheme 3.7. Synthetic scheme of 2-mercaptoethyl-2-mercaptoacetate (MEtAc) and 3-mercaptopropyl 2-mercaptoacetate (MPrAc).

Although both dithiols were prepared for this purpose, only MEtAc was employed in the thiol-ene cross-linking reaction with PIVC. When reacted under the same conditions used for the irreversible systems, MEtAc successfully generated an insoluble polymer, indicating effective incorporation into the structure (Scheme 3.8A).

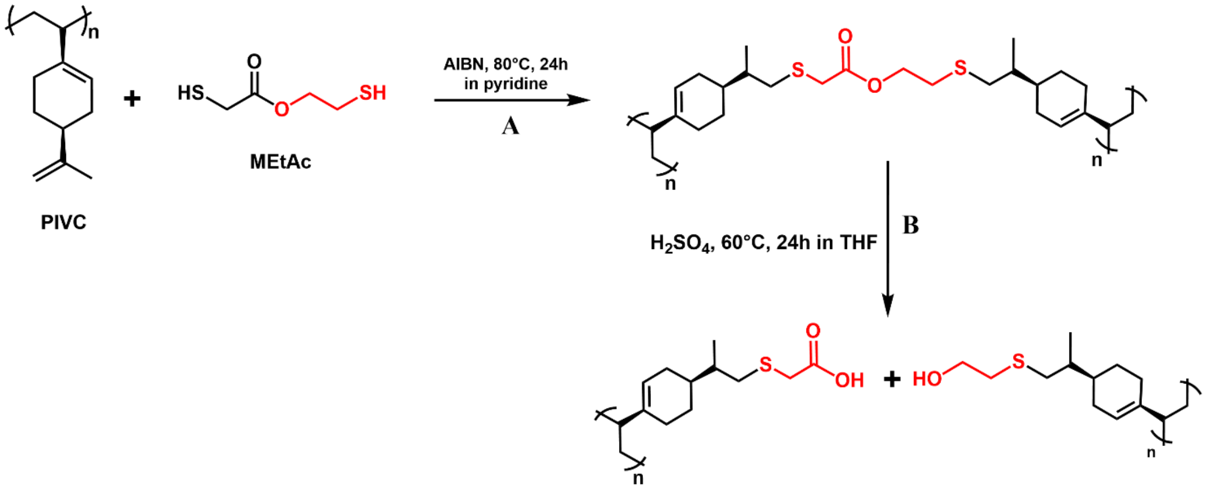

Scheme 3.8. Thiol-ene reaction of PIVC with MEtAc (A); Hydrolysis reaction of the ester group (B).

As observed for the cross-linking with simple aliphatic dithiols, the increasing of the glass transition temperature to temperatures above 250 °C in the DSC thermogram confirmed the formation of a rigid three-dimensional architecture (Figure 3.13a, red curve), while Raman spectroscopy showed the characteristic C-S stretching vibration, demonstrating that the thiol-ene addition had occurred (Figure 3.13b).

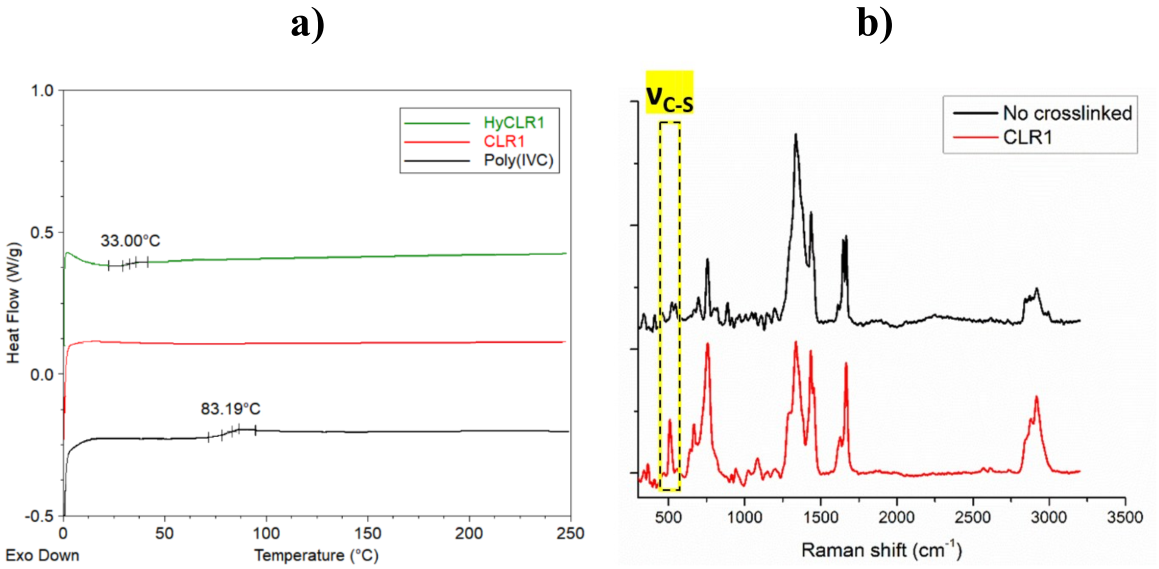

Figure 3.13. a) DSC thermograms and b) Raman spectra of the PIVC samples before and after crosslinking.

A first exploratory attempt to hydrolyze the ester bond (Scheme 3.8B) was conducted using H_2SO_4 in THF at 60 °C for 24 h. Although the cross-linked material remained insoluble in common organic solvents, the DSC analysis (Figure 3.13a, green curve) clearly revealed the appearance of a new glass transition at 33 °C, significantly lower than the T_g of the original PIVC homopolymer (≈ 83 °C). This observation confirms that hydrolysis partially occurred: cleavage of the ester bond generates two pendant fragments, one terminating in a carboxylic acid group and the other in an alcohol. These fragments remain attached to the main polymer backbone but no longer connect two chains of PIVC. Thus, the network loses part of its cross-link density while simultaneously acquiring flexible side-groups capable of increasing local segmental mobility. Both effects contribute to lowering the T_g. Reduced cross-link density decreases the constraints on chain motion, while the newly formed pendant acid and alcohol functions act as internal plasticizers, disrupting packing and facilitating segmental relaxation.

The decrease in T_g provides direct evidence that the ester-based cross-links are susceptible to cleavage and that controlled reversible cross-linking of PIVC through MEtAc is possible. Optimization of the hydrolysis conditions will be necessary to achieve full network breakdown and solubilization in future studies.

From an application-oriented perspective, the thiol-ene crosslinking strategies explored in this work are particularly attractive due to their intrinsic scalability and industrial relevance. Thiol-ene reactions are known for their high efficiency, robustness, and tolerance toward oxygen and functional groups, features that make them well suited for large-scale processing and industrial implementation. The use of thermally initiated conditions, commercially available dithiols, and relatively mild reaction parameters further supports the potential transferability of these approaches beyond laboratory scale. Moreover, the possibility of introducing cleavable ester-based cross-links provides an additional advantage in the context of sustainable polymer design, enabling materials that combine structural robustness during use with the prospect of controlled degradation, recyclability, or reprocessing at the end of life. Together, these characteristics highlight the relevance of thiol-ene crosslinking as a versatile platform for the development of advanced, bio-based polymer networks with potential industrial applicability.

3.6 Copolymerization of IVC with Linear Terpenes and 1PB

To extend the study to the synthesis of new polymers from renewable sources, the IVC was copolymerized with two linear terpenes, β-myrcene and β-ocimene, and *trans*-1-phenyl-1,3-butadiene (1PB) (Scheme 3.9). The copolymerization reactions were carried out under controlled conditions to ensure the efficient incorporation of the terpene monomers into the polymer backbone.

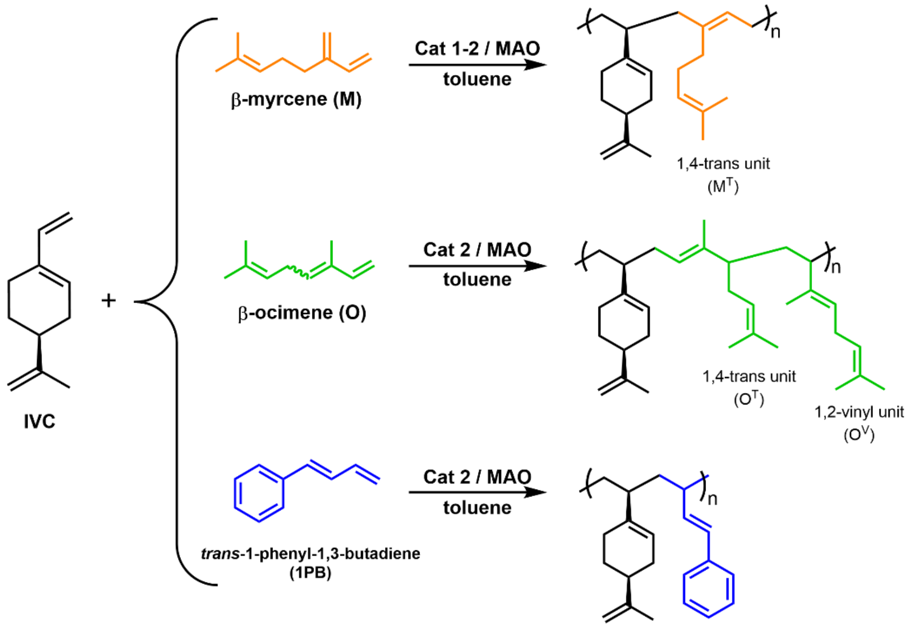

Scheme 3.9. Copolymerization of IVC with linear terpenes and 1PB promoted by [OSSO]-titanium complexes **1** and **2**.

The resulting copolymers were characterized using various techniques, including NMR spectroscopy, gel permeation chromatography (GPC), and differential scanning calorimetry (DSC). These analyses provided insights into the composition, molecular weight distribution, and thermal properties of the copolymers. The results, summarized in Table 3.5, demonstrate the successful synthesis of IVC-based copolymers with different properties, highlighting the potential of β-myrcene, β-ocimene and 1PB as comonomers in the development of sustainable polymeric materials.

Table 3.5. Copolymerization of IVC with linear terpenes and 1PB in presence of catalysts **1-2**/MAO.

Run[a]	**C / feed (mol%)**	**Cat**	**Yield (%)**	**M_n (Kg/mol)**[c]	**Đ**[c]	**Polymer composition (%)**[b]		**T_g (°C)**[d]
						C (mol%)	**IVC (mol%)**	
1	M / 50	1	35	28.1	2.0	36	64	33.6
2	M / 80	1	17	12.3	2.6	74	26	-30.2
3	M / 50	2	40	18.8	2.1	24	78	36.3
4	M / 80	2	16	13.5	3.9	58	42	-30.2
5	O / 50	2	78	53.3	3.1	55	45	27.4
6	O / 80	2	52	40.4	2.6	79	21	3.4
7	1PB / 20	2	96	162.3	2.4	21	79	70.4
8	1PB / 30	2	> 99	149.4	2.5	32	68	72.5 / 114.5
9	1PB / 50	2	98	152.4	1.9	49	51	71.9 / 106.1

[a] Reaction conditions: Catalyst ($5.0 \cdot 10^{-6}$ mol), ([IVC]+[C])/[Ti] = 1000, [Al]/[Ti] = 500, toluene (5 mL), 80°C, 24 h. [b] Determined by ^{1}H and ^{13}C NMR spectroscopy. [c] Determined by GPC. [d] Determined by DSC. C= comonomer.

Several one-pot one-step one-step copolymerizations of IVC with both linear terpenes were conducted, varying the molar ratios of the monomers. For the copolymerizations of IVC with β-myrcene, a comparison between catalyst **1** and catalyst **2**, both activated by methylaluminoxane (MAO), was performed. The results indicate that, although yields are similar, catalyst **1** results in a higher incorporation of myrcene in the final polymer, for example from 24 mol% to 36 mol% (runs 1 and 3, Table 3.5). This finding aligns with previous results,[28,69] which showed that catalyst **1** had superior performance in the homopolymerization of β-myrcene, while catalyst **2** was more efficient for β-ocimene. Indeed, in the copolymerization with β-ocimene, catalyst **2** was employed, resulting in the formation of copolymers that closely match the molar ratios of the two monomers used. The copolymers were characterized using ^1H NMR and ^{13}C NMR (Figure 3.14) to reveal their microstructure. The results indicate that with β-myrcene, the copolymer predominantly exhibits 1,4-*trans* insertion (M^T); with β-ocimene, as expected, both 1,4-*trans* (O^T) and 1,2-vinyl (O^V) insertions were observed.

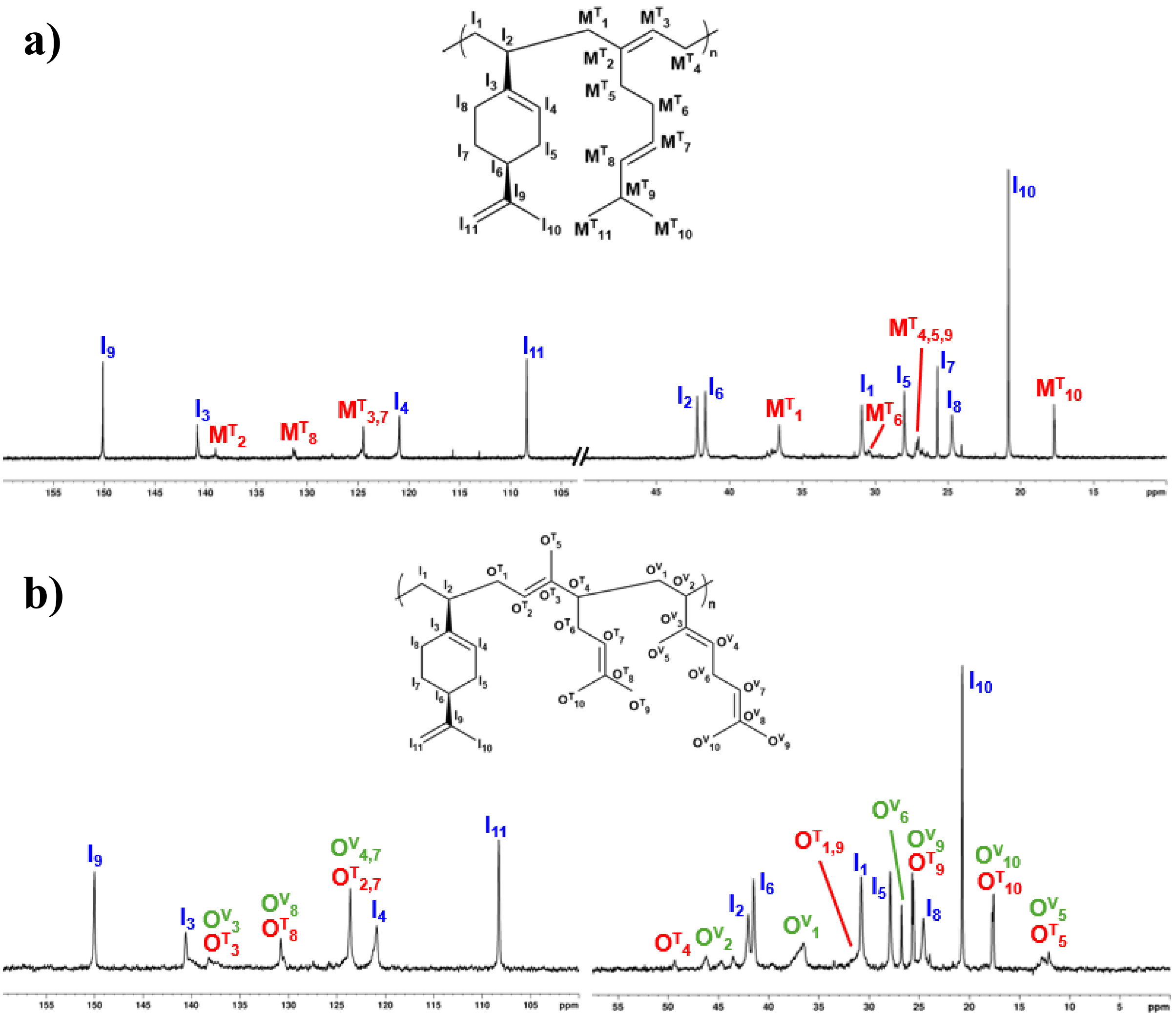

Figure 3.14. ^{13}C NMR (100 MHz, $CDCl_3$, 298 K) of a) IVCM copolymer from entry **3** and b) IVCO copolymer from entry **5** of Table 3.5.

GPC analyses showed monomodal profiles, and the Đ values were consistent with their copolymeric nature. Additionally, molecular weights and yields decreased with increasing terpene content in the polymer. DSC curves (see Appendix 3) of the copolymers revealed the presence of a single glass transition temperature (T_g), which significantly decreased as the terpene content increased, indicating significant effects on the polymer characteristics.

In the copolymerizations with 1PB, IVC is almost completely consumed (98-99%), achieving nearly quantitative yields. This increased reactivity could be explained by the potential influence of the comonomer in Ziegler-Natta polymerization. Specifically, the presence of a comonomer might modify the coordination environment or the electronic structure of the catalytic sites, facilitating the insertion of 1PB into the growing polymer chain and thereby increasing its reactivity.[92] The ^{1}H and ^{13}C NMR spectra suggest a multiblock structure also in this case (Figure 3.15).

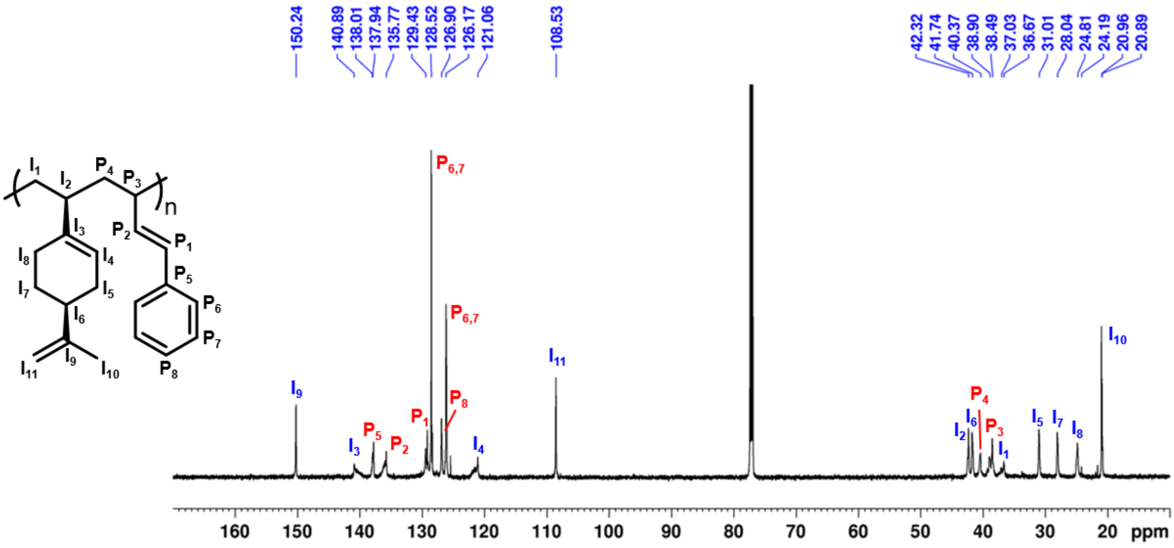

Figure 3.15. ^{13}C NMR (100 MHz, $CDCl_3$, 298 K) of PPBI copolymer from run **9**, Table 3.5.

In all cases, the GPC analyses revealed monomodal profiles, and the Đ values confirmed the copolymeric nature of the samples, whereas the XRD profiles (Figure 3.16, left) indicate that all the samples are amorphous. Additionally, the DSC curves recorded in the 1st heating scan (Figures 3.16, right) showed, at temperatures greater than ≈100 °C, the presence of spurious exothermic and/or endothermic peaks. They are due to a portion of chain segments undergoing cross-link reactions, and also, in part, to slight degradation. Moreover, the occurrence of cross-linking reactions was indicated by the presence of a glass transition in the 2nd DSC heating traces of the samples **8** and **9**, with 1PB content of 32 and 49 mol%, at temperatures of ≈106 and 144 °C, respectively, that is at temperatures significantly greater than those of the homopolymers. These samples showed a second glass transition at temperatures lower or similar to those of the corresponding homopolymers, indicating phase separation of cross-linked and non-cross-linked segments in different domains. The sample **7**, with 1PB content of 20 mol%, instead, showed a single glass transition temperature, due to the good miscibility of

IVC and 1PB sequences. Interestingly, for the uncross-linked fraction of the PPBI copolymers, the effect on the glass transition temperature was less pronounced, as the two homopolymers exhibit similar T_g values.

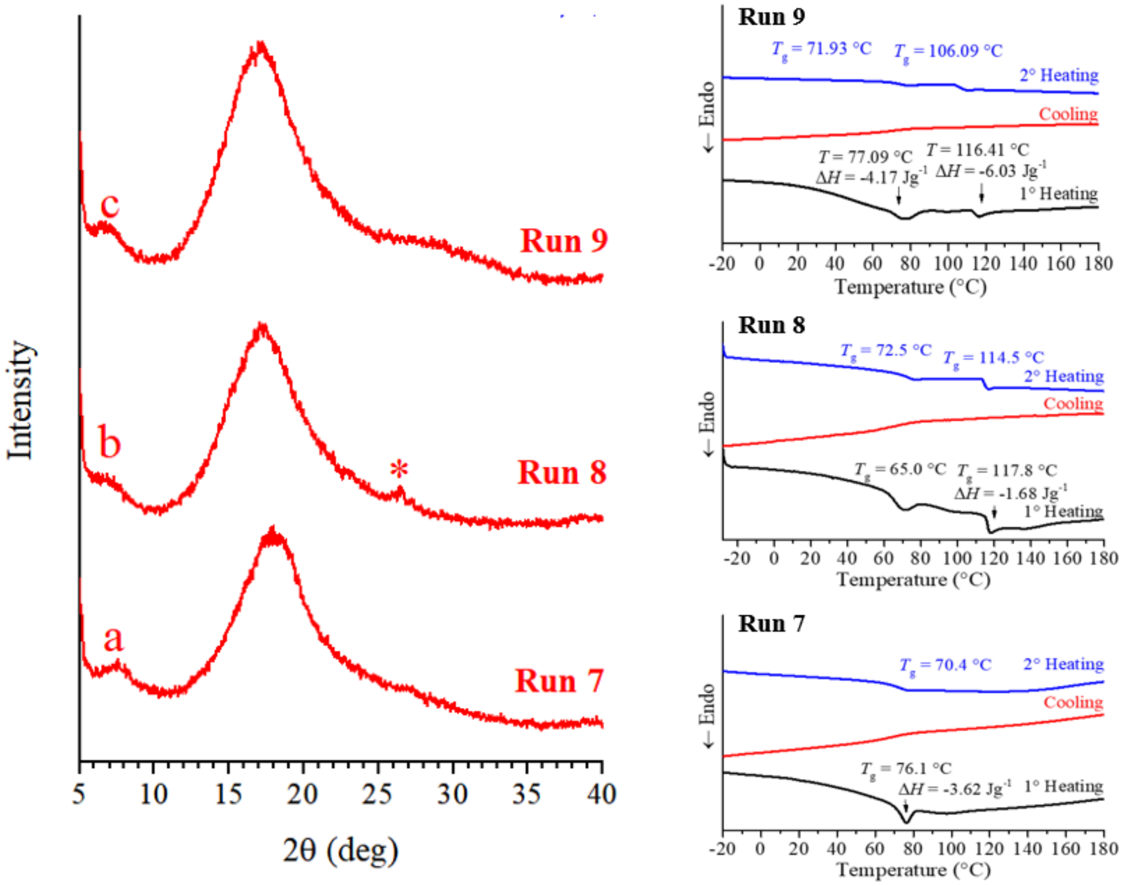

Figure 3.16. X-ray powder diffraction profiles (left) of as synthesized samples **7** (a), **8** (b) and **9** (c) and corresponding DSC curves (right). The star at 2θ ≈ 27 ° (curve b, left) indicate the presence of a small amount of some crystalline impurity (e.g. catalyst remnant).

Preliminary tensile measurements for the PPBI series, reported in Figure 3.17, reveal that samples **7**, **8** and **9** exhibit relatively high Young's modulus values (ranging from 130 to 300 MPa) and low elongation at break. These combined features indicate a rigid and brittle mechanical behavior, consistent with their elevated glass transition temperatures and with the intrinsic stiffness imparted by the polymer backbone. The stress-strain curves further highlight the limited deformability before failure, confirming the predominantly glassy nature of these materials at room temperature.

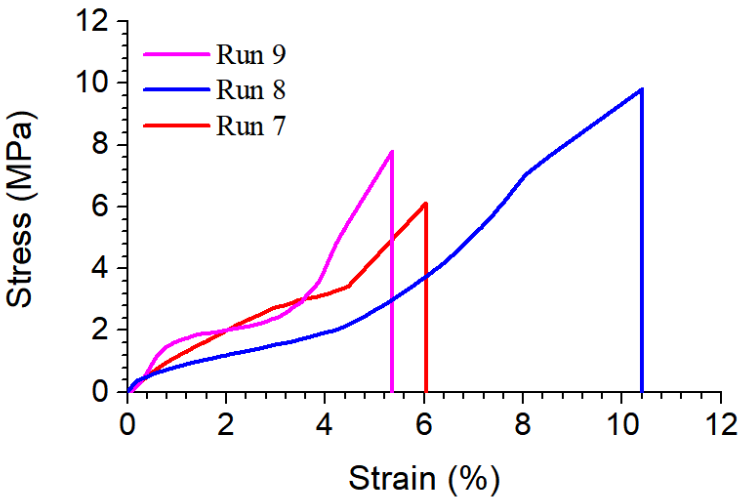

Figure 3.17. Stress-strain curves measured at room temperature using the deformation rate $v/l_0 = 0.1$ mm min^{-1} mm^{-1}, of the samples **7**, **8** and **9**, Table 3.5.

3.7 Conclusion

Stereoselective polymerization of VCH using the two [OSSO]-type titanium catalysts revealed a clear difference in performance, with catalyst **2** consistently providing higher activity, regioselectivity and stereocontrol. Under identical conditions, it enabled the formation of PVCH samples with exclusive 3,4-insertion and exceptionally high isotacticity (*mmmm* > 99%), as confirmed by NMR analyses. These polymers exhibited glass transition temperatures that increased with both molecular weight and regioselectivity, but, despite their remarkable microstructural regularity, remained completely amorphous. Even prolonged annealing or solution-based crystallization attempts failed to induce crystallinity, highlighting PVCH as an unusual example of a perfectly regular polymer that nonetheless resists crystallization. Hydrogenation experiments further confirmed the high stereoregularity of the chains, yielding semicrystalline isotactic poly(vinylcyclohexane).

The copolymerization studies demonstrated how profoundly the comonomer structure and polymerization strategy influence the final materials. One-pot two-step VCH/styrene copolymerizations proceeded very efficiently, affording high-molecular-weight diblock copolymers with high styrene incorporation and correspondingly high T_g values. Conversely, one-pot one-step copolymerizations led to lower yields and molecular weights due to the competitive behavior of the monomers, and the resulting copolymers exhibited more random microstructures and reduced thermal transitions. When β-myrcene and β-ocimene were used, their lower intrinsic reactivity resulted in copolymers enriched in VCH and featuring mixed insertion modes, with significantly lower glass-transition temperatures due to the enhanced flexibility imparted by the terpene units.

Given the excellent isospecificity observed for VCH, the polymerization of the bio-based monomer IVC was also examined. Catalyst **2** again proved highly effective, affording isotactic PIVC across the explored temperature range. Like PVCH, the polymer was completely amorphous and unable to crystallize, although its T_g values were distinctly lower and followed an opposite trend with molecular weight. These observations reflect the influence of the isopropenyl substituent on chain packing and mobility. Mechanical tests further showed that both PVCH and PIVC behave as rigid and fragile materials at room temperature.

The presence of a pendant exocyclic double bond in PIVC made it particularly suitable for thiol-ene crosslinking, and this reactivity was successfully exploited to produce both irreversible and potentially reversible networks. Reactions with simple dithiols readily produced insoluble materials in which the glass transition disappeared, whereas the thermal stability of the backbone remained essentially unchanged. Spectroscopic analyses confirmed the efficient incorporation of sulfur and the formation of C-S bonds. Furthermore, the synthesis of ester-containing dithiols enabled the preparation of crosslinked networks featuring hydrolytically cleavable junctions, thus opening the way to reversible or degradable architectures.

Finally, copolymerizations of IVC with β-myrcene, β-ocimene and 1PB expanded the library of renewable-based materials accessible with these catalytic systems. Differences between catalysts **1** and **2** mirrored their behavior in homopolymerizations, with catalyst **1** favoring higher myrcene incorporation and catalyst **2** performing better with β-ocimene. The resulting copolymers were consistently amorphous and displayed thermal properties strongly dependent on composition. In systems involving 1PB, multiblock microstructures and partial crosslinking effects gave rise to complex thermal responses and higher T_g values in selected domains, while mechanical testing confirmed the formation of rigid, glassy materials.

3.8 Experimental Section

3.8.1 Materials and methods. Reagents and solvents were purchased from Sigma-Aldrich, Merck or TCI chemicals. Solvents were dried and distilled before use. All air- and/or water-sensitive compound manipulations were carried out using a glovebox or standard Schlenk techniques under an N_2 atmosphere. Commercial grade toluene (Sigma-Aldrich) was dried over calcium chloride, refluxed 48 h under a nitrogen atmosphere over sodium and distilled before use. Methylaluminoxane (MAO; 10 wt% solution in toluene; Sigma-Aldrich) was used as received. Dichloro{1,4-dithiabutanediyl-2,20-bis(4,6-di-alkylphenoxy)} titanium complexes (**1**) and (**2**) were synthesized according to the literature procedure.[28] NMR spectra were recorded on a Bruker AM 300 spectrometer (300 MHz for ^{1}H; 75 MHz for ^{13}C), a Bruker AVANCE 400 spectrometer (400 MHz for ^{1}H; 100 MHz for ^{13}C) and a Bruker ASCEND 600 spectrometer (600 MHz for ^{1}H; 150 MHz for ^{13}C). ^{1}H and ^{13}C chemical shifts are listed in parts per million (ppm) referenced to tetramethylsilane (TMS) using the protio residual signal of the deuterated solvent. Spectra are reported as chemical shift (δ ppm), multiplicity and integration. Multiplicity is abbreviated as follows: singlet (s), doublet (d), triplet (t), multiplet (m), broad (br), overlapped (o). The number-average molecular weights (M_n) and molecular weight distributions of polymers (dispersity, $Đ$) were evaluated by gel permeation chromatography (GPC) using an Agilent 1260 Infinity Series GPC chromatograph equipped with an RI, PLGPC 220 refractive index detector. All measurements were performed with THF as the eluent at a 1.0 mL/min flow rate at 35°C. Monodisperse poly(styrene) polymers were used as calibration standards. Differential scanning calorimetry (DSC) analyses were carried out with a Mettler Toledo DSC-822 apparatus in a flowing N_2 atmosphere at a rate of 10°C/min. Powder wide-angle X-ray diffraction (p-WAXD) profiles were collected in reflection mode using a multipurpose PANalytical Empyrean diffractometer using the Ni-filtered Cu Kα radiation ($\lambda = 0.154$ nm). Solution cast film where prepared by dissolving 100 mg of polymers in 15 mL of solvent (toluene or chloroform), by slow evaporation of solvent. Tensile properties were measured at room temperature using an Instron universal testing machine on rectangular specimens cut from toluene cast films with width, length and thickness of 3, 10 and 0.5 mm, respectively. Stress-strain curves were measured according to the ASTM D638-22 by stretching the specimens until failure using the ratio between the drawing speed and the specimen gauge length equal to 10 mm/(mm min). The final curves were averaged over at least five independent experiments.

3.8.2 Monomers syntheses. 1-Vinylcyclohexene (VCH) was synthesized according to the literature.[80] 1-Ethynylcyclohexene (13.5 mL) was selectively hydrogenated over Pd/$CaCO_3$ (poisoned with lead, 1.0 g), at 1 bar of hydrogen for 8 hours at room temperature in pentane (100 mL). The catalyst was then removed by filtration over celite, and the solvent was distilled under reduced pressure. The residue was purified by column chromatography on silica gel (100% *n*-heptane), followed by anhydrification over CaH_2, to obtain 1-vinylcyclohexene in 72% yield. ^{1}H NMR (600 MHz, CD_2Cl_2) δ: 6.35 (1H, dd, *J* 17.5, 10.7 Hz, $\underline{H}C{=}CH_2$), 5.77 (1H, br t, $C{=}C\underline{H}$), 5.07 (1H, d, *J* 17.5 Hz, $HC{=}C\underline{H_2}$, *trans*), 4.88 (1H, d, *J* 10.7 Hz, $HC{=}C\underline{H_2}$, *cis*), 2.15-2.13 (4H, m, $C\underline{H_2}C{=}CHC\underline{H_2}$), 1.68 (2H, m, $C{=}CHCH_2C\underline{H_2}$), 1.61 (2H, m, $C\underline{H_2}CH_2C{=}CH$).

S-4-isopropenyl-1-vinyl-1-cyclohexene (IVC) was synthesized according to the literature.[81] Potassium *tert*-butoxide (7.4 g, 66.0 mmol) was added in portions to a suspension of methyltriphenylphosphonium bromide (21.4 g, 60.0 mmol) in dry THF (50 mL), and the reaction mixture was stirred at room temperature (RT) for 2 h. (*S*)-(−)-Perillaldehyde (7.5 g, 50.0 mmol) was then dropwise added into the above described reaction mixture at 0 °C. After stirring overnight at RT, the reaction was quenched by adding water, and the organics were extracted with diethyl ether. The organic solution was dried over $MgSO_4$, and the solvent was subsequently removed under reduced pressure. The residue was treated with *n*-hexane to precipitate triphenylphosphine oxide, and the solution was concentrated and purified by column chromatography on silica gel to give IVC with yield of 57%. ^{1}H NMR (400 MHz, $CDCl_3$, ppm): δ 6.38 (dd, J = 17.2, 10.8 Hz, 1H, $CH_2{=}C\underline{H}\text{-}C$), 5.78 (s, 1H, $C{=}C\underline{H}\text{-}CH_2$), 5.08 (d, J = 17.2 Hz, 1H, $CH{=}C\underline{H_2}$), 4.92 (d, J = 10.8 Hz, 1H, $CH{=}C\underline{H_2}$), 4.74 (s, 2H, $C{=}C\underline{H_2}$), 2.19 (t, 5H, $C\text{-}C\underline{H_2}\text{-} CH_2{+}CH_2\text{-}C\underline{H}\text{-}CH_2{+}CH\text{-}C\underline{H_2}\text{-}CH$), 1.92 (m, 1H, $CH\text{-}C\underline{H_2}\text{-}CH_2$), 1.76 (s, 3H, $C\text{-}C\underline{H_3}$), 1.52 (m, 1H, $CH\text{-}C\underline{H_2}\text{-}CH_2$).

3.8.3 Polymerization of 1-vinylcyclohexene (VCH) (runs 1-8, Table 3.1). The metal complex (complex **1** or **2**, 10 μmol) was added into a 10 mL Schlenk tube equipped with a magnetic stirrer and dissolved in 3 mL of dry toluene. Methylaluminoxane (MAO) was added, and the solution was left stirring for 30 minutes to pre-activate the metal complex. Then VCH (3 mmol, 0.3 g) was added, and the system was placed in a thermostated oil bath and stirred for 18 h. The polymers were coagulated in an excess of acidified methanol, washed several times with methanol, recovered by filtration and dried in the vacuum oven overnight.

3.8.4 Polymerization of *S*-4-isopropenyl-1-vinyl-1-cyclohexene (IVC) (runs 1-4, Table 3.3). Complex **2** (10 μmol) was added into a 10 mL Schlenk tube equipped with a magnetic stirrer and dissolved in 3 mL of dry toluene. Methylaluminoxane (MAO) was added, and the solution was left stirring for 30 minutes to pre-activate the metal complex. Then IVC (2 mmol, 0.3 g) was added, and the system was placed in a thermostated oil bath at 80°C and stirred for 18 h. The polymers were coagulated in an excess of acidified methanol, washed several times with methanol, recovered by filtration and dried in the vacuum oven overnight.

3.8.5 Hydrogenation of poly(vinylcyclohexene) (run 8, Table 3.1). Poly(vinylcyclohexene) was hydrogenated by dissolving polymer in 30 mL of *n*-decane in an autoclave, thermostated at 130°C in a sand bath, in the presence of 200 mg of palladium on charcoal and 30 bar of hydrogen. After 48 h, the mixture was filtered over celite and poured into ethanol. The polymer was recovered by filtration and dried in vacuum.

3.8.6 Copolymerization of VCH with linear terpenes and styrene (runs 1-5, Table 3.2). Complex **2** (5 μmol) was added into a 10 mL Schlenk tube equipped with a magnetic stirrer and dissolved in 4 mL of dry toluene. Methylaluminoxane (MAO) was added, and the solution was left stirring for 30 minutes to pre-activate the metal complex. Then both comonomers (VCH and styrene/myrcene/ocimene) were dissolved in 1 mL of dry toluene and added, and the system was placed in a thermostated oil bath at 40°C and stirred for 18 h. The polymers were coagulated in an excess of acidified methanol, washed several times with methanol, recovered by filtration and dried in the vacuum oven overnight.

3.8.7 Copolymerization of IVC with linear terpenes and 1PB (runs 1-9, Table 3.5). The metal complex (complex **1** or **2**, 5 μmol) was added into a 10 mL Schlenk tube equipped with a magnetic stirrer and dissolved in 4 mL of dry toluene. Methylaluminoxane (MAO) was added, and the solution was left stirring for 30 minutes to pre-activate the metal complex. Then both comonomers (IVC and myrcene/ocimene/1PB) were dissolved in 1 mL of dry toluene and added, and the system was placed in a thermostated oil bath at 80°C and stirred for 24 h. The polymers were coagulated in an excess of acidified methanol containing 2,6-di-tert-butyl-4-methylphenol (BHT), washed several times with methanol, recovered by filtration and dried in the vacuum oven overnight.

3.8.8 Synthesis of dithiols for reversible crosslinking. In a 25 mL two-neck round-bottom flask equipped with a magnetic stir bar and under a nitrogen atmosphere, methyl thioglicolate (1.2 eq), *p*-toluenesulfonic acid (0.05 eq), and the mercaptoalcohol (MEtOH or MPrOH, 1 eq) were added. The reaction mixture was stirred at 50°C for three days. The crude mixture was then dissolved in 20 mL of chloroform and washed three times with 100 mL of aqueous sodium bicarbonate, followed by three washes with 100 mL of distilled water. The organic phase was dried over anhydrous $MgSO_4$, filtered, and concentrated under reduced pressure. The crude product was further purified by column chromatography using a hexane:EtOAc (98:2) eluent mixture.

3.8.9 Crosslinking reactions of PIVC. In a 25 mL two-neck round-bottom flask equipped with a magnetic stir bar and under a nitrogen atmosphere, PIVC (0.2 g) was added and dissolved in dry pyridine (3 mL). AIBN was then added, followed by the dithiol. A reflux condenser was connected to the flask, and the system was placed in a thermostated bath at 80°C with continuous stirring for 24 hours. After this time, the polymer became insoluble. Pyridine was removed under reduced pressure, and the resulting polymer was washed three times with chloroform and then with methanol. The product was filtered and recovered for further analysis.

Chapter 4

Stereoselective (Co)Polymerization of a Biobased Linear Diene Catalyzed by [OSSO]-Titanium Complexes

4.1 (E)-4,8-dimethyl-1,3,7-nonatriene: state of art

(E)-4,8-dimethyl-1,3,7-nonatriene (DMNT) is a renewable conjugated diene naturally present in volatile mixtures emitted by plants and in defense signals induced by insects. Structurally characterized by a linear C_9 backbone with three double bonds and two methyl substituents, DMNT belongs to the family of biogenic terpenoid dienes and represents an attractive monomeric platform for sustainable polymer development. In addition to its natural occurrence, DMNT can be synthetically accessed from fully biobased precursors: in particular, it can be obtained from citral, the major component of lemongrass oil, through a Wittig olefination (Scheme 4.1).

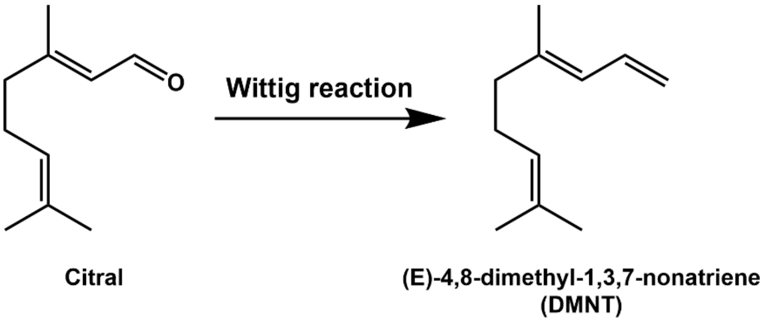

Scheme 4.1. Generic Scheme of the Wittig Reaction of Citral.

Despite this straightforward access from renewable feedstocks, the polymerization of DMNT remained largely unexplored because the sterically bulky substituents dramatically reduce the reactivity of double bonds. Indeed, only radical polymerization of DMNT has been reported, with poorly efficient radical polymerizations producing low-molecular-weight, atactic materials.[93]

Only recently has coordination polymerization of DMNT been achieved and this study remains the only example reported in the literature. Using rare-earth metal catalysts, Jiang *et al.* demonstrated that DMNT can be transformed into structurally well-defined polymers with distinct regio- and stereochemical selectivity.[94] Fluorenyl scandium complexes activated by

$[Ph_3C][B(C_6F_5)_4]$ and Al^iBu_3, efficiently produced highly 1,2-regioregular poly(DMNT) with 1,2-insertion (>99%) and low glass-transition temperatures (-34 to -39 °C). Conversely, asymmetric diiminophosphinato rare-earth complexes afforded perfect *trans*-1,4-poly(DMNT) (>99%), with catalytic activity increasing in the order Sc < Lu < Y, consistent with the need for a spacious coordination site to accommodate the bulky monomer (Scheme 4.2).

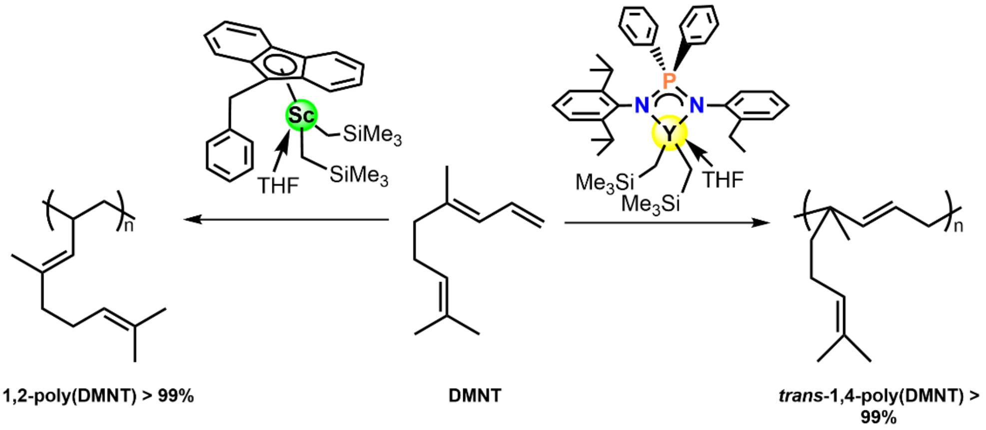

Scheme 4.2. Polymerization of DMNT by Rare Earth Metal Catalysts.

In addition, the yttrium catalyst enabled the one-pot one-step synthesis of a 3,4-polyisoprene-b-*trans*-1,4-poly(DMNT) diblock copolymer, highlighting its dual selectivity toward different dienes. Overall, these results establish that DMNT is a renewable and versatile monomer capable of producing both 1,2- and *trans*-1,4-regulated elastomers through rare earth-mediated coordination polymerization.

In the following sections of this work, the stereoselective polymerization of DMNT will be further investigated using titanium complexes bearing OSSO-type ligands, with the aim of accessing highly isotactic poly(DMNT), a microstructure not yet reported in literature and potentially capable of imparting enhanced mechanical strength or semicrystalline behavior relative to previously described amorphous materials. Moreover, the copolymerization of DMNT with other natural monomers, such as β-myrcene and β-ocimene, as well as with more rigid bio-derived dienes such as IVC and 1PB, will be explored with the goal of producing fully renewable copolymers with tunable mechanical properties. Depending on the comonomer, these materials may exhibit characteristics ranging from soft elastomeric behavior to thermoplastic elastomer performance.

4.2 Isospecific Polymerization of (E)-4,8-dimethyl-1,3,7-nonatriene (DMNT)

The efficiency of the two titanium complexes bearing [OSSO]-type ligands (**1** and **2**, Figure 2.3), activated by MAO, was evaluated in the stereoselective polymerization of DMNT and the results are summarized in Table 4.1.

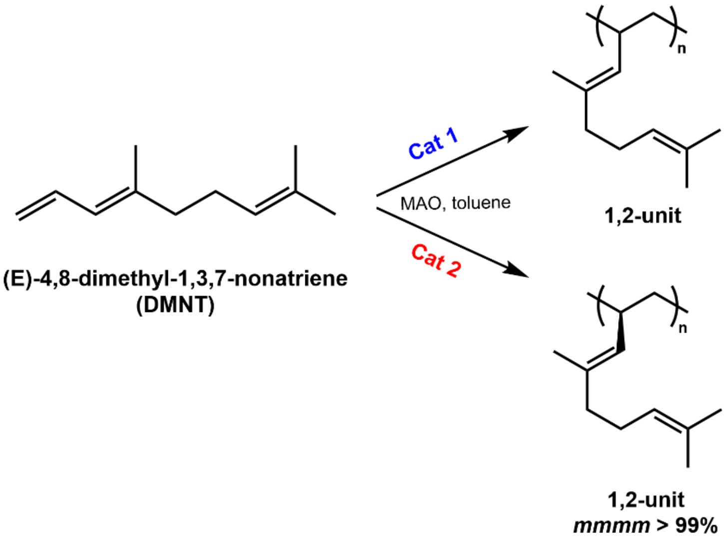

Scheme 4.3. Polymerization of DMNT promoted by [OSSO]-titanium complexes **1** and **2**.

Table 4.1. Homopolymerization of DMNT in presence of catalysts **1** and **2** activated with MAO.

Run [a]	Cat	*T* (°C)	Time (h)	Yield (%)	1,2- (%) [b]	*mmmm* (%) [b]	M_n (Kg/mol) [c]	Đ [c]	T_g (°C) [d]
1	**1**	25	24	73	> 99	*n.d.*	27.6	10.8	-36.7
2	**1**	40	24	76	> 99	*n.d.*	29.8	6.0	-37.0
3	**1**	80	24	89	> 99	*n.d.*	21.3	2.8	-34.4
4	**2**	25	24	92	> 99	> 99	72.4	3.2	-37.4
5	**2**	40	24	38	> 99	> 99	61.1	2.5	-39.1
6	**2**	80	24	72	> 99	> 99	40.1	2.3	-30.9
7	**2**	25	6	66	> 99	> 99	94.9	2.2	-40.2
8	**2**	25	10	83	> 99	> 99	102.4	2.1	-37.9
9	**2**	25	18	90	> 99	> 99	86.2	2.3	-38.6

[a] Reaction conditions: Catalyst ($1.0 \cdot 10^{-5}$ mol), [Al]/[Ti] = 500, DMNT (2 mmol, 0.3 g), toluene (3 mL). [b] Determined by ^{1}H and ^{13}C NMR spectroscopy. [c] Determined by GPC. [d] Determined by DSC.

Both catalysts demonstrated a significant capability to promote the polymerization of DMNT with excellent 1,2-regioselectivity, a result consistently reproduced across all tested temperatures (25, 40, and 80 °C). This strong preference for 1,2-insertion confirms that the sterically congested double bonds of DMNT can still be efficiently activated by titanium-OSSO complexes, provided that the catalyst environment remains sufficiently open to accommodate the monomer. Furthermore, catalyst **2** outperformed **1** in converting DMNT into higher molecular weight polymers delivering not only regioselective but also exceptionally stereoselective polymerization outcomes. Its greater steric hindrance produced highly isotactic poly(DMNT), with *mmmm* > 99%.

The isotacticity was confirmed through ^{1}H NMR analysis, where two distinct resonances at 1.15 ppm and 0.77 ppm (Figure 4.1a) were assigned to the diastereotopic protons of the $-CH_2$ group along the polymer backbone. Notably, these signals are absent in all previously reported spectra for poly(DMNT) available in the literature obtained using rare-earth catalysts, where the $-CH_2$ group typically appears as a single broad signal, consistent with an atactic microstructure.[94] The clear splitting observed in our samples thus represents a diagnostic and unambiguous proof of isotactic configuration, highlighting a microstructural feature never before reported for this monomer.

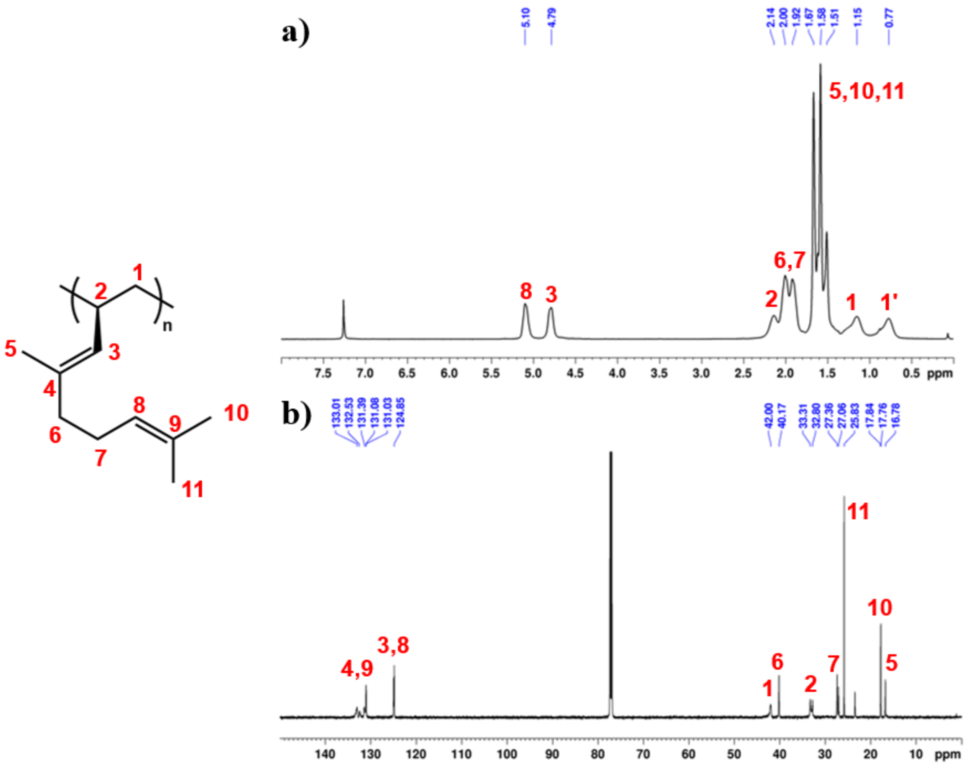

Figure 4.1. a) ^{1}H NMR (600 MHz, $CDCl_3$, 298 K) and b) ^{13}C NMR (150 MHz, $CDCl_3$, 298 K) of 1,2-isotactic poly(DMNT) from run **4**, Table 4.1.

The favorable temperature for polymerization was 25°C, where the highest yield is obtained within the same reaction time (entry 4, Table 4.1). Once the optimal temperature was established, the influence of reaction times was evaluated (entries 7-9, Table 4.1). Extended reaction times lead to increased polymer yields but also to reduced molecular weights, a trend reasonably attributable to enhanced chain transfer or termination processes that occur more frequently during extended reaction periods. The regulation of molecular weights aligns with the performance exhibited by [OSSO]-type titanium complexes as single-site catalysts in the polymerization of diene monomers, as demonstrated by the dispersity (*Đ*) values obtained from GPC analysis (see Appendix 4).

All samples exhibit a single glass-transition temperature, with values ranging from -34 °C to -40 °C and the presence of a single T_g confirms that these materials are amorphous (Figure 4.2). The elastomeric nature of the polymers, combined with their high stereoregularity, makes them promising candidates for applications requiring flexibility and elasticity over a wide temperature range, such as rubbers or thermoplastic elastomers.

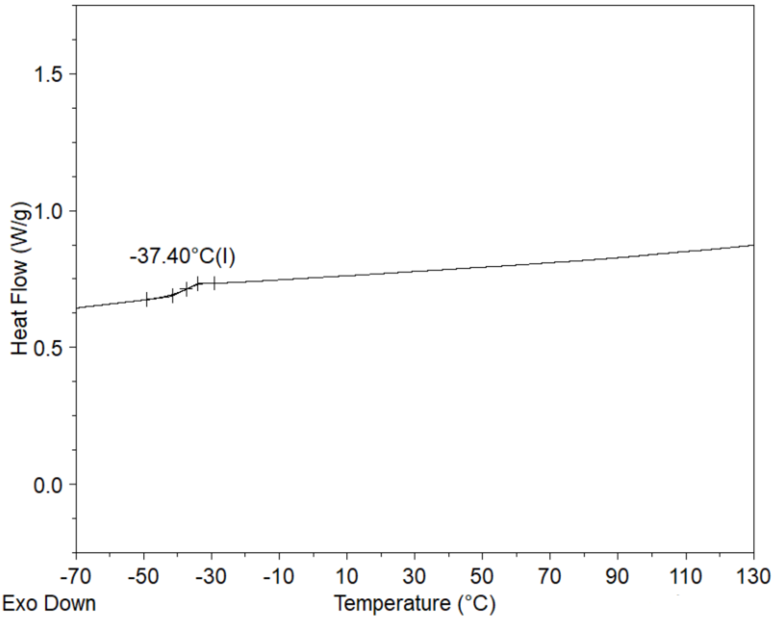

Figure 4.2. DSC thermograms of 1,2-isotactic poly(DMNT) from entry **4**, Table 4.1.

4.3 Copolymerization of DMNT with Linear Terpenes

To expand the structural versatility of DMNT-based materials and to explore the influence of renewable comonomers on the resulting polymer microstructure and properties, the copolymerization of DMNT with linear terpenes such as β-myrcene (M) and β-ocimene (O) was systematically investigated using catalyst **2** (Scheme 4.4). The experimental results are summarized in Table 4.2.

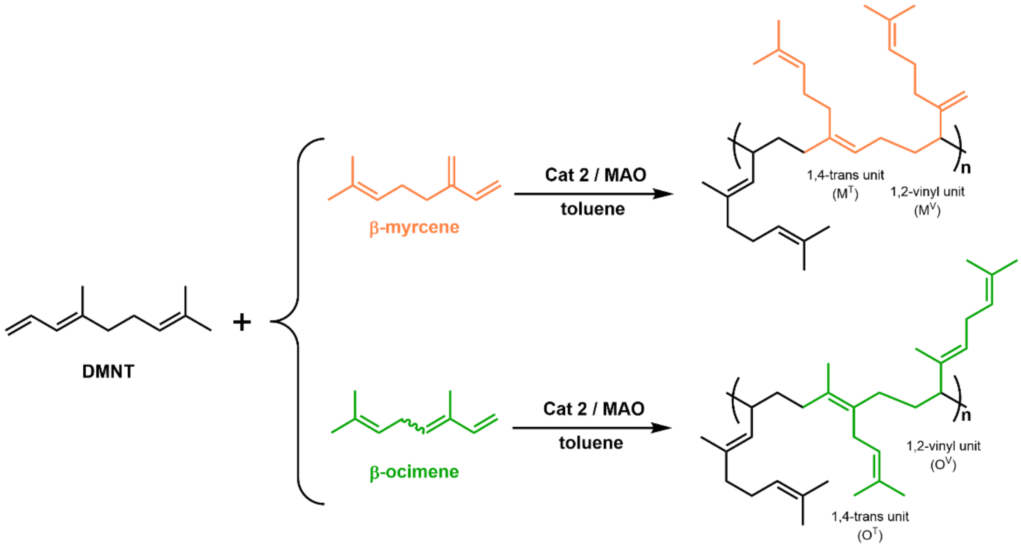

Scheme 4.4. Copolymerization of DMNT with linear terpenes promoted by [OSSO]-titanium complex **2**.

The first copolymerizations performed with β-myrcene (runs 1-3) shows that varying the reaction temperature while keeping the monomer feed constant produces a clear and systematic trend. At 25 °C (run 1), β-myrcene incorporation reaches only 12 mol%, whereas increasing the temperature to 40 °C (run 2) moderately enhances insertion to 20 mol%. A remarkable improvement is observed at 80 °C (run 3), where incorporation rises to 37 mol%. This trend suggests that the insertion of the linear terpene is significantly facilitated at higher temperatures. Based on this evidence, 80 °C was selected as the optimal temperature for subsequent studies.

At this optimized temperature, the effect of comonomer feed composition was investigated (runs 4-6). As expected, increasing the amount of β-myrcene in the feed results in higher incorporation within the polymer, rising from 27 mol% (run 4) to 49 mol% (run 6). This trend confirms that the catalytic system maintains excellent reactivity over a wide range of comonomer concentrations. Despite this improved incorporation, molecular weights decrease progressively with increasing β-myrcene content. This behavior may be associated with enhanced chain-transfer processes or reduced propagation efficiency when high levels of the more flexible terpene are present. Also, the glass transition temperature systematically decreases as more terpene is incorporated, moving from -39.7 °C (run 4) to -54.7 °C (run 6) and the single T_g observed for each material confirms the amorphous nature of these copolymers.

Table 4.2. Copolymerization of DMNT with linear terpenes in presence of catalyst **2**/MAO.

Run[a]	**Terp. / feed (mol%)**	**Temp. (°C)**	**Yield (%)**	**M_n (Kg/mol)**[c]	**Đ**[c]	**Polymer composition (%)**[b]		**T_g (°C)**[d]
						Terp. (mol%)	**DMNT (mol%)**	
1	M / 50	25	23	29.7	2.3	12	88	-42.6
2	M / 50	40	44	19.2	2.1	20	80	-43.3
3	M / 50	80	44	12.0	1.9	37	63	-46.3
4	M / 20	80	74	16.6	2.0	27	73	-39.7
5	M / 70	80	29	12.4	1.9	40	60	-51.8
6	M / 80	80	24	12.3	1.8	49	51	-54.7
7	O / 20	80	78	42.9	2.4	38	62	-33.2
8	O / 50	80	62	37.4	2.2	44	56	-33.6
9	O / 70	80	45	35.0	2.9	50	50	-31.5
10	O / 80	80	63	31.1	2.4	54	46	-24.5

[a] Reaction conditions: Catalyst **2** ($5.0\cdot10^{-6}$ mol), ([DMNT]+[Terp.])/[Ti] = 1000, [Al]/[Ti] = 500, toluene (5 mL), 24 h. [b] Determined by ^{1}H and ^{13}C NMR spectroscopy. [c] Determined by GPC. [d] Determined by DSC.

A distinct behavior is observed in the copolymerizations involving β-ocimene (runs 7-10). Even at a relatively low feed content of 20 mol% (run 7), β-ocimene displays a high tendency toward incorporation, reaching 33 mol%, significantly higher than the analogous myrcene system under identical conditions. This enhanced reactivity is accompanied by notably higher molecular weights, indicating more efficient propagation. When the ocimene feed is increased (runs 8-10), incorporation follows a similar positive trend, rising from 44 to 51 mol% as the O:DMNT ratio increases. In all cases, molecular weights remain comparatively high (31-37 kg mol^{-1}), and the yields exceed those obtained with myrcene, further highlighting the favorable polymerization behavior of β-ocimene.

The evolution of the glass transition temperatures shows a trend opposite to that observed for the myrcene-based copolymers. In this case, T_g increases with increasing ocimene incorporation, rising from -33.6 °C (run 8) to -24.5 °C (run 10). This behavior reflects the intrinsic thermal properties of the homopolymers: poly(ocimene) exhibits a T_g of approximately -30 °C, significantly higher than that of poly(myrcene), which lies around -60 °C.[69] As observed in all systems, the presence of a single T_g confirms the nature of these materials.

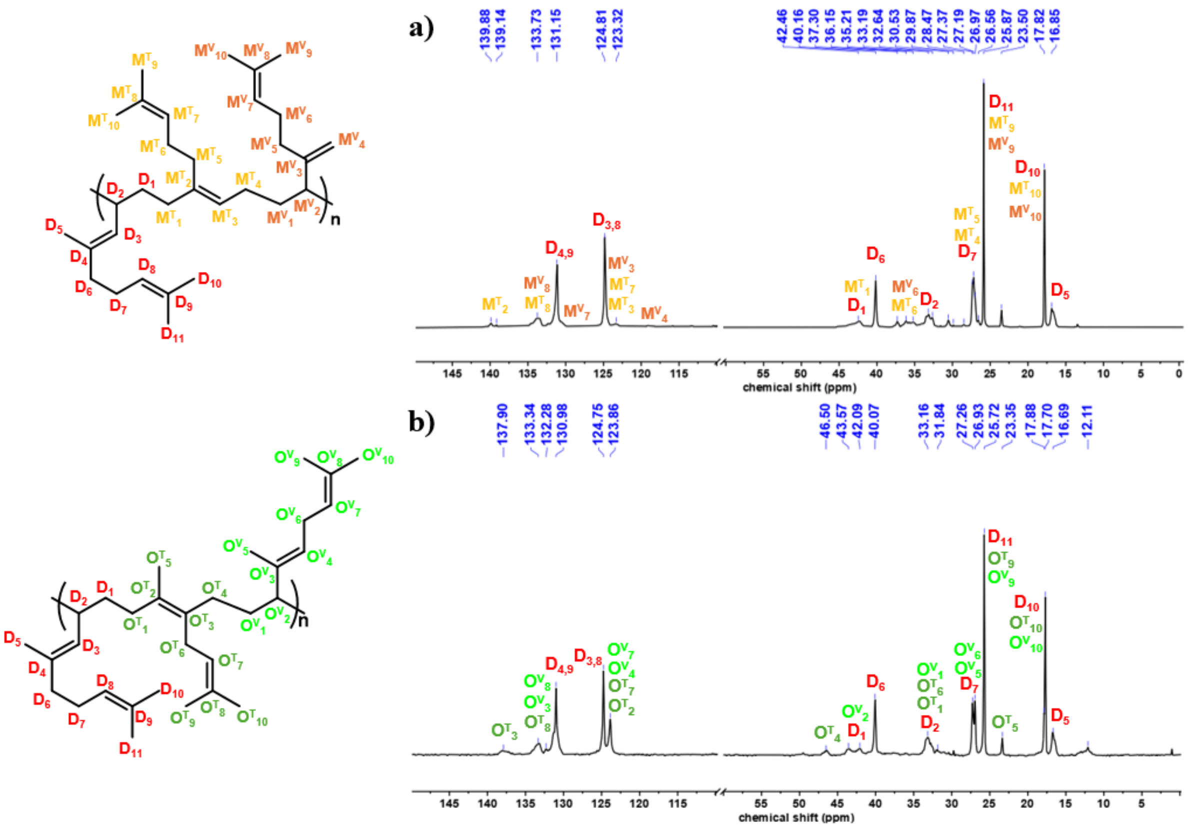

Figure 4.3. ^{13}C NMR (100 MHz, $CDCl_3$, 298 K) of a) DMNT-M copolymer from entry **5** and b) DMNT-O copolymer from entry **9** of Table 4.2.

The copolymers were further characterized by ^1H and ^{13}C NMR spectroscopy (Figure 4.3) to elucidate their microstructure. The results revealed, in both cases, the coexistence of 1,4-*trans* and 1,2-vinyl insertions, as expected. These microstructural features, combined with the trends in incorporation and thermal data, suggest that the resulting materials may possess a multiblock architecture, most likely of random or tapered nature.

4.4 Copolymerization of DMNT with IVC and 1PB

To further investigate the versatility of DMNT-based copolymer systems, additional copolymerizations were performed with two comonomers of different structural complexity: 4-isopropenyl-1-vinyl-1-cyclohexene (IVC) and 1-phenyl-1,3-butadiene (1PB) (Scheme 4.5).

These monomers were selected to study how their structural rigidity influences the thermal behavior of the resulting materials. The results are summarized in Table 4.3.

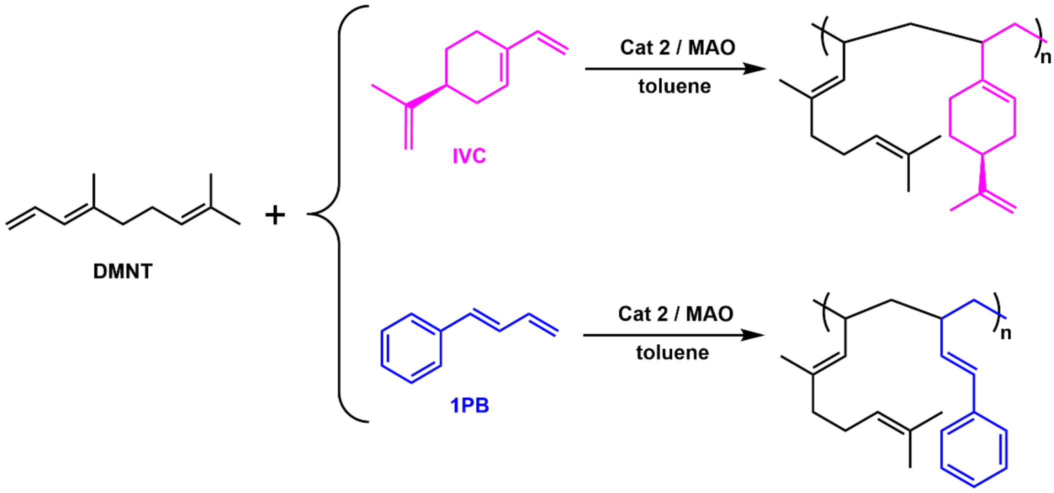

Scheme 4.5. Copolymerization of DMNT with 1PB and IVC promoted by [OSSO]-titanium complex **2**.

Table 4.3. Copolymerization of DMNT with IVC and 1PB in presence of catalyst **2**/MAO.

Run [a]	C / feed (mol%)	Temp. (°C)	Yield (%)	M_n (Kg/mol)[c]	Đ[c]	Polymer composition (%)[b]		T_g (°C)[d]
						C (mol%)	DMNT (mol%)	
1	IVC / 50	25	15	43.0	2.8	39	61	-29.4
2	IVC / 50	40	28	88.9	2.5	34	66	-12.8
3	IVC / 50	80	28	66.5	2.7	35	65	-3.2
4	IVC / 20	40	82	88.0	2.4	16	84	-37.0
5	IVC / 70	40	70	180.7	2.2	72	28	41.7
6	IVC / 80	40	46	107.0	3.9	76	24	49.1
7	1PB / 50	25	5	152.3	3.0	53	47	17.5
8	1PB / 50	40	66	123.1	2.6	57	43	24.9
9	1PB / 50	80	77	53.2	2.3	51	49	13.4
10	1PB / 20	40	86	91.1	2.3	17	83	-19.4
11	1PB / 70	40	72	154.3	2.1	71	29	40.3
12	1PB / 80	40	69	179.6	1.6	79	21	58.2

[a] Reaction conditions: Catalyst **2** ($5.0 \cdot 10^{-6}$ mol), ([DMNT]+[C])/[Ti] = 1000, [Al]/[Ti] = 500, toluene (5 mL), 24 h. [b] Determined by ^{1}H and ^{13}C NMR spectroscopy. [c] Determined by GPC. [d] Determined by DSC. C= comonomer.

In the copolymerizations performed with IVC (runs 1-3), a comparison across temperatures at constant feed composition shows that increasing the temperature from 25 to 40 °C improves both yield and molecular weight (runs 1-2), while maintaining comparable incorporation levels of the comonomer. Raising the temperature further to 80 °C (run 3) does not significantly modify the IVC content in the polymer and does not offer advantages in terms of molecular weight. On this basis, 40 °C was selected as the optimal temperature, having provided the most favorable balance between yield and molecular weight under identical feed conditions.

At 40 °C, the effect of feed composition was examined (runs 4-6). The incorporation of IVC aligns closely with its abundance in the feed, increasing from 16 mol% (run 4) to 76 mol% (run 6). The molecular weights vary considerably, reaching particularly high values in 30:70 (DMNT:IVC) compositions (run 5), suggesting that the interaction between sterics and monomer concentration significantly influences the propagation efficiency. The glass transition temperatures shift toward higher values as the content of IVC in the copolymer increases, consistent with the intrinsic rigidity of the cyclic comonomer relative to poly(DMNT) (Figure 4.4A).

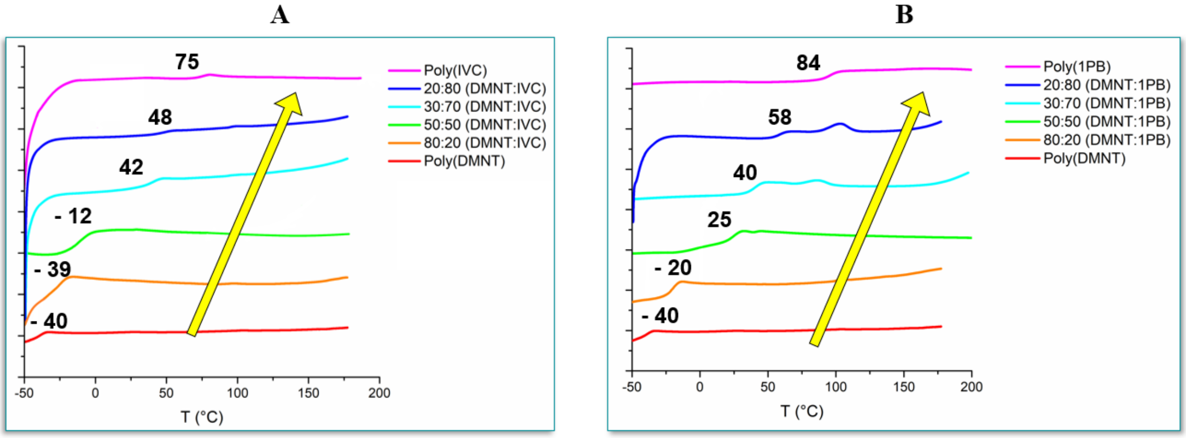

Figure 4.4. Comparison between DSC thermograms of DMNT-IVC copolymers (A) and DMNT-1PB copolymers (B) relative to the different compositions.

A different scenario emerges from the 1PB-based copolymerizations (runs 7-12). Even at 25 °C (run 7), the incorporation of 1PB is remarkably high (53 mol%), and the resulting polymers display very high molecular weights, highlighting the strong reactivity of this conjugated aromatic diene. Increasing the temperature to 40 °C (run 8) maintains high incorporation (57 mol%) and affords even higher yields, while 80 °C (run 9) leads to lower molecular weights, likely due to enhanced chain-transfer or decreased propagation efficiency at elevated temperatures. For this reason, and analogously to what was observed for IVC, 40 °C was selected as the most suitable temperature for exploring feed composition trends.

Varying the feed at 40 °C (runs 10-12) results in a progressive increase in 1PB incorporation, rising from 17 mol% to 79 mol% as the comonomer fraction increases. The molecular weights remain consistently high in all cases, reaching a maximum in the 30:70 (DMNT:1PB) compositions (run 11). The glass transition temperatures follow the expected trend due to the rigid aromatic structure of 1PB: increasing incorporation results in progressively higher T_g values, ranging from -19.4 °C to +58.2 °C, confirming the strong stiffening effect conferred by the phenyl-substituted monomer (Figure 4.4B).

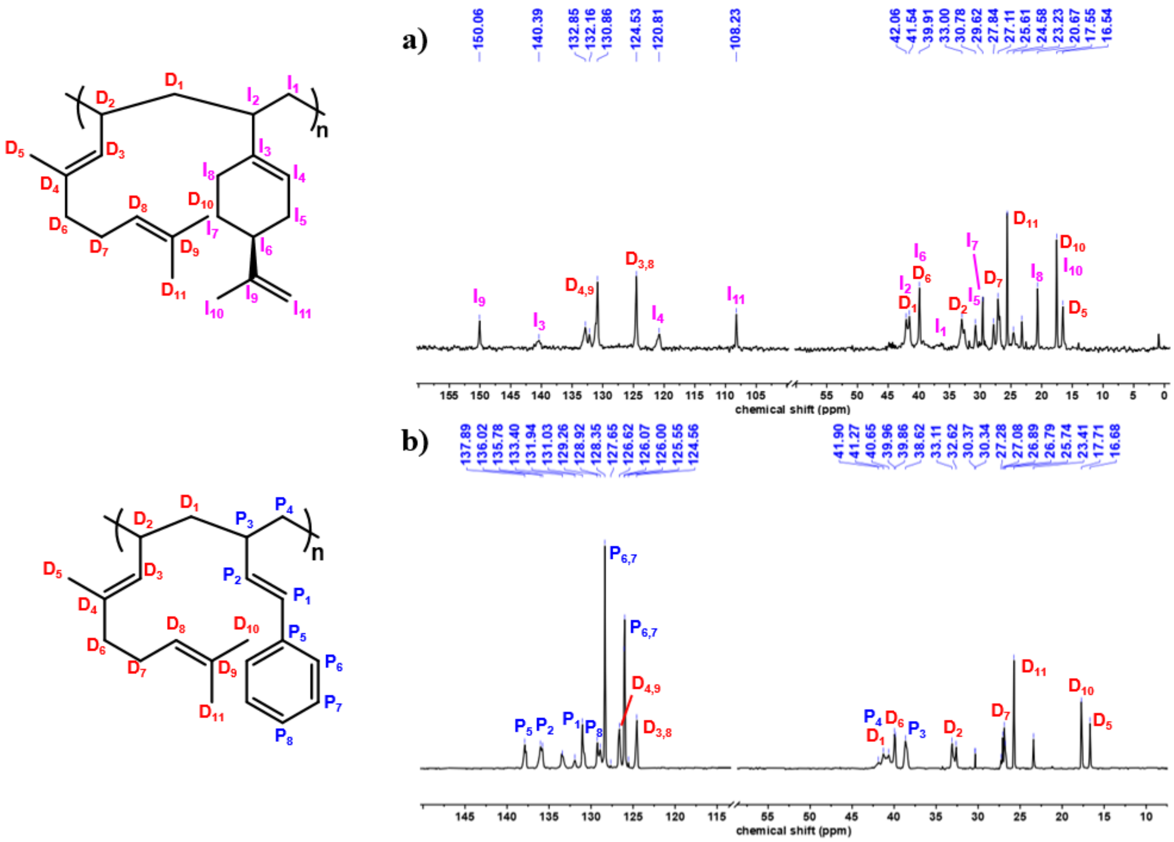

Figure 4.5. ^{13}C NMR (100 MHz, $CDCl_3$, 298 K) of a) DMNT-IVC copolymer from entry **2** and b) DMNT-1PB copolymer from entry **8** of Table 4.3.

Microstructural analysis conducted by ^1H and ^{13}C NMR spectroscopy (Figure 4.5) shows that all three comonomers, IVC, 1PB, and DMNT, are incorporated exclusively through their characteristic 1,2- or 3,4-insertion modes. No evidence of alternative insertion pathways was detected, confirming that catalyst **2** retains its high regioselectivity even in the presence of structurally diverse dienes. Despite the uniform insertion mode and thermal behavior suggest that the materials may adopt multiblock architectures, most likely of random or tapered nature, arising from the differing reactivity ratios between DMNT and each comonomer.

Furthermore, it is interesting that, given their structural characteristics, DMNT and 1PB prove to be exceptionally promising bioderived analogues of butadiene and styrene, respectively, two pillars of the global elastomer industry. Their molecular architecture faithfully reproduces the key reactivity elements of their fossil counterparts, positioning them as realistic candidates for the production of next-generation sustainable SBR and SBS. In this context, "one-pot one-step" copolymerizations can mirror the typical composition of commercial SBR, which generally contains about 80% butadiene by weight and about 20% styrene by weight. The copolymer from run 10 may therefore be the closest structural and compositional analogue to real SBR, allowing for a direct and meaningful comparison. The final copolymer exhibited a single glass transition at approximately -19 °C. This value is particularly significant when compared to fossil-derived SBR, whose T_g typically lies between -50 and -60 °C, depending on the styrene content and microstructural distribution. Although the renewable copolymer displays a higher T_g, its position remains well within the elastomeric regime, confirming that DMNT can indeed function as a renewable analogue of butadiene, providing rubber-like flexibility while offering a tunable softness through incorporation of bio-aromatic 1PB.

To reproduce the SBS architecture, instead, a sequential monomer addition strategy was used, using the typical 15:70:15 feed ratio that defines A-B-A thermoplastic elastomers, using catalyst **2** at 40°C. This approach successfully yielded a 1PB-DMNT-1PB triblock that consistently mirrored the initial composition and displayed two sharply separated glass transitions, at -36.4 °C and +100 °C and M_n= 50.1 Kg/mol.

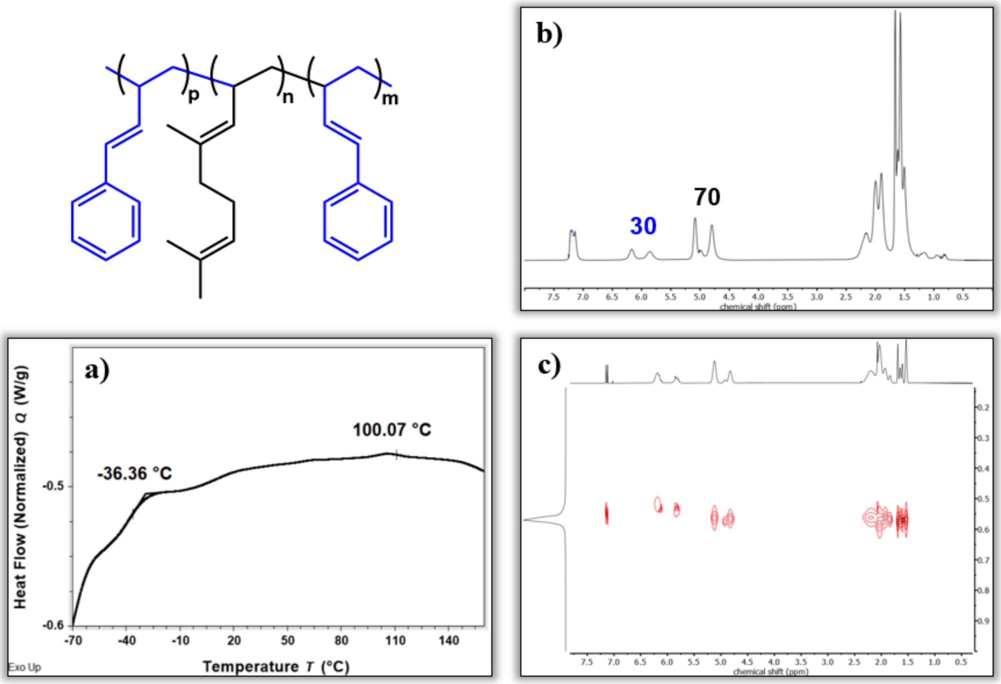

Figure 4.6. a) DSC thermogram; b) ^{1}H NMR (400 MHz, $CDCl_3$, 298 K) and c) 2D DOSY NMR (400 MHz, $CDCl_3$, 298 K) of the ABA triblock copolymer.

The presence of dual T_g is the hallmark of phase-segregated thermoplastic elastomers, and is consistent with commercial SBS, whose polybutadiene core block typically has T_g values between -50 and -60 °C, while the polystyrene end blocks fall between +95 and +105 °C. The fact that the high-temperature T_g (+100 °C) of the bio-based triblock aligns perfectly with the styrenic T_g of fossil-derived SBS is particularly remarkable, demonstrating that 1PB can fully emulate the hard-block thermal performance of styrene. At the same time, the DMNT-rich segment displays a T_g of -36.4 °C, slightly higher than that of polybutadiene but still well within the elastomeric regime, confirming that DMNT behaves as a genuine renewable diene capable of supporting rubber-like flexibility.

In other words, the DMNT-1PB system not only replicates the architecture of SBR and SBS, but also matches, and in some respects even approaches, their thermal performance windows, providing a compelling demonstration that high-performance elastomers can be synthesized from renewable and structurally complex monomers without sacrificing functionality.

4.5 Cytotoxicity Screening of Bio-Based Homopolymers by MTT Assay

A final interesting aspect is the study of the interaction with biological systems of homopolymers obtained from natural aldehydes. Poly(DMNT), together with the other two bio-based materials poly(1PB) and poly(IVC), was subjected to preliminary cytotoxicity tests in order to probe their interaction with biological systems. Specifically, the cytocompatibility of these homopolymers was evaluated via standard MTT assays on HepG2 cells, a widely used human hepatocellular carcinoma line that models the primary site of xenobiotic metabolism. Cells were exposed to polymer solutions at 10 and 50 µg mL^{-1} for 24, 48 and 72 h, with untreated and DMSO-treated cells as negative controls (Figure 4.7).

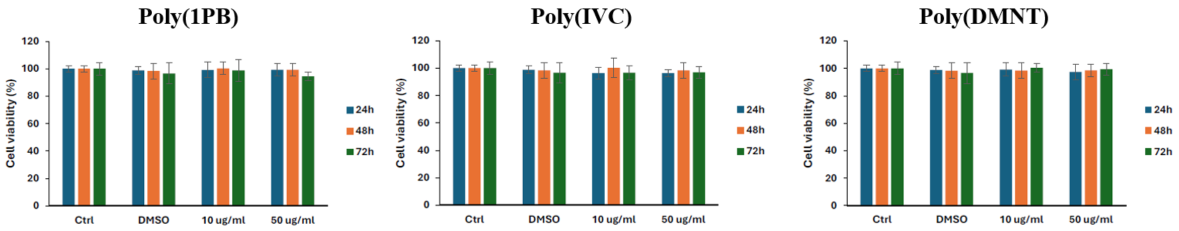

Figure 4.7. Histograms of the MTT cell viability assay on poly(1PB), poly(IVC) and poly(DMNT).

In all cases, cell viability remained close to or above 100% relative to the untreated control, and no reduction exceeded the 30% threshold commonly adopted in ISO 10993-5 as an indicator of cytotoxic potential.[95] Thus, under the tested conditions, all three polymers can be considered non-cytotoxic up to 50 μg mL^{-1}. Notably, for poly(1PB) and poly(IVC), limited solubility likely reduced the effective polymer concentration from nominal values, but no adverse effects on mitochondrial activity were detected even at the limits of solubility. While these *in vitro* data do not constitute a complete biocompatibility assessment, they clearly demonstrate that the conversion of natural derived dienes to well-defined high molecular weight polymers via [OSSO]-Ti catalysis can produce non-cytotoxic materials in a relevant human liver model. This significantly strengthens the prospects of these sustainable polymers for applications where a safe biological interface is crucial, such as soft devices, coatings or encapsulation matrices in contact with biological fluids and tissues.

4.6 Conclusion

The titanium OSSO-type complexes proved highly efficient in promoting the polymerization of DMNT with complete 1,2-regioselectivity. Catalyst **2** stood out for its ability to provide exceptionally stereoregular poly(DMNT), with *mmmm* > 99%, a level of isotacticity never previously reported for this monomer. The diagnostic splitting of the $-CH_2$ resonances in the ^1H NMR spectra provided definitive evidence of this unprecedented microstructural control. The optimal temperature for homopolymerization was identified as 25 °C, balancing high yields and controlled molecular weight growth, while time extension experiments revealed the predicted chain transfer and termination processes leading to lower molecular weights. All samples exhibited a single glass transition between -34 and -40 °C, confirming their amorphous and elastomeric nature.

The introduction of linear terpenes enabled fine-tuning of the thermal and structural properties of DMNT-based materials. β-Myrcene incorporation increased markedly with temperature, while β-ocimene displayed a higher intrinsic reactivity and yielded copolymers with correspondingly higher T_g values. NMR analysis confirmed the predicted insertion modes for both monomers, and the combined thermal and compositional trends are consistent with random or tapered multiblock architectures governed by the distinct reactivities of the monomers.

Copolymerizations with IVC and 1PB further demonstrated how monomer rigidity influences polymer properties. IVC incorporation remained proportional to its feed ratio, while 1PB produced materials with high molecular weights and T_g values ranging from elastomer to glassy. Catalyst **2** consistently preserved regio- and stereoselective insertion across all systems, highlighting its robustness toward structurally diverse bio-derived dienes.

Due to their structural characteristics, DMNT and 1PB both appear to be promising sustainable alternatives to butadiene and styrene. The one-pot one-step DMNT:1PB copolymer with an 80:20 composition, designed as a renewable analogue of SBR, exhibited a T_g around -20 °C, confirming elastomeric behavior despite being higher than commercial SBR. The sequential triblock 1PB-DMNT-1PB, prepared as a renewable counterpart of SBS, showed two well-separated T_g values (-36.4 °C and +100 °C), reproducing the essential thermal characteristics of hard-soft styrenic thermoplastic elastomers. These results illustrate that renewable monomers can successfully recreate the functional profiles of conventional SBR and SBS while offering a path toward high-performance, bio-based elastomeric materials.

The preliminary MTT assays on HepG2 cells showed that all the bio-based homopolymer, poly(1PB), poly(IVC), and poly(DMNT) are non-cytotoxic up to 50 μg mL^{-1} under the tested conditions, providing an encouraging first indication that these natural-aldehyde-derived polymers can combine controlled microstructure and tunable properties with a benign short-term interaction with hepatic cells.

4.7 Experimental Section

4.6.1 Materials and methods. Reagents and solvents were purchased from Sigma-Aldrich, Merck or TCI chemicals. Solvents were dried and distilled before use. All air- and/or water-sensitive compound manipulations were carried out using a glovebox or standard Schlenk techniques under an N_2 atmosphere. Commercial grade toluene (Sigma-Aldrich) was dried over calcium chloride, refluxed 48 h under a nitrogen atmosphere over sodium and distilled before use. Methylaluminoxane (MAO; 10 wt% solution in toluene; Sigma-Aldrich) was used as received. Dichloro{1,4-dithiabutanediyl-2,20-bis(4,6-di-alkylphenoxy)} titanium complexes (**1**) and (**2**) were synthesized according to the literature procedure.[28] NMR spectra were recorded on a Bruker AM 300 spectrometer (300 MHz for ^{1}H; 75 MHz for ^{13}C), a Bruker AVANCE 400 spectrometer (400 MHz for ^{1}H; 100 MHz for ^{13}C) and a Bruker ASCEND 600 spectrometer (600 MHz for ^{1}H; 150 MHz for ^{13}C). ^{1}H and ^{13}C chemical shifts are listed in parts per million (ppm) referenced to tetramethylsilane (TMS) using the protio residual signal of the deuterated solvent. Spectra are reported as chemical shift (δ ppm), multiplicity and integration. Multiplicity is abbreviated as follows: singlet (s), doublet (d), triplet (t), multiplet (m), broad (br), overlapped (o). The number-average molecular weights (M_n) and molecular weight distributions of polymers (dispersity, $Đ$) were evaluated by gel permeation chromatography (GPC) using an Agilent 1260 Infinity Series GPC chromatograph equipped with an RI, PLGPC 220 refractive index detector. All measurements were performed with THF as the eluent at a 1.0 mL/min flow rate at 35°C. Monodisperse poly(styrene) polymers were used as calibration standards. Differential scanning calorimetry (DSC) analyses were carried out with a Mettler Toledo DSC-822 apparatus in a flowing N_2 atmosphere at a rate of 10°C/min.

4.6.2 Monomers synthesis. Methyltriphenylphosphonium bromide (11.7 g, 33 mmol) was suspended in 50 mL of anhydrous THF under a nitrogen atmosphere. *n*-Butyllithium (36.3 mmol, 20.6 mL, 1.6 mol/L, hexane) was then slowly added at 0°C, and the solution was warmed to room temperature for 2 h. Then, a THF solution of citral (4.56 g, 30 mmol) was transferred, and the reaction was performed for additional 2 h and quenched with saturated NH_4Cl solution (10 mL, 5.0 wt-%). The crude solid product was extracted with either (30 mL), filtered through a pad of celite and dried with anhydrous Na_2SO_4 layer. The solution was separated and concentrated in vacuum, and the resultant product was purified by column chromatography in 88% yield. ^{1}H NMR (500 MHz, $CDCl_3$, 25°C): δ = 6.59 (m, 1H), 5.90 (d, 1H), 5.14 (m, 2H), 5.00 (m, 1H), 2.20 (m, 1H), 2.11 (m, 3H), 1.79 (d, 3H), 1.71 (s, 3H), 1.64 (s, 3H).

4.6.3 Polymerization of (E)-4,8-dimethyl-1,3,7-nonatriene (DMNT) (runs 1-9, Table 4.1). The metal complex (**1** or **2**, 10 μmol) was added into a 10 mL Schlenk tube equipped with a magnetic stirrer and dissolved in 3 mL of dry toluene. Methylaluminoxane (MAO) was added, and the solution was left stirring for 30 minutes to pre-activate the metal complex. Then DMNT (2 mmol, 0.3 g) was added, and the system was placed in an oil bath thermostated to the desired temperature (25, 40 or 80 °C) and stirred for the required time. The polymers were coagulated in an excess of acidified methanol, washed several times with methanol, recovered by filtration and dried in the vacuum oven overnight.

4.6.4 Copolymerization of DMNT with linear terpenes (runs 1-10, Table 4.2). Complex **2** (5 μmol) was added into a 10 mL Schlenk tube equipped with a magnetic stirrer and dissolved in 4 mL of dry toluene. Methylaluminoxane (MAO) was added, and the solution was left stirring for 30 minutes to pre-activate the metal complex. Then both comonomers (DMNT and myrcene/ocimene) were dissolved in 1 mL of dry toluene and added, and the system was placed in a thermostated oil bath to the desired temperature (25, 40 or 80 °C) and stirred for 24 h. The polymers were coagulated in an excess of acidified methanol containing 2,6-di-tert-butyl-4-methylphenol (BHT), washed several times with methanol, recovered by filtration and dried in the vacuum oven overnight.

4.6.5 Copolymerization of DMNT with IVC and 1PB (runs 1-12, Table 4.3). Complex **2** (5 μmol) was added into a 10 mL Schlenk tube equipped with a magnetic stirrer and dissolved in 4 mL of dry toluene. Methylaluminoxane (MAO) was added, and the solution was left stirring for 30 minutes to pre-activate the metal complex. Then both comonomers (DMNT and IVC/1PB) were dissolved in 1 mL of dry toluene and added, and the system was placed in a thermostated oil bath to the desired temperature (25, 40 or 80 °C) and stirred for 24 h. The polymers were coagulated in an excess of acidified methanol containing 2,6-di-tert-butyl-4-methylphenol (BHT), washed several times with methanol, recovered by filtration and dried in the vacuum oven overnight.

4.6.6 One-pot two-step copolymerization of DMNT and 1PB. Complex **2** (5 μmol) was added into a 10 mL Schlenk tube equipped with a magnetic stirrer and dissolved in 5 mL of dry toluene. Methylaluminoxane (MAO) was added, and the solution was left stirring for 30 minutes to pre-activate the metal complex. Then 1PB (150 eq) was and added, and the system was placed in a thermostated oil bath at 40 °C and stirred for 16 h. After this time, the DMNT (700 eq) was added, and the system was left to stir for a further 8 hours and finally the 1PB (150 eq) was added again. The polymer was coagulated in an excess of acidified methanol containing 2,6-di-tert-butyl-4-methylphenol (BHT), washed several times with methanol, recovered by filtration and dried in the vacuum oven overnight.

Chapter 5

Kinetic Studies via *In Situ* NMR and Determination of the Reactivity Ratios of Copolymerizations

5.1 Introduction

A fundamental aspect of understanding chain copolymerization is the quantitative determination of reactivity ratios, parameters that describe the relative tendency of each monomer to be incorporated into the growing polymer chain. Over the years, several analytical and kinetic methods have been developed to estimate these parameters, each based on different approximations of the underlying copolymerization kinetics. The earliest and most widely used approach is the Mayo-Lewis terminal model,[96] which considers a monomer mix of two components M_1 and M_2 and the four possible propagating reactions at the chain end:

$$\begin{aligned} M_1^* + M_1 &\xrightarrow{k_{11}} M_1 M_1^* \\ M_1^* + M_2 &\xrightarrow{k_{12}} M_1 M_2^* \\ M_2^* + M_2 &\xrightarrow{k_{22}} M_2 M_2^* \\ M_2^* + M_1 &\xrightarrow{k_{21}} M_2 M_1^* \end{aligned}$$

The reactivity ratios are then defined as:

$$r_1 = \frac{k_{11}}{k_{12}}, r_2 = \frac{k_{22}}{k_{21}} \tag{1}$$

where k_{ij} is the rate constant for insertion of monomer j into a chain ending with monomer i. The fundamental differential form of the equation is:

$$\frac{d[M_1]}{d[M_2]} = \frac{[M_1]\,(r_1[M_1] + [M_2])}{[M_2]\,([M_1] + r_2[M_2])} \tag{2}$$

which can be written in mole-fraction form as:

$$F_1 = \frac{r_1 f_1^2 + f_1 f_2}{r_1 f_1^2 + 2 f_1 f_2 + r_2 f_2^2} \tag{3}$$

where f_i are the mole fractions of the monomers in the feed and F_i the mole fractions in the instantaneous copolymer.

Although powerful, this differential form requires analysis at very low conversion (typically <5-10%), where the monomer feed composition remains essentially constant. Because this model assumes that the composition of the feed remains effectively constant, in practice it is often evaluated by performing several polymerizations at varying feed ratios, isolating the copolymer, and analysing its composition by ^{1}H-NMR, ^{13}C-NMR or FT-IR.

To facilitate graphical estimation of reactivity ratios, several linearization methods have been proposed, including the Fineman-Ross equation[97] and the Kelen-Tüdös[98] equation, both derived from algebraic rearrangements of the Mayo-Lewis relationship. These approaches rely on determining copolymer composition at low conversions for a series of feed compositions. More rigorous integrated treatments, such as the Meyer-Lowry equation,[99] extend the validity of the terminal model to moderate conversions by integrating the differential form numerically, although still requiring compositional analysis of isolated copolymers.

A major conceptual advance was introduced by Jaacks, who developed an integrated excess-monomer method that bypasses the need to determine copolymer composition.[100] By conducting the copolymerization with a large excess of one monomer, propagation occurs predominantly through active chains bearing that monomer as terminal unit. Under these conditions, the complex competition between two distinct chain ends collapses to an effectively one-terminal process, yielding the remarkably simple integrated relationship:

$$\ln\left(\frac{[M_1]_t}{[M_1]_0}\right) = r_1 \ln\left(\frac{[M_2]_t}{[M_2]_0}\right) \tag{4}$$

which allows determination of r_1 directly from monomer consumption, as monitored for example by gas chromatography or, more recently, *in situ* NMR. This method tolerates high conversion data and avoids polymer isolation, making it particularly attractive when copolymer analysis is difficult or unreliable.

Further refinement came with the non-terminal model of Beckingham, Lynd, and Sanoja (BLS),[101] motivated by the observation that in many ionic or coordination polymerizations the reactivity of the propagating chain is independent of the terminal monomer unit. Assuming a single active species and monomer-dependent rate constants k_A and k_B, the authors derived fully integrated expressions linking the total conversion p_{AB} to the individual monomer conversions p_A and p_B. Reactivity ratios are then obtained by fitting the experimental monomer consumption traces across the entire conversion range, eliminating the need to restrict the analysis to low conversion or to rely on terminal effects that may not be operative. Under the assumption of a single active species with monomer-dependent rate constants $k_A$and k_B, fully integrated expressions relate individual conversions $p_A(t)$ and $p_B(t)$ to the total conversion $p_{AB}(t)$, enabling extraction of:

$$r_A = \frac{k_A}{k_B}, r_B = \frac{k_B}{k_A} \tag{5}$$

via curve fitting of the monomer consumption profiles.

Reactivity ratios (r_A, r_B) describe the statistical incorporation of monomer into a single chain resulting in one of several limiting cases:

- $r_A \approx r_B \gg 1$, each monomer overwhelmingly prefers homopropagation, leading essentially to a mixture of *two independent homopolymers*.
- $r_A \approx r_B > 1$, homopropagation remains favored, but rare cross-propagation events can trigger the formation of *block copolymers*, as once a chain incorporates the other monomer, it tends to continue propagating with that monomer.
- $r_A \approx r_B \approx 1$, each propagating chain end adds either monomer with comparable probability, yielding a *random copolymer*, in which the instantaneous composition faithfully reflects the feed ratio.
- $r_A \approx r_B \approx 0$, neither monomer is able to homopolymerize and each can add only the other, resulting in strictly *alternating copolymers*.
- $r_A \gg 1 \gg r_B$, monomer A is preferentially consumed in the early stages of polymerization, giving rise to an initial segment rich in monomer A; once monomer A becomes depleted, the chain increasingly incorporates monomer B. Such systems naturally produce *gradient or tapered copolymers*, where compositional changes progress continuously along the chain contour.

5.2 The Role of Real-Time ^{1}H NMR Spectroscopy

The application of *in situ* NMR spectroscopy to monitor carbanionic copolymerizations has emerged as a uniquely powerful method for quantifying monomer consumption and reconstructing the evolving sequence distribution along the polymer chain. This approach has proven especially effective in the field of living anionic polymerization, where the strict absence of termination and transfer ensures a direct correspondence between monomer conversion and propagation kinetics. Within this methodological landscape, the group of Holger Frey has played a central and pioneering role, systematically developing and applying in situ NMR techniques to quantify reactivity ratios and establish monomer reactivity orders in a wide variety of copolymerizations. Their contributions span from early real-time ^{1}H NMR monitoring of classical diene-styrene systems to more complex biobased monomers, epoxides, and modifier-controlled anionic copolymerizations.[102]

The first demonstration of this capability was reported in 2010, when Obermeier *et al.* used online in situ ^{1}H NMR to monitor the anionic copolymerization of ethylene oxide (EO) with the novel protected amino-glycidol monomer DBAG (N,N-dibenzyl amino glycidol) in real time.[103] In this study, the copolymerization mixture was sealed in an NMR tube and spectra were recorded every 30 seconds, enabling direct measurement of monomer consumption and compositional drift throughout the reaction (Figure 5.1). The time-resolved disappearance of the DBAG methine proton at 3.02 ppm and the EO proton signal at 2.61 ppm revealed that both monomers remained present until full conversion and exhibited similar reactivities, leading to random copolymers with only a slight tapering toward the end of the reaction.

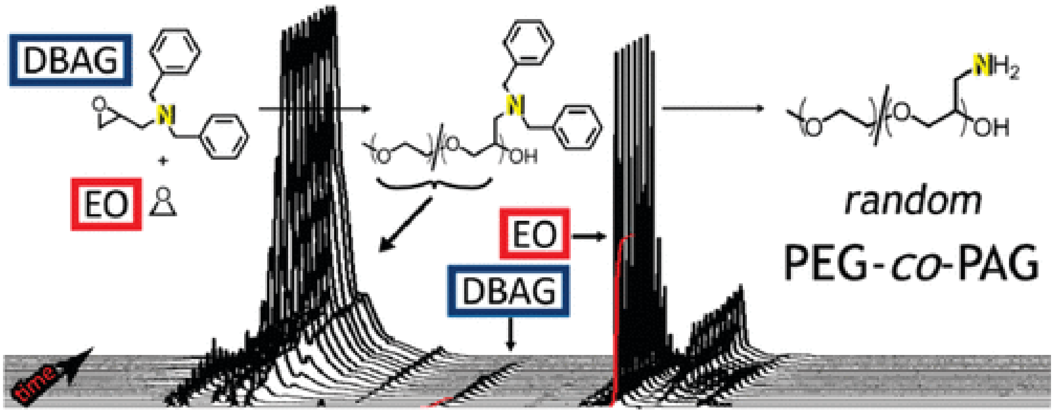

Figure 5.1. Time-resolved 400 MHz ^{1}H NMR spectrum of copolymerization of ethylene oxide and N,N-dibenzyl amino glycidol monitored in DMSO-d_6.[103]

In 2013, Natalello *et al.* applied in situ ^{1}H NMR spectroscopy for the first time to living carbanionic copolymerizations conducted in C_6D_{12}, enabling real-time tracking of monomer consumption for *p*-(1-ethoxyethoxy)styrene (pEES), 4-tert-butoxystyrene (tBuOS), and styrene (S).[104] The decay of the vinylic signals revealed that the pEES/tBuOS system shows only minor differences in reactivity, producing nearly random copolymers with a slight tapering. In contrast, the S/pEES system exhibited a pronounced reactivity mismatch: Fineman-Ross analysis gave $r_S = 1.34$ and $r_{pEES} = 0.47$, evidencing preferential early incorporation of styrene followed by progressive enrichment in pEES along the chain (Figure 5.2).

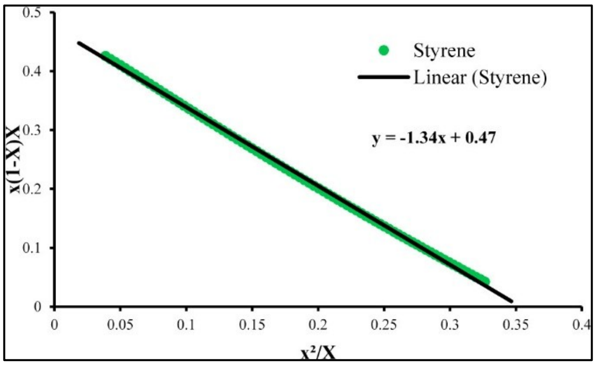

Figure 5.2. Determination of the *r*-parameters by the Fineman-Ross equation for the system S/pEES.[102]

Later, Grune *et al.* extended the approach to bio-based monomers by using in situ ^{1}H NMR kinetics to follow the statistical anionic copolymerization of β-myrcene with styrene, 4-methylstyrene (4MS) and isoprene, extracting rate constants, reactivity ratios and composition profiles directly during polymerization.[105] Myrcene/isoprene copolymerization showed only moderately disparate reactivity ($r_{Myr} = 4.4$; $r_I = 0.23$), yielding smooth gradient copolymers. In contrast, myrcene/styrene and myrcene/4-methylstyrene displayed extremely diverging reactivities ($r_{Myr} = 36$; $r_S = 0.028$ and $r_{Myr} = 140$; $r_{4MS} = 0.0074$), producing intrinsically block-like tapered copolymers despite the statistical polymerization protocol (Figure 5.3). Real-time analysis of a Myr/I/4MS terpolymerization further revealed that introducing isoprene selectively modifies the gradient of 4MS, making the architecture more block-like. Guided by these kinetic insights, a library of Myr/S copolymers and Myr/I/4MS terpolymers was synthesized, all with narrow dispersities and two distinct T_g values, confirming phase segregation.

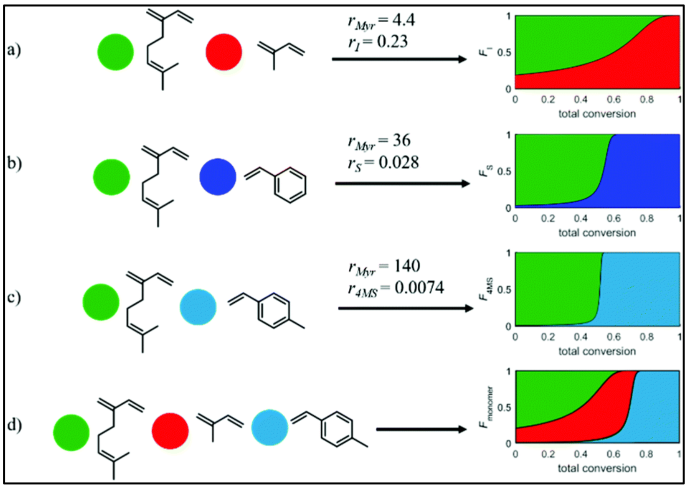

Figure 5.3. Simulated composition profiles of myrcene co- and terpolymers.[103]

Finally, Wahlen *et al.* further broadened the scope of renewable monomers by exploring β-farnesene, another bio-derived terpene, as a comonomer for styrene under statistical anionic conditions.[106] In situ ^{1}H NMR methodology determined highly diverging reactivity ratios (r_{Far} = 27, r_S = 0.037) and the authors derived algebraic expressions for molar and volume composition profiles under terminal and non-terminal models (Figure 5.4). These kinetic insights guided the one-pot one-step synthesis of well-defined tapered tri- and pentablock copolymers PS-*b*-P(Far-co-S) and PS-*b*-P(Far-co-S)-*b*-PS with controlled polydiene volume fractions (0.50-0.68), which showed lamellar or hexagonally packed cylindrical morphologies with domain spacings comparable to polyisoprene analogues, as well as a systematic increase in mechanical toughness when moving from β-farnesene to β-myrcene to isoprene and, importantly, significantly reduced solution viscosities for the polyfarnesene-based bottlebrush architectures that enabled facile electrospinning into fine microfiber meshes.

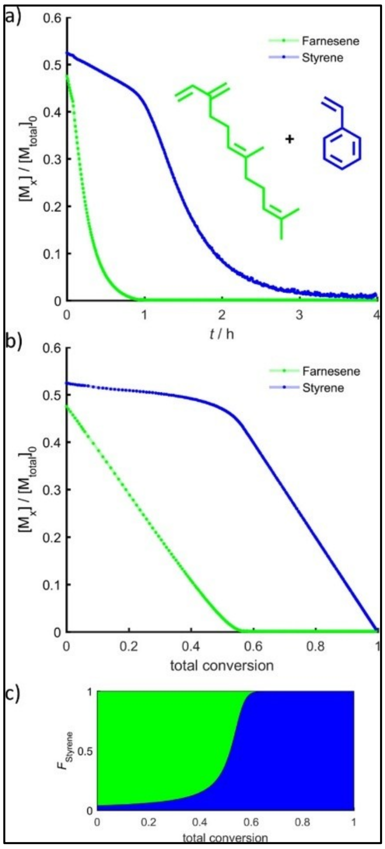

Figure 5.4. (a) Time-conversion plots. (b) Comonomer concentrations as a function of total conversion. (c) Calculated molar composition profile of the corresponding tapered copolymer.[104]

Building on this conceptual framework, the present work extends, for the first time, the application of *in situ* NMR kinetics to a non-living coordination polymerization of conjugated dienes, catalyzed by a titanium [OSSO]-complex bearing cumyl substituents on the aromatic rings (catalyst **2**, Figure 2.3). In the following sections, the homopolymerization kinetics of 1PB, IVC and DMNT were quantified by *in situ* NMR. Subsequently, the reactivity ratios for all pairwise copolymerizations among these monomers, and additional combinations with β-myrcene and β-ocimene were determined using either the Jaacks or BLS approach, depending on which kinetic model best described the experimental data. The results discussed here were obtained during the abroad period of the PhD, carried out as a six-month research stay in the group of Prof. Dr. Holger Frey at Johannes Gutenberg University Mainz (JGU), Germany.

5.3 Homopolymerization Kinetics

In situ ^{1}H NMR spectroscopy was applied to investigate the coordination-insertion homopolymerization of the three bio-based dienes: 1-phenyl-1,3-butadiene (1PB), 4-isopropenyl-1-vinyl-1-cyclohexene (IVC), and (E)-4,8-dimethyl-1,3,7-nonatriene (DMNT), representing aromatic, cyclic, and linear architectures, respectively.

In all cases, the monomers were carefully purified and rigorously dried prior to use, and the polymerization kinetics were monitored in sealed NMR tubes. Each tube contained catalyst **2** (1 eq.), MAO as cocatalyst (Al/Ti = 500), and toluene-d_8 as solvent. After 30 min of pre-activation of the catalytic system, the monomer (1000 eq.), dissolved in a small amount of toluene, was added, and the reaction was followed by acquiring a ^{1}H NMR spectrum every 2 minutes. For each monomer, the NMR experiment was conducted at the temperature previously identified as optimal in conventional homopolymerization experiments, ensuring that the kinetic profiles could be directly related to the most efficient catalytic conditions.

The *in situ* ^{1}H NMR homopolymerization of 1PB was performed at 80 °C for 24 h. The monomer conversion over time was determined by integrating the 1PB signals between 5.0 and 5.3 ppm (Figure 5.5). As the reaction proceeds, the intensity of these monomer vinyl proton resonances progressively decreases, while new signals grow in the polymer region, for instance those observed between 5.9 and 6.1 ppm, which are attributed to poly(1PB).

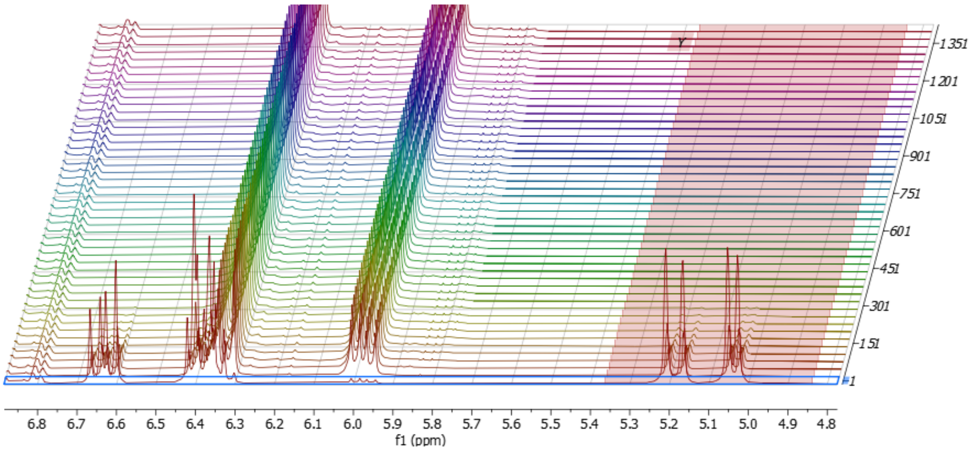

Figure 5.5. Stacked ^{1}H NMR spectra (400 MHz, toluene-d_8, 353 K) of the *in situ* NMR kinetics study of the homopolymerization of 1PB.

The corresponding kinetic plot (Figure 5.6), reporting monomer conversion as a function of time, shows that 1PB is consumed almost quantitatively within approximately 8 h under these strictly anhydrous conditions.

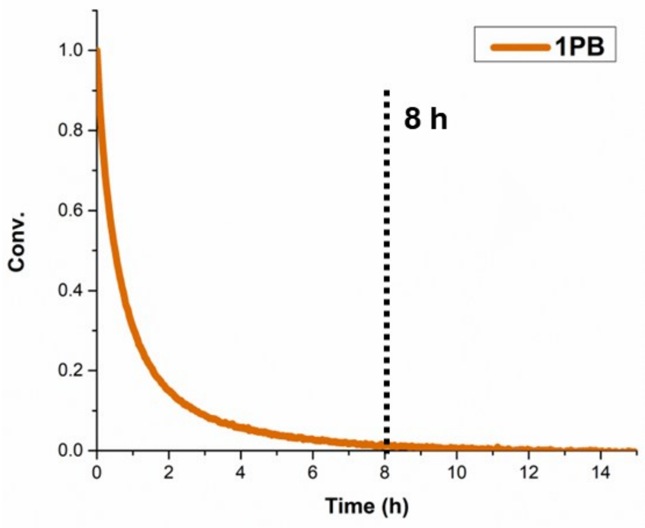

Figure 5.6. Time-conversion plot of the homopolymerization of 1PB.

The polymer isolated at the end of the reaction exhibits a molecular weight M_n = 78.1 kg mol^{-1} and a dispersity Đ = 1.5. These molecular weights are significantly higher than those previously obtained when non-dried monomer was used, where the conversion reached a plateau at approximately 63% even after 48 h in Schlenk tube experiments (run 9, Table 2.1, Chapter 2). A plausible explanation is that the presence of water or protic impurities in the non-anhydrous monomer partially deactivates the active titanium species or promotes chain transfer and termination processes, thus limiting both the achievable conversion and the degree of polymerization. In NMR tube experiments, the combination of completely dried monomer, reduced total reaction volume, and efficient scavenging by MAO extends the lifetime of the active centers and increases the average number of monomer insertions per chain, resulting in higher M_n and quantitative monomer consumption. Thermally, the polymer shows a glass transition temperature of 87.6 °C, which closely matches the T_g obtained from the conventional Schlenk-tube method. In all cases, the resulting poly(1PB) maintains a high regioselectivity toward 3,4-insertion and a high degree of isotacticity, confirming that the microstructural control exerted by catalyst **2** is preserved under the *in situ* NMR conditions.

The same experimental strategy was applied to the homopolymerization of IVC, which was conducted at 80 °C, identified as the most suitable temperature based on the previous optimization studies. In the *in situ* ^{1}H NMR experiment, the monomer conversion was quantified by integrating the isolated vinylic resonance of IVC located between 6.2 and 6.4 ppm (Figure 5.7). As polymerization progresses, the gradual decrease in intensity of this well-resolved signal provides a reliable measure of monomer consumption, while new resonances associated with the growing polymer backbone emerge.

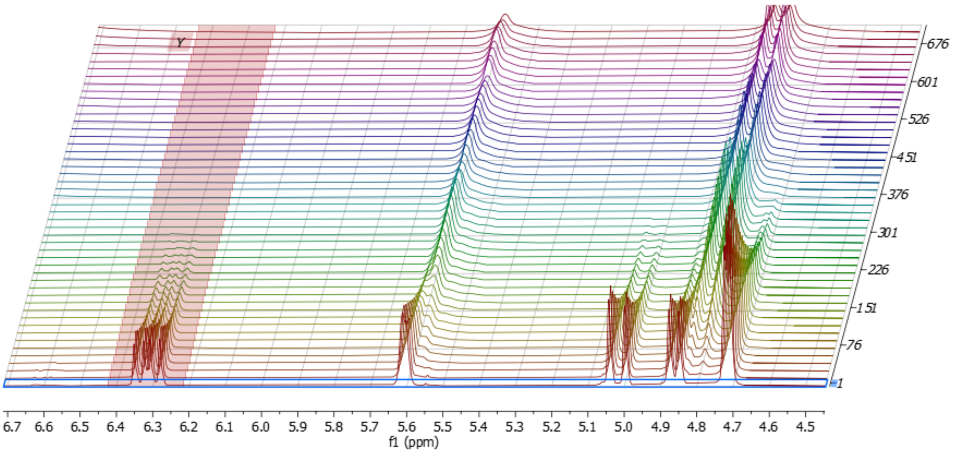

Figure 5.7. Stacked ^{1}H NMR spectra (400 MHz, toluene-d$_8$, 353 K) of the *in situ* NMR kinetics study of the homopolymerization of IVC.

The corresponding kinetic profile in Figure 5.8 clearly shows that IVC undergoes complete conversion within approximately 11 hours under these anhydrous NMR-tube conditions.

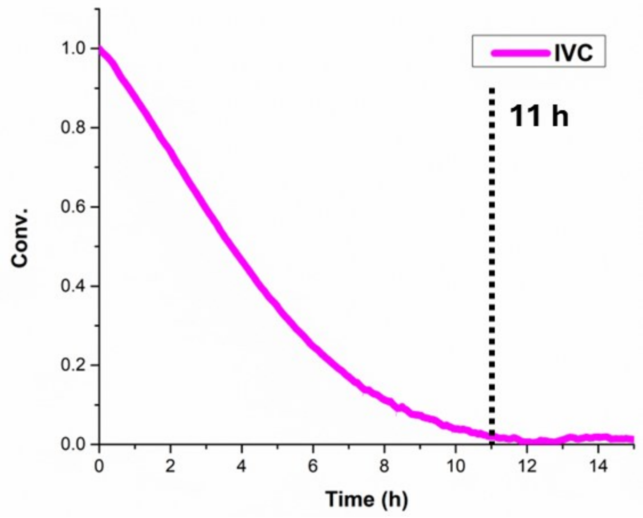

Figure 5.8. Time-conversion plot of the homopolymerization of IVC.

The polymer isolated at the end of the experiment exhibits a molecular weight M_n = 123.3 kg mol^{-1} and a dispersity Đ = 2.4. These values are fully consistent with those previously obtained in Schlenk-tube polymerizations, confirming that the reaction conducted in the NMR tube faithfully reproduces the catalytic behaviour observed on a larger scale (run 3, Table 3.3, Chapter 3). The polymer displays a glass transition temperature of 75.1 °C, a value that is directly comparable to the T_g obtained via the conventional method. The resulting poly(IVC) retains the high regioselectivity toward 3,4-insertion characteristic of catalyst **2**, together with a high degree of isotacticity. This demonstrates that microstructural control is preserved under *in situ* NMR conditions, even for a cyclic monomer such as IVC.

Finally, the homopolymerization of the linear diene DMNT was also examined under *in situ* ^{1}H NMR conditions. In this case, the reaction was carried out at 25 °C, which had previously been identified as the optimal temperature in conventional experiments. The consumption of DMNT over time was monitored by integrating the monomer signal in the range 5.8-6.0 ppm (Figure 5.9).

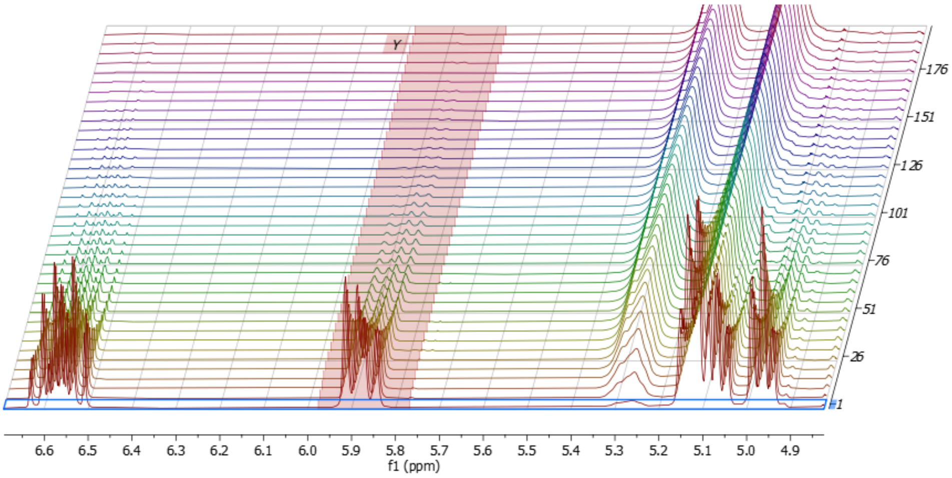

Figure 5.9. Stacked ^{1}H NMR spectra (400 MHz, toluene-d$_8$, 298 K) of the *in situ* NMR kinetics study of the homopolymerization of DMNT.

The corresponding kinetic plot in Figure 5.10 shows that the monomer is quantitatively converted within approximately 5 h.

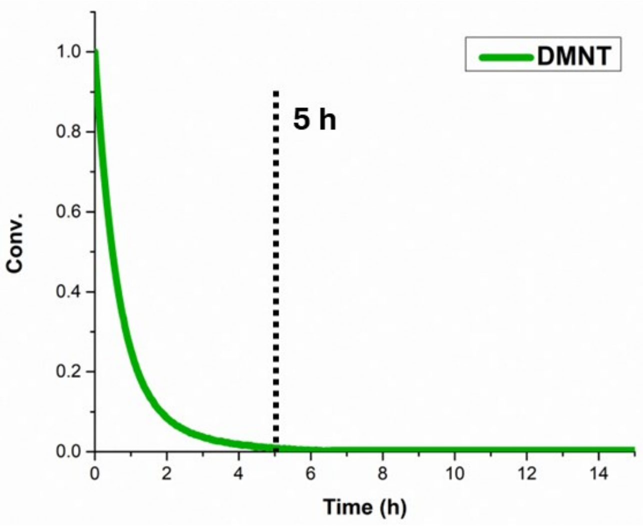

Figure 5.10. Time-conversion plot of the homopolymerization of DMNT.

The polymer isolated at the end of the NMR-tube experiment displays a molecular weight M_n = 62.1 kg mol^{-1} and a dispersity Đ = 2.3. These values are slightly lower than those obtained in the Schlenk-tube polymerization, where M_n = 72.4 kg mol^{-1} was reached after 24 h under otherwise comparable conditions (run 4, Table 4.1, Chapter 4). A plausible explanation is that the NMR-tube setup inherently operates under more dilute conditions due to the use of toluene-d$_8$ and the restricted reaction volume. Lower effective monomer concentration can alter the balance between propagation and chain-transfer events, increasing the relative fraction of shorter chains and thus reducing the average molecular weight. Additional factors may further contribute to this behaviour. The very small reaction volume and limited manipulation associated with NMR-tube loading can increase the sensitivity of the system to traces of protic or coordinating impurities. Moreover, in a small NMR tube the diffusion of monomer, cocatalyst, and growing polymer chains to and from the active centres may be limited, particularly in the later stages of the reaction as viscosity increases. This restricted mass transport can slow down propagation and enhance the probability of chain-transfer or premature termination, ultimately leading to shorter average chain lengths. By contrast, in a Schlenk-tube polymerization, the larger reaction volume and efficient stirring typically ensure more homogeneous mixing and more effective mass transfer, favouring controlled chain growth.

Despite these differences in molar mass, the poly(DMNT) obtained in the NMR-tube experiment retains the high microstructural control previously observed: it is predominantly 1,2-regioregular and exhibits a high degree of isotacticity. From a thermal point of view, the polymer shows a glass transition temperature of -37.0 °C, which is fully consistent with the T_g of -37.4 °C measured for the material prepared in the Schlenk tube. The excellent agreement between these values indicates that, despite the slight differences in molecular weight and dispersity, the overall chain flexibility and microstructure of the two samples are essentially comparable.

For DMNT, the influence of the cocatalyst concentration on the polymerization behaviour was also systematically investigated. Two additional kinetic experiments were performed by varying the Al/Ti ratio to 250 and 1000, respectively. Based on the role of MAO as both activator and potential chain-transfer agent, one might anticipate that lowering the Al/Ti ratio would reduce the number of active sites and slow down the reaction while favouring higher molecular weights, whereas increasing it to 1000 would accelerate the kinetics at the expense of M_n due to more frequent chain-transfer events. Experimentally, however, both modified conditions (Al/Ti = 250 and 1000) resulted in kinetic profiles that are slower than the reference experiment at Al/Ti = 500 (Figure 5.11), while the resulting molecular weights are higher in both cases: M_n = 94.9 kg mol^{-1} for Al/Ti = 250 and M_n = 98.8 kg mol^{-1} for Al/Ti = 1000, compared to M_n = 62.1 kg mol^{-1} at Al/Ti = 500.

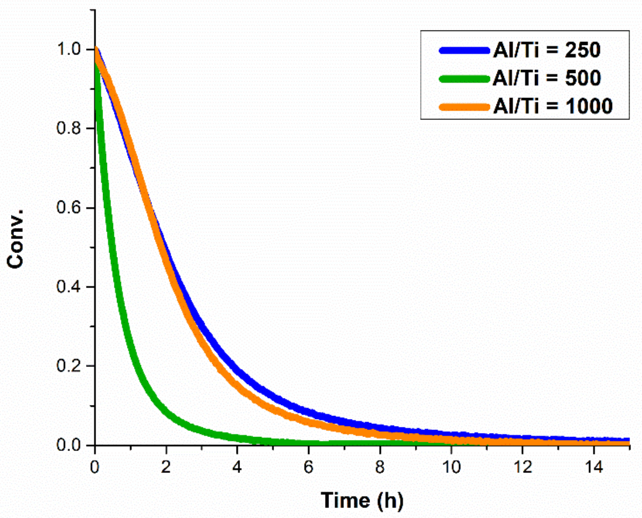

Figure 5.11. Time-conversion plots of the homopolymerization of DMNT at different Al/Ti ratios.

This behaviour can be rationalized by considering that MAO plays a dual role, and that the overall activity and chain-growth characteristics reflect a delicate balance between site creation, site deactivation, and chain-transfer processes. At low Al/Ti (250), the lower amount of MAO likely leads to incomplete activation of the titanium precursor and a reduced number of effective active centres. Consequently, the global rate of monomer consumption decreases, but each active site can grow longer chains because chain-transfer events mediated by MAO are less frequent, leading to higher M_n. At very high Al/Ti (1000), the situation is different but leads to a similar outcome: an excess of MAO may generate a larger fraction of dormant or over-coordinated species, or promote deactivation pathways, effectively reducing the concentration of truly propagating centres. The few surviving active sites then maintain chain growth for longer periods, again producing higher molecular weights, while the overall reaction rate is penalized. The Al/Ti ratio of 500 therefore appears to represent a near-optimal compromise where the number of active centres is maximized and the rate of propagation is high, but at the cost of more frequent chain-transfer reactions that limit the achievable M_n. A similar dependence of activity on the Al/Ti ratio has been reported for Ti(IV)/MAO systems based on salalen ligands, where the highest activity is observed around Al/Ti $\approx$ 500, while both lower and higher MAO loadings lead to decreased activities due to incomplete activation or catalyst poisoning by excess trialkylaluminum.[107]

5.4 Determination of Reactivity Ratios in Copolymerizations

In order to determine the relative reactivity of the conjugated diene monomers towards the same titanium [OSSO]-type coordination site (catalyst **2**), copolymerizations were monitored in situ by ^{1}H NMR spectroscopy and the monomer conversions were analysed using both the excess-monomer method of Jaacks and the non-terminal model BSL. Although coordination polymerizations catalysed by homogeneous Ziegler-Natta or single-site catalysts may undergo chain transfer and termination events, the present system behaves in a quasi-living fashion on the time scale of monomer consumption. This is evidenced by the excellent linearity of the Jaacks plots up to ca. 70-80% overall conversion and by the consistent reactivity ratios obtained from the Jaacks and BSL analyses.

5.4.1. Copolymerization of 1PB with Linear Terpenes

Copolymerizations were carried out at 80 °C for 24 h using an initial 1PB:Terpene feed ratio of 80:20 mol%, respectively, with spectra acquired every 2 minutes.

In the 1PB/β-myrcene system, 1PB was fully consumed after approximately 5 hours, significantly faster than in its homopolymerization (≈ 8 h), suggesting that the presence of β-myrcene modifies the environment of the metal center (Figure 5.12). This enhanced reactivity of 1PB can be attributed to a comonomer effect, whereby the presence of β-myrcene accelerates the polymerization of 1PB. In contrast, β-myrcene itself remained essentially unreacted throughout the entire experiment, fully consistent with Schlenk-tube copolymerizations that produced polymers with extremely low myrcene incorporation even when the terpene was used in large excess (runs 4-5, Table 2.2, Chapter 2).

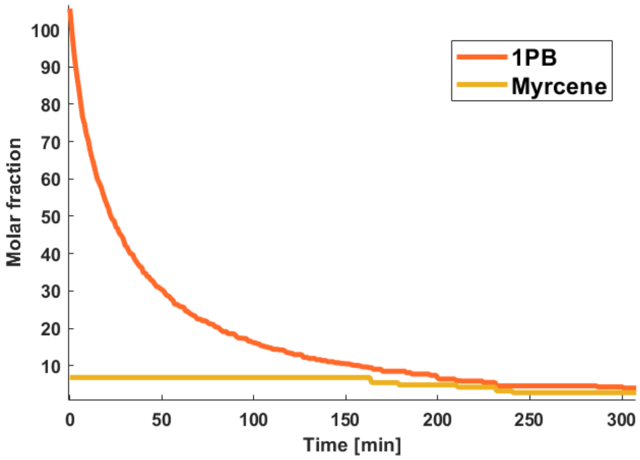

Figure 5.12. Time-conversion plots of the copolymerization of 1PB (orange) and β-myrcene (yellow).

The kinetic analysis reinforces this interpretation. The data do not follow the linear form expected for the Meyer-Lowry equation. Instead, the experimental points describe a curved trajectory, consistent with a system in which only one monomer is effectively consumed while the concentration of the second monomer remains nearly constant (Figure 5.13a). This indicates that the two monomers do not compete for incorporation at the active chain end and that the process does not constitute a true copolymerization, but rather a homopolymerization of 1PB occurring in the presence of a non-reactive or very weakly reactive comonomer.

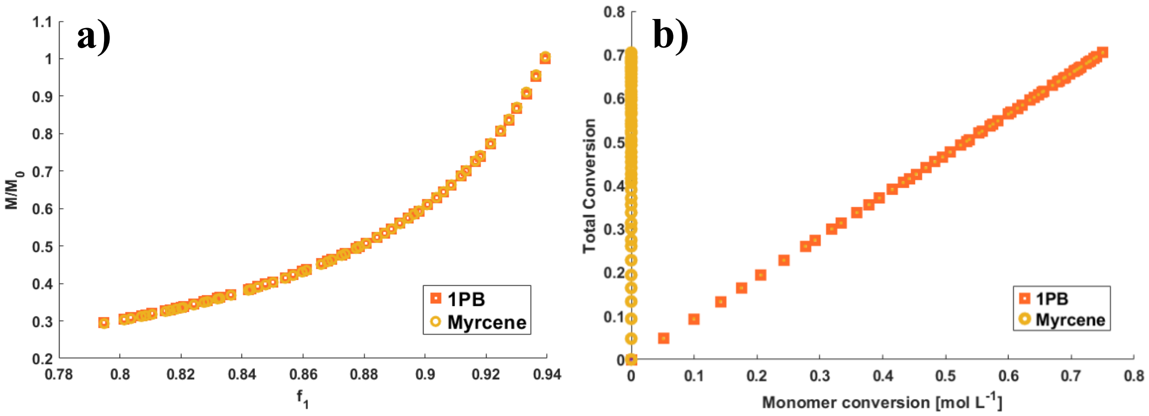

Figure 5.13. Comparison of (a) terminal model (Meyer-Lowry) and (b) non-terminal model (BSL) for the determination of reactivity ratios in the copolymerization of 1PB with β-myrcene.

A similar conclusion emerges from the BSL method (Figure 5.13b). When applied to the 1PB/β-myrcene dataset, one monomer (1PB) appeared to follow a quasi-linear trend, while the other remained at essentially zero conversion for the entire duration of the experiment. The regression yielded $r_{1PB} = 0$ and $r_{Myrc} = 4.84 \times 10^{-5}$, values that would formally correspond to a strongly alternating system ($r_1 \approx r_2 \approx 0$). However, this interpretation is incompatible with the actual experimental behavior, in which only 1PB is consumed while β-myrcene remains unreacted. This discrepancy demonstrates that the assumptions underlying the BSL model are not satisfied, and that these reactivity ratios are merely mathematical artefacts without physical meaning, arising from forcing an ideal copolymerization formalism onto a system that chemically behaves as a single-monomer polymerization in the presence of an “inert” comonomer.

In contrast, the 1PB/β-ocimene system exhibits a more classical copolymerization behavior. Here again 1PB is fully consumed in approximately 5 hours, but β-ocimene shows measurable incorporation (Figure 5.14).

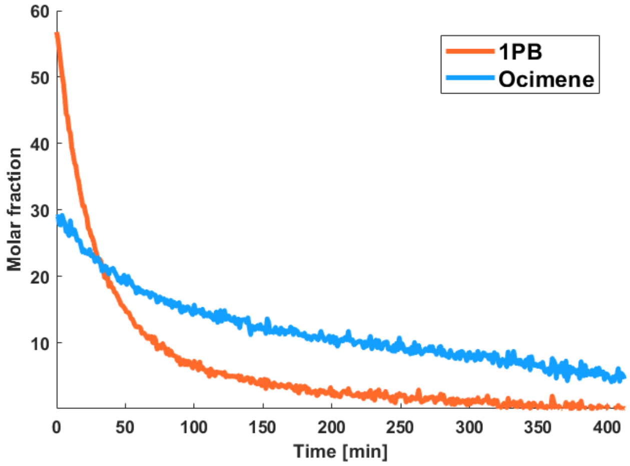

Figure 5.14. Time-conversion plots of the copolymerization of 1PB (orange) and β-ocimene (blue).

The kinetic data display linearity in the Jaacks plot up to about 80% conversion (R^2= 0.98), a regime in which the assumptions of the Jaacks formalism remain reasonably valid. The derived apparent reactivity ratios are r_{1PB} = 3.2 and r_{Ocim} = 0.31, implying that 1PB-ended chains preferentially add another 1PB unit, while ocimene-ended chains favor cross-propagation with 1PB (Figure 5.15). Deviations from linearity beyond ~80% conversion arise from exhaustion of 1PB and the resulting compositional drift.

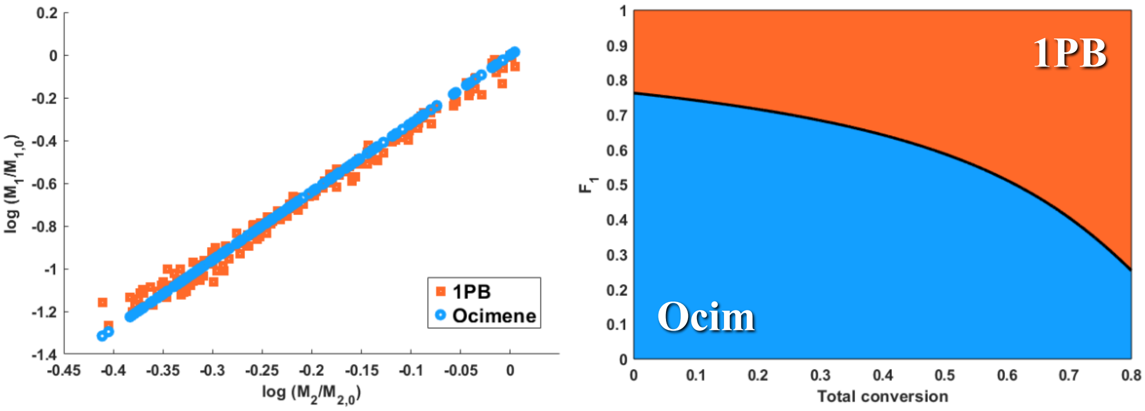

Figure 5.15. Terminal model (Jaacks) for the determination of reactivity ratios in the copolymerization of 1PB with β-ocimene (left) and copolymer composition as a function of 80% conversion (right).

Overall, this indicates that the resulting materials are gradient copolymers, initially rich in 1PB and progressively enriched in β-ocimene toward the chain end.

After the kinetic study, the recovered polymers were characterized using 2D DOSY NMR, GPC, and DSC. The two-dimensional spectra clearly show the formation of the copolymer as the peaks relating to the two segments have the same diffusivity coefficient (see Appendix 5). The following table summarizes the reaction conditions used and the molecular mass and T_g values obtained for each of them:

Copolymer	**Monomer feed (mol%)**	**Temp. (°C)**	**M_n (Kg/mol)**	**Đ**	**T_g (°C)**
1PB/Myr	80/20	80	45.4	1.5	49.3
1PB/Ocim	80/20	80	52.6	1.7	66.2

5.4.2. Copolymerization of IVC with Linear Terpenes and 1PB

The same *in situ* ^{1}H NMR methodology was applied to investigate the copolymerization behaviour of IVC with β-myrcene, β-ocimene and 1-phenyl-1,3-butadiene (1PB), allowing real-time monitoring of monomer consumption under the same experimental conditions used for the 1PB-based systems.

All reactions were carried out at 80 °C and monitored for 24 h, using an initial IVC/terpene feed of 80/20 mol% for the β-myrcene and β-ocimene copolymerizations, while a 40/60 mol% ratio was employed for the IVC/1PB system, respectively.

In the IVC/β-myrcene copolymerization, IVC was consumed quantitatively within approximately 5 hours, a significantly shorter time compared to its homopolymerization, where complete conversion required around 11 hours (Figure 5.16).

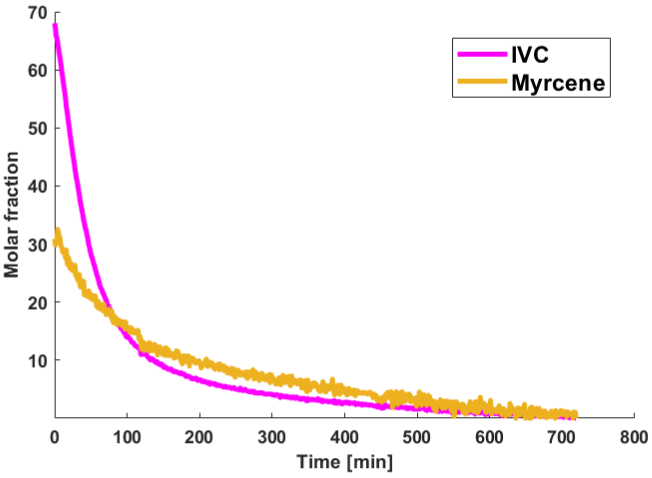

Figure 5.16. Time-conversion plots of the copolymerization of IVC (pink) and β-myrcene (yellow).

This acceleration mirrors the behaviour observed in the 1PB-based copolymerizations and can be attributed to a comonomer effect, whereby the presence of β-myrcene enhances the effective polymerization rate of IVC. β-myrcene polymerized more slowly but ultimately reached quantitative conversion, in stark contrast to its behaviour in the presence of 1PB, where it remained essentially unreacted. Application of the Jaacks method revealed a linear relationship up to 90% overall conversion (R^2= 0.97), resulting in reactivity ratios of r_{IVC} = 2.1 and r_{Myrc} = 0.47 (Figure 5.17). These values indicate that an IVC-ended chain tends to insert preferentially another IVC unit, while a myrcene-ended chain favours cross-propagation with IVC, leading to a progressive compositional drift that results in a gradient copolymer increasingly enriched in β-myrcene as the reaction proceeds.

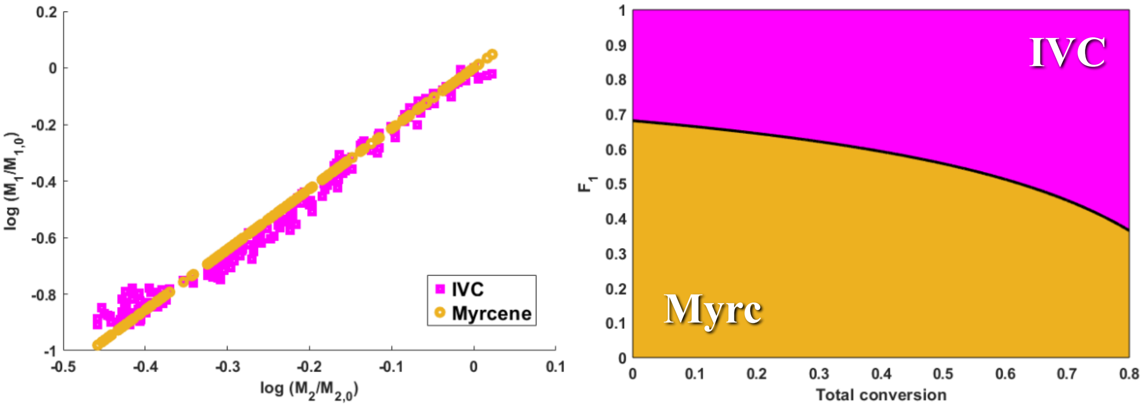

Figure 5.17. Terminal model (Jaacks) for the determination of reactivity ratios in the copolymerization of IVC with β-myrcene (left) and copolymer composition as a function of 90% conversion (right).

A similar but more pronounced trend was observed in the IVC/β-ocimene copolymerization. Here, IVC reacted even more rapidly, reaching full conversion in approximately 3 hours, again evidencing a strong comonomer effect (Figure 5.18).

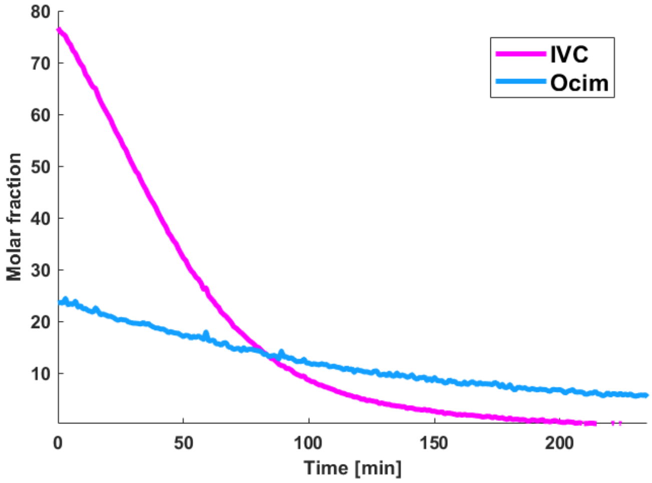

Figure 5.18. Time-conversion plots of the copolymerization of IVC (pink) and β-ocimene (blue).

β-Ocimene followed a slower polymerization trajectory but was clearly incorporated as the reaction progressed. The kinetic data provided an excellent linear Jaacks plot up to 90% conversion (R^2= 0.99), from which apparent reactivity ratios of $r_{IVC} = 3.3$ and $r_{Ocim} = 0.30$ were extracted (Figure 5.19). This stronger imbalance in reactivity relative to the myrcene system results in a similarly tapered copolymer, initially dominated by IVC sequences and gradually enriched in β-ocimene as the monomer composition shifts during polymerization.

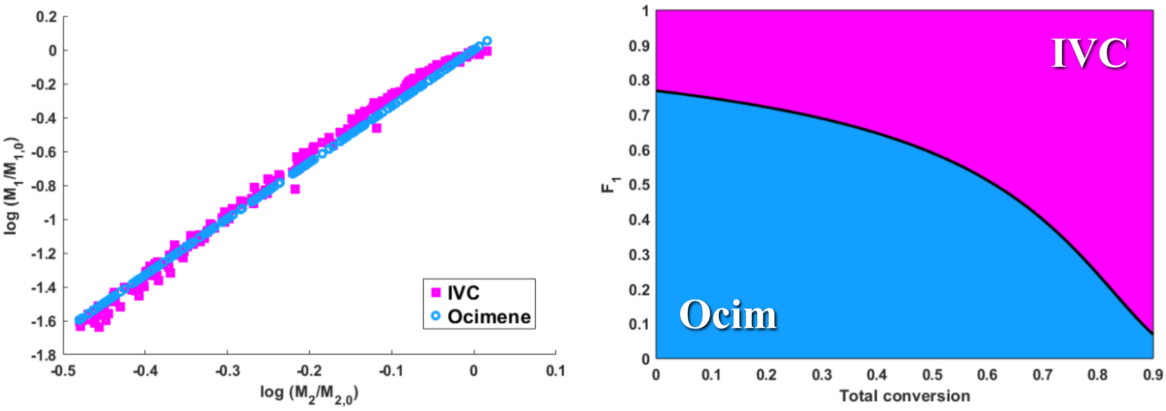

Figure 5.19. Terminal model (Jaacks) for the determination of reactivity ratios in the copolymerization of IVC with β-ocimene (left) and copolymer composition as a function of 90% conversion (right).

A markedly different behaviour was found in the IVC/1PB system. In this case, 1PB proved to be the more reactive monomer, reaching complete conversion within approximately 2 hours, whereas IVC polymerized more slowly (Figure 5.20).

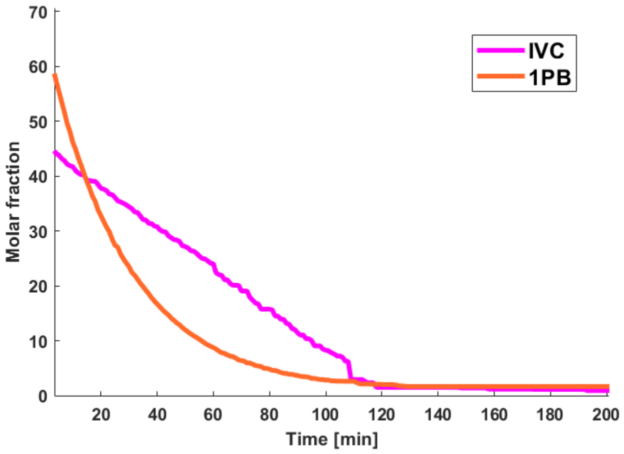

Figure 5.20. Time-conversion plots of the copolymerization of IVC (pink) and 1PB (orange).

This inversion relative to the terpene systems leads to a reversed compositional evolution, in which the early stages of polymerization produce chains strongly enriched in 1PB. The preferential incorporation of 1PB is reflected in the kinetic parameters: a 1PB-ended chain favours addition of another 1PB unit, while an IVC-ended chain also tends to insert 1PB rather than IVC, resulting in an overall bias toward 1PB incorporation at low conversion. Only once the 1PB concentration diminishes does IVC insertion become progressively more significant. The Jaacks method was applicable up to 70% total conversion (R^2= 0.99), yielding r_{IVC} = 0.36 and r_{1PB} = 2.76, values that confirm the formation of a tapered copolymer with a smooth compositional transition from 1PB-rich to increasingly IVC-rich sequences along the polymer chain (Figure 5.21).

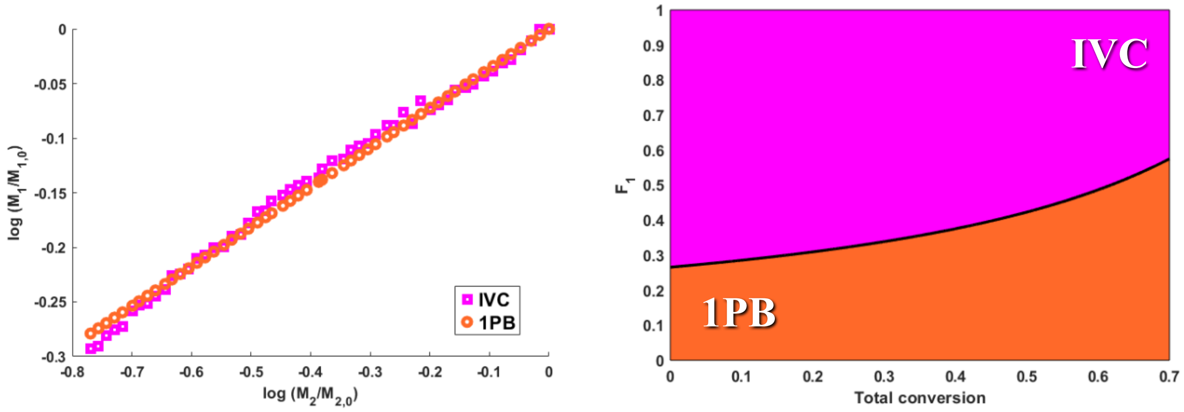

Figure 5.21. Terminal model (Jaacks) for the determination of reactivity ratios in the copolymerization of IVC with 1PB (left) and copolymer composition as a function of 70% conversion (right).

After the kinetic study, the recovered polymers were characterized using 2D DOSY NMR, GPC, and DSC. The two-dimensional spectra clearly show the formation of the copolymer as the peaks relating to the two segments have the same diffusivity coefficient (see Appendix 5). The following table summarizes the reaction conditions used and the molecular mass and T_g values obtained for each of them:

Copolymer	**Monomer feed (mol%)**	**Temp. (°C)**	**M_n (Kg/mol)**	**Đ**	**T_g (°C)**
IVC/Myr	80/20	80	28.3	2.7	49.2
IVC/Ocim	80/20	80	79.2	2.3	59.5
IVC/1PB	40/60	80	117.4	1.6	73.8

5.4.3. Copolymerization of DMNT with Linear Terpenes, IVC and 1PB

The study was further extended to the copolymerization of DMNT with β-myrcene, β-ocimene, IVC and 1PB, employing the same in situ ^{1}H NMR approach to evaluate monomer consumption and determine apparent reactivity ratios.

All copolymerizations were performed using an initial DMNT/comonomer feed of 80/20 mol%, with the reactions involving the terpene comonomers conducted at 80 °C, whereas those with IVC and 1PB were carried out at 40 °C, corresponding to the optimal temperatures previously identified for these monomers.

In the DMNT/β-myrcene system, DMNT was consumed remarkably quickly, reaching complete conversion within approximately 1 hour, while β-myrcene polymerized more slowly but ultimately also reached full conversion (Figure 5.22).

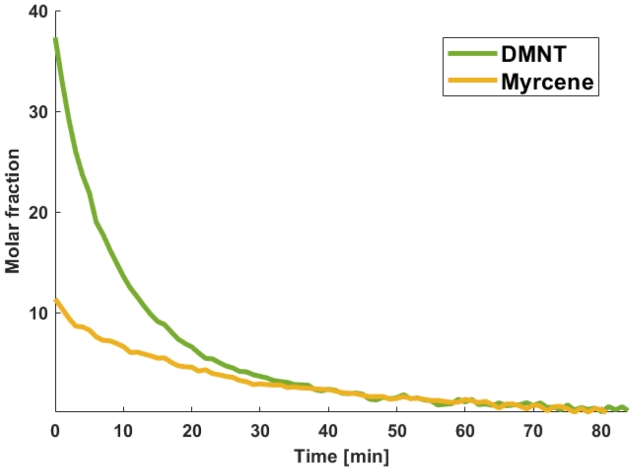

Figure 5.22. Time-conversion plots of the copolymerization of DMNT (green) and β-myrcene (yellow).

The Jaacks plot exhibited excellent linearity up to about 90% conversion (R^2= 0.99), from which reactivity ratios of r_{DMNT}= 1.8 and r_{Myrc} = 0.56 were obtained (Figure 5.23). These values reveal a moderate preference for self-propagation of DMNT over cross-propagation with myrcene, while a myrcene-ended chain favours insertion of DMNT rather than myrcene itself. As a result, the copolymer displays a gradual compositional drift, producing a gradient architecture in which the early segments are enriched in DMNT and the relative myrcene content increases as the reaction proceeds.

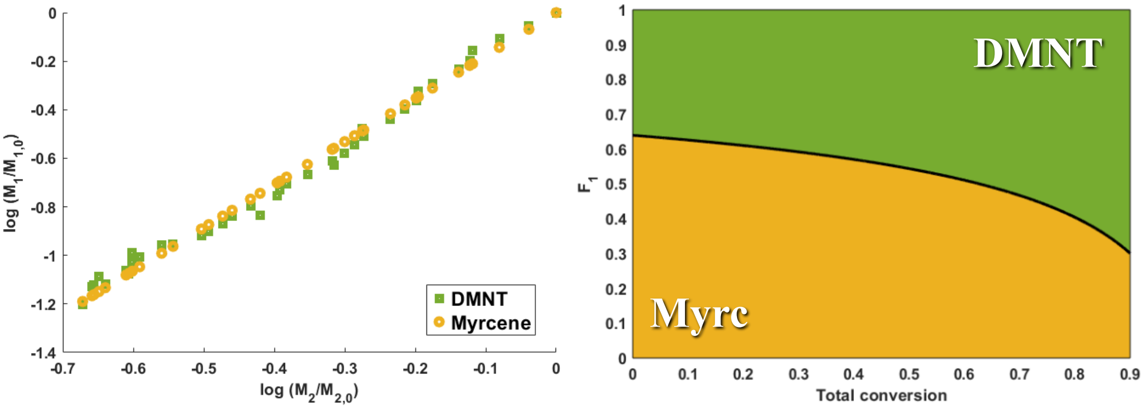

Figure 5.23. Terminal model (Jaacks) for the determination of reactivity ratios in the copolymerization of DMNT with β-myrcene (left) and copolymer composition as a function of 90% conversion (right).

A similar but more pronounced behaviour was observed in the DMNT/β-ocimene copolymerization. In this case, DMNT was consumed even more rapidly, reaching complete conversion in only about 30 minutes, while β-ocimene again polymerized at a slower rate but was progressively incorporated (Figure 5.24).

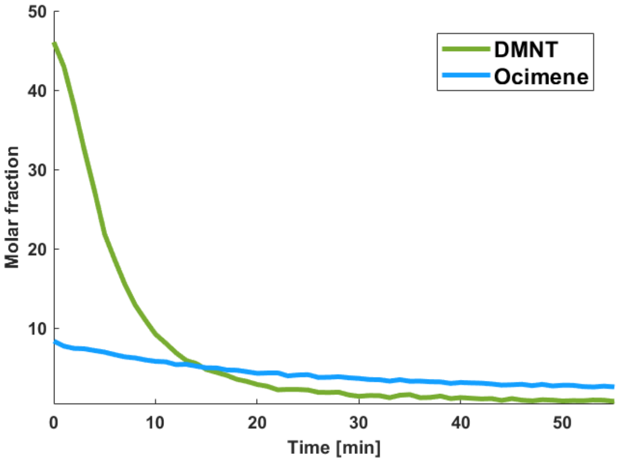

Figure 5.24. Time-conversion plots of the copolymerization of DMNT (green) and β-ocimene (blue).

The Jaacks method remained valid up to 90% conversion (R^2= 0.98), giving reactivity ratios of r_{DMNT} = 4.3 and r_{Ocim} = 0.23 (Figure 5.25). This stronger disparity between the two monomers indicates that a DMNT-ended chain overwhelmingly favours the addition of another DMNT unit, whereas an ocimene-ended chain also tends to propagate with DMNT rather than with its own monomer. Consequently, the resulting copolymer shows a very pronounced tapered character, with a steep gradient from DMNT-rich to ocimene-rich segments that closely reflects the strong difference in intrinsic reactivity between the two monomers.

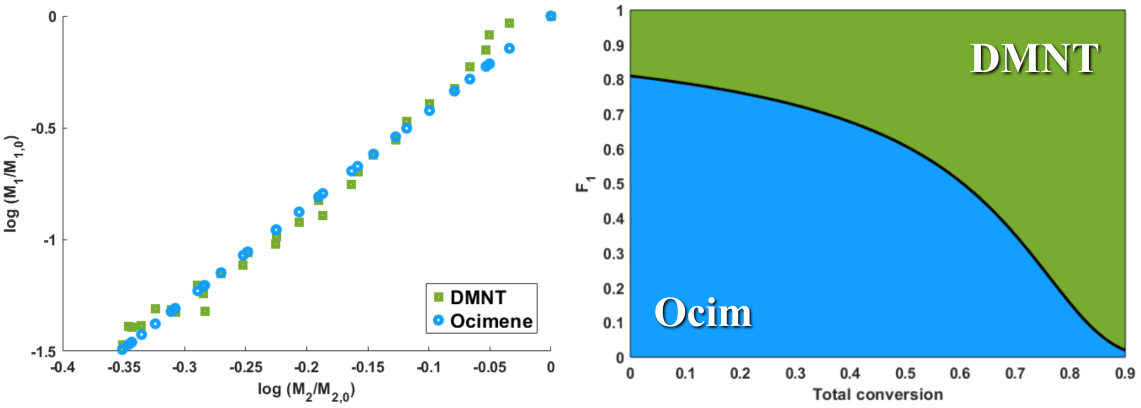

Figure 5.25. Terminal model (Jaacks) for the determination of reactivity ratios in the copolymerization of DMNT with β-ocimene (left) and copolymer composition as a function of 90% conversion (right).

In the DMNT/IVC system, operated at 40 °C, a different, but still gradient-type, behavior emerged. Here, DMNT reached complete conversion in approximately 2 and a half hours, while IVC followed a slower kinetic profile but again polymerized quantitatively over the course of the reaction (Figure 5.26).

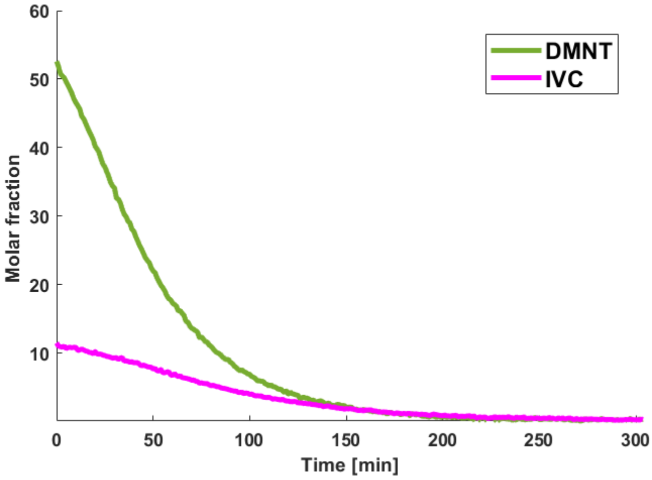

Figure 5.26. Time-conversion plots of the copolymerization of DMNT (green) and IVC (pink).

The Jaacks analysis was applicable up to around 80% conversion (R^2= 0.99) and provided apparent reactivity ratios of r_{DMNT} = 2.1 and r_{IVC} = 0.48 (Figure 5.27). These values reveal that DMNT retains a significant preference for self-propagation, while IVC also tends to insert DMNT more readily than IVC itself. As in the previous systems, this imbalance generates a copolymer with a gradient structure, initially dominated by DMNT units and gradually incorporating increasing amounts of IVC as the DMNT concentration diminishes.

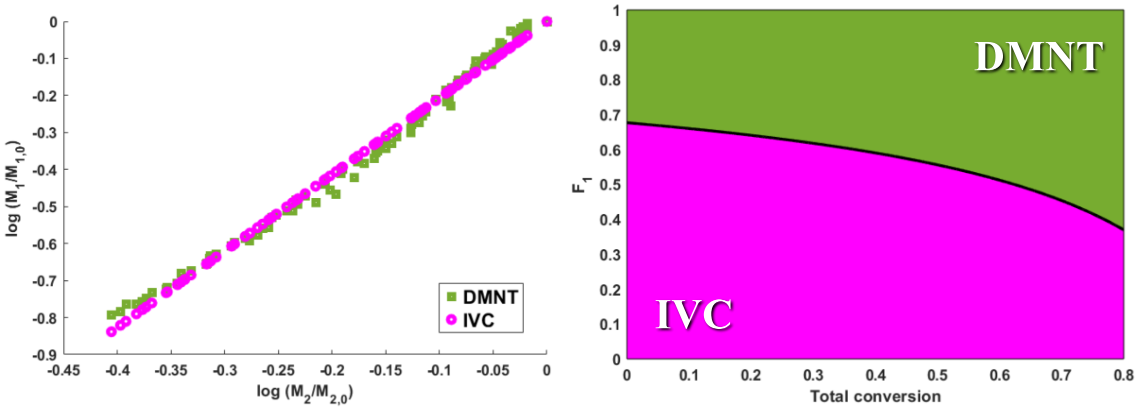

Figure 5.27. Terminal model (Jaacks) for the determination of reactivity ratios in the copolymerization of DMNT with IVC (left) and copolymer composition as a function of 80% conversion (right).

A distinct scenario was encountered in the copolymerization of DMNT with 1PB, also performed at 40 °C. In this case, DMNT was consumed in about 90 minutes, but 1PB also displayed substantial reactivity, leading to a more balanced interplay between the two monomers (Figure 5.28).

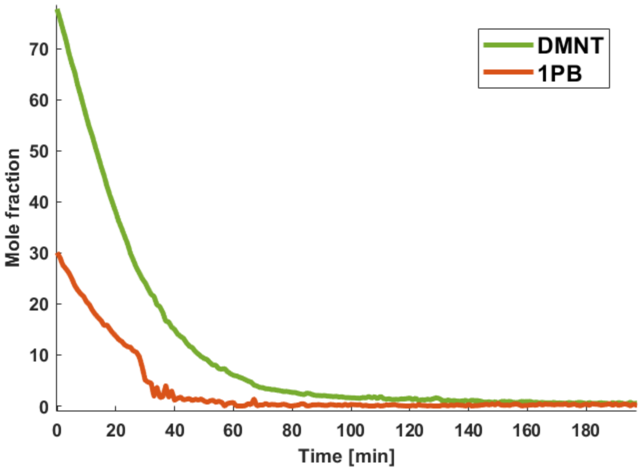

Figure 5.28. Time-conversion plots of the copolymerization of DMNT (green) and 1PB (orange).

Unlike the terpene-based systems, the Jaacks model did not satisfactorily linearize the kinetic data, whereas the BSL treatment provided a better fit, exhibiting good linearity up to approximately 70% conversion. The resulting apparent reactivity ratios, $r_{DMNT} = 0.90$ and $r_{1PB} = 1.1$, indicate that both monomers possess comparable tendencies toward self- and cross-propagation, with no dominant bias toward incorporation of one monomer over the other (Figure 5.29). This behaviour of both reactivity ratios is characteristic of a random copolymerization, yielding a polymer in which the distribution of DMNT and 1PB units along the chain is statistically uniform rather than compositionally graded.

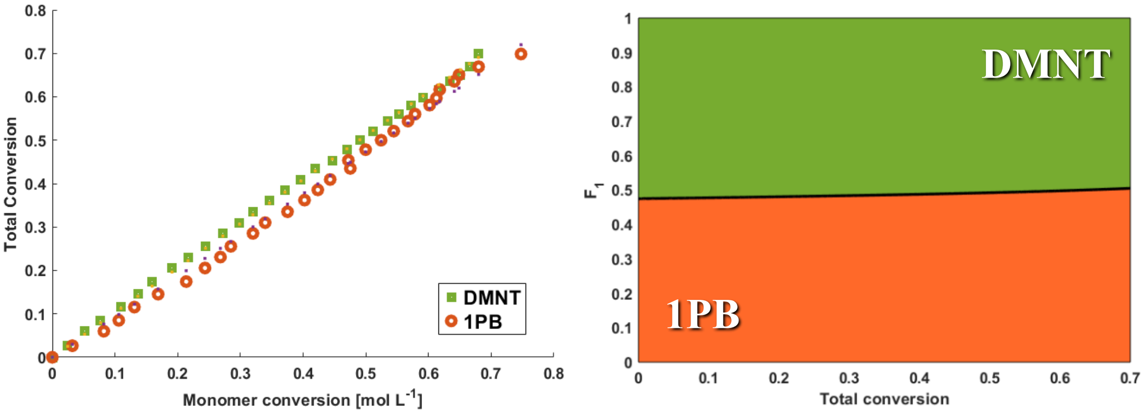

Figure 5.29. Non-terminal model (BSL) for the determination of reactivity ratios in the copolymerization of DMNT with 1PB (left) and copolymer composition as a function of 70% conversion (right).

After the kinetic study, the recovered polymers were characterized using 2D DOSY NMR, GPC, and DSC. The two-dimensional spectra clearly show the formation of the copolymer as the peaks relating to the two segments have the same diffusivity coefficient (see Appendix 5). The following table summarizes the reaction conditions used and the molecular mass and T_g values obtained for each of them:

Copolymer	**Monomer feed (mol%)**	**Temp. (°C)**	**M_n (Kg/mol)**	**Đ**	**T_g (°C)**
DMNT/Myr	80/20	80	43.7	1.6	-9.4
DMNT/Ocim	80/20	80	48.0	1.7	-32.7
DMNT/IVC	80/20	40	65.5	1.9	-23.7
DMNT/1PB	80/20	40	70.5	2.2	-20.9

Overall, these results highlight the versatile reactivity of DMNT when paired with different comonomers. With β-myrcene, β-ocimene and IVC, DMNT consistently acts as the more reactive species, producing tapered copolymers whose gradients reflect the relative rates of monomer consumption. In contrast, the DMNT/1PB system displays a substantially more balanced kinetic interplay, resulting in a predominantly random copolymer.

5.5 Conclusion

Real-time ^{1}H NMR spectroscopy, combined with appropriate kinetic models, can be successfully extended from classical living anionic systems to a non-living coordination polymerization catalysed by a titanium [OSSO]-type complex. By monitoring monomer consumption directly in the NMR tube and analysing the resulting conversion profiles with the Jaacks and BLS models, it was possible to quantify reactivity ratios for a broad family of bio-based conjugated dienes and terpenes, and to reconstruct the corresponding compositional drifts along the copolymer chains.

The homopolymerization studies of 1PB, IVC and DMNT under anhydrous conditions established the intrinsic reactivity and optimal temperatures for each monomer, while confirming that the microstructural control exerted by catalyst **2** (high 3,4-regioselectivity and isotacticity) is fully preserved in the NMR tube. For 1PB and IVC, the *in situ* experiments reproduced the conversion profiles and molecular weights observed in Schlenk-tube experiments, whereas for DMNT the NMR setup led to slightly lower M_n but identical microstructure and T_g. The systematic variation of the Al/Ti ratio in DMNT polymerization further revealed the dual role of MAO as activator and chain-transfer agent and showed that an intermediate Al/Ti ≈ 500 maximizes activity at the expense of molecular weight, whereas both lower and higher loadings slow down the kinetics but yield longer chains.

Building on these kinetic studies, a comprehensive series of copolymerizations was carried out to establish the relative reactivity ratios among 1PB, IVC, DMNT, β-myrcene and β-ocimene using the same titanium catalyst. The 1PB/β-myrcene system emerged as a limiting case where genuine copolymerization does not occur: 1PB is fully consumed while myrcene remains essentially unreacted, and both Meyer-Lowry and BSL analyses fail to yield physically meaningful reactivity ratios. In practice, the reaction behaves as a homopolymerization of 1PB in the presence of a non- or very poorly reactive comonomer. In contrast, the 1PB/β-ocimene system follows the Jaacks model up to ~80% conversion, giving $r_{1PB} = 3.2$ and $r_{Ocim} = 0.31$ and leading to gradient copolymers initially enriched in 1PB and progressively richer in β-ocimene.

The IVC-based copolymerizations reveal a clear change in reactivity landscape. When combined with β-myrcene or β-ocimene, IVC is the more reactive monomer, and in both cases the Jaacks plots are linear up to high conversions (≈90%), yielding $r_{IVC} > 1$ and $r_{Terpene} < 1$. This results in gradient and tapered copolymers that start IVC-rich and gradually incorporate increasing amounts of terpene as the reaction proceeds, with a more pronounced gradient in the case of β-ocimene (r_{IVC} = 3.3; r_{Ocim} = 0.30) than for β-myrcene (r_{IVC} = 2.1; r_{Myrc} = 0.47). When IVC is copolymerized with 1PB, the trend is inverted: 1PB becomes the dominant monomer, is consumed more rapidly, and the Jaacks analysis up to 70% conversion (r_{IVC} = 0.36; r_{1PB} = 2.76) shows that both IVC- and 1PB-ended chains preferentially insert 1PB at low conversion. The resulting copolymer is gradient, but with the opposite behavior: they begin 1PB-rich and gradually become richer in IVC as 1PB is consumed.

The DMNT copolymerizations further refine the monomer reactivity hierarchy and broaden the accessible spectrum of chain architectures. With β-myrcene and β-ocimene at 80 °C, DMNT is consumed extremely rapidly (within 1 h and 30 min, respectively), while the terpene comonomers are incorporated more slowly but quantitatively. The Jaacks analysis up to 90% conversion yields r_{DMNT} = 1.8, r_{Myrc} = 0.56 and r_{DMNT} = 4.3, r_{Ocim} = 0.23, confirming the formation of gradient or strongly tapered copolymers in which DMNT dominates the early segments and the terpene content increases along the chain. At 40 °C, DMNT also remains more reactive than IVC (r_{DMNT} = 2.1; r_{IVC} = 0.48), again producing gradient copolymers enriched in DMNT at the beginning and gradually incorporating IVC. A qualitatively different behaviour is observed in the DMNT/1PB system, where both monomers show comparable reactivities. Here the BLS formalism provides the best description of the data up to ~70% conversion, yielding nearly equal reactivity ratios ($r_{DMNT} \approx r_{IVC} \approx 1$) and indicating a truly random copolymerization, with a statistically uniform distribution of DMNT and 1PB units along the chain rather than a compositional gradient.

Across these systems, the kinetic observations converge on a common picture: under the chosen conditions, chain propagation occurs predominantly at a single type of active site, and termination and transfer events are kinetically minor on the timescale of monomer consumption. This allows the use of nonterminal kinetic models in which the reactivity of the propagating species is governed mainly by the identity of the incoming monomer rather than by the last incorporated unit. Within this approximation, Jaacks and BLS analyses provide reliable apparent reactivity ratios that can be used to predict compositional drift and, by extension, microstructure-dependent properties. The good agreement between the two approaches for genuine copolymer systems validates their extension from classical living anionic polymerizations to these titanium-catalysed coordination processes and supports the view that the [OSSO] catalysts operate under conditions close to “pseudo-living” behaviour for most of the reaction.

5.6 Experimental Section

5.6.1 Materials and methods. All chemicals and solvents were purchased from Acros Organics Co. and Sigma-Aldrich Co. All air- and/or water-sensitive compound manipulations were carried out using a glovebox or standard Schlenk techniques under an Ar atmosphere. Methylaluminoxane (MAO; 10 wt% solution in toluene; Sigma-Aldrich) was used as received. Toluene-d_8 was purchased from Deutero GmbH. All the monomers (1PB, IVC, DMNT, β-myrcene and β-ocimene) were synthesized as reported in the previous chapters and purified by distillation over CaH_2 and degassed by three freeze-thaw cycles prior to use. NMR spectra were recorded on a Bruker Avance II 400 spectrometer working at 400 MHz (^1H NMR). NMR chemical shifts are referenced relative to tetramethylsilane. Standard SEC was performed with THF as the mobile phase (flow rate 1 mL min^{-1}) on a SDV column set from PSS (SDV 10^3, SDV 10^5, SDV 10^6) at 30 °C. Calibration was carried out using PS standards. For determination of the thermal properties of the polymers, differential scanning calorimetry (DSC) was performed with a Mettler Toledo DSC-1 in a temperature range from -80 °C to 200 °C with a heating rate of 10 K min^{-1}.

5.6.2 ^{1}H-NMR kinetics studies. The catalyst/solvent mixtures were prepared in a glovebox. A stock solution of catalyst **2** was prepared in toluene at a known concentration (0.01 M). For all (co)polymerization, 115 µL of this solution (1.15 µmol, 1 mg, 1 eq.) was used and placed in an NMR tube sealed with a rubber septum to which 0.2 mL of toluene-d_8 was added. The monomers ([M1]+[M2]/[Ti] = 1000) were weighed and mixed with 0.1 mL of toluene-d_8. Outside the glovebox, MAO (Al/Ti = 500) was added, and the system was left for 30 min to allow for catalyst pre-activation. An NMR spectrum of the mixture was recorded before the start of polymerization. Once the monomer(s) were added, the acquisition of the NMR spectra began. Each spectrum was measured with time intervals of every two minutes from the other. The temperature was varied as appropriate (25, 40 or 80°C). At the end of each kinetic analysis, the contents of the NMR tube were dissolved in the minimal amount of $CHCl_3$ and the polymer was precipitated in an acidified methanol solution containing BHT as an antioxidant, filtered, and dried in a vacuum oven overnight.

5.6.3 Determination of reactivity ratios and microstructure. To determine the reactivity ratios, the proton signals of each monomer were carefully integrated and used. Data sets from the copolymerisation experiments were fitted to both the ideal, non-terminal model (BSL) and the terminal model (Jaacks). The reactivity ratios determined by the *in situ* method were used to simulate the gradient structure of the copolymerisation.

Chapter 6

General Conclusions and Outlook

The transition from a fossil-based polymer to a biobased one is one of the major challenges of contemporary materials science. Conventional polymers derived from dienes and styrene form the basis of elastomers, thermoplastic elastomers, and a wide range of plastics, but their production is still rooted in non-renewable resources and often relies on metal catalysts that are toxic or difficult to manage in terms of environmental impact. Developing new macromolecular architectures from renewable monomers is therefore not sufficient in itself: the synthetic tools used to access these materials must also be compatible with a more sustainable scenario.

In this context, conjugated dienes derived from natural aldehydes and terpenes offer a renewable and structurally rich feedstock, while titanium complexes containing [OSSO]-type ligands offer a promising catalytic platform. Titanium is abundant, relatively inexpensive, and generally considered less toxic than many transition metals commonly employed in polymerization catalysis. Within this framework, the work presented in this thesis demonstrates that a family of [OSSO]-type titanium complexes (**1** and **2**, Figure 6.1), activated with MAO, can exert an exceptional level of regio- and stereocontrol over a broad set of renewable conjugated dienes, aromatic, cyclic and linear, enabling the synthesis of homopolymers and copolymers with finely tuned microstructures and properties. In particular, the monomers investigated form a coherent family: 1-phenyl-1,3-butadiene (1PB), obtained from cinnamaldehyde, a major component of cinnamon essential oil; 1-vinylcyclohexene (VCH), not bio-based but structurally analogous to the renewable cyclic monomer (*S*)-4-isopropenyl-1-vinyl-1-cyclohexene (IVC), derived from perillaldehyde, present in *Perilla* plants; and (E)-4,8-dimethyl-1,3,7-nonatriene (DMNT), synthesized from citral, the main constituent of citronella oil (Figure 6.2). Together with β-myrcene and β-ocimene, these monomers allowed access to a wide range of polymers entirely, or largely, based on renewable sources.

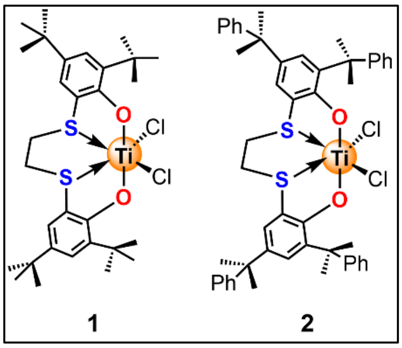

Figure 6.1. Structures of the titanium-[OSSO] complexes **1** and **2**.

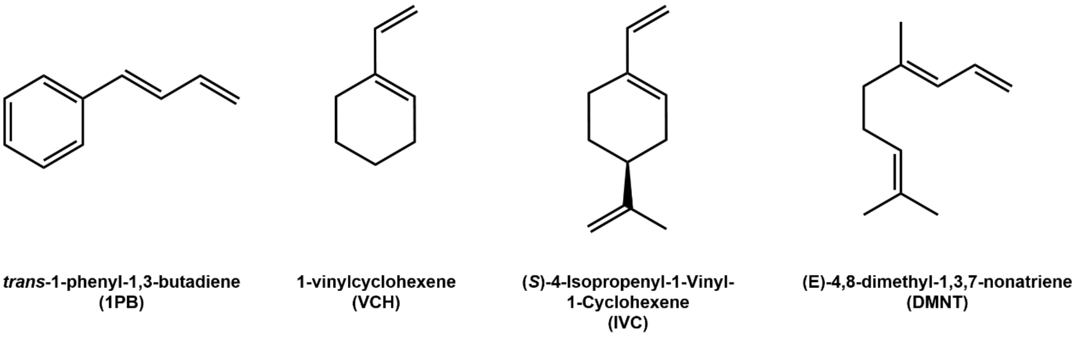

Figure 6.2. Structures of the Investigated Monomers.

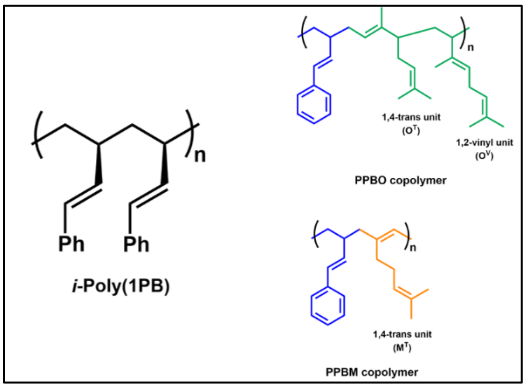

Figure 6.3. 3,4-isotactic poly(1PB) and Its Copolymers.

The aromatic monomer (1PB) provided a first illustration of the role of ligand sterics on regio- and stereocontrol. When 1PB was polymerized with the tert-butyl-substituted catalyst **1**, incomplete 3,4-regioselectivity, low yields and bimodal molecular-weight distributions were obtained. In contrast, the cumyl-substituted catalyst **2**, in combination with MAO, proved highly efficient, delivering 3,4-regioselective and isotactic poly(1PB) with *mmmm* > 99% and 3,4-insertion > 99% under optimized conditions (Figure 6.3). Microstructural and thermal characterization revealed that the resulting 3,4-isotactic poly(1PB) samples are essentially amorphous. Post-polymerization hydrogenation of isotactic poly(1PB) further highlighted the sensitivity of thermal properties to backbone structure. Saturation of the double bonds caused a dramatic reduction in T_g, from approximately 80°C to 17°C, increasing the flexibility of the backbone. Through this simple post-polymerization step, a rigid, glassy material was transformed into a much softer polymer. 1PB was then copolymerized with linear terpenes (Figure 6.3). In 1PB/β-ocimene copolymerizations catalysed by complex **2**, the final copolymer composition closely mirrored the initial monomer feed, and the maximum 1PB conversion remained comparable to that of its homopolymerization. NMR, SEC and DSC analyses indicated amorphous copolymers with microstructures consistent with multiblock architectures. The incorporation of β-ocimene occurred through both 1,4-*trans* and 1,2-vinyl insertions. DSC and TGA highlighted partial cross-linking above 100 °C and the presence of phase-separated domains whose glass transitions depended strongly on terpene content. In contrast, the copolymerization with β-myrcene reflected its lower reactivity towards the catalyst **2**, resulting in polymers dominated by 1PB units. Switching to catalyst **1** increased β-myrcene incorporation but at the cost of reduced molecular weights and yields.

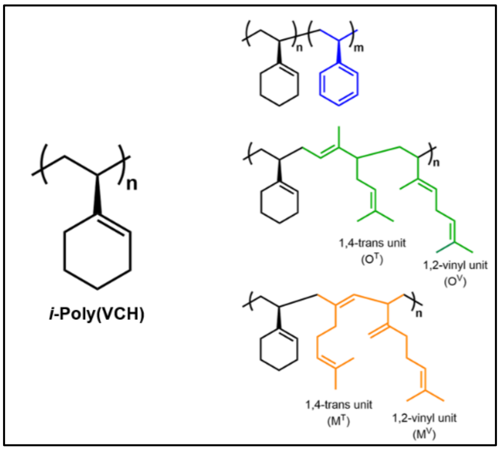

Figure 6.4. 3,4-isotactic poly(VCH) and Its Copolymers.

Stereoselective polymerization of cyclic dienes provided a complementary perspective on how ring structure and substituents influence both microstructure and material behaviour. For 1-vinylcyclohexene (VCH), catalyst **2** consistently outperformed catalyst **1**, affording PVCH with exclusive 3,4-insertion and exceptionally high isotacticity (*mmmm* > 99%) (Figure 6.4). The T_g increased with both molecular weight and regioselectivity, yet the polymers remained completely amorphous. PVCH thus emerges as an unusual example of a perfectly regular polymer that resists crystallization, highlighting how conformational constraints and the arrangement of side groups can hinder packing despite high stereoregularity. Hydrogenation experiments confirmed the underlying isotactic microstructure by yielding semicrystalline isotactic poly(vinylcyclohexane), demonstrating that crystallinity is not absent because of configurational disorder but rather because of the specific conformational and packing landscape imposed by the VCH motif. Sequential VCH/styrene copolymerizations proceeded efficiently to give high-molecular-weight diblock copolymers with high styrene content and high T_g values (Figure 6.4). In contrast, one-pot one-step copolymerizations led to lower yields and molecular weights due to competitive coordination of the two monomers, and the resulting copolymers displayed more random microstructures with broadened and reduced thermal transitions. When VCH was copolymerized with β-myrcene or β-ocimene, their lower reactivity produced VCH-enriched copolymers with mixed insertion modes and significantly lower T_g values, reflecting the increased flexibility imparted by the terpene units (Figure 6.4).

On this basis, the bio-based cyclic diene (*S*)-4-isopropenyl-1-vinyl-1-cyclohexene (IVC) was explored as a fully renewable counterpart. Catalyst **2** again proved highly effective, delivering isotactic PIVC across the investigated temperature range (Figure 6.5). Like PVCH, PIVC was entirely amorphous and resistant to crystallization, but its T_g values were lower and showed an opposite trend with molecular weight, reflecting the influence of the additional isopropenyl substituent on chain packing and segmental mobility. The pendant exocyclic double bond in PIVC was then exploited as a chemical handle for thiol-ene crosslinking. Reactions with simple

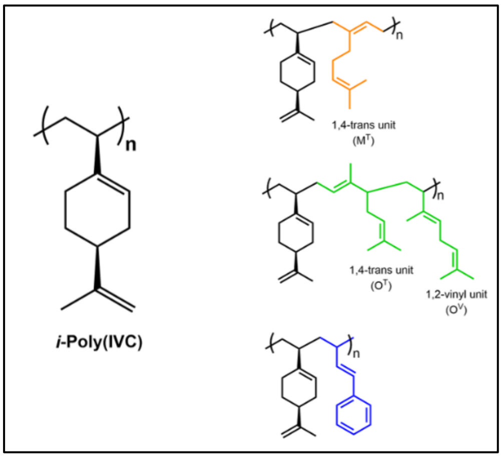

Figure 6.5. 3,4-isotactic poly(IVC) and Its Copolymers.

aliphatic dithiols rapidly produced insoluble networks in which the original glass transition (ca. 80°C) increased dramatically to values above 250°C in DSC, while the thermal stability of the backbone remained essentially unchanged. To introduce reversibility, ester-containing dithiols were synthesized and used to build networks featuring hydrolysable junctions. As in the irreversible case, the formation of a rigid three-dimensional architecture was evidenced by the shift of the original Tg to values above 250 °C. A first exploratory hydrolysis using H_2SO_4 in THF at 60 °C did not fully solubilize the network, but DSC revealed the appearance of a new glass transition at 33 °C, much lower than the $T_g \approx 83$ °C of the PIVC homopolymer. This behaviour shows that ester cleavage occurred: breaking the crosslinks generates two pendant fragments, one bearing a carboxylic acid and the other an alcohol, both still attached to the main chain. The overall cross-link density is reduced, and new flexible side groups are introduced, simultaneously decreasing topological constraints and disrupting packing. Further optimization of the hydrolysis conditions should allow full network breakdown and solubilization and will be an important target for future work on recyclable and reprocessable bio-based networks. Copolymerizations of IVC with β-myrcene, β-ocimene and 1PB expanded the accessible space of renewable materials (Figure 6.5). As observed for other systems, catalyst **1** tended to favour higher myrcene incorporation at the expense of molecular weight, whereas catalyst **2** performed better with β-ocimene. All IVC-based copolymers were amorphous and exhibited thermal properties that depended strongly on composition. In IVC/terpene copolymers, T_g values decreased with increasing terpene content, consistent with well-mixed amorphous phases and a progressive softening. In IVC/1PB copolymers, the combination of two rigid monomers, showed high T_g values and mechanical behaviour corresponding to rigid, glassy materials.

Linear (E)-4,8-dimethyl-1,3,7-nonatriene (DMNT), derived from citral, represented an even more interesting example for the catalytic system. The titanium [OSSO] complexes promoted its polymerization with complete 1,2-regioselectivity; catalyst **2**, in particular, provided exceptionally stereoregular poly(DMNT) with *mmmm* > 99%, a level of isotacticity not previously reported for this monomer (Figure 6.6). An optimal temperature of 25 °C was identified, balancing high yields with controlled molecular-weight growth, while prolonged

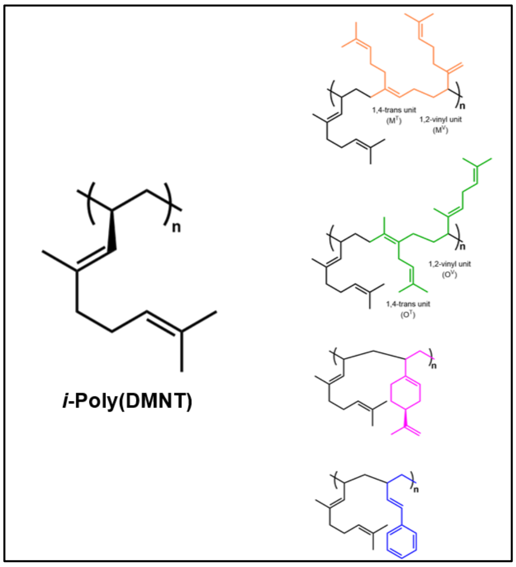

Figure 6.6. 1,2-isotactic poly(DMNT) and Its Copolymers.

reaction times highlighted chain transfer and termination processes that eventually lowered M_n. All poly(DMNT) samples exhibited a single glass transition between -34 and -40 °C, confirming their amorphous and elastomeric nature. Introducing linear terpenes into DMNT polymerizations allowed the properties of the resulting materials to be finely adjusted (Figure 6.6). β-myrcene incorporation increased markedly with temperature, while β-ocimene displayed higher intrinsic reactivity, giving copolymers with higher T_g at analogous compositions. NMR analyses confirmed the expected insertion modes, and the combined thermal and compositional trends indicated random or tapered multiblock architectures governed by the reactivity differences between DMNT and the terpenes. Extending copolymerization to IVC and 1PB revealed the strong influence of comonomer rigidity: IVC incorporation remained proportional to its feed ratio, and the resulting DMNT/IVC copolymers showed intermediate T_g values, whereas DMNT/1PB copolymers achieved high molecular weights and glass transitions spanning from elastomeric to glassy regimes (Figure 6.6). In all cases, catalyst **2** preserved its high regio- and stereoselectivity, underscoring its robustness across structurally diverse bio-derived dienes. Because of their structural features, DMNT and 1PB together emerge as promising sustainable alternatives to butadiene and styrene. The one-pot one-step DMNT:1PB copolymer with 80:20 composition, conceived as a renewable SBR analogue, exhibited a T_g around -20 °C, confirming elastomeric behaviour despite being higher than typical commercial SBR. The sequential 1PB-DMNT-1PB triblock copolymer, designed as a renewable SBS counterpart, displayed two well-separated transitions at -36.4 °C and +100 °C, reproducing the essential thermal characteristics of hard-soft thermoplastic elastomers. These results convincingly illustrate that renewable monomers can recreate the functional profiles of conventional SBR and SBS and open a realistic route toward high-performance, fully bio-based elastomeric materials.

A unifying element of this work is the systematic use of real-time ^{1}H NMR spectroscopy to deepen kinetic understanding and gain predictive control over these coordination polymerizations. By monitoring monomer consumption directly in sealed NMR tubes and analysing the resulting conversion profiles with Jaacks and nonterminal BLS models, it was possible to determine reactivity ratios for a broad set of bio-based dienes and terpenes and to reconstruct the corresponding compositional drifts along the chains. Homopolymerization studies of 1PB, IVC, and DMNT confirmed that the intrinsic reactivity and optimum temperatures identified in the Schlenk tube experiments are preserved in the NMR setup and that the high 3,4-regioselectivity and isotacticity of catalyst **2** are maintained unchanged. For 1PB and IVC, conversion and molecular-weight trends were reproduced almost quantitatively; for DMNT, the NMR-tube conditions led to slightly lower M_n but identical microstructure and T_g. Systematic variation of the Al/Ti ratio in DMNT polymerization highlighted the dual role of MAO as activator and chain transfer agent, revealing that an intermediate Al/Ti ratio ≈ 500 maximizes activity but reduces molecular weight, while both lower and higher loadings slow down the kinetics favoring higher M_n.

On this kinetic basis, a comprehensive series of copolymerizations was used to study the relative reactivity of 1PB, IVC, DMNT, β-myrcene, and β-ocimene. The 1PB/β-myrcene system emerged as a limiting case in which copolymerization is essentially absent: 1PB is fully consumed while β-myrcene remains largely unreacted, and both Meyer-Lowry and BLS analyses fail to yield physically meaningful reactivity ratios. In contrast, 1PB/β-ocimene followed the Jaacks model up to ~80% conversion, leading to gradient copolymers initially enriched in 1PB and progressively richer in β-ocimene as the reaction proceeds. IVC-based copolymerizations revealed a different reactivity landscape: in IVC/β-myrcene and IVC/β-ocimene, IVC is more reactive, and linear Jaacks plots up to ≈90% conversion indicate gradient or tapered chains that start IVC-rich and gradually incorporate the terpenes, with a more pronounced gradient for β-ocimene ($r_{IVC} = 3.3$; *rOcim* = 0.30) than for β-myrcene ($r_{IVC} = 2.1$; $r_{Myrc} = 0.47$). In IVC/1PB, the trend is inverted: 1PB becomes the dominant monomer, and Jaacks analysis up to 70% conversion shows that both IVC- and 1PB-ended chains preferentially insert 1PB at low conversion, giving gradient copolymers. DMNT copolymerizations further refined the reactivity hierarchy. At 80 °C, DMNT was consumed extremely rapidly in the presence of β-myrcene and β-ocimene, while the terpenes were incorporated more slowly but quantitatively. Jaacks analyses up to 90% conversion gave r_{DMNT} and r_{Terp} values consistent with gradient or strongly tapered chains in which DMNT forms the initial segments and the terpene content increases along the chain. At 40 °C, DMNT remained more reactive than IVC, again yielding gradient copolymers initially enriched in DMNT. A qualitatively different behaviour was observed for DMNT/1PB, where both monomers displayed comparable reactivities. Here, the nonterminal BLS formalism provided the best description up to ~70% conversion, indicating a truly random copolymerization with a statistically uniform distribution of DMNT and 1PB units along the backbone.

Finally, although these are only preliminary in vitro tests, it is nevertheless worth emphasizing that the three homopolymers obtained from natural aldehydes, poly(1PB), poly(IVC) and poly(DMNT), proved to be non-cytotoxic in MTT assays on HepG2 cells, an encouraging result that supports the idea that such bio-based materials could eventually be considered for application in areas where a favourable cellular response is essential, such as soft biointerfaces and coatings for biomedical devices, tissue-engineering scaffolds, or encapsulation matrices for the controlled release of active species.

The results of this thesis highlight how renewable conjugated dienes and terpenes, when combined with stereoselective [OSSO]-type titanium catalysis and *in situ* NMR analysis, offer a powerful route to sustainable polymer design. The ability to obtain homopolymers, copolymers and bio-based analogues of industrial materials such as SBR and SBS demonstrates the versatility of these systems and their potential to replace fossil-derived counterparts.

This work demonstrates the feasibility of obtaining rigid, high-T_g materials, soft elastomers, and finely tunable amorphous copolymers while maintaining a high degree of microstructural control. This diversity, derived entirely from renewable resources, directly addresses key environmental challenges and expands the possibilities for advanced polymer applications. Looking ahead, the approach presented here provides a solid foundation for further advances. Expanding the monomer portfolio, refining catalyst design, and exploring post-polymerization modifications will open new opportunities for functional, recyclable, and circular materials. Further mechanical, aging, and biological studies could help position the most promising candidates for real-world use.

In conclusion, this thesis demonstrates that titanium [OSSO]-catalyzed stereoselective polymerization is a compelling strategy for transforming natural building blocks into high-performance, renewable thermoplastic elastomers and elastomers. It establishes a clear path for the design of sustainable polymeric materials that combine structural precision, functional adaptability, and environmental responsibility.

Bibliography

(1) Koppala, B. C. N.; Povari, S.; Alam, S.; Rao, V. V. B.; Nakka, L.; Chenna, S. Comparative Assessment on Thermo-Chemical Conversion of Different Waste Plastics to Value Added Syngas: Thermodynamic Investigation. *Environ. Dev. Sustain.* **2024**. https://doi.org/10.1007/s10668-024-04811-2.

(2) Nayanathara Thathsarani Pilapitiya, P. G. C.; Ratnayake, A. S. The World of Plastic Waste: A Review. *Clean. Mater.* **2024**, *11*, 100220. https://doi.org/10.1016/j.clema.2024.100220.

(3) Chen, J.; Wang, W.; Zou, C.; Chen, C. Mechanical Recycling of Mixed Plastics by Supramolecular Dynamic Cross-Linking Strategy. *J. Am. Chem. Soc.* **2025**, *147* (28), 24747–24758. https://doi.org/10.1021/jacs.5c06330.

(4) Frączak, D. Chemical Recycling of Polyolefins (PE, PP): Modern Technologies and Products. In *Waste Material Recycling in the Circular Economy - Challenges and Developments*; S. Achilias, D., Ed.; IntechOpen, 2022. https://doi.org/10.5772/intechopen.99084.

(5) *Applied Polymer Science*, Second Edition.; Tess, R. W., Poehlein, G. W., Eds.; ACS Symposium Series; American Chemical Society: Washington, D.C., 1985; Vol. 285. https://doi.org/10.1021/bk-1985-0285.

(6) Sauter, D.; Taoufik, M.; Boisson, C. Polyolefins, a Success Story. *Polymers* **2017**, *9* (6), 185. https://doi.org/10.3390/polym9060185.

(7) Coates, G. W. Precise Control of Polyolefin Stereochemistry Using Single-Site Metal Catalysts. *Chem. Rev.* **2000**, *100* (4), 1223–1252. https://doi.org/10.1021/cr990286u.

(8) Sisanth, K. S.; Thomas, M. G.; Abraham, J.; Thomas, S. General Introduction to Rubber Compounding. In *Progress in Rubber Nanocomposites*; Elsevier, 2017; pp 1–39. https://doi.org/10.1016/B978-0-08-100409-8.00001-2.

(9) Claverie, J. P.; Schaper, F. Ziegler-Natta Catalysis: 50 Years after the Nobel Prize. *MRS Bull.* **2013**, *38* (3), 213–218. https://doi.org/10.1557/mrs.2013.52.

(10) Mülhaupt, R. Catalytic Polymerization and Post Polymerization Catalysis Fifty Years After the Discovery of Ziegler's Catalysts. *Macromol. Chem. Phys.* **2003**, *204* (2), 289–327. https://doi.org/10.1002/macp.200290085.

(11) Chen, C. Designing Catalysts for Olefin Polymerization and Copolymerization: Beyond Electronic and Steric Tuning. *Nat. Rev. Chem.* **2018**, *2* (5), 6–14. https://doi.org/10.1038/s41570-018-0003-0.

(12) Mella, M.; Izzo, L.; Capacchione, C. Role of the Metal Center in the Ethylene Polymerization Promoted by Group 4 Complexes Supported by a Tetradentate [OSSO]-Type Bis(Phenolato) Ligand. *ACS Catal.* **2011**, *1* (11), 1460–1468. https://doi.org/10.1021/cs200333z.

(13) Paradiso, V.; Capaccio, V.; Lamparelli, D. H.; Capacchione, C. [OSSO]-Bisphenolate Metal Complexes: A Powerful and Versatile Tool in Polymerization Catalysis. *Coord. Chem. Rev.* **2021**, *429*, 213644. https://doi.org/10.1016/j.ccr.2020.213644.

(14) Beckerle, K.; Capacchione, C.; Ebeling, H.; Manivannan, R.; Mülhaupt, R.; Proto, A.; Spaniol, T. P.; Okuda, J. Stereospecific Post-Metallocene Polymerization Catalysts: The Example of Isospecific Styrene Polymerization. *J. Organomet. Chem.* **2004**, *689* (24), 4636–4641. https://doi.org/10.1016/j.jorganchem.2004.08.019.

(15) Paradiso, V.; Capaccio, V.; Lamparelli, D. H.; Capacchione, C. Metal Complexes Bearing Sulfur-Containing Ligands as Catalysts in the Reaction of CO2 with Epoxides. *Catalysts* **2020**, *10* (8), 825. https://doi.org/10.3390/catal10080825.

(16) Capacchione, C.; Proto, A.; Ebeling, H.; Mülhaupt, R.; Möller, K.; Spaniol, T. P.; Okuda, J. Ancillary Ligand Effect on Single-Site Styrene Polymerization: Isospecificity of Group 4 Metal Bis(Phenolate) Catalysts. *J. Am. Chem. Soc.* **2003**, *125* (17), 4964–4965. https://doi.org/10.1021/ja029968g.

(17) Lian, B.; Beckerle, K.; Spaniol, T. P.; Okuda, J. Regioselective 1-Hexene Oligomerization Using Cationic Bis(Phenolato) Group 4 Metal Catalysts: Switch from 1,2- to 2,1-Insertion. *Angew. Chem. Int. Ed.* **2007**, *46* (44), 8507–8510. https://doi.org/10.1002/anie.200703218.

(18) Meppelder, G.-J. M.; Halbach, T. S.; Spaniol, T. P.; Mülhaupt, R.; Okuda, J. A Vanadium(V) Complex with a Tetradentate [OSSO]-Type Bis(Phenolato) Ligand: Synthesis, Structure, and Ethylene Polymerization Activity. *J. Organomet. Chem.* **2009**, *694* (7–8), 1235–1237. https://doi.org/10.1016/j.jorganchem.2008.11.008.

(19) Toda, T.; Nakata, N.; Matsuo, T.; Ishii, A. Synthesis, Structure, and 1-Hexene Polymerization Catalytic Ability of Group 5 Metal Complexes Incorporating an [OSSO]-Type Ligand. *ACS Catal.* **2013**, *3* (8), 1764–1767. https://doi.org/10.1021/cs4003996.

(20) Della Monica, F.; Maity, B.; Pehl, T.; Buonerba, A.; De Nisi, A.; Monari, M.; Grassi, A.; Rieger, B.; Cavallo, L.; Capacchione, C. [OSSO]-Type Iron(III) Complexes for the Low-Pressure Reaction of Carbon Dioxide with Epoxides: Catalytic Activity, Reaction Kinetics, and Computational Study. *ACS Catal.* **2018**, *8* (8), 6882–6893. https://doi.org/10.1021/acscatal.8b01695.

(21) Della Monica, F.; Paradiso, V.; Grassi, A.; Milione, S.; Cavallo, L.; Capacchione, C. A Novel [OSSO]-Type Chromium(III) Complex as a Versatile Catalyst for Copolymerization of Carbon Dioxide with Epoxides. *Chem. – Eur. J.* **2020**, *26* (24), 5347–5353. https://doi.org/10.1002/chem.201905455.

(22) Niknam, F.; Capaccio, V.; Kleybolte, M.; Lamparelli, D. H.; Winnacker, M.; Fiorani, G.; Capacchione, C. [OSSO]-Type Chromium(III) Complexes for the Reaction of CO_2 with Epoxides. *ChemPlusChem* **2022**, *87* (8), e202200038. https://doi.org/10.1002/cplu.202200038.

(23) Paradiso, V.; Della Monica, F.; Lamparelli, D. H.; D'Aniello, S.; Rieger, B.; Capacchione, C. Dinuclear [OSSO]-Fe Complexes for the Reaction of CO_2 with Epoxides. *Catal. Sci. Technol.* **2021**, *11* (14), 4702–4707. https://doi.org/10.1039/D1CY00622C.

(24) Niknam, F.; Denk, A.; Buonerba, A.; Rieger, B.; Grassi, A.; Capacchione, C. Dinuclear Chromium Complexes with [OSSO]-Type Ligands in the Copolymerization of Epoxides with CO_2 and Phthalic Anhydride. *Catal. Sci. Technol.* **2023**, *13* (16), 4684–4692. https://doi.org/10.1039/D3CY00832K.

(25) Ma, H.; Spaniol, T. P.; Okuda, J. Rare Earth Metal Complexes Supported by 1, -Dithiaalkanediyl- Bridged Bis(Phenolato) Ligands: Synthesis, Characterization and Ring-Opening Polymerization Catalysis of L-Lactide. *Dalton Trans*.

(26) Konkol, M.; Spaniol, T. P.; Kondracka, M.; Okuda, J. Lutetium Alkyl and Hydride Complexes in a Non-Cyclopentadienyl Coordination Environment. *Dalton Trans.* **2007**, No. 36, 4095. https://doi.org/10.1039/b710228n.

(27) Ma, H.; Melillo, G.; Oliva, L.; Spaniol, T. P.; Englert, U.; Okuda, J. Aluminium Alkyl Complexes Supported by [OSSO] Type Bisphenolato Ligands: Synthesis, Characterization and Living Polymerization of Rac-Lactide. *Dalton Trans.* **2005**, No. 4, 721. https://doi.org/10.1039/b416875e.

(28) Capacchione, C.; Manivannan, R.; Barone, M.; Beckerle, K.; Centore, R.; Oliva, L.; Proto, A.; Tuzi, A.; Spaniol, T. P.; Okuda, J. Isospecific Styrene Polymerization by Chiral Titanium Complexes That Contain a Tetradentate [OSSO]-Type Bis(Phenolato) Ligand. *Organometallics* **2005**, *24* (12), 2971–2982. https://doi.org/10.1021/om050120l.

(29) Capacchione, C.; D'Acunzi, M.; Motta, O.; Oliva, L.; Proto, A.; Okuda, J. Isolated Ethylene Units in Isotactic Polystyrene Chain: Stereocontrol of an Isospecific Post-Metallocene Titanium Catalyst. *Macromol. Chem. Phys.* **2004**, *205* (3), 370–373. https://doi.org/10.1002/macp.200300115.

(30) Milione, S.; Cuomo, C.; Capacchione, C.; Zannoni, C.; Grassi, A.; Proto, A. Stereoselective Polymerization of Conjugated Dienes and Styrene−Butadiene Copolymerization Promoted by Octahedral Titanium Catalyst. *Macromolecules* **2007**, *40* (16), 5638–5643. https://doi.org/10.1021/ma070543u.

(31) Costabile, C.; Capacchione, C.; Saviello, D.; Proto, A. Mechanistic Studies on Conjugated Diene Polymerizations Promoted by a Titanium Complex Containing a Tetradentate [OSSO]-Type Bis(Phenolato) Ligand. *Macromolecules* **2012**, *45* (16), 6363–6370. https://doi.org/10.1021/ma3011697.

(32) Capacchione, C.; Proto, A.; Okuda, J. Synthesis of Branched Polyethylene by Ethylene Homopolymerization Using Titanium Catalysts That Contain a Bridged Bis(Phenolate) Ligand. *J. Polym. Sci. Part Polym. Chem.* **2004**, *42* (11), 2815–2822. https://doi.org/10.1002/pola.20104.

(33) Lapenta, R.; Buonerba, A.; Luciano, E.; Della Monica, F.; De Nisi, A.; Monari, M.; Grassi, A.; Capacchione, C.; Milione, S. Phenylene-Bridged OSSO-Type Titanium Complexes in the Polymerization of Ethylene and Propylene. *ACS Omega* **2018**, *3* (9), 11608–11616. https://doi.org/10.1021/acsomega.8b01550.

(34) Capacchione, C.; Proto, A.; Ebeling, H.; Mülhaupt, R.; Okuda, J. Copolymerization of Ethylene with Styrene Catalyzed by a Linked Bis(Phenolato) Titanium Catalyst. *J. Polym. Sci. Part Polym. Chem.* **2006**, *44* (6), 1908–1913. https://doi.org/10.1002/pola.21292.

(35) Capacchione, C.; Avagliano, A.; Proto, A. Ethylene−Butadiene Copolymerization Promoted by Titanium Complex Containing a Tetradentate [OSSO]-Type Bis(Phenolato) Ligand. *Macromolecules* **2008**, *41* (13), 4573–4575. https://doi.org/10.1021/ma800864y.

(36) Proto, A.; Avagliano, A.; Saviello, D.; Capacchione, C. Copolymerization of Ethylene with 4-Methyl-1,3-Pentadiene Promoted by Titanium Complexes Containing a Tetradentate [OSSO]-Type Bis(Phenolato) Ligand. *Macromolecules* **2009**, *42* (18), 6981–6985. https://doi.org/10.1021/ma901293k.

(37) Proto, A.; Avagliano, A.; Saviello, D.; Ricciardi, R.; Capacchione, C. Living, Isoselective Polymerization of Styrene and Formation of Stereoregular Block Copolymers via Sequential Monomer Addition. *Macromolecules* **2010**, *43* (14), 5919–5921. https://doi.org/10.1021/ma101246x.

(38) Buonerba, A.; Fienga, M.; Milione, S.; Cuomo, C.; Grassi, A.; Proto, A.; Capacchione, C. Binary Copolymerization of *p* -Methylstyrene with Butadiene and Isoprene Catalyzed by Titanium Compounds Showing Different Stereoselectivity. *Macromolecules* **2013**, *46* (21), 8449–8457. https://doi.org/10.1021/ma401621v.

(39) Zhu, Y.; Romain, C.; Williams, C. K. Sustainable Polymers from Renewable Resources. *Nature* **2016**, *540* (7633), 354–362. https://doi.org/10.1038/nature21001.

(40) Thomsett, M. R.; Storr, T. E.; Monaghan, O. R.; Stockman, R. A.; Howdle, S. M. Progress in the Synthesis of Sustainable Polymers from Terpenes and Terpenoids. *Green Mater.* **2016**, *4* (3), 115–134. https://doi.org/10.1680/jgrma.16.00009.

(41) Rohmer, M.; Rohmer, M. The Discovery of a Mevalonate-Independent Pathway for Isoprenoid Biosynthesis in Bacteria, Algae and Higher Plants†. *Nat. Prod. Rep.* **1999**, *16* (5), 565–574. https://doi.org/10.1039/a709175c.

(42) Lamparelli, D. H.; Winnacker, M.; Capacchione, C. Stereoregular Polymerization of Acyclic Terpenes. *ChemPlusChem* **2022**, *87* (1), e202100366. https://doi.org/10.1002/cplu.202100366.

(43) *Handbook of Essential Oils: Science, Technology, and Applications, Second Edition*, 2nd ed.; Baser, K. H. C., Buchbauer, G., Eds.; CRC Press: Boca Raton, 2015. https://doi.org/10.1201/b19393.

(44) Roberts, W. J.; Day, A. R. A Study of the Polymerization of α- and β-Pinene with Friedel—Crafts Type Catalysts. *J. Am. Chem. Soc.* **1950**, *72* (3), 1226–1230. https://doi.org/10.1021/ja01159a044.

(45) Della Monica, F.; Kleij, A. W. From Terpenes to Sustainable and Functional Polymers. *Polym. Chem.* **2020**, *11* (32), 5109–5127. https://doi.org/10.1039/D0PY00817F.

(46) Byrne, C. M.; Allen, S. D.; Lobkovsky, E. B.; Coates, G. W. Alternating Copolymerization of Limonene Oxide and Carbon Dioxide. *J. Am. Chem. Soc.* **2004**, *126* (37), 11404–11405. https://doi.org/10.1021/ja0472580.

(47) Peña Carrodeguas, L.; González-Fabra, J.; Castro-Gómez, F.; Bo, C.; Kleij, A. W. AlIII-Catalysed Formation of Poly(Limonene)Carbonate: DFT Analysis of the Origin of Stereoregularity. *Chem. – Eur. J.* **2015**, *21* (16), 6115–6122. https://doi.org/10.1002/chem.201406334.

(48) Winnacker, M. Polyamides Derived from Terpenes: Advances in Their Synthesis, Characterization and Applications. *Eur. J. Lipid Sci. Technol.* **2023**, *125* (5), 2300014. https://doi.org/10.1002/ejlt.202300014.

(49) Roth, S.; Funk, I.; Hofer, M.; Sieber, V. Chemoenzymatic Synthesis of a Novel Borneol-Based Polyester. *ChemSusChem* **2017**, *10* (18), 3574–3580. https://doi.org/10.1002/cssc.201701146.

(50) Nsengiyumva, O.; Miller, S. A. Synthesis, Characterization, and Water-Degradation of Biorenewable Polyesters Derived from Natural Camphoric Acid. *Green Chem.* **2019**, *21* (5), 973–978. https://doi.org/10.1039/C8GC03990A.

(51) Zhang, D.; Hillmyer, M. A.; Tolman, W. B. Catalytic Polymerization of a Cyclic Ester Derived from a “Cool” Natural Precursor. *Biomacromolecules* **2005**, *6* (4), 2091–2095. https://doi.org/10.1021/bm050076t.

(52) You, F.; Shi, W.; Yan, X.; Wang, X.; Shi, X. Polymerization of Bio-Derived Conjugated Dienes with Rare-Earth-Metal Complexes. *Chem. – Asian J.* **2022**, *17* (23), e202200892. https://doi.org/10.1002/asia.202200892.

(53) Ren, X.; Guo, F.; Fu, H.; Song, Y.; Li, Y.; Hou, Z. Scandium-Catalyzed Copolymerization of Myrcene with Ethylene and Propylene: Convenient Syntheses of Versatile Functionalized Polyolefins. *Polym. Chem.* **2018**, *9* (10), 1223–1233. https://doi.org/10.1039/C8PY00039E.

(54) Guo, G.; Wu, X.; Yan, X.; Yan, L.; Li, X.; Zhang, S.; Qiu, N. Unprecedentedly High Activity and/or High Regio-/Stereoselectivity of Fluorenyl-Based CGC Allyl-Type H3:H1-Tert-Butyl(Dimethylfluorenylsilyl)Amido Ligated Rare Earth Metal Monoalkyl Complexes in Olefin Polymerization. *Polymers* **2019**, *11* (5), 836. https://doi.org/10.3390/polym11050836.

(55) Yu, X.; Li, M.; Hong, J.; Zhou, X.; Zhang, L. Living 3,4-(Co)Polymerization of Isoprene/Myrcene and One-Pot Synthesis of a Polyisoprene Blend Catalyzed by Binuclear Rare-Earth Metal Amidinate Complexes. *Chem. – Eur. J.* **2019**, *25* (10), 2569–2576. https://doi.org/10.1002/chem.201804944.

(56) Georges, S.; Touré, A. O.; Visseaux, M.; Zinck, P. Coordinative Chain Transfer Copolymerization and Terpolymerization of Conjugated Dienes. *Macromolecules* **2014**, *47* (14), 4538–4547. https://doi.org/10.1021/ma5008896.

(57) Loughmari, S.; Hafid, A.; Bouazza, A.; El Bouadili, A.; Zinck, P.; Visseaux, M. Highly Stereoselective Coordination Polymerization of β-Myrcene from a Lanthanide-Based Catalyst: Access to Bio-Sourced Elastomers. *J. Polym. Sci. Part Polym. Chem.* **2012**, *50* (14), 2898–2905. https://doi.org/10.1002/pola.26069.

(58) Georges, S.; Hashmi, O. H.; Bria, M.; Zinck, P.; Champouret, Y.; Visseaux, M. Efficient One-Pot Synthesis of End-Functionalized *Trans* -Stereoregular Polydiene Macromonomers. *Macromolecules* **2019**, *52* (3), 1210–1219. https://doi.org/10.1021/acs.macromol.8b01520.

(59) Liu, B.; Li, L.; Sun, G.; Liu, D.; Li, S.; Cui, D. Isoselective 3,4-(Co)Polymerization of Bio-Renewable Myrcene Using NSN-Ligated Rare-Earth Metal Precursor: An Approach to a New Elastomer. *Chem. Commun.* **2015**, *51* (6), 1039–1041. https://doi.org/10.1039/C4CC08962F.

(60) Liu, B.; Han, B.; Zhang, C.; Li, S.; Sun, G.; Cui, D. Renewable β-Myrcene Polymerization Initiated by Lutetium Alkyl Complexes Ligated by Imidophosphonamido Ligand. *Chin. J. Polym. Sci.* **2015**, *33* (5), 792–796. https://doi.org/10.1007/s10118-015-1629-8.

(61) Peng, D.; Du, G.; Zhang, P.; Yao, B.; Li, X.; Zhang, S. Regio- and Stereochemical Control in Ocimene Polymerization by Half-Sandwich Rare-Earth Metal Dialkyl Complexes. *Macromol. Rapid Commun.* **2016**, *37* (12), 987–992. https://doi.org/10.1002/marc.201600102.

(62) Yang, F.; Li, X. Novel Cationic Rare Earth Metal Alkyl Catalysts for Precise Olefin Polymerization. *J. Polym. Sci. Part Polym. Chem.* **2017**, *55* (14), 2271–2280. https://doi.org/10.1002/pola.28617.

(63) León, R. D. de; López, R.; Valencia, L.; Mendoza, R.; Cabello, J.; Enríquez, J. Towards Bioelastomers via Coordination Polymerization of Renewable Terpenes Using Neodymium-Based Catalyst Systems. *Key Eng. Mater.* **2018**, *779*, 115–121. https://doi.org/10.4028/www.scientific.net/KEM.779.115.

(64) Laur, E.; Welle, A.; Vantomme, A.; Brusson, J.-M.; Carpentier, J.-F.; Kirillov, E. Stereoselective Copolymerization of Styrene with Terpenes Catalyzed by an Ansa-Lanthanidocene Catalyst: Access to New Syndiotactic Polystyrene-Based Materials. *Catalysts* **2017**, *7* (12), 361. https://doi.org/10.3390/catal7120361.

(65) Raynaud, J.; Wu, J. Y.; Ritter, T. Iron-Catalyzed Polymerization of Isoprene and Other 1,3-Dienes. *Angew. Chem.* **2012**, *124* (47), 11975–11978. https://doi.org/10.1002/ange.201205152.

(66) Li, W.; Zhao, J.; Zhang, X.; Gong, D. Capability of PN3-Type Cobalt Complexes toward Selective (Co-)Polymerization of Myrcene, Butadiene, and Isoprene: Access to Biosourced Polymers. *Ind. Eng. Chem. Res.* **2019**, *58* (8), 2792–2800. https://doi.org/10.1021/acs.iecr.8b05866.

(67) Jia, X.; Li, W.; Zhao, J.; Yi, F.; Luo, Y.; Gong, D. Dual Catalysis of the Selective Polymerization of Biosourced Myrcene and Methyl Methacrylate Promoted by Salicylaldiminato Cobalt(II) Complexes with a Pendant Donor. *Organometallics* **2019**, *38* (2), 278–288. https://doi.org/10.1021/acs.organomet.8b00708.

(68) Marvel, C. S.; Hwa, C. C. L. Polymyrcene. *J. Polym. Sci.* **1960**, *45* (145), 25–34. https://doi.org/10.1002/pol.1960.1204514503.

(69) Naddeo, M.; Buonerba, A.; Luciano, E.; Grassi, A.; Proto, A.; Capacchione, C. Stereoselective Polymerization of Biosourced Terpenes β-Myrcene and β-Ocimene and Their Copolymerization with Styrene Promoted by Titanium Catalysts. *Polymer* **2017**, *131*, 151–159. https://doi.org/10.1016/j.polymer.2017.10.028.

(70) Lamparelli, D. H.; Paradiso, V.; Monica, F. D.; Proto, A.; Guerra, S.; Giannini, L.; Capacchione, C. Toward More Sustainable Elastomers: Stereoselective Copolymerization of Linear Terpenes with Butadiene. *Macromolecules* **2020**, *53* (5), 1665–1673. https://doi.org/10.1021/acs.macromol.9b02646.

(71) Pragliola, S.; Cipriano, M.; Boccia, A. C.; Longo, P. Polymerization of Phenyl-1,3-Butadienes in the Presence of Ziegler-Natta Catalysts. *Macromol. Rapid Commun.* **2002**,

23 (5–6), 356–361. https://doi.org/10.1002/1521-3927(20020401)23:5/6%253C356::AID-MARC356%253E3.0.CO;2-V.

(72) Lin, J.; Wang, F.; Zhang, C.; Liu, H.; Li, D.; Zhang, X. Copolymerization of 1,3-Butadiene with Phenyl/Phenethyl Substituted 1,3-Butadienes: A Direct Strategy to Access Pendant Phenyl Functionalized Polydienes. *RSC Adv.* **2021**, *11* (38), 23184–23191. https://doi.org/10.1039/D1RA02467A.

(73) Jiang, Y.; Kang, X.; Zhang, Z.; Li, S.; Cui, D. Syndioselective 3,4-Polymerization of 1-Phenyl-1,3-Butadiene by Rare-Earth Metal Catalysts. *ACS Catal.* **2020**, *10* (9), 5223–5229. https://doi.org/10.1021/acscatal.9b04590.

(74) You, F.; Wang, X.; Shi, W.; Yan, X.; Shi, X. Rare-Earth-Metal-Catalyzed Highly 3,4-Regioselective Polymerization of Polar 1-Phenyl-1,3-Butadiene Derivates. *Polym. Chem.* **2023**, *14* (38), 4445–4453. https://doi.org/10.1039/D3PY00798G.

(75) Marzocchi, R.; Grimaldi, I.; Ruiz De Ballesteros, O.; Femina, G.; Guida, A.; Ricciardi, R.; Morvillo, P.; Capacchione, C.; Auriemma, F. Synthesis and Characterization of β-Myrcene-Styrene and β-Ocimene-Styrene Copolymers. *Macromol. Rapid Commun.* **2025**, *46* (2), 2400641. https://doi.org/10.1002/marc.202400641.

(76) Capacchione, C.; Saviello, D.; Ricciardi, R.; Proto, A. Living, Isoselective Polymerization of 4-Methyl-1,3-Pentadiene and Styrenic Monomers and Synthesis of Highly Stereoregular Block Copolymers via Sequential Monomer Addition. *Macromolecules* **2011**, *44* (20), 7940–7947. https://doi.org/10.1021/ma201442w.

(77) Quan, Y.; Liu, Q.; Zhang, S.; Zhang, S. Comparison of the Morphology, Chemical Composition and Microstructure of Cryptocrystalline Graphite and Carbon Black. *Appl. Surf. Sci.* **2018**, *445*, 335–341. https://doi.org/10.1016/j.apsusc.2018.03.182.

(78) Golemba, F. J.; Guillet, J. E.; Nyburg, S. C. Synthesis and Crystal Structure of Isotactic Poly-4-Phenyl-1-Butene. *J. Polym. Sci. [A1]* **1968**, *6* (5), 1341–1349. https://doi.org/10.1002/pol.1968.150060525.

(79) Longo, P.; Grassi, A.; Grisi, F.; Milione, S. Polymerization of 1-Vinylcyclohexene in the Presence of Group 4 Metallocenes – MAO Catalysts. *Macromol. Rapid Commun.* **1998**, *19* (5), 229–233. https://doi.org/10.1002/marc.1998.030190501.

(80) Hahn, C.; Rauschenbach, M.; Frey, H. Merging Styrene and Diene Structures to a Cyclic Diene: Anionic Polymerization of 1-Vinylcyclohexene (VCH). *Angew. Chem. Int. Ed.* **2023**, *62* (28), e202302907. https://doi.org/10.1002/anie.202302907.

(81) Liu, H.; You, F.; Shi, W.; Hu, X.; So, Y.-M.; Shi, X. Rare-Earth-Metal Catalyzed Highly Regio- and Stereoselective Polymerization of Terpene-Derived Conjugated Dienes. *Polym. Chem.* **2023**, *14* (38), 4474–4480. https://doi.org/10.1039/D3PY00959A.

(82) Ammendola, P.; Tancredi, T.; Zambelli, A. Isotactic Polymerization of Styrene and Vinylcyclohexane in the Presence of Carbon-13-Enriched Ziegler-Natta Catalyst: Regioselectivity and Enantioselectivity of the Insertion into Metal-Methyl Bonds. *Macromolecules* **1986**, *19* (2), 307–310. https://doi.org/10.1021/ma00156a011.

(83) Auriemma, F.; De Rosa, C.; Di Caprio, M. R.; Di Girolamo, R.; Coates, G. W. Crystallization of Alternating Limonene Oxide/Carbon Dioxide Copolymers: Determination of the Crystal Structure of Stereocomplex Poly(Limonene Carbonate). *Macromolecules* **2015**, *48* (8), 2534–2550. https://doi.org/10.1021/acs.macromol.5b00157.

(84) Auriemma, F.; De Rosa, C.; Di Caprio, M. R.; Di Girolamo, R.; Ellis, W. C.; Coates, G. W. Stereocomplexed Poly(Limonene Carbonate): A Unique Example of the Cocrystallization of Amorphous Enantiomeric Polymers. *Angew. Chem. Int. Ed.* **2015**, *54* (4), 1215–1218. https://doi.org/10.1002/anie.201410211.

(85) Drayer, W. F.; Simmons, D. S. Sequence Effects on the Glass Transition of a Model Copolymer System. *Macromolecules* **2022**, *55* (14), 5926–5937. https://doi.org/10.1021/acs.macromol.2c00664.

(86) Larrain, R.; Tagle, L. H.; Diaz, F. R. Glass Transition Temperature-Molecular Weight Relation for Poly(Hexamethylene Perchloroterephthalamide). *Polym. Bull.* **1981**, *4* (8), 487–490. https://doi.org/10.1007/BF00255705.

(87) Stoddart, A.; Feast, W. J.; Rannard, S. P. Synthesis and Thermal Studies of Aliphatic Polyurethane Dendrimers: A Geometric Approach to the Flory–Fox Equation for Dendrimer Glass Transition Temperature. *Soft Matter* **2012**, *8* (4), 1096–1108. https://doi.org/10.1039/C1SM06725G.

(88) Resetco, C.; Hendriks, B.; Badi, N.; Du Prez, F. Thiol–Ene Chemistry for Polymer Coatings and Surface Modification – Building in Sustainability and Performance. *Mater Horiz* **2017**, *4* (6), 1041–1053. https://doi.org/10.1039/C7MH00488E.

(89) Kazybayeva, D. S.; Irmukhametova, G. S.; Khutoryanskiy, V. V. Thiol-Ene "Click Reactions" as a Promising Approach to Polymer Materials. *Polym. Sci. Ser. B* **2022**, *64* (1), 1–16. https://doi.org/10.1134/S1560090422010055.

(90) Lowe, A. B. Thiol-Ene "Click" Reactions and Recent Applications in Polymer and Materials Synthesis. *Polym Chem* **2010**, *1* (1), 17–36. https://doi.org/10.1039/B9PY00216B.

(91) Kim, S.; Wittek, K. I.; Lee, Y. Synthesis of Poly(Disulfide)s with Narrow Molecular Weight Distributions *via* Lactone Ring-Opening Polymerization. *Chem. Sci.* **2020**, *11* (19), 4882–4886. https://doi.org/10.1039/D0SC00834F.

(92) Zhang, L.; Fan, Z.; Fu, Z. DEPENDENCE OF THE DISTRIBUTION OF ACTIVE CENTERS ON MONOMER IN SUPPORTED ZIEGLER-NATTA CATALYSTS. *Chin. J. Polym. Sci.* **2011**.

(93) Trumbo, D. L. Synthesis, Polymerization, and Copolymerization of 2,6-Dimethyl-Nona-2,6,8-Triene. *J. Polym. Sci. Part Polym. Chem.* **1996**, *34* (7), 1343–1346. https://doi.org/10.1002/(SICI)1099-0518(199605)34:7%253C1343::AID-POLA23%253E3.0.CO;2-8.

(94) Jiang, Y.; Zhang, Z.; Li, S.; Cui, D. Coordination Polymerization of Renewable (*E*)-4, 8-DIMETHYL -1,3, 7-NONATRIENE by RARE-EARTH Metal Catalysts. *Chin. J. Chem.* **2022**, *40* (16), 1939–1944. https://doi.org/10.1002/cjoc.202200140.

(95) López-García, J.; Lehocký, M.; Humpolíček, P.; Sáha, P. HaCaT Keratinocytes Response on Antimicrobial Atelocollagen Substrates: Extent of Cytotoxicity, Cell Viability and Proliferation. *J. Funct. Biomater.* **2014**, *5* (2), 43–57. https://doi.org/10.3390/jfb5020043.

(96) Mayo, F. R.; Lewis, F. M. Copolymerization. I. A Basis for Comparing the Behavior of Monomers in Copolymerization; The Copolymerization of Styrene and Methyl Methacrylate. *J. Am. Chem. Soc.* **1944**, *66* (9), 1594–1601. https://doi.org/10.1021/ja01237a052.

(97) Fineman, M.; Ross, S. D. Linear Method for Determining Monomer Reactivity Ratios in Copolymerization. *J. Polym. Sci.* **1950**, *5* (2), 259–262. https://doi.org/10.1002/pol.1950.120050210.

(98) Kelen, T.; TÜd[Otilde]s, F. Analysis of the Linear Methods for Determining Copolymerization Reactivity Ratios. I. A New Improved Linear Graphic Method. *J. Macromol. Sci. Part - Chem.* **1975**, *9* (1), 1–27. https://doi.org/10.1080/00222337508068644.

(99) Meyer, V. E.; Lowry, G. G. Integral and Differential Binary Copolymerization Equations. *J. Polym. Sci. A* **1965**, *3* (8), 2843–2851. https://doi.org/10.1002/pol.1965.100030811.

(100) Jaacks, V. A Novel Method of Determination of Reactivity Ratios in Binary and Ternary Copolymerizations. *Makromol. Chem.* **1972**, *161* (1), 161–172. https://doi.org/10.1002/macp.1972.021610110.

(101) Beckingham, B. S.; Sanoja, G. E.; Lynd, N. A. Simple and Accurate Determination of Reactivity Ratios Using a Nonterminal Model of Chain Copolymerization. *Macromolecules* **2015**, *48* (19), 6922–6930. https://doi.org/10.1021/acs.macromol.5b01631.

(102) Rauschenbach, M.; Meier-Merziger, M.; Frey, H. Green Perspective Drives the Renaissance of Anionic Diene Polymerization. *Polym. Chem.* **2024**, *15* (42), 4297–4311. https://doi.org/10.1039/D4PY00805G.

(103) Obermeier, B.; Wurm, F.; Frey, H. Amino Functional Poly(Ethylene Glycol) Copolymers via Protected Amino Glycidol. *Macromolecules* **2010**, *43* (5), 2244–2251. https://doi.org/10.1021/ma902245d.

(104) Natalello, A.; Werre, M.; Alkan, A.; Frey, H. Monomer Sequence Distribution Monitoring in Living Carbanionic Copolymerization by Real-Time^1 H NMR Spectroscopy. *Macromolecules* **2013**, *46* (21), 8467–8471. https://doi.org/10.1021/ma401847y.

(105) Grune, E.; Bareuther, J.; Blankenburg, J.; Appold, M.; Shaw, L.; Müller, A. H. E.; Floudas, G.; Hutchings, L. R.; Gallei, M.; Frey, H. Towards Bio-Based Tapered Block Copolymers: The Behaviour of Myrcene in the Statistical Anionic Copolymerisation. *Polym. Chem.* **2019**, *10* (10), 1213–1220. https://doi.org/10.1039/C8PY01711E.

(106) Wahlen, C.; Blankenburg, J.; Von Tiedemann, P.; Ewald, J.; Sajkiewicz, P.; Müller, A. H. E.; Floudas, G.; Frey, H. Tapered Multiblock Copolymers Based on Farnesene and Styrene: Impact of Biobased Polydiene Architectures on Material Properties. *Macromolecules* **2020**, *53* (23), 10397–10408. https://doi.org/10.1021/acs.macromol.0c02118.

(107) Li, S.; Zhu, Y.; Liang, H.; Xie, X.; Zhan, Y.; Liang, G.; Zhu, F. The Influences of Electronic Effect and Isomerization of Salalen Titanium(IV) Complexes on Ethylene Polymerization in the Presence of Methylaluminoxane. *RSC Adv.* **2019**, *9* (71), 41824–41831. https://doi.org/10.1039/C9RA08899G.

Appendix 2

2.1 NMR Spectra

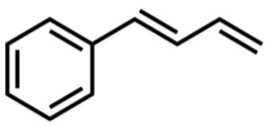

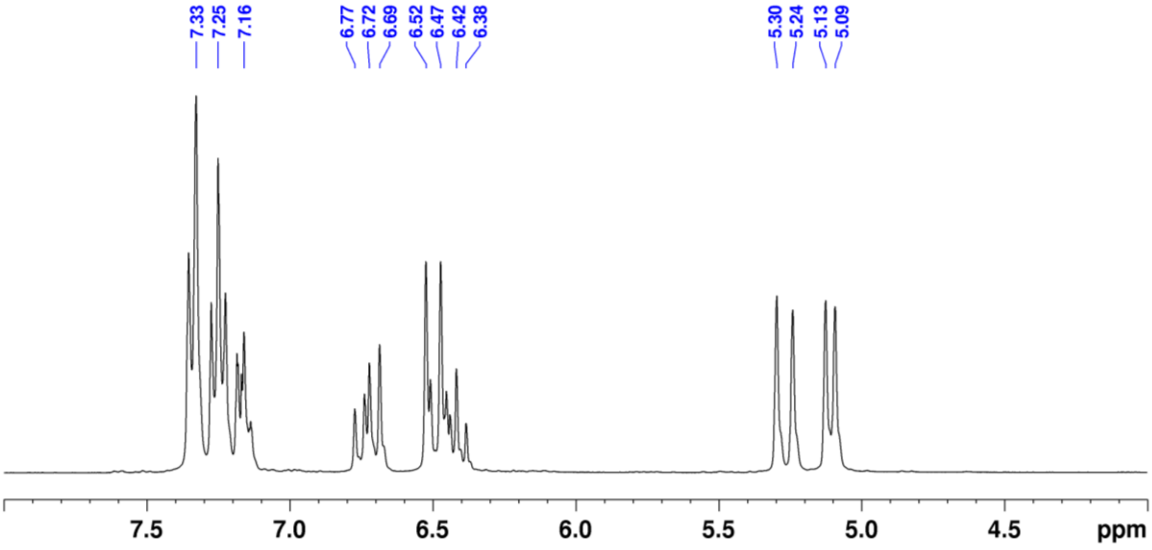

Figure S2.1. ^{1}H NMR (400 MHz, $CDCl_3$, 298 K) of *trans*-1-phenyl-1,3-butadiene (1PB).

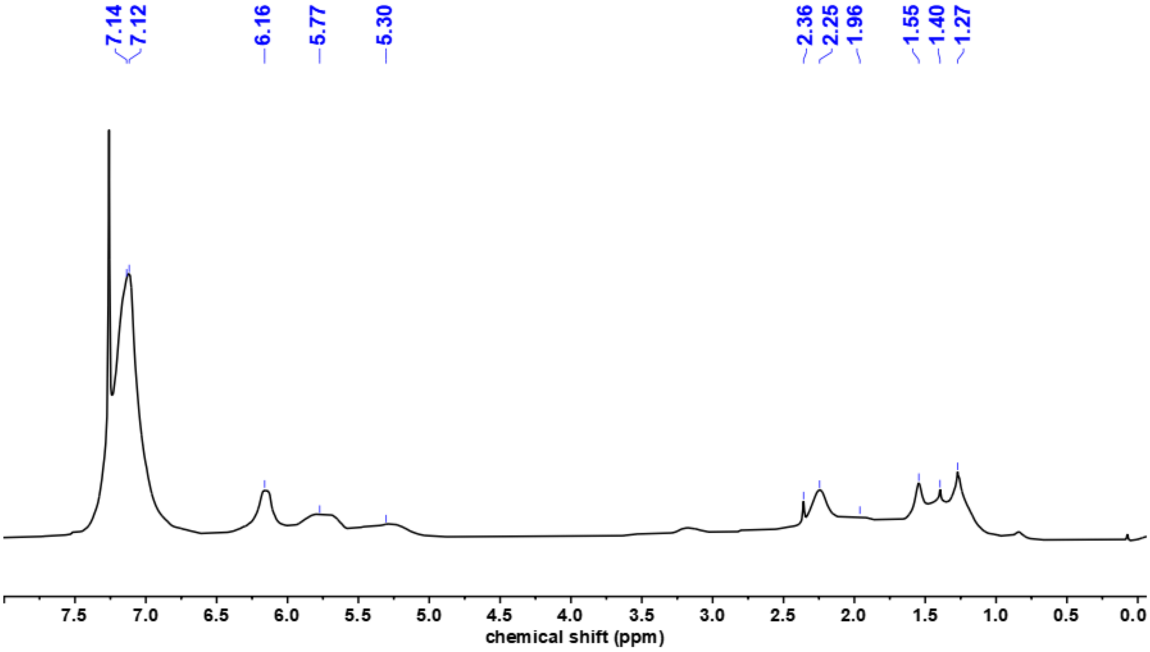

Figure S2.2. ^{1}H NMR (400 MHz, $CDCl_3$, 298 K) of poly(1PB) obtained with catalyst **1** (run **3**, Table 2.1).

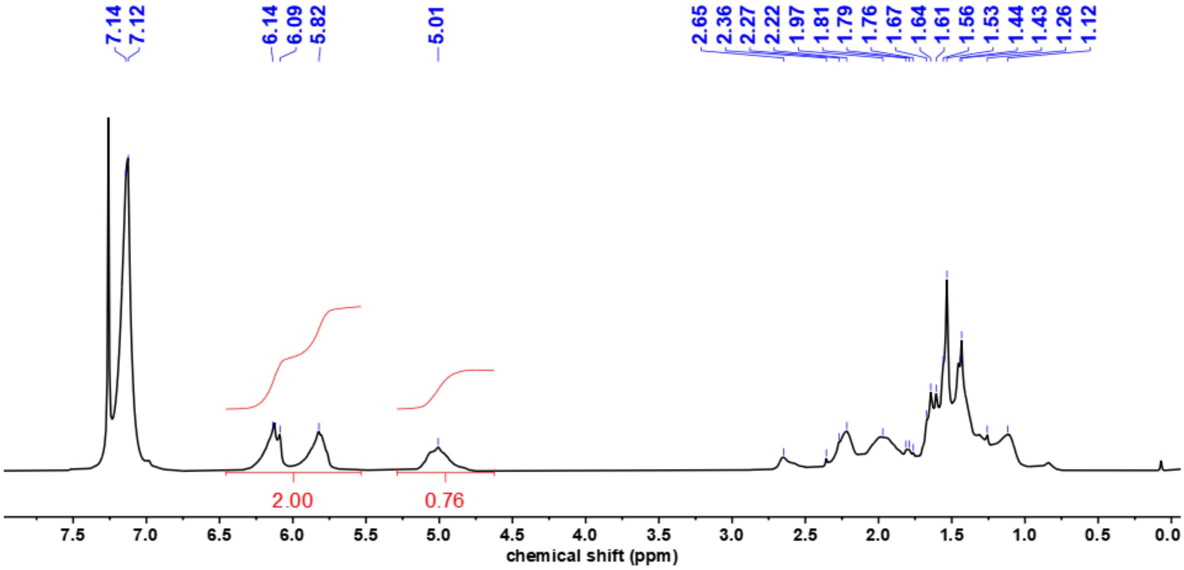

Figure S2.3. ^{1}H NMR (400 MHz, $CDCl_3$, 298 K) of PPBO copolymer from run **1**, Table 2.2.

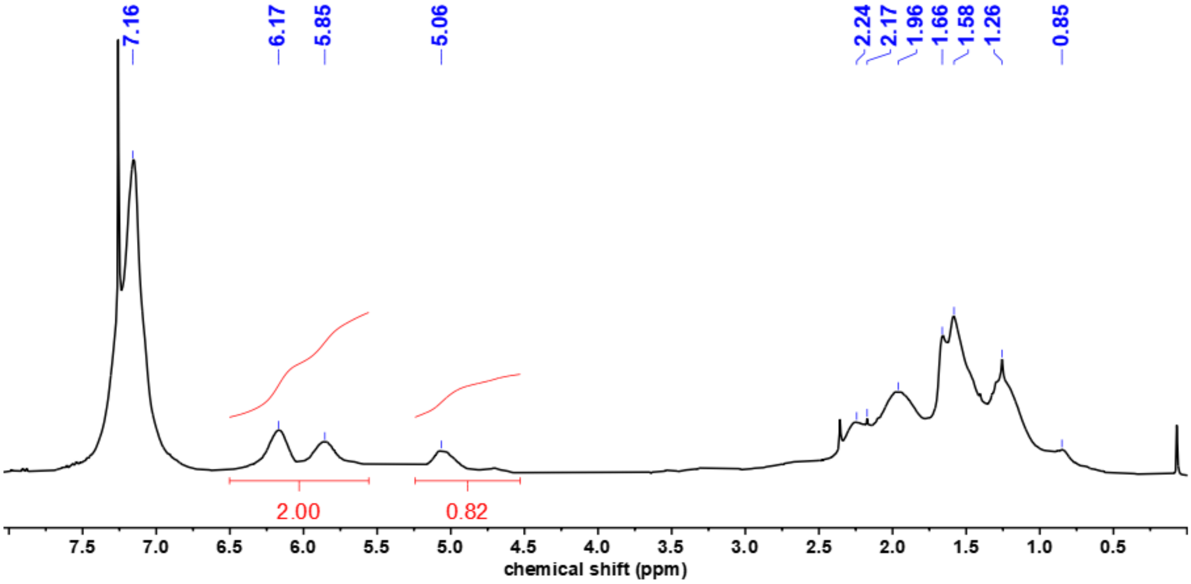

Figure S2.4. ^{1}H NMR (400 MHz, $CDCl_3$, 298 K) of PPBM copolymer from run **6**, Table 2.2.

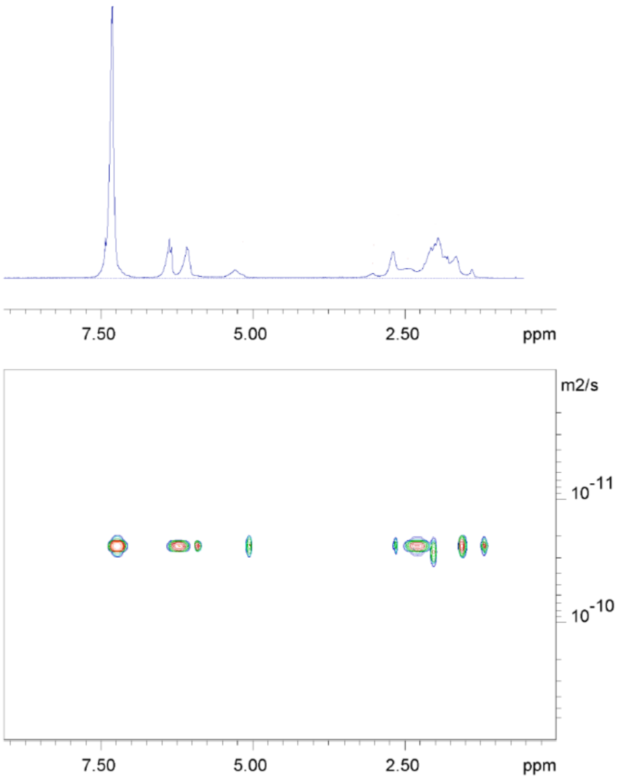

Figure S2.5. 2D DOSY NMR spectra (400 MHz, $CDCl_3$, 298 K) of PPBO copolymer from run **1**, Table 2.2.

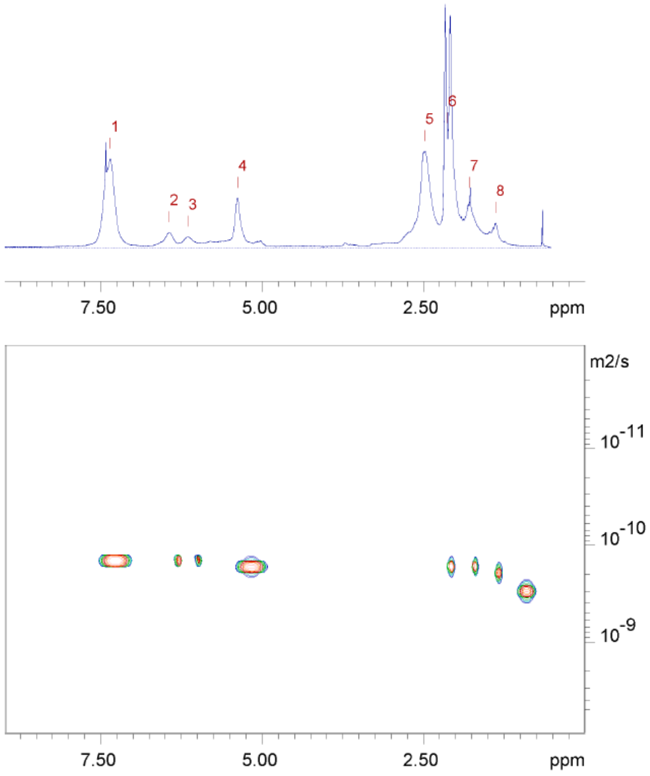

Figure S2.6. 2D DOSY NMR spectra (400 MHz, $CDCl_3$, 298 K) of PPBM copolymer from run **7**, Table 2.2.

2.2 Determination of Copolymer Compositions

- **Determination of 1PB and O contents in PPBO copolymers by ^{1}H NMR ($CDCl_3$, 298 K).**

$$1PB\ (mol\%) = \frac{\frac{A_{1PB}}{2}}{A_{TOT}} x\ 100$$

$$O\ (mol\%) = \frac{A_{Ocim}}{A_{TOT}} x\ 100$$

where: A_{1PB} is the area of the signals at δ = 6.00 ppm and A_{Ocim} is the area of the signal at δ = 5.01 ppm (Figure S2.3).

And:

$$A_{TOT} = \frac{A_{1PB}}{2} + A_{Ocim}$$

- **Determination of 1PB and M contents in PPBM copolymers by ^{1}H NMR ($CDCl_3$, 298 K).**

$$1PB\ (mol\%) = \frac{\frac{A_{1PB}}{2}}{A_{TOT}} x\ 100$$

$$M\ (mol\%) = \frac{A_{Myr}}{A_{TOT}} x\ 100$$

where: A_{1PB} is the area of the signals at δ = 6.00 ppm and A_{Myr} is the area of the signal at δ = 5.06 ppm (Figure S2.4).

And:

$$A_{TOT} = \frac{A_{1PB}}{2} + A_{Myr}$$

2.3 DSC Thermal Analyses

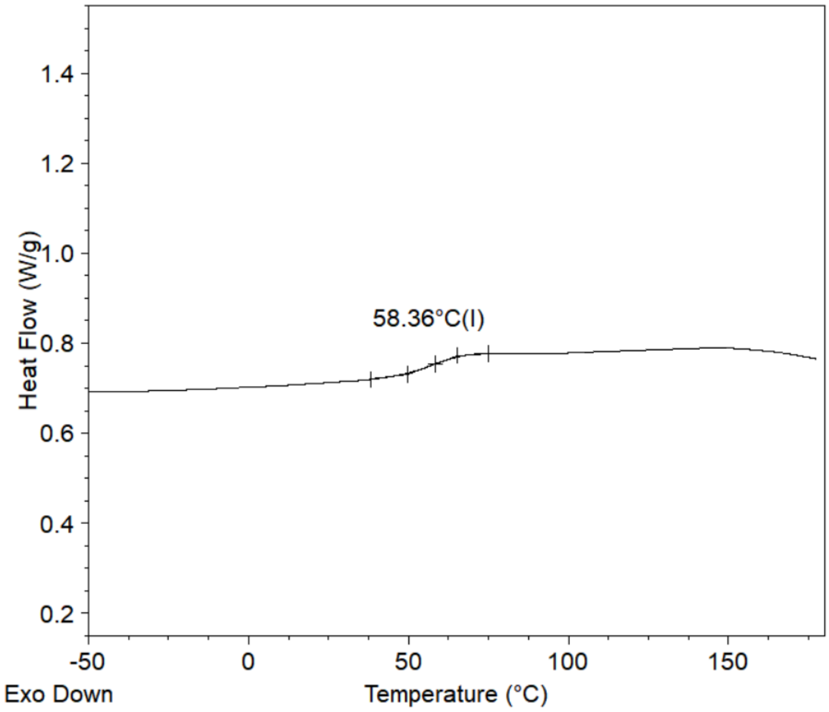

Figure S2.7. DSC curve of PPBM copolymer from run **6**, Table 2.2.

2.4 Thermogravimetric Analyses

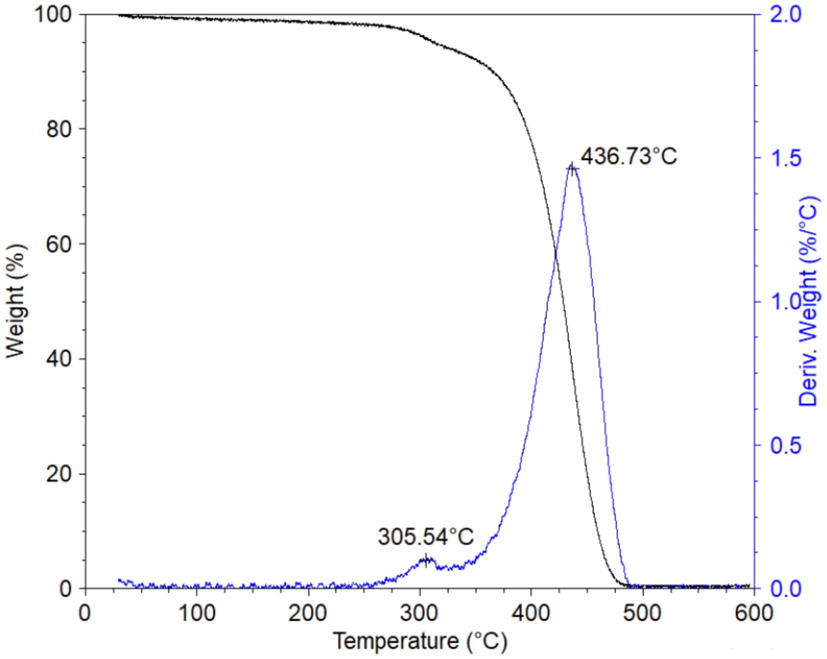

Figure S2.8. TGA traces of 3,4-isotactic poly(1PB) from run **6**, Table 2.1.

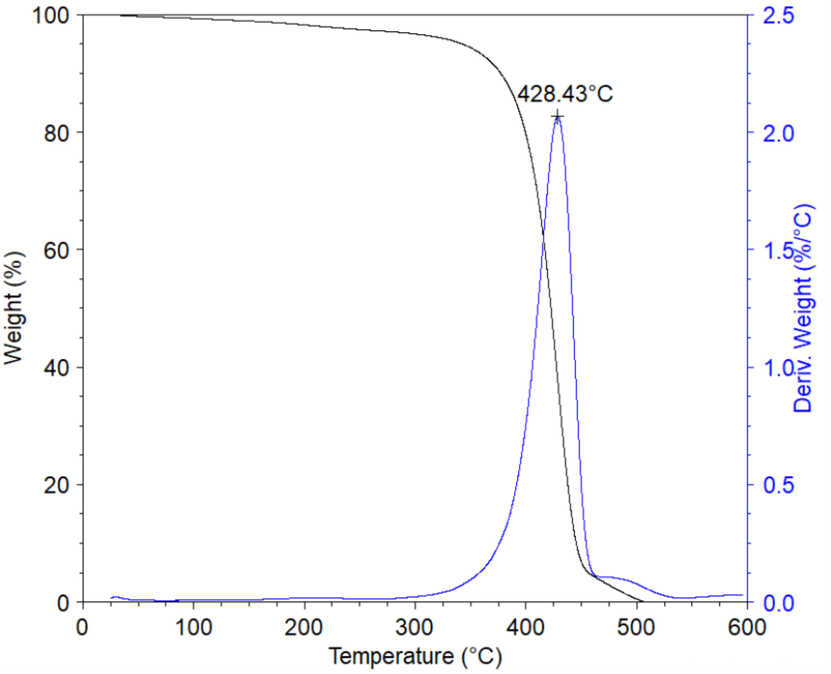

Figure S2.9. TGA traces of 3,4-isotactic poly(1PB) after hydrogenation.

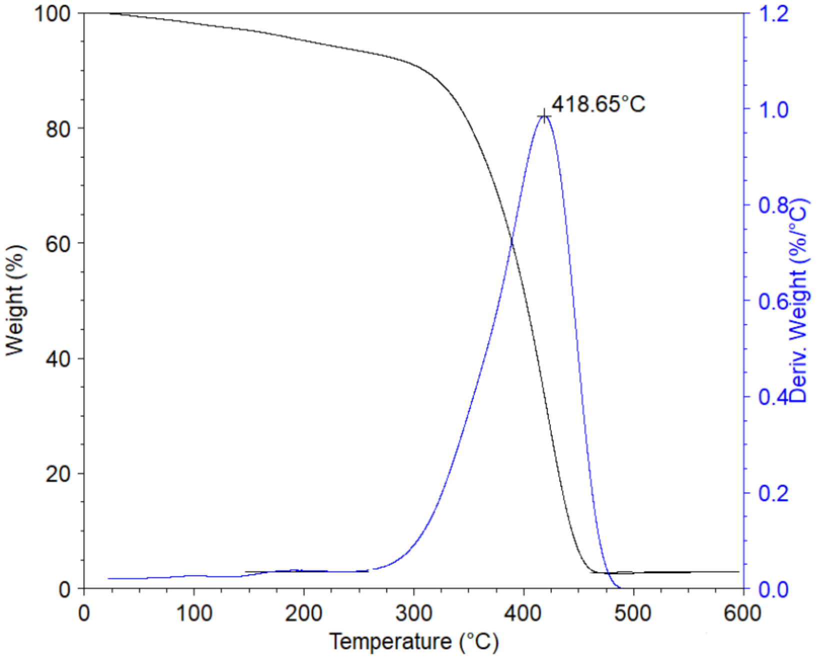

Figure S2.10. TGA traces of the PPBO copolymer from run **1**, Table 2.2.

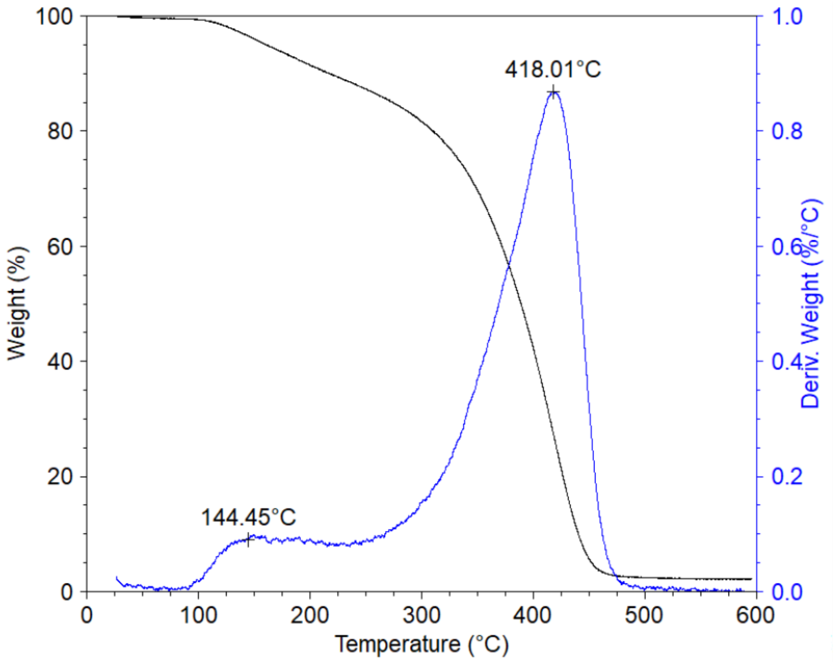

Figure S2.11. TGA traces of the PPBM copolymer from run **7**, Table 2.2.

2.5 GPC Analyses

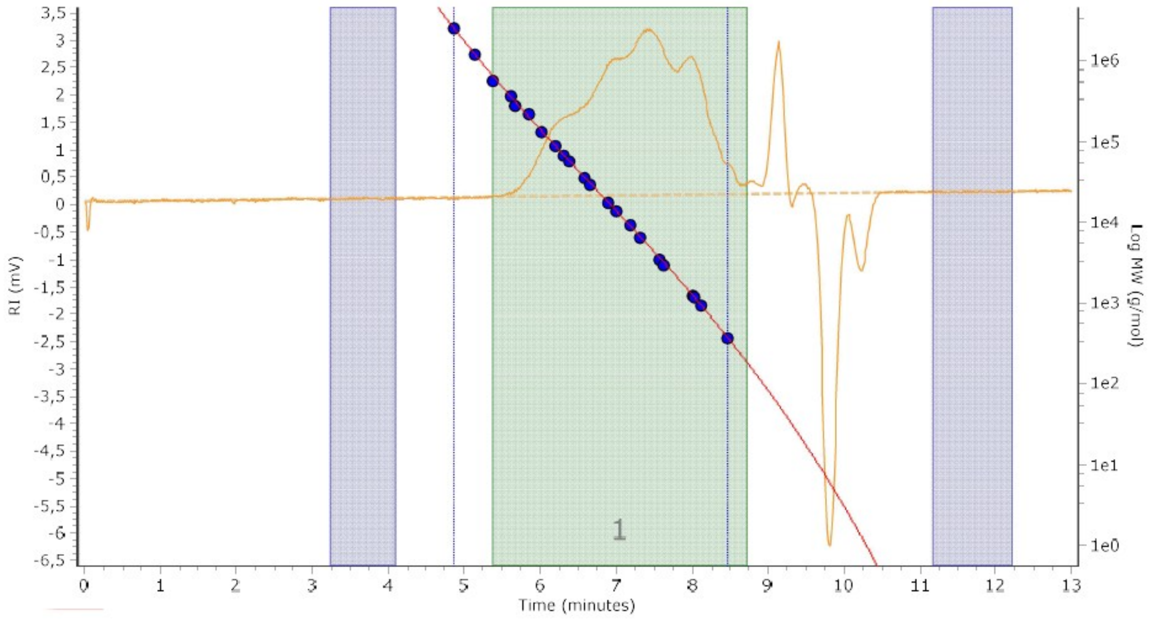

Molecular Weight Averages

Peak	Mp (g/mol)	Mn (g/mol)	Mw (g/mol)	Mz (g/mol)	Mz+1 (g/mol)	Mv (g/mol)	PD
Peak 1	4922	2621	23318	105059	208106	17089	8,897

Figure S2.12. GPC curve of poly(1PB) from run **3**, Table 2.1.

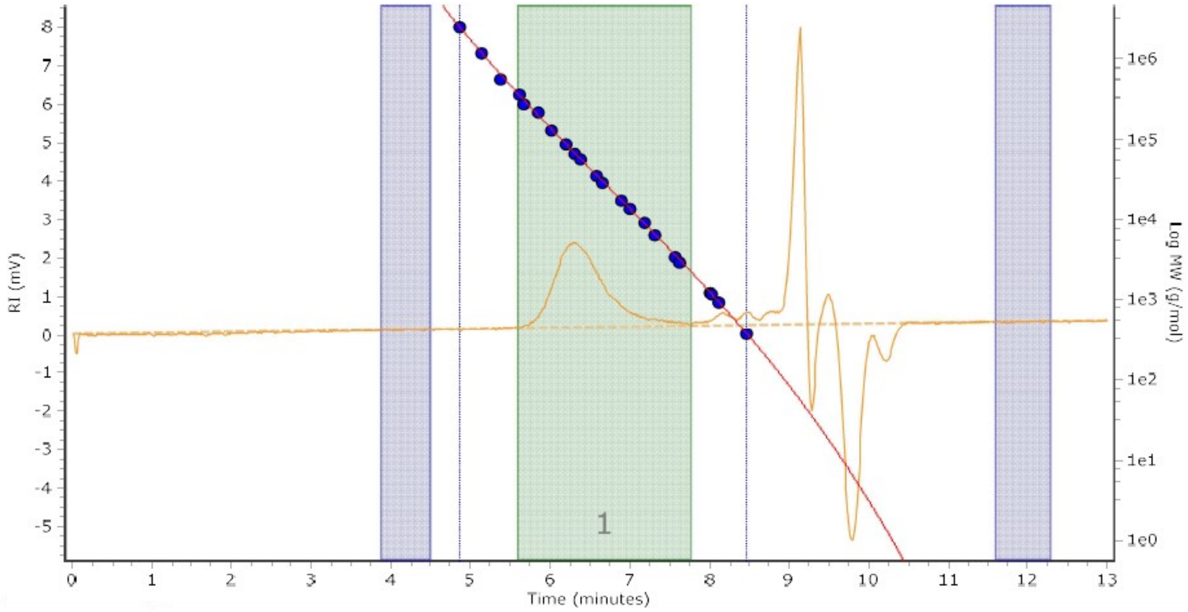

Molecular Weight Averages

Peak	Mp (g/mol)	Mn (g/mol)	Mw (g/mol)	Mz (g/mol)	Mz+1 (g/mol)	Mv (g/mol)	PD
Peak 1	70580	30986	66260	100138	135260	61504	2,138

Figure S2.13. GPC curve of 3,4-isotactic poly(1PB) from run **6**, Table 2.1.

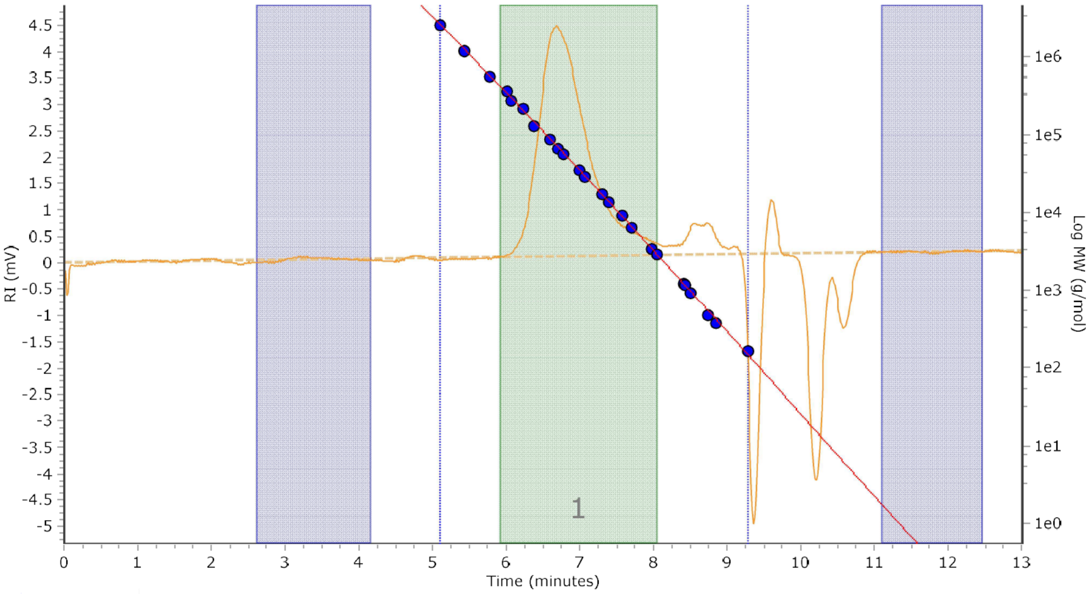

Peak	Mp (g/mol)	Mn (g/mol)	Mw (g/mol)	Mz (g/mol)	Mz+1 (g/mol)	Mv (g/mol)	PD
Peak 1	72573	30843	65556	98427	130318	60815	2.125

Figure S2.14. GPC curve of 3,4-isotactic poly(1PB) after hydrogenation.

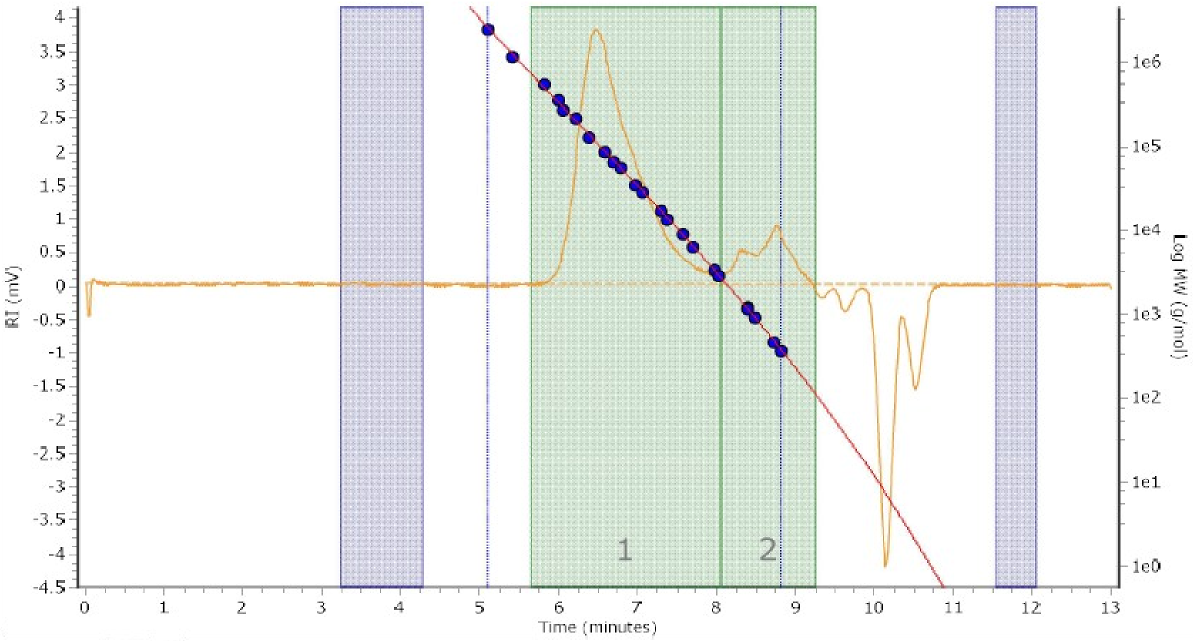

Molecular Weight Averages

Peak	Mp (g/mol)	Mn (g/mol)	Mw (g/mol)	Mz (g/mol)	Mz+1 (g/mol)	Mv (g/mol)
Peak 1	107959	40407	94895	147069	197381	87342
Peak 2	465	501	788	1183	1546	736

PD
2.348
1.573

Figure S2.15. GPC curve of PPBO copolymer from run **1**, Table 2.2.

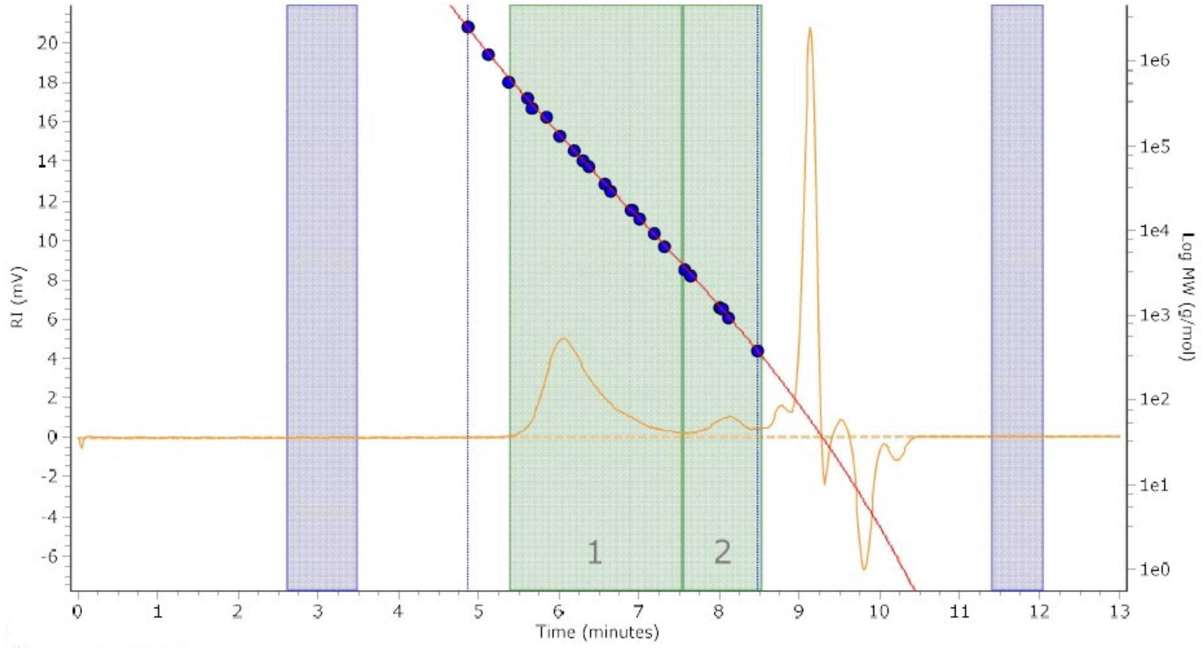

Molecular Weight Averages

Peak	Mp (g/mol)	Mn (g/mol)	Mw (g/mol)	Mz (g/mol)	Mz+1 (g/mol)	Mv (g/mol)	PD
Peak 1	117229	45035	104576	164995	225002	96076	2.322
Peak 2	926	837	1181	1642	2134	1121	1.411

Figure S2.16. GPC curve of PPBM copolymer from run **4**, Table 2.2.

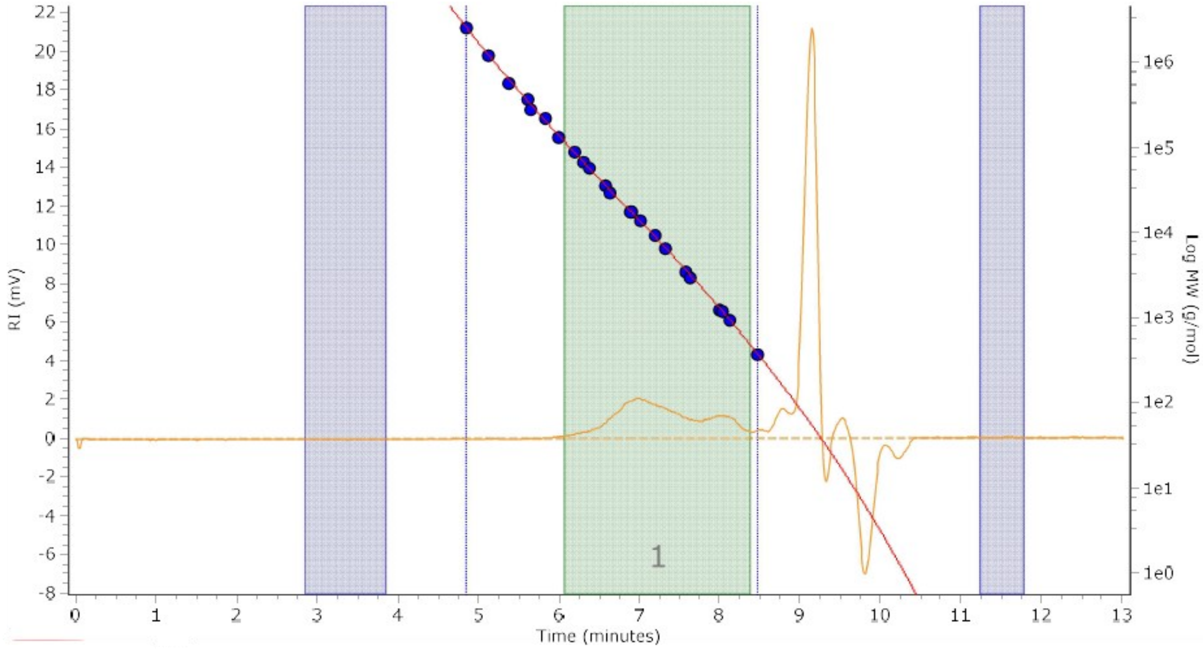

Molecular Weight Averages

Peak	Mp (g/mol)	Mn (g/mol)	Mw (g/mol)	Mz (g/mol)	Mz+1 (g/mol)	Mv (g/mol)	PD
Peak 1	14047	3273	13422	32654	53913	11320	4.101

Figure S2.17. GPC curve of PPBM copolymer from run **6**, Table 2.2.

2.6 Mechanical Properties

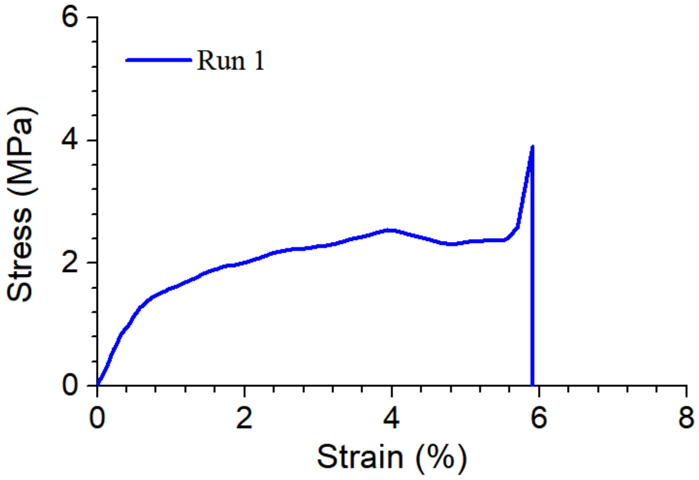

Figure S2.18. Stress-strain curves measured at room temperature using the deformation rate $v/l_0 = 0.1$ mm min^{-1} mm^{-1}, PPBO copolymer from run **1**, Table 2.2

Appendix 3

3.1 NMR Spectra

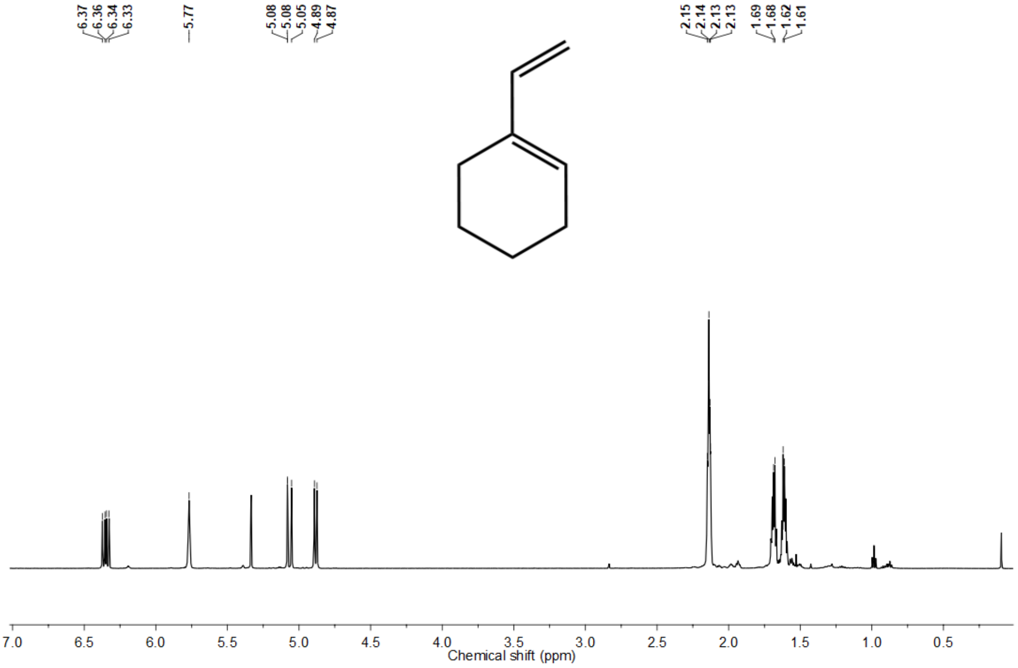

Figure S3.1. ^{1}H NMR spectrum of 1-vinylcyclohexene (600 MHz, CD_2Cl_2, 298 K).

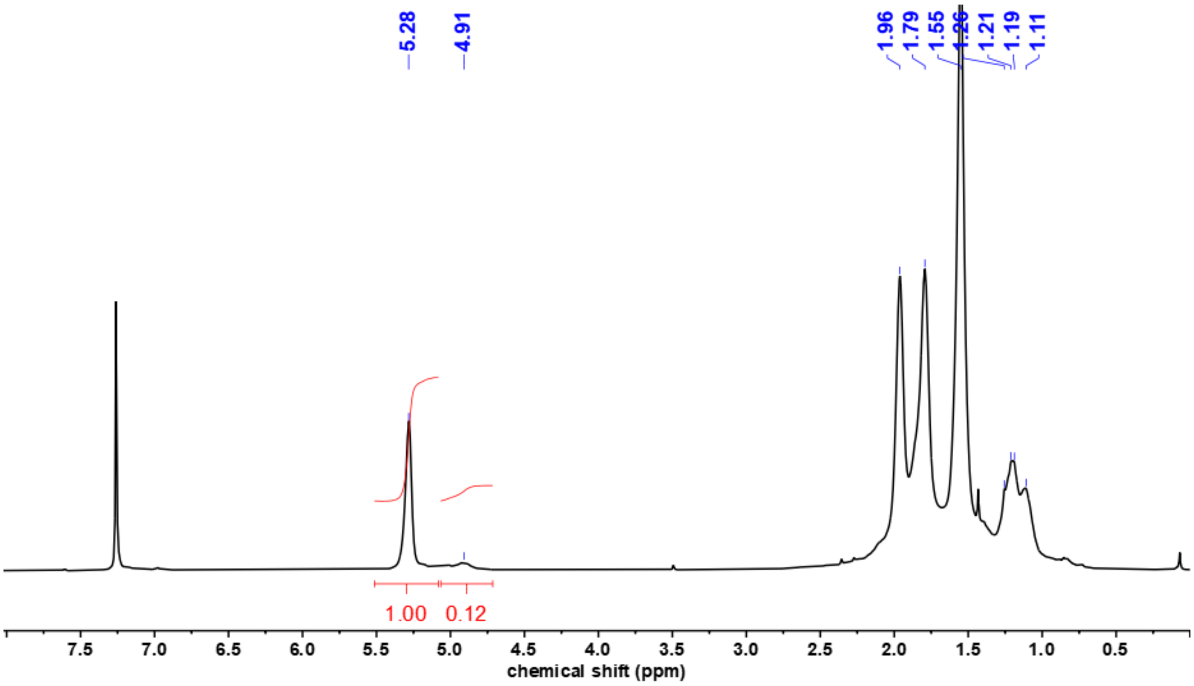

Figure S3.2. ^{1}H NMR (400 MHz, $CDCl_3$, 298 K) of PVCH obtained with catalyst **1** (run **2**, Table 3.1). The peak at 5.29 ppm is related to the olefin proton of the 3.4 unit; the peak at 4.91 is related to the olefin proton of the 1,4-insertion.

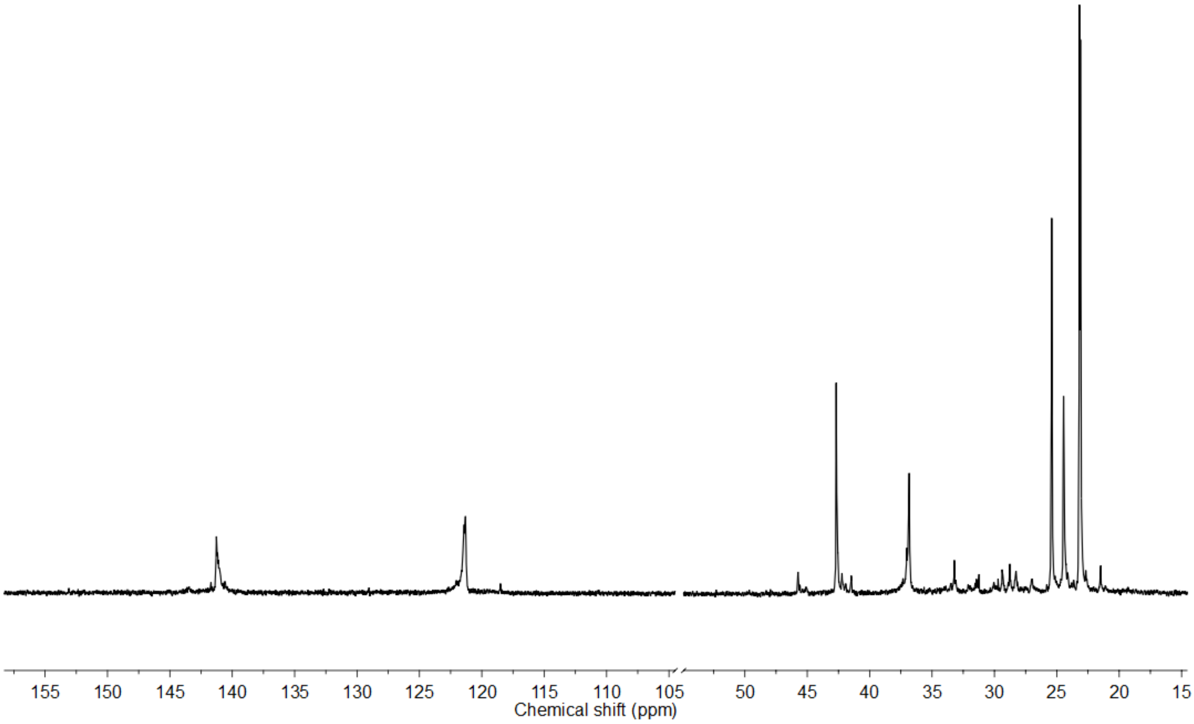

Figure S3.3.^{13}C NMR (100 MHz, $CDCl_3$, 298 K) of PVCH (run **2**, Table 3.1) obtained with catalyst **1.**

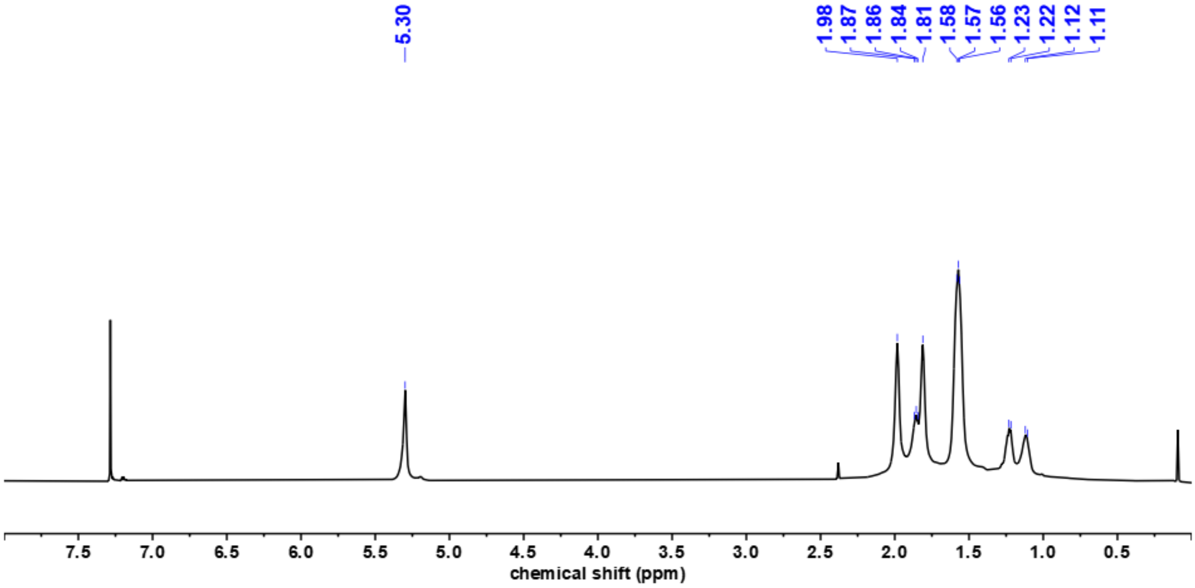

Figure S3.4. ^{1}H NMR (600 MHz, $CDCl_3$, 298 K) of PVCH obtained with catalyst **2** (run **3**, Table 3.1).

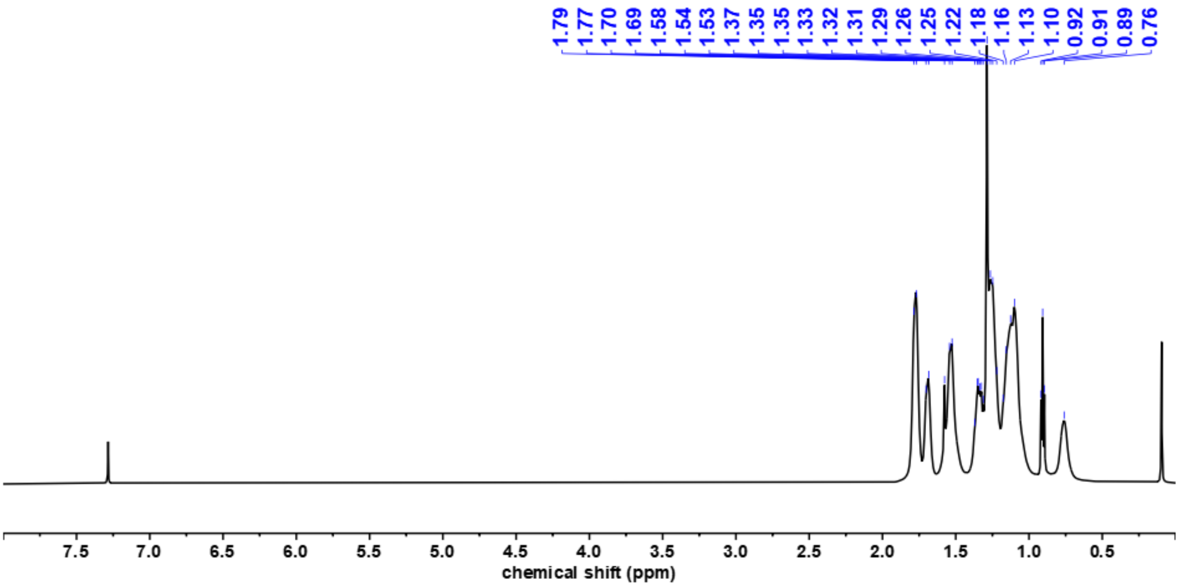

Figure S3.5. ^{1}H NMR (600 MHz, $CDCl_3$, 298 K) of PVCH after hydrogenation.

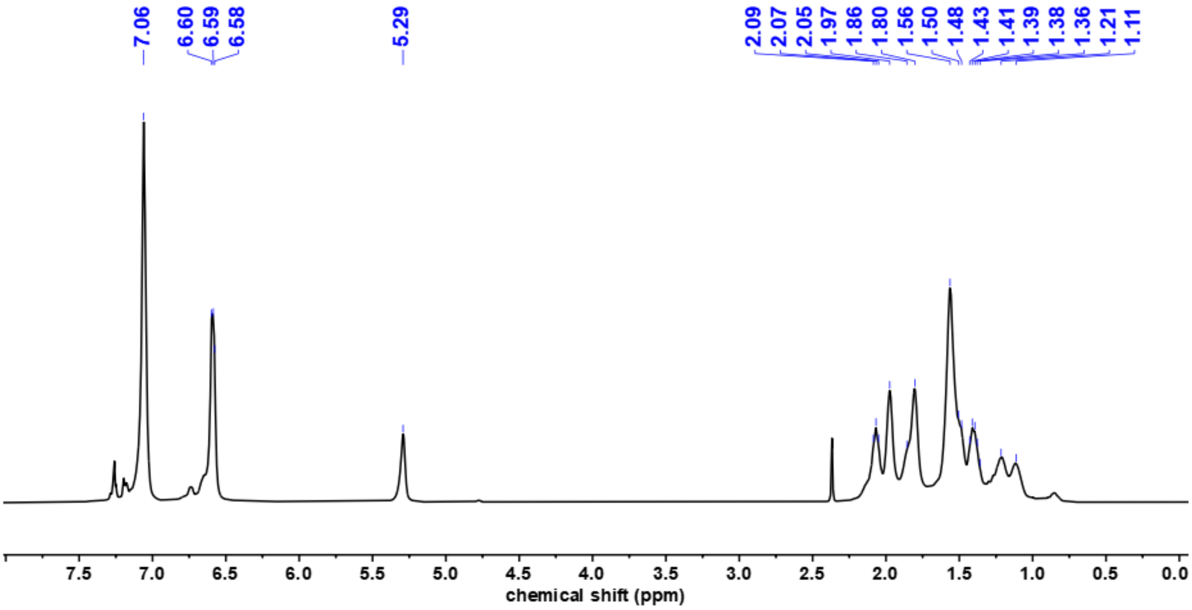

Figure S3.6. ^{1}H NMR (400 MHz, $CDCl_3$, 298 K) of PVCHS copolymer obtained by sequential monomer addition (run **2**, Table 3.2).

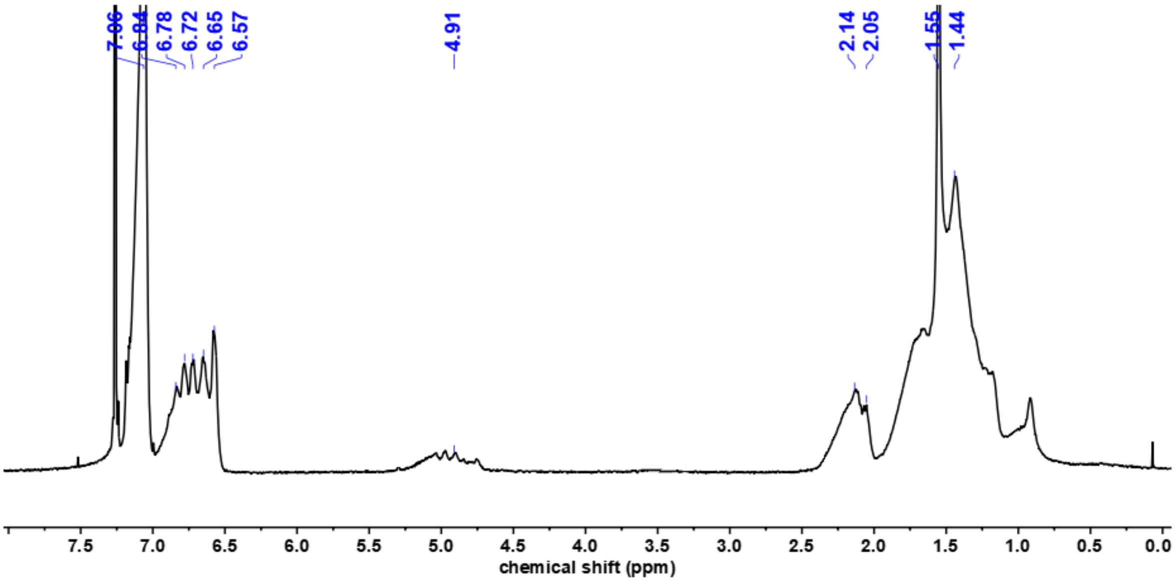

Figure S3.7. ^{1}H NMR (400 MHz, $CDCl_3$, 298 K) of PVCHS copolymer obtained by one-pot one-step reaction (run **3**, Table 3.2).

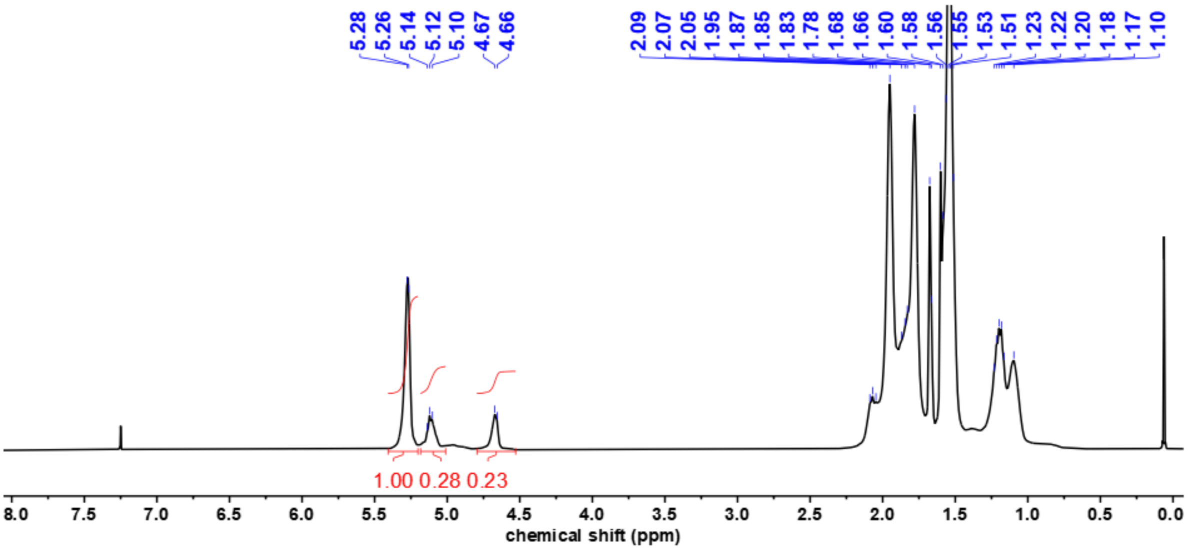

Figure S3.8. ^{1}H NMR (400 MHz, $CDCl_3$, 298 K) of PVCHM copolymer obtained by one-pot one-step reaction (run **4**, Table 3.2).

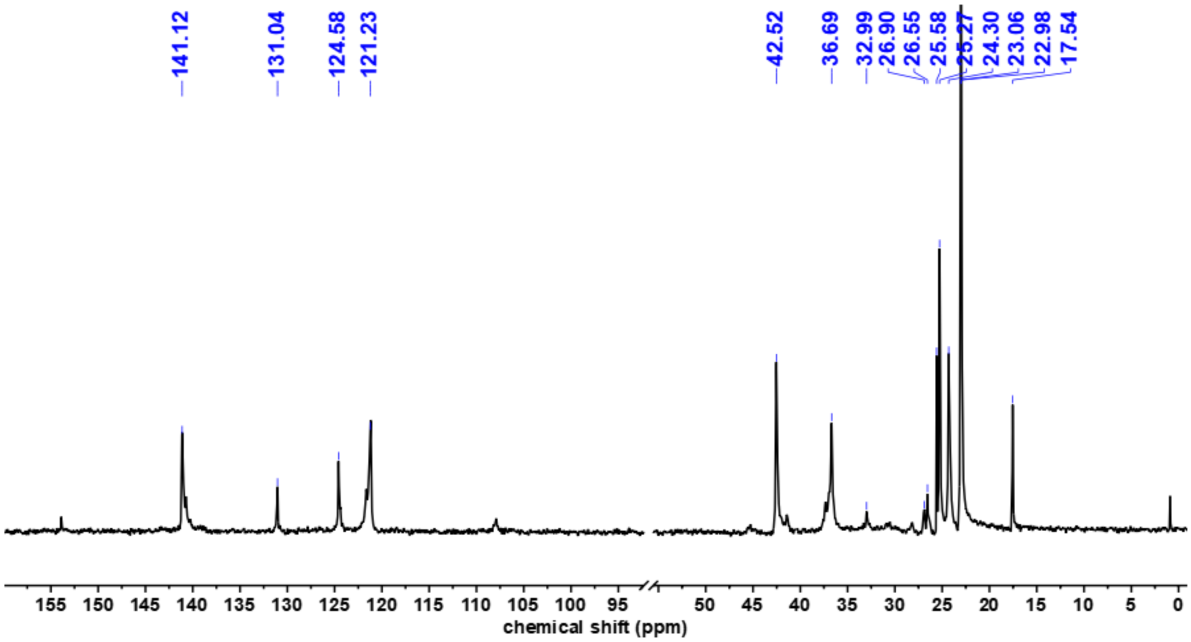

Figure S3.9. ^{13}C NMR (100 MHz, $CDCl_3$, 298 K) of PVCHM copolymer obtained by one-pot one-step reaction (run **4**, Table 3.2).

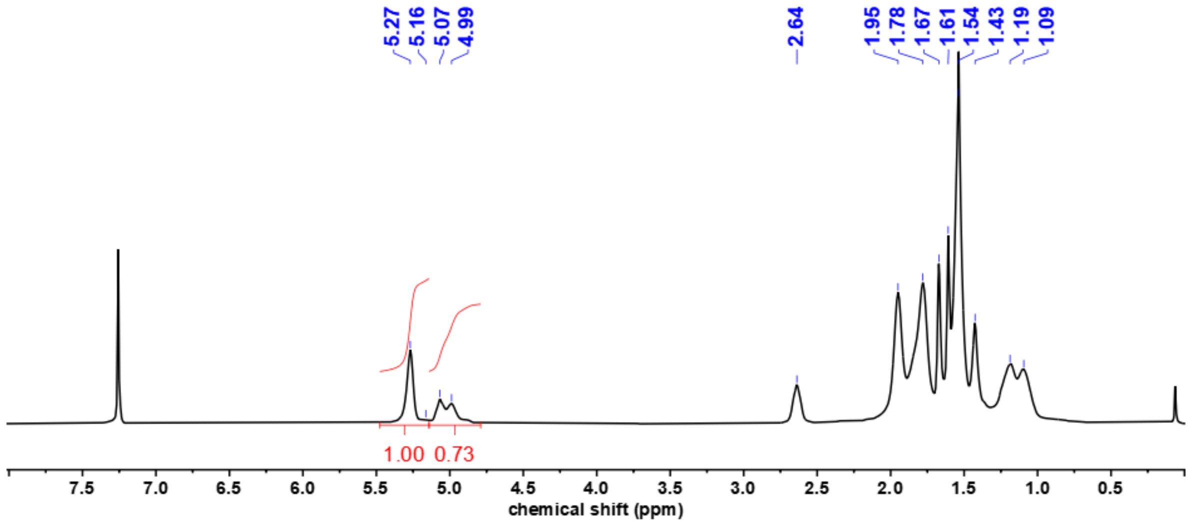

Figure S3.10. ^{1}H NMR (300 MHz, $CDCl_3$, 298 K) of PVCHO copolymer obtained by one-pot one-step reaction (run **5**, Table 3.2).

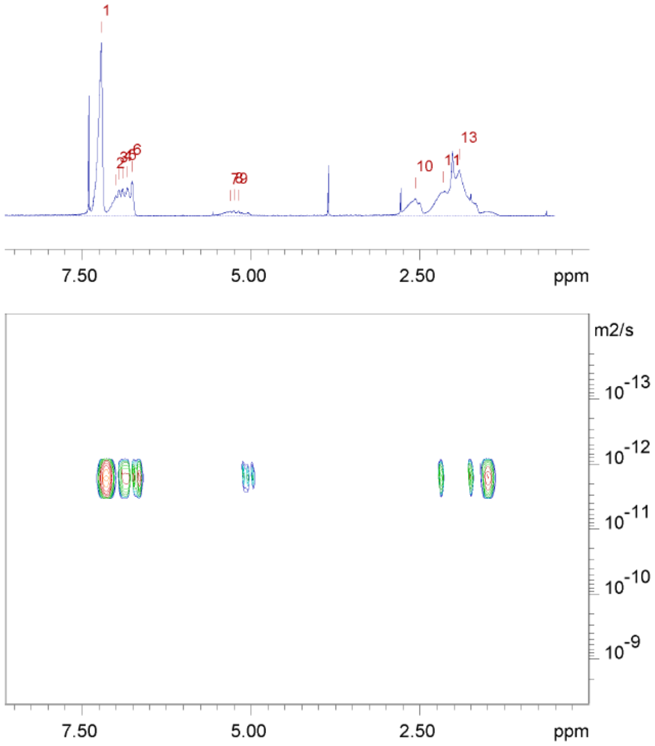

Figure S3.11. 2D DOSY NMR spectra (400 MHz, $CDCl_3$, 298 K) of PVCHS copolymer from run **3**, Table 3.2.

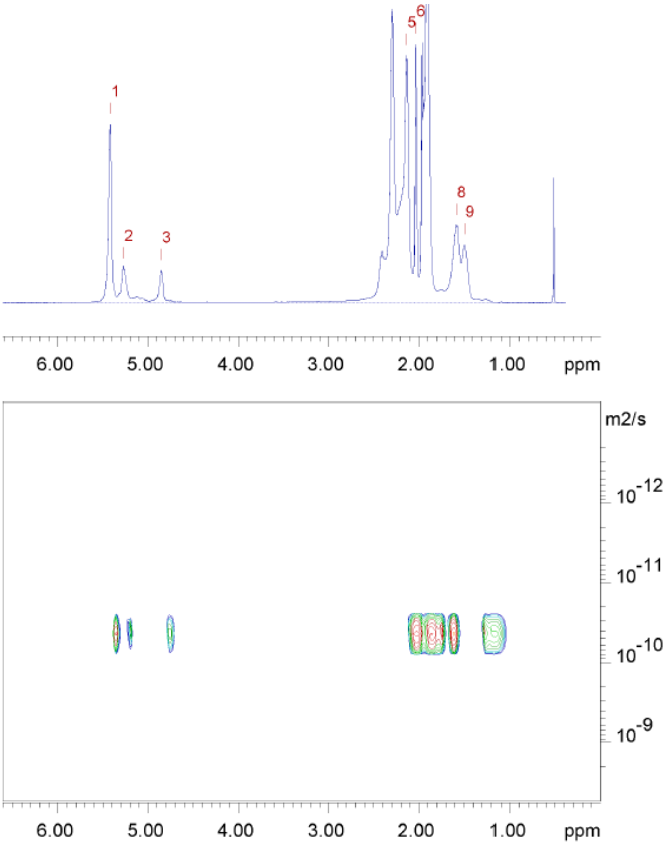

Figure S3.12. 2D DOSY NMR spectra (400 MHz, $CDCl_3$, 298 K) of PVCHM copolymer from run **4**, Table 3.2.

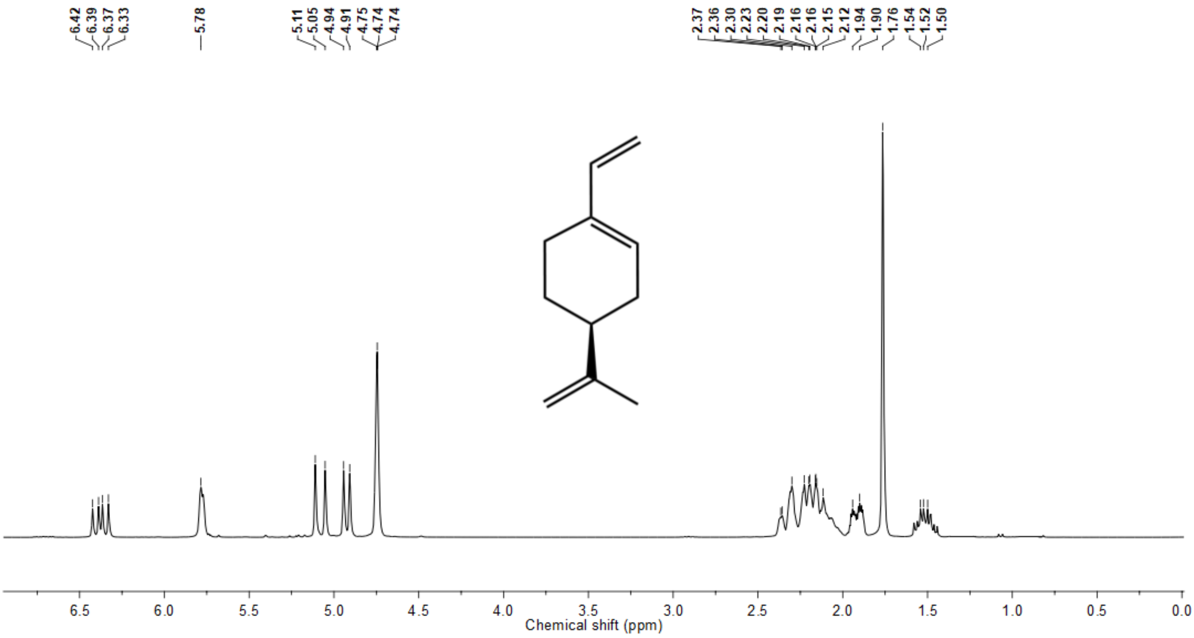

Figure S3.13. ^{1}H NMR spectrum of *S*-4-isopropenyl-1-vinyl-1-cyclohexene (300 MHz, $CDCl_3$, 298 K).

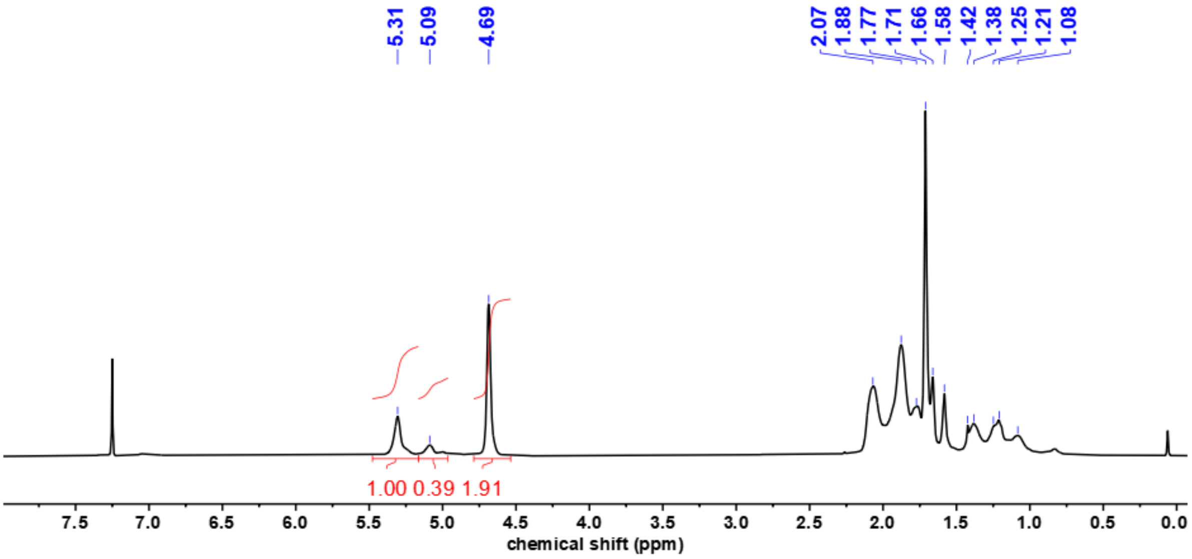

Figure S3.14. ^{1}H NMR (300 MHz, $CDCl_3$, 298 K) of PIVCM copolymer from run **1**, Table 3.5.

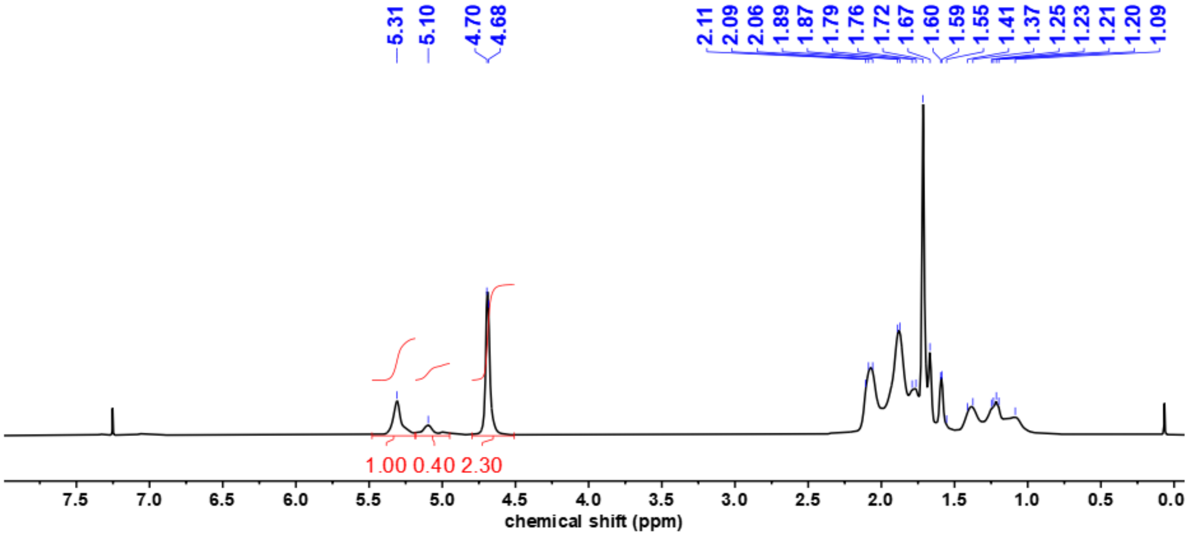

Figure S3.15. ^{1}H NMR (300 MHz, $CDCl_3$, 298 K) of PIVCM copolymer from run **3**, Table 3.5.

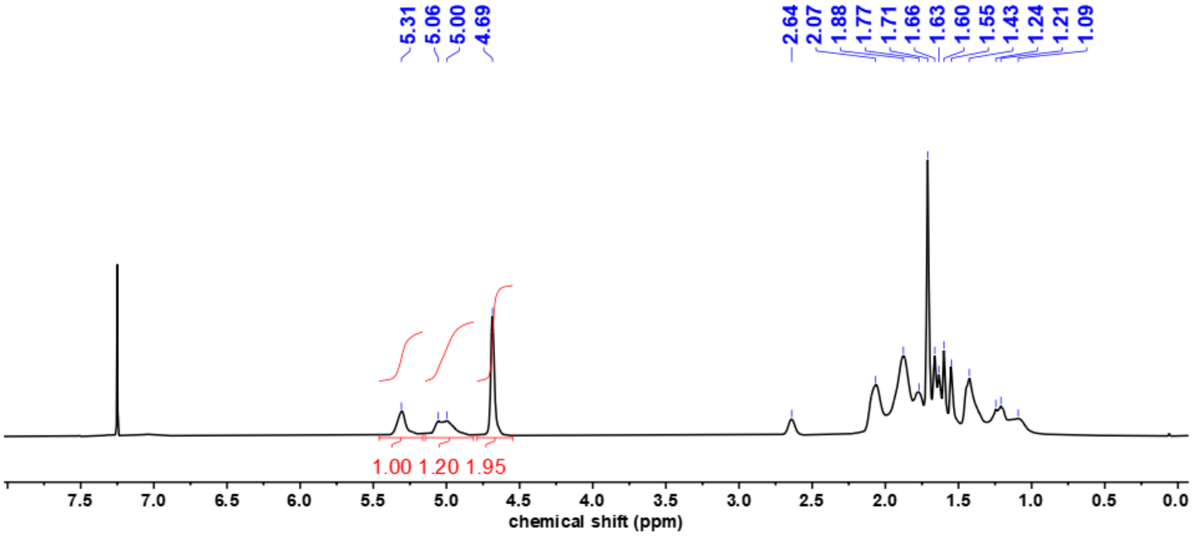

Figure S3.16. ^{1}H NMR (300 MHz, $CDCl_3$, 298 K) of PIVCO copolymer from run **5**, Table 3.5.

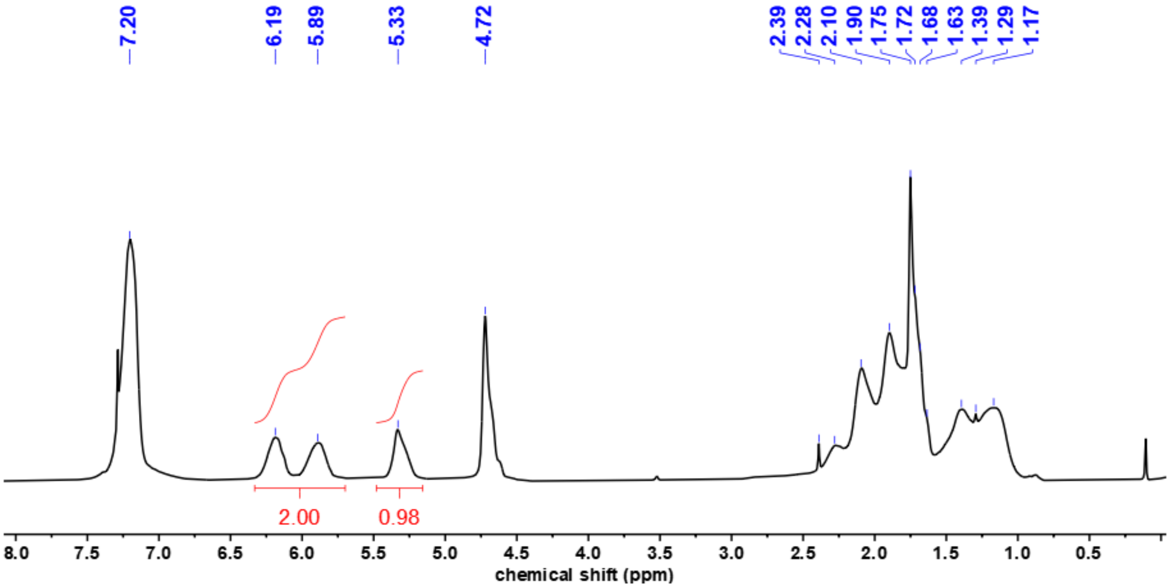

Figure S3.17. ^{1}H NMR (400 MHz, $CDCl_3$, 298 K) of PIVCPB copolymer from run **9**, Table 3.5.

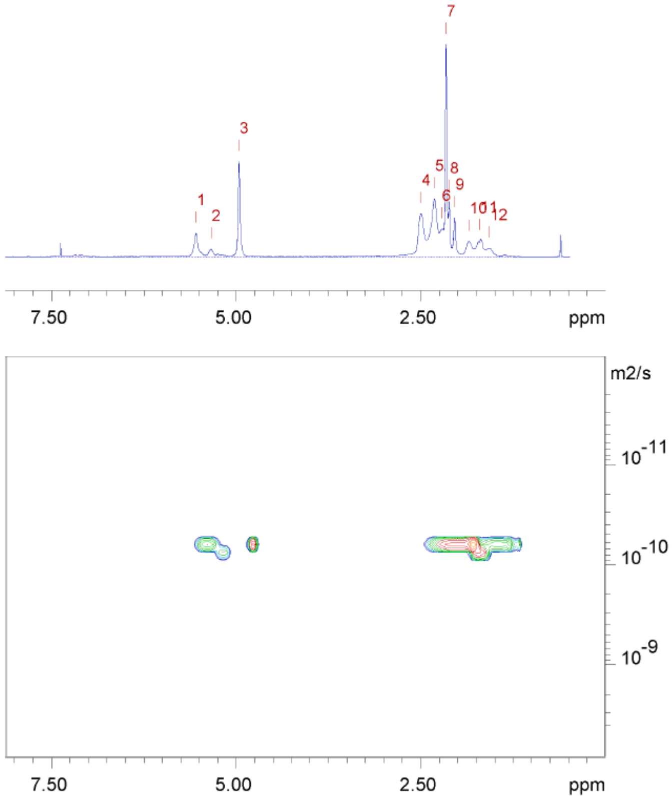

Figure S3.18. 2D DOSY NMR spectra (400 MHz, $CDCl_3$, 298 K) of PIVCM copolymer from run **3**, Table 3.5.

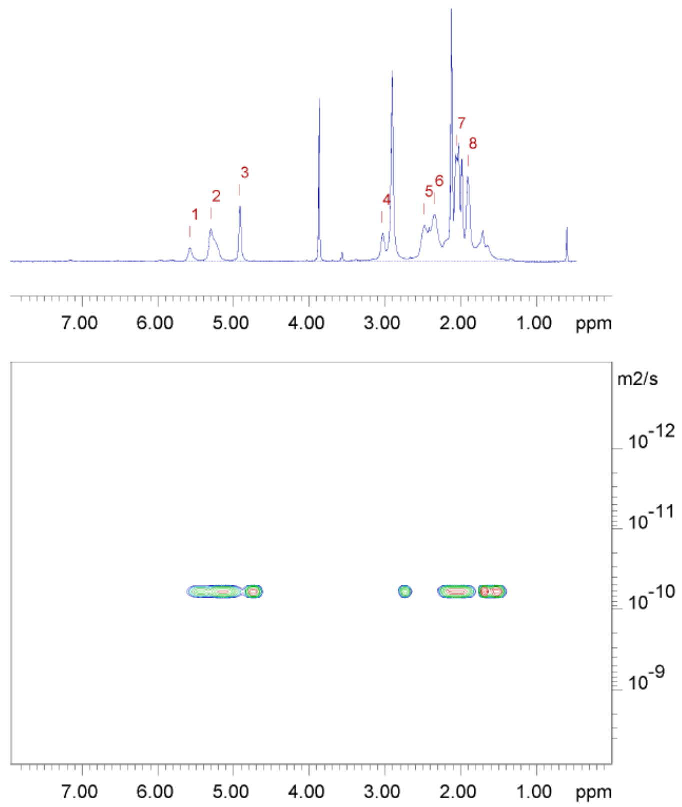

Figure S3.19. 2D DOSY NMR spectra (400 MHz, $CDCl_3$, 298 K) of PIVCO copolymer from run **6**, Table 3.5.

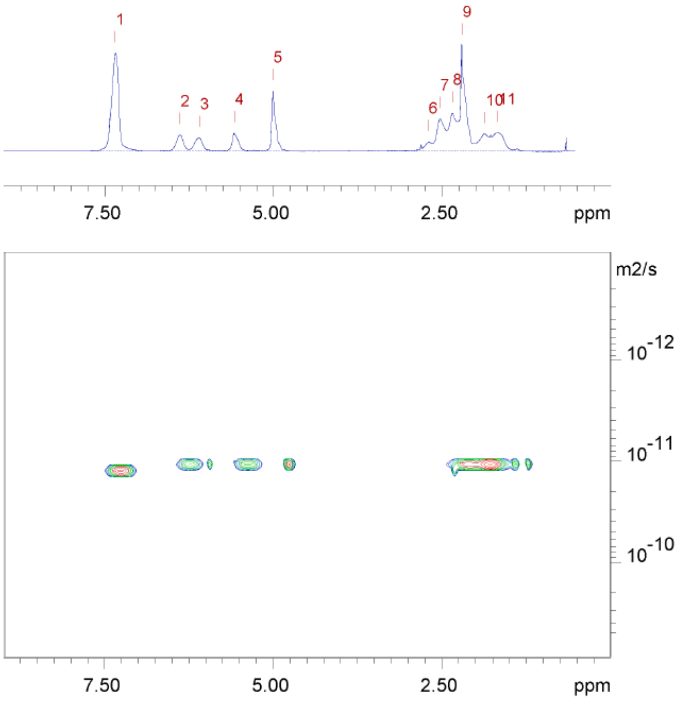

Figure S3.20. 2D DOSY NMR spectra (400 MHz, $CDCl_3$, 298 K) of PIVCPB copolymer from run **9**, Table 3.5.

3.2 Determination of Copolymer Compositions

- **Determination of VCH and S contents in PVCHS copolymers by ^{1}H NMR ($CDCl_3$, 298 K).**

$$VCH\ (mol\%) = \frac{A_{VCH}}{A_{TOT}} x\ 100$$

$$S\ (mol\%) = \frac{\frac{A_S}{5}}{A_{TOT}} x\ 100$$

where: A_{VCH} is the area of the signals at δ = 5.29 ppm and A_S is the area of the signal at δ = 6.50-7.25 ppm (Figure S3.6).

And:

$$A_{TOT} = A_{VCH} + \frac{A_S}{5}$$

- **Determination of VCH and M contents in PVCHM copolymers by ^{1}H NMR ($CDCl_3$, 298 K).**

$$VCH\ (mol\%) = \frac{A_{VCH}}{A_{TOT}} x\ 100$$

$$M\ (mol\%) = \frac{\frac{A_{Myr}}{2}}{A_{TOT}} x\ 100$$

where: A_{VCH} is the area of the signals at δ = 5.28 ppm and A_{Myr} is the area of the signal at δ = 4.66-5.12 ppm (Figure S3.8).

And:

$$A_{TOT} = A_{VCH} + \frac{A_{Myr}}{2}$$

- **Determination of VCH and O contents in PVCHO copolymers by ^{1}H NMR ($CDCl_3$, 298 K).**

$$VCH\ (mol\%) = \frac{A_{VCH}}{A_{TOT}} x\ 100$$

$$O\ (mol\%) = \frac{\frac{A_{Ocim}}{2}}{A_{TOT}} x\ 100$$

where: A_{IPB} is the area of the signals at δ = 5.27 ppm and A_{Ocim} is the area of the signal at δ = 4.99-5.16 ppm (Figure S3.10).

And:

$$A_{TOT} = A_{VCH} + \frac{A_{Ocim}}{2}$$

- **Determination of IVC and M contents in PIVCM copolymers by ^{1}H NMR ($CDCl_3$, 298 K).**

$$IVC\ (mol\%) = \frac{A_{IVC}}{A_{TOT}} x\ 100$$

$$M\ (mol\%) = \frac{A_{Myr}}{A_{TOT}} x\ 100$$

where: A_{IVC} is the area of the signals at δ = 5.31 ppm and A_{Myr} is the area of the signal at δ = 5.10 ppm (Figure S3.15).

And:

$$A_{TOT} = A_{IVC} + A_{Myr}$$

- **Determination of IVC and O contents in PIVCO copolymers by ^{1}H NMR ($CDCl_3$, 298 K).**

$$IVC\ (mol\%) = \frac{A_{IVC}}{A_{TOT}} x\ 100$$

$$O\ (mol\%) = \frac{\frac{A_{Ocim}}{2}}{A_{TOT}} x\ 100$$

where: A_{IVC} is the area of the signals at δ = 5.31 ppm and A_{Ocim} is the area of the signal at δ = 5.00-5.06 ppm (Figure S3.16).

And:

$$A_{TOT} = A_{IVC} + \frac{A_{Ocim}}{2}$$

- **Determination of IVC and 1PB contents in PIVCPB copolymers by ^{1}H NMR ($CDCl_3$, 298 K).**

$$IVC\ (mol\%) = \frac{A_{IVC}}{A_{TOT}} x\ 100$$

$$1PB\ (mol\%) = \frac{\frac{A_{1PB}}{2}}{A_{TOT}} x\ 100$$

where: A_{IVC} is the area of the signals at δ = 5.33 ppm and A_{1PB} is the area of the signal at δ = 5.75-6.50 ppm (Figure S3.17).

And:

$$A_{TOT} = A_{IVC} + \frac{A_{1PB}}{2}$$

3.3 DSC Thermal Analyses

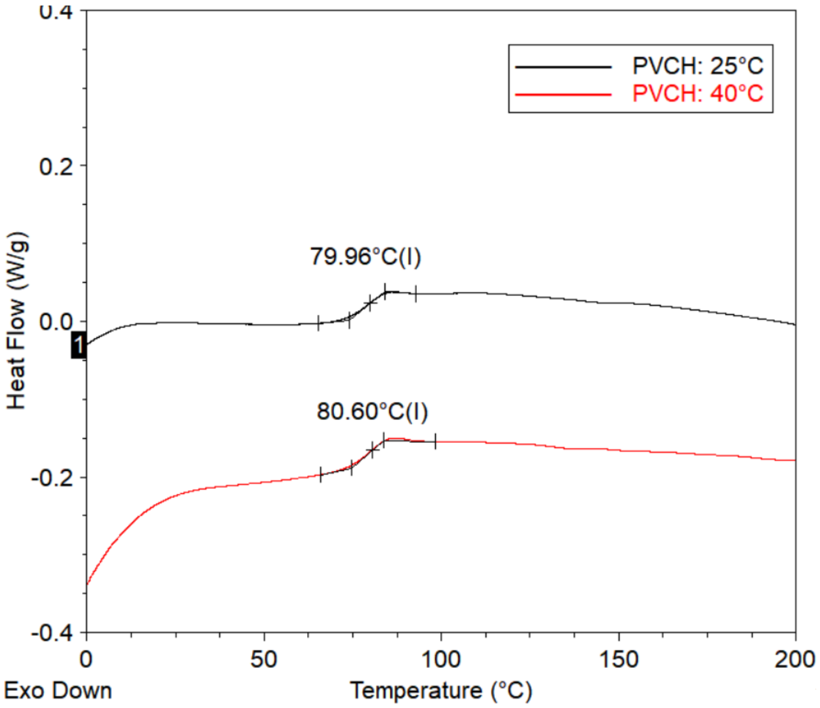

Figure S3.21. DSC thermograms of PVCH obtained with catalyst **1** at different temperatures (runs **1** and **2**, Table 3.1).

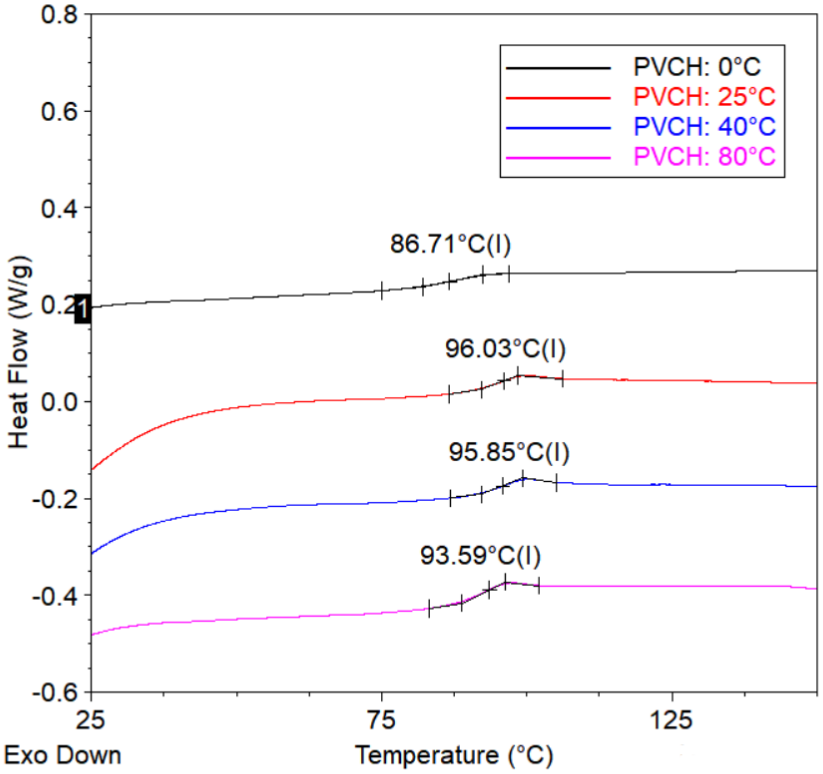

Figure S3.22. DSC thermograms of PVCH obtained with catalyst **2** at different temperatures (runs **3, 4, 5** and **6**, Table 3.1).

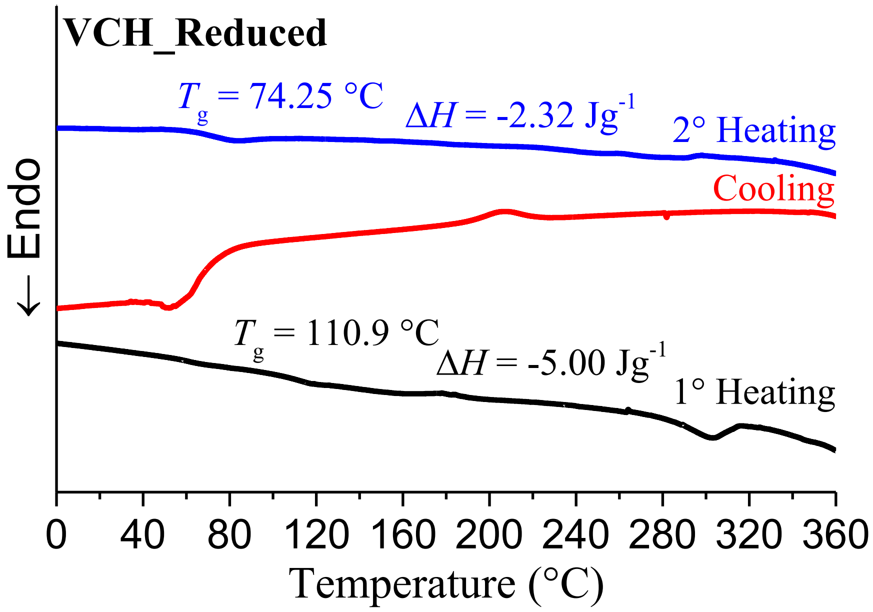

Figure S3.23. DSC thermograms of the hydrogenated PVCH.

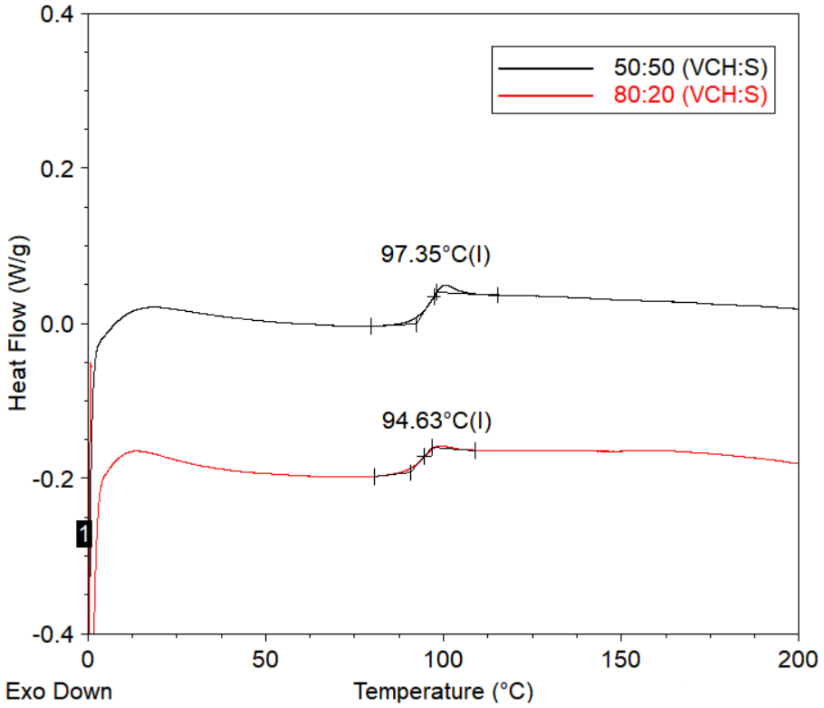

Figure S3.24. DSC thermograms of PVCHS copolymer obtained by sequential monomer addition (runs **1** and **2**, Table 3.2).

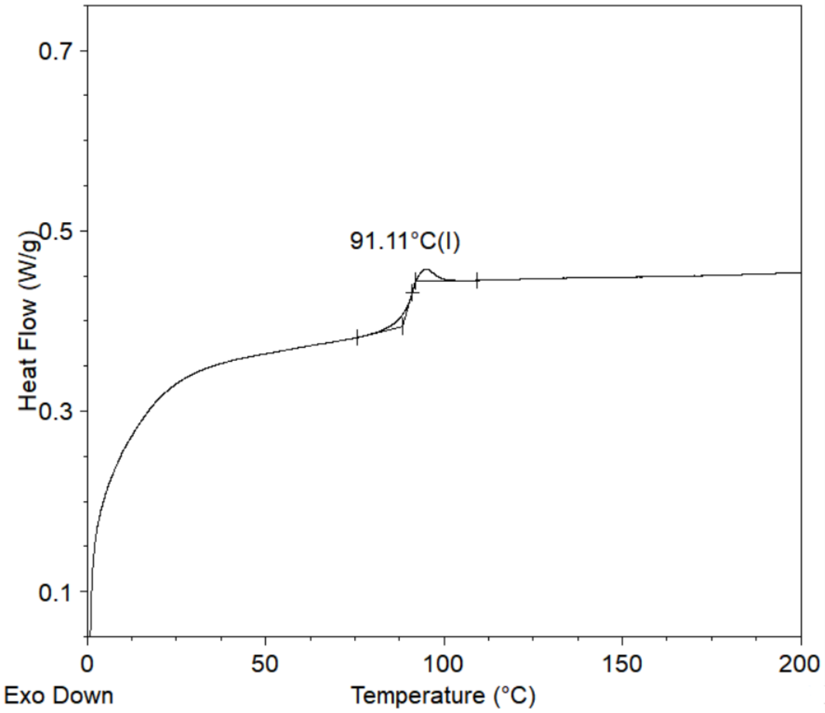

Figure S3.25. DSC thermogram of PVCHS copolymer obtained by one-pot one-step reaction (run **3**, Table 3.2).

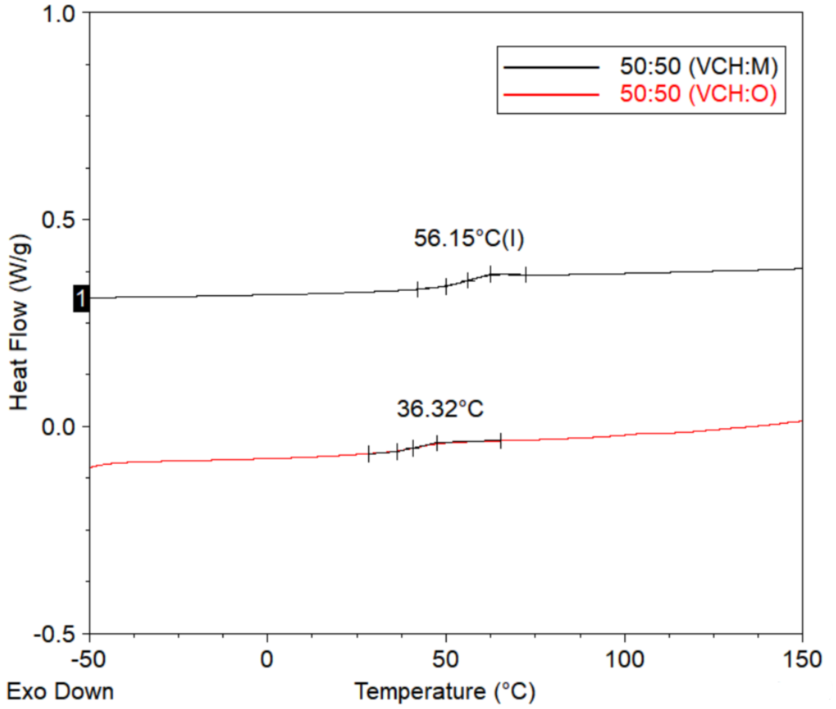

Figure S3.26. DSC thermogram of PVCHM and PVCHO copolymer obtained by one-pot one-step reaction (runs **4** and **5**, Table 3.2).

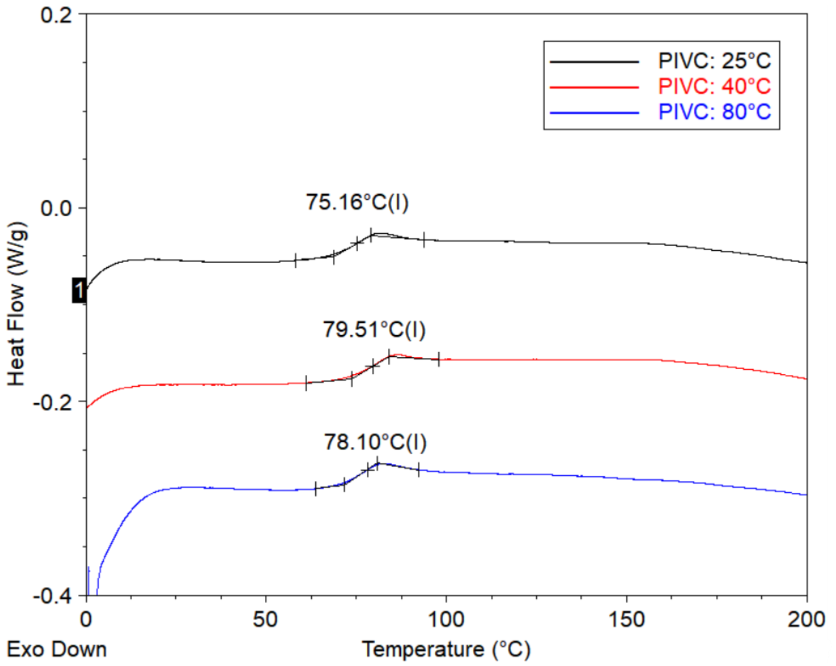

Figure S3.27. DSC thermograms of PIVC obtained with catalyst **2** at different temperatures (runs **1, 2** and **3**, Table 3.3).

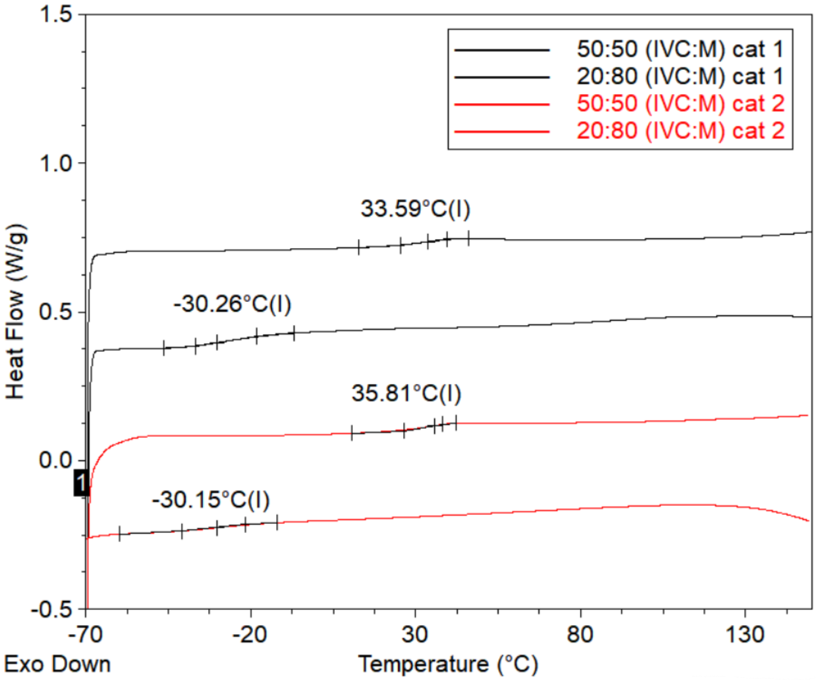

Figure S3.28. DSC thermograms of IVCM copolymers obtained with catalyst **1** (black curves) and catalyst **2** (red curves), runs **1-4**, Table 3.5.

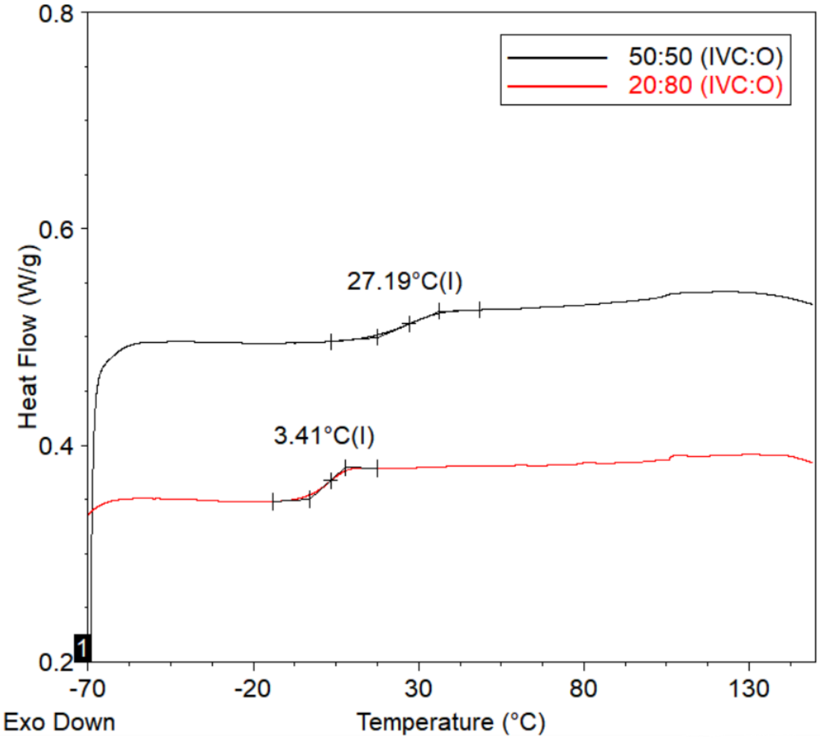

Figure S3.29. DSC thermograms of IVCO copolymers from runs **5** and **6**, Table 3.5.

3.4 Thermogravimetric Analyses

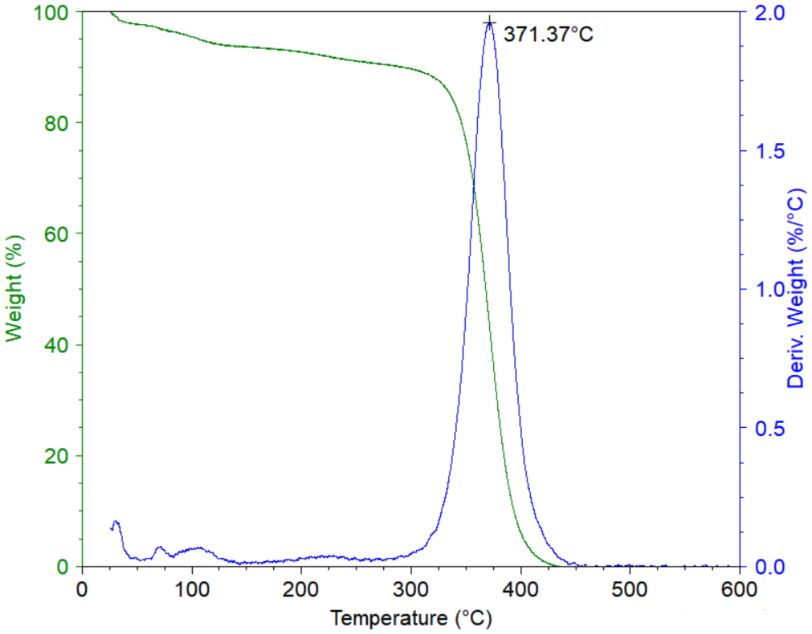

Figure S3.30. TGA traces of the PVCH from run **5**, Table 3.1.

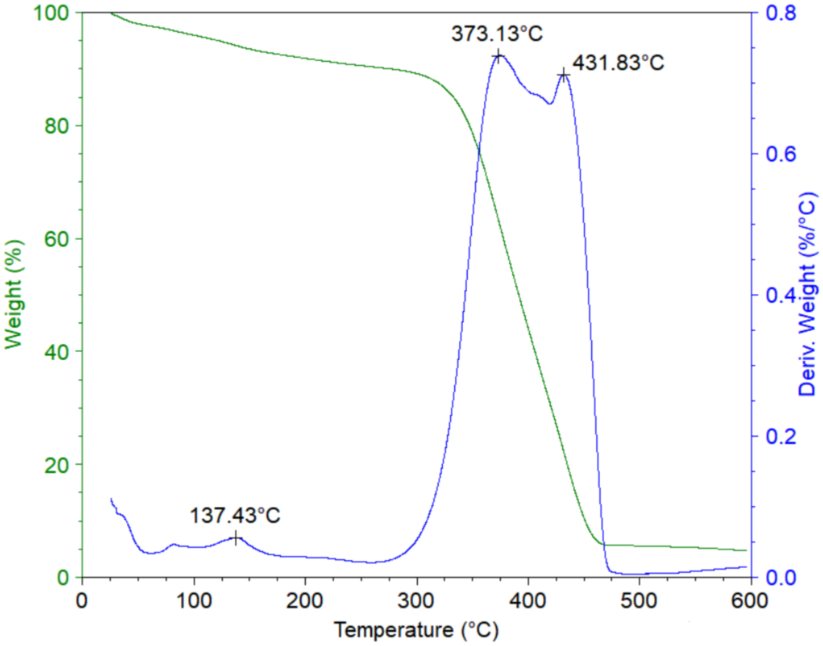

Figure S3.31. TGA traces of the PIVC from run **3**, Table 3.3.

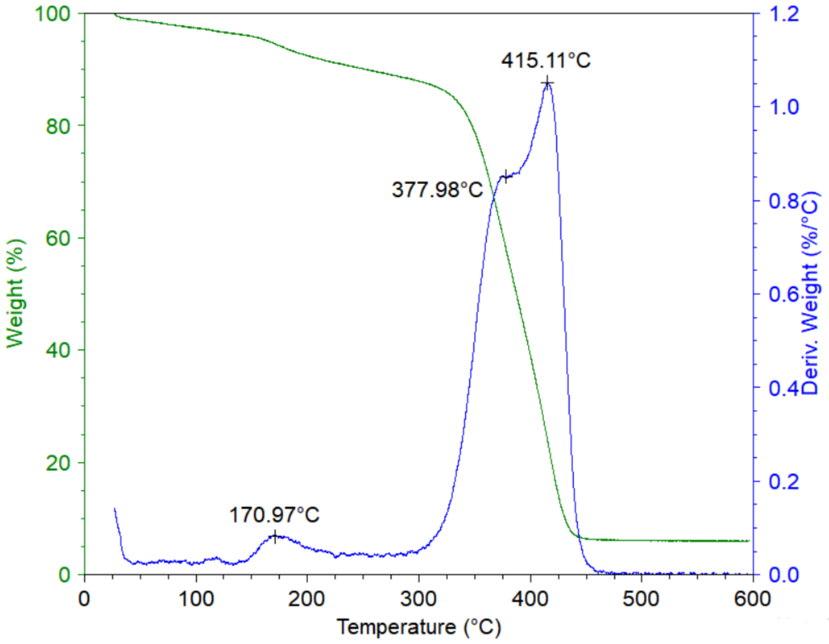

Figure S3.32. TGA traces of the PIVCM from run **1**, Table 3.5.

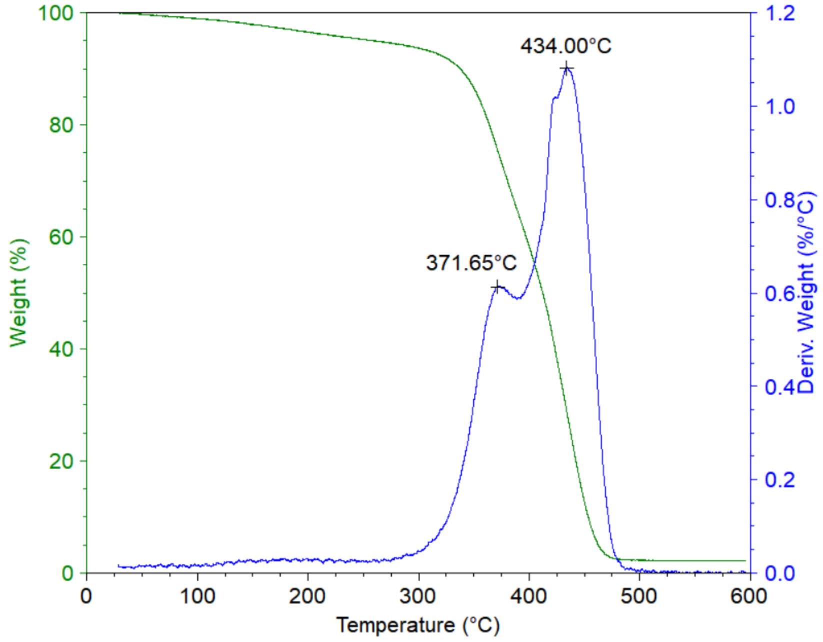

Figure S3.33. TGA traces of the PIVCM from run **3**, Table 3.5.

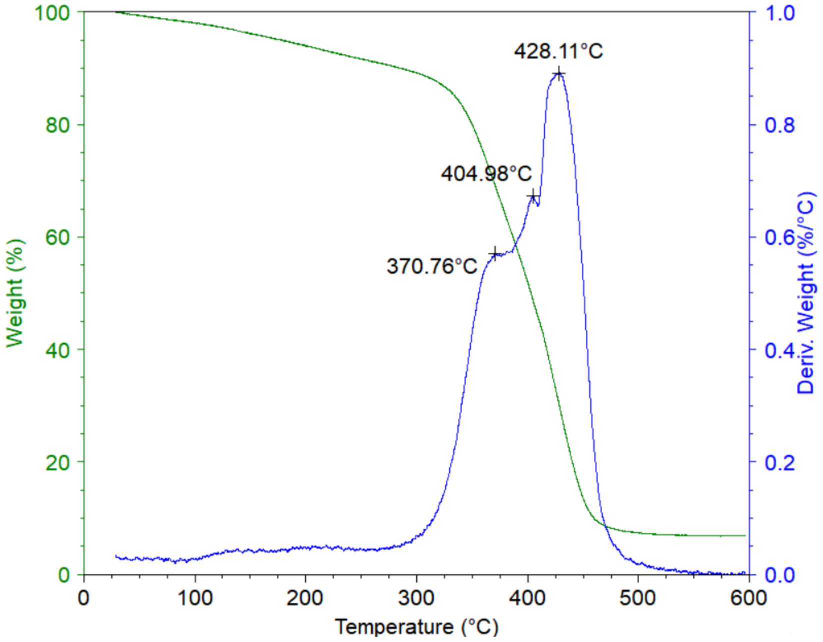

Figure S3.34. TGA traces of the PIVCO from run **5**, Table 3.5.

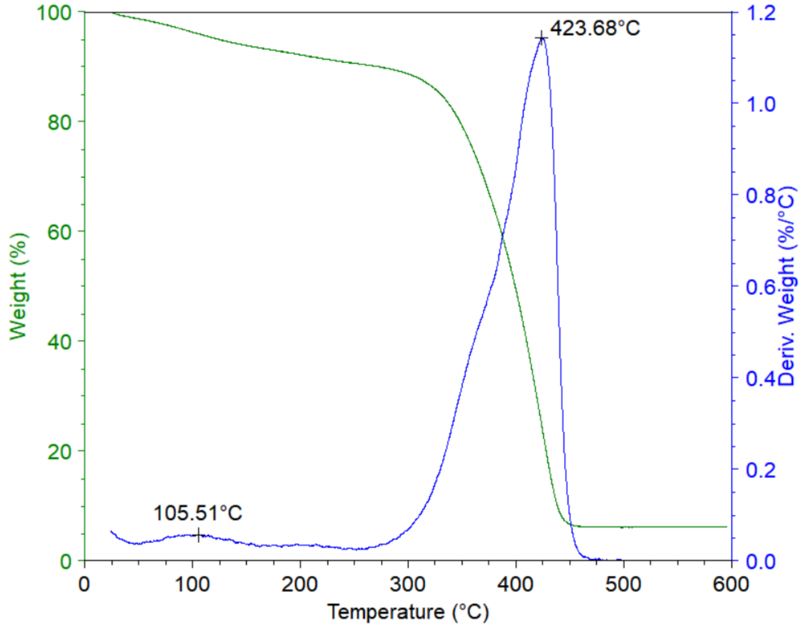

Figure S3.35. TGA traces of the PIVCPB from run **9**, Table 3.5.

3.5 GPC Analyses

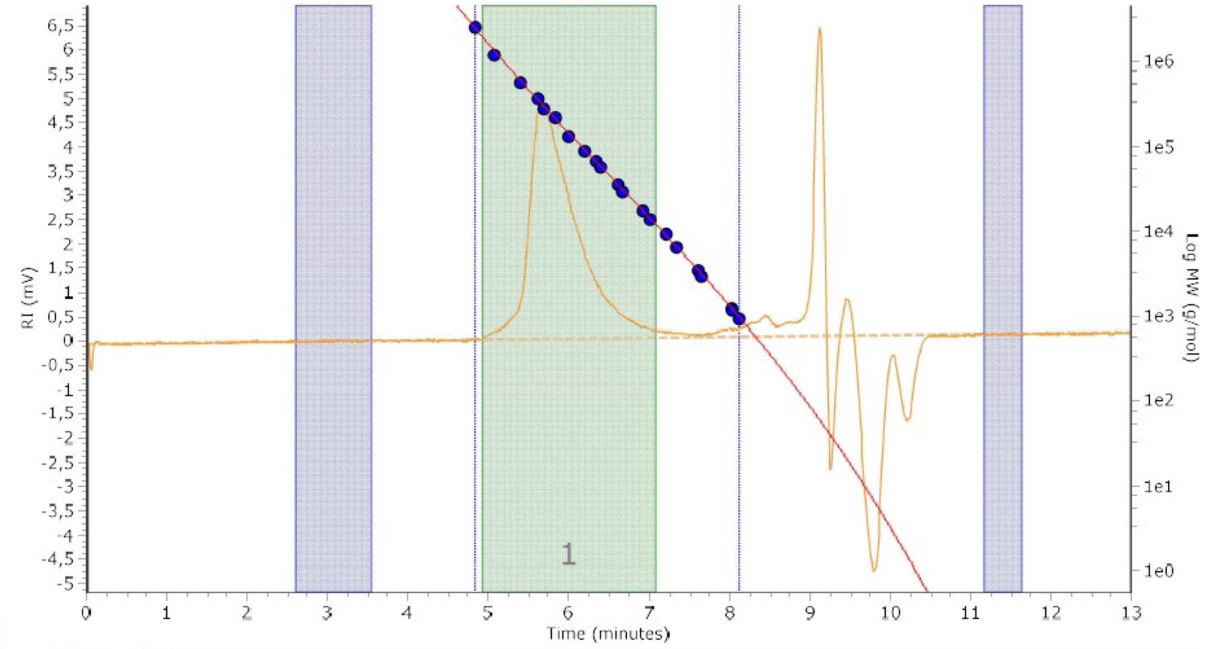

Molecular Weight Averages

Peak	Mp (g/mol)	Mn (g/mol)	Mw (g/mol)	Mz (g/mol)	Mz+1 (g/mol)	Mv (g/mol)	PD
Peak 1	301894	102962	247060	406443	673196	227676	2,4

Figure S3.36. GPC curve of PVCH from run **5**, Table 3.1.

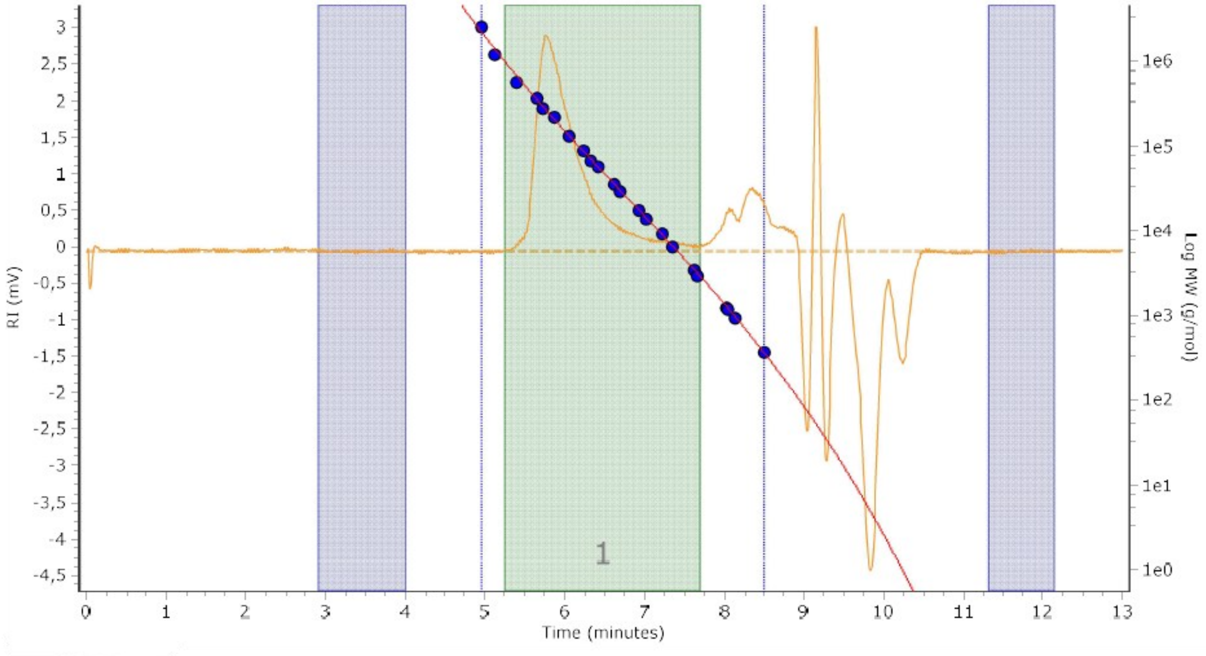

Molecular Weight Averages

Peak	Mp (g/mol)	Mn (g/mol)	Mw (g/mol)	Mz (g/mol)	Mz+1 (g/mol)	Mv (g/mol)	PD
Peak 1	246281	63322	184264	261608	322521	171406	2,91

Figure S3.37. GPC curve of PVCH after hydrogenation.

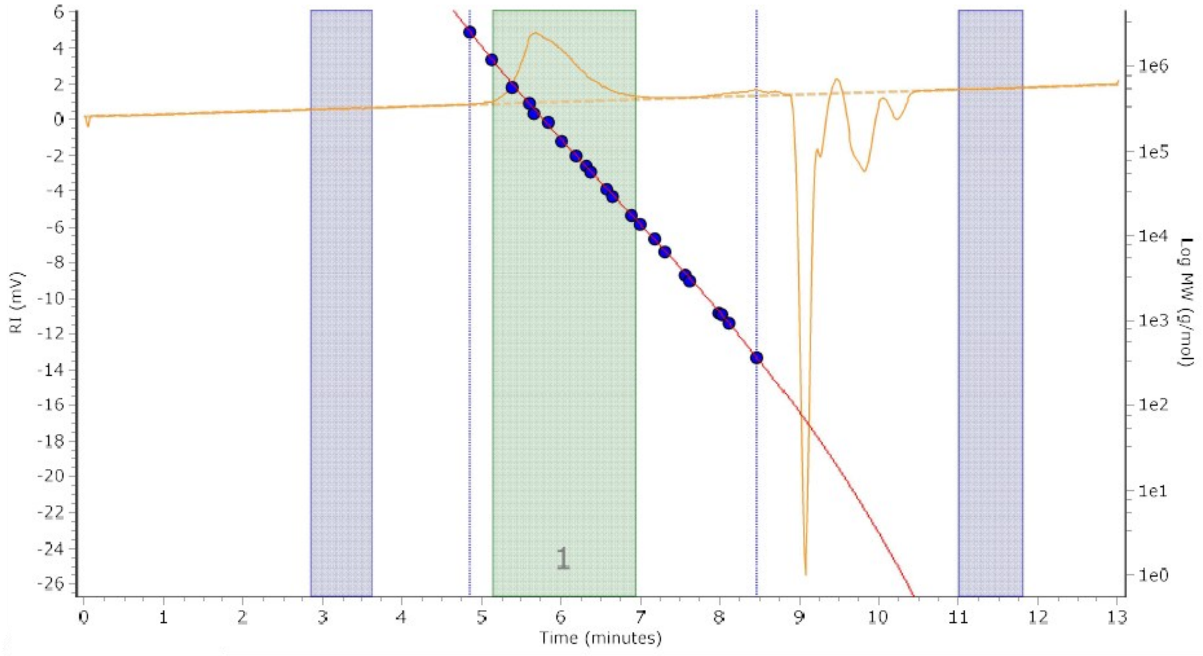

Molecular Weight Averages

Peak	Mp (g/mol)	Mn (g/mol)	Mw (g/mol)	Mz (g/mol)	Mz+1 (g/mol)	Mv (g/mol)	PD
Peak 1	294068	118971	234396	367556	500019	216295	1,97

Figure S3.38. GPC curve of PVCHS from run **2**, Table 3.2.

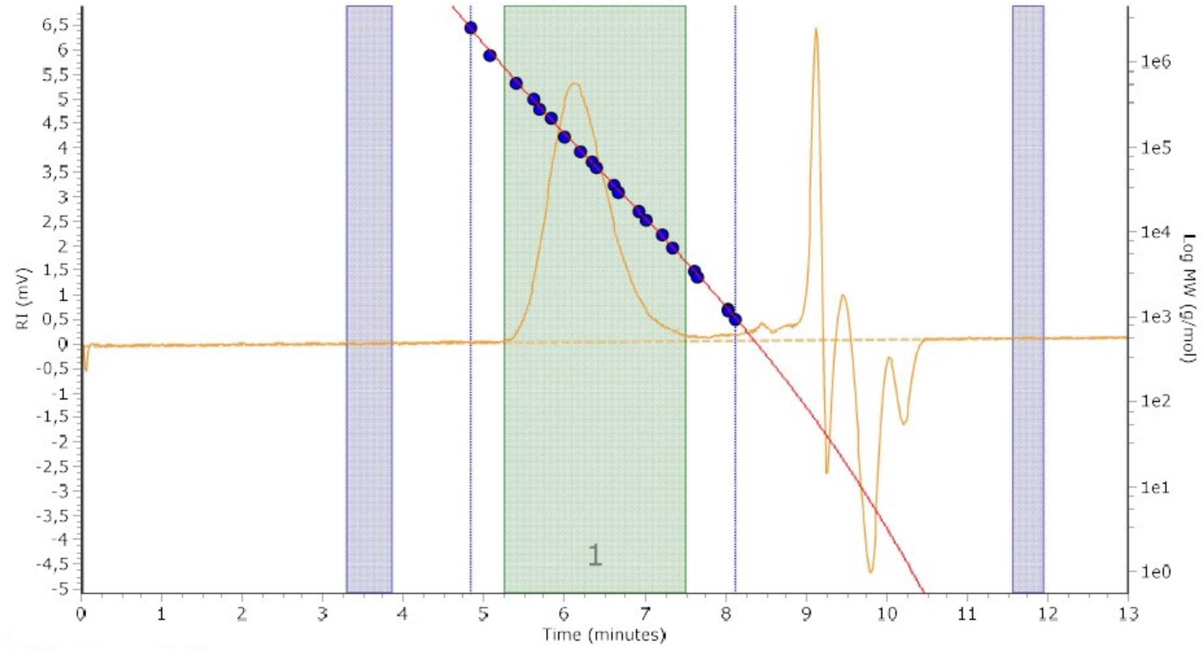

Molecular Weight Averages

Peak	Mp (g/mol)	Mn (g/mol)	Mw (g/mol)	Mz (g/mol)	Mz+1 (g/mol)	Mv (g/mol)	PD
Peak 1	101837	55971	117565	194754	280754	107696	2,1

Figure S3.39. GPC curve of PVCHS from run **3**, Table 3.2.

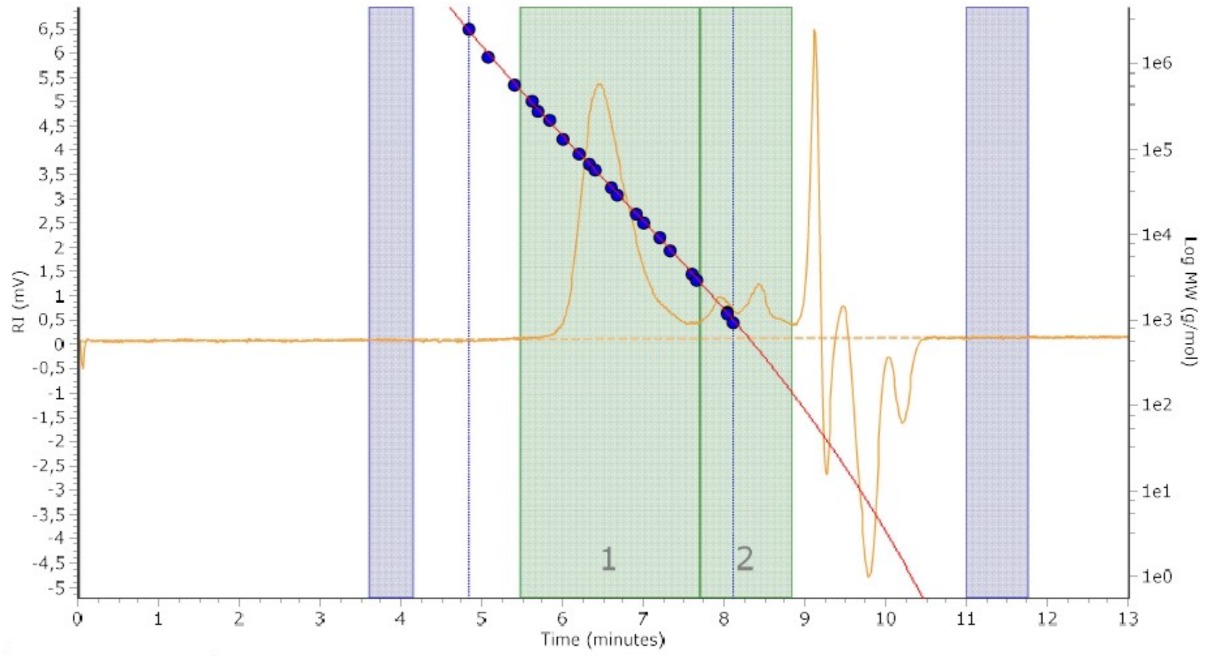

Molecular Weight Averages

Peak	Mp (g/mol)	Mn (g/mol)	Mw (g/mol)	Mz (g/mol)	Mz+1 (g/mol)	Mv (g/mol)	PD
Peak 1	47524	24952	46392	72362	121869	43263	1,859
Peak 2	436	507	891	1359	1713	825	1,757

Figure S3.40. GPC curve of PVCHM from run **4**, Table 3.2.

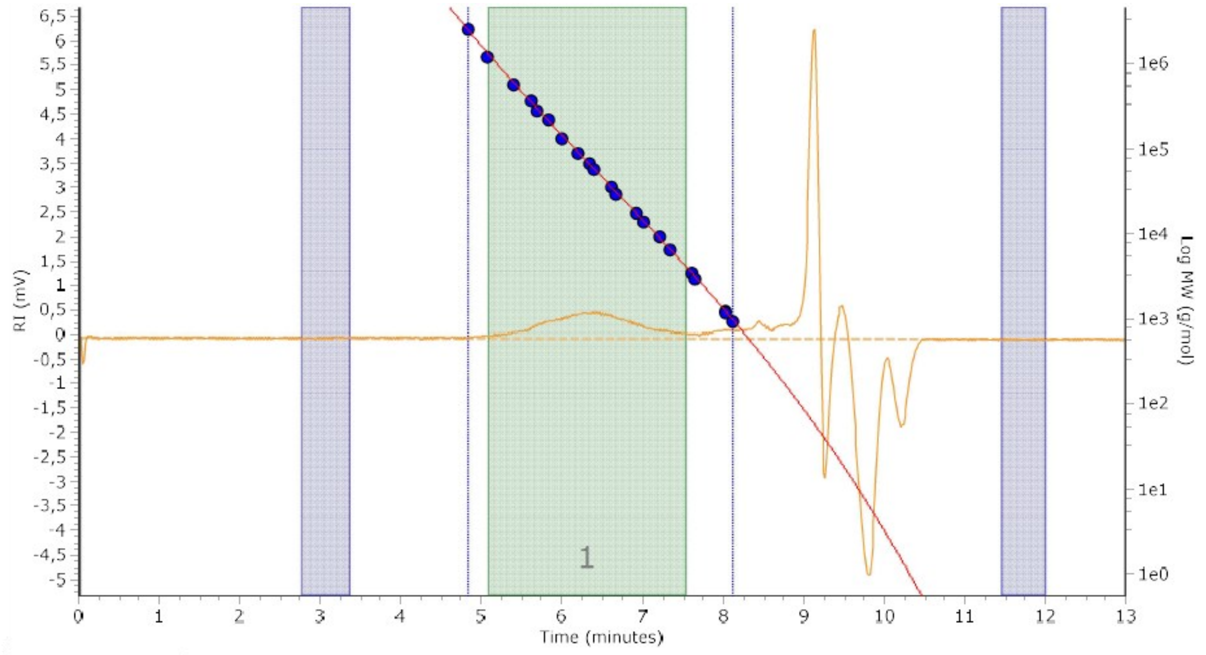

Molecular Weight Averages

Peak	Mp (g/mol)	Mn (g/mol)	Mw (g/mol)	Mz (g/mol)	Mz+1 (g/mol)	Mv (g/mol)	PD
Peak 1	51275	30901	125881	371594	647795	103174	4,074

Figure S3.41. GPC curve of PVCHO from run **5**, Table 3.2.

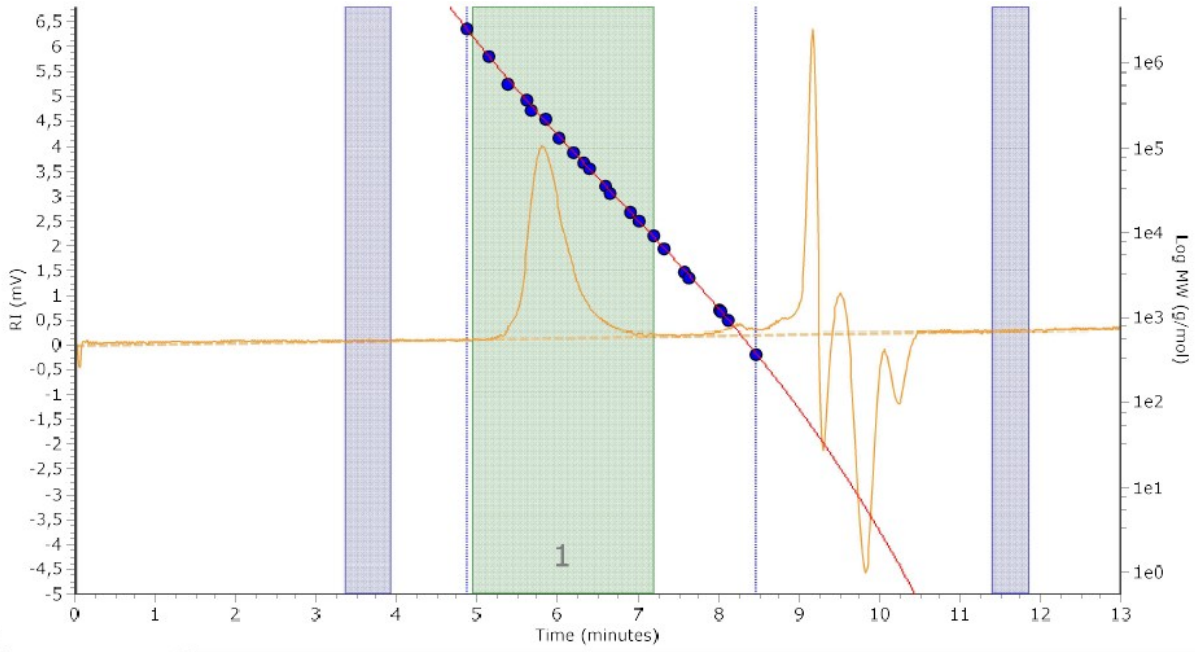

Molecular Weight Averages

Peak	Mp (g/mol)	Mn (g/mol)	Mw (g/mol)	Mz (g/mol)	Mz+1 (g/mol)	Mv (g/mol)	PD
Peak 1	221467	123980	200827	272733	365006	190758	1,62

Figure S3.42. GPC curve of PIVC from run **3**, Table 3.3.

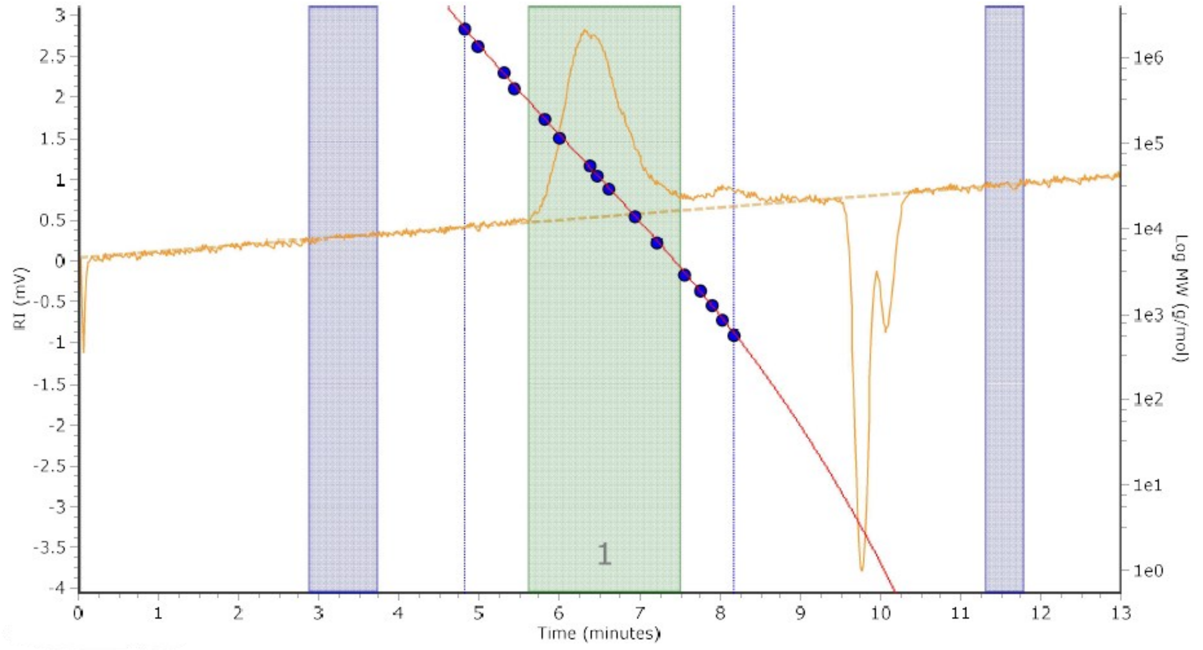

Molecular Weight Averages

Peak	Mp (g/mol)	Mn (g/mol)	Mw (g/mol)	Mz (g/mol)	Mz+1 (g/mol)	Mv (g/mol)	PD
Peak 1	61863	28059	57058	90963	125030	52498	2.034

Figure S3.43. GPC curve of PIVCM from run **1**, Table 3.5.

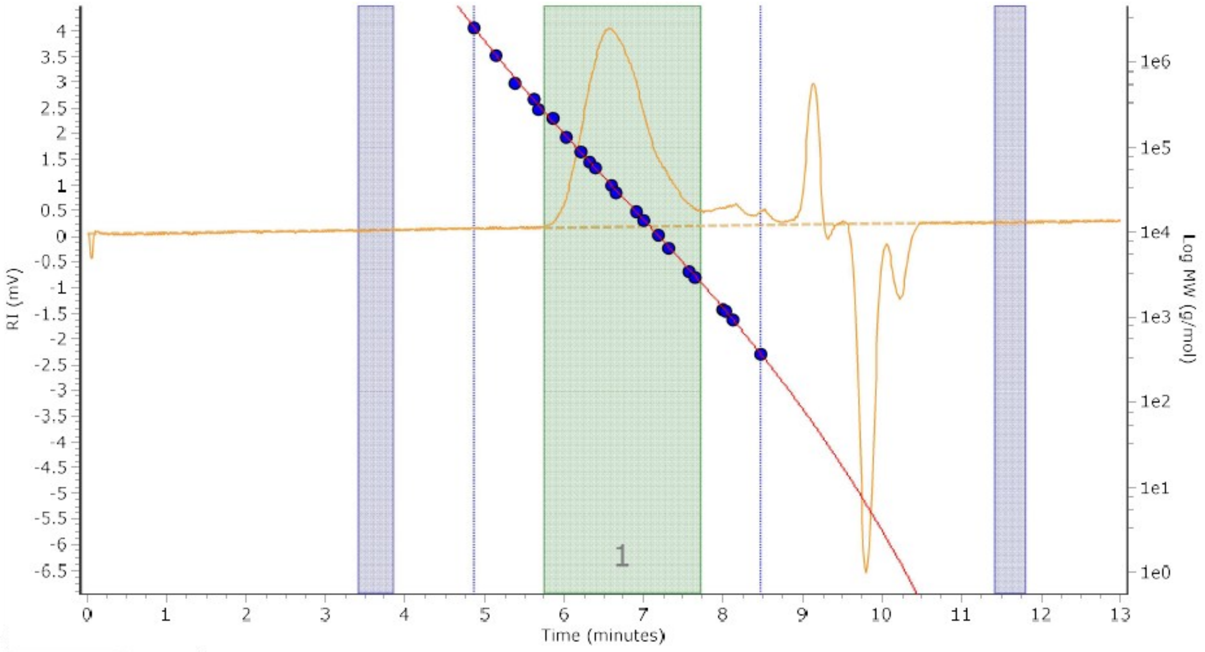

Molecular Weight Averages

Peak	Mp (g/mol)	Mn (g/mol)	Mw (g/mol)	Mz (g/mol)	Mz+1 (g/mol)	Mv (g/mol)	PD
Peak 1	38082	18841	38588	63650	90423	35341	2.048

Figure S3.44. GPC curve of PIVCM from run **3**, Table 3.5.

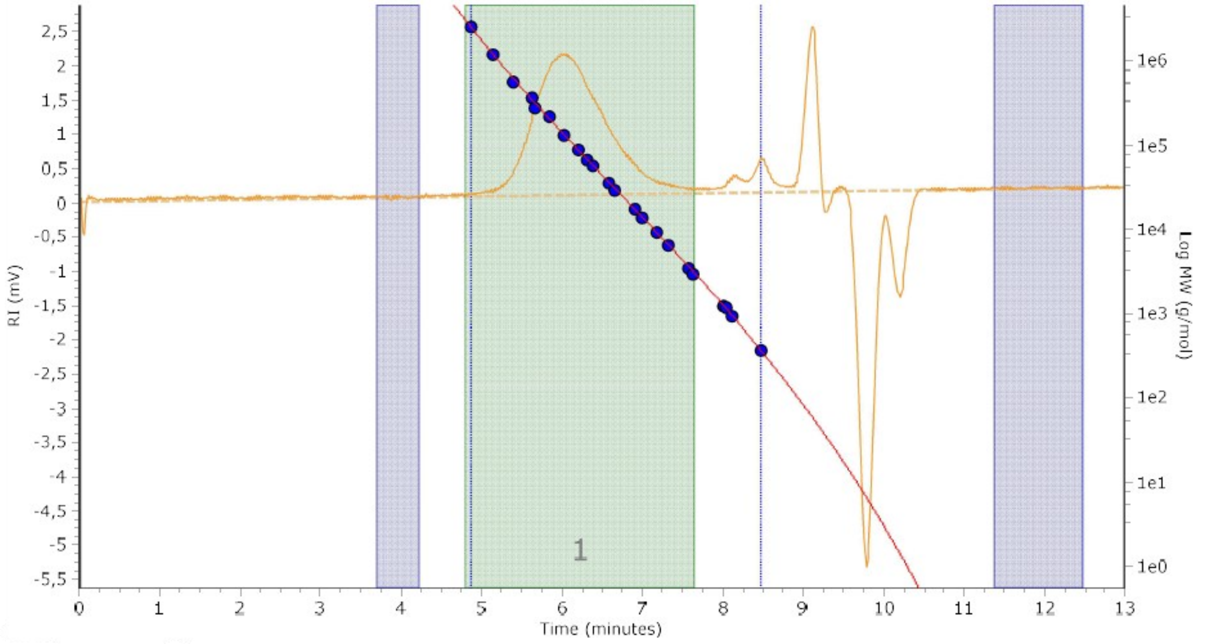

Molecular Weight Averages

Peak	Mp (g/mol)	Mn (g/mol)	Mw (g/mol)	Mz (g/mol)	Mz+1 (g/mol)	Mv (g/mol)	PD
Peak 1	131934	53308	165748	423151	1006100	143735	3,109

Figure S3.45. GPC curve of PIVCO from run **5**, Table 3.5.

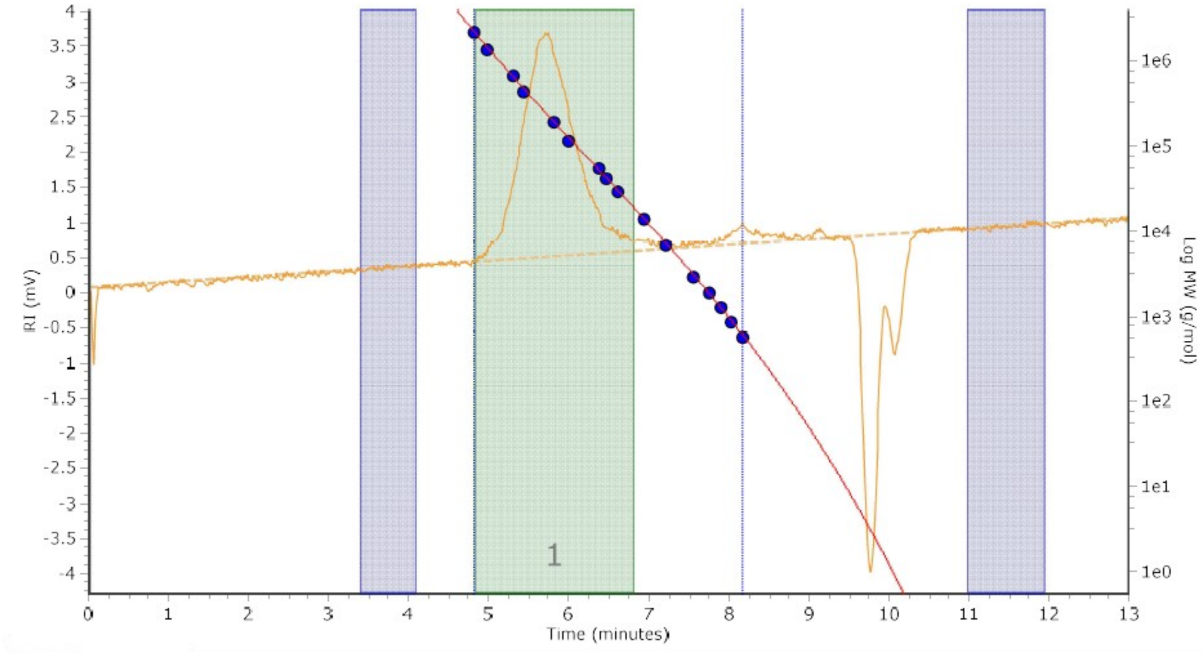

Molecular Weight Averages

Peak	Mp (g/mol)	Mn (g/mol)	Mw (g/mol)	Mz (g/mol)	Mz+1 (g/mol)	Mv (g/mol)	PD
Peak 1	249875	152362	289859	485829	743551	266565	1.902

Figure S3.46. GPC curve of PIVCPB from run **9**, Table 3.5.

Appendix 4

4.1 NMR Spectra

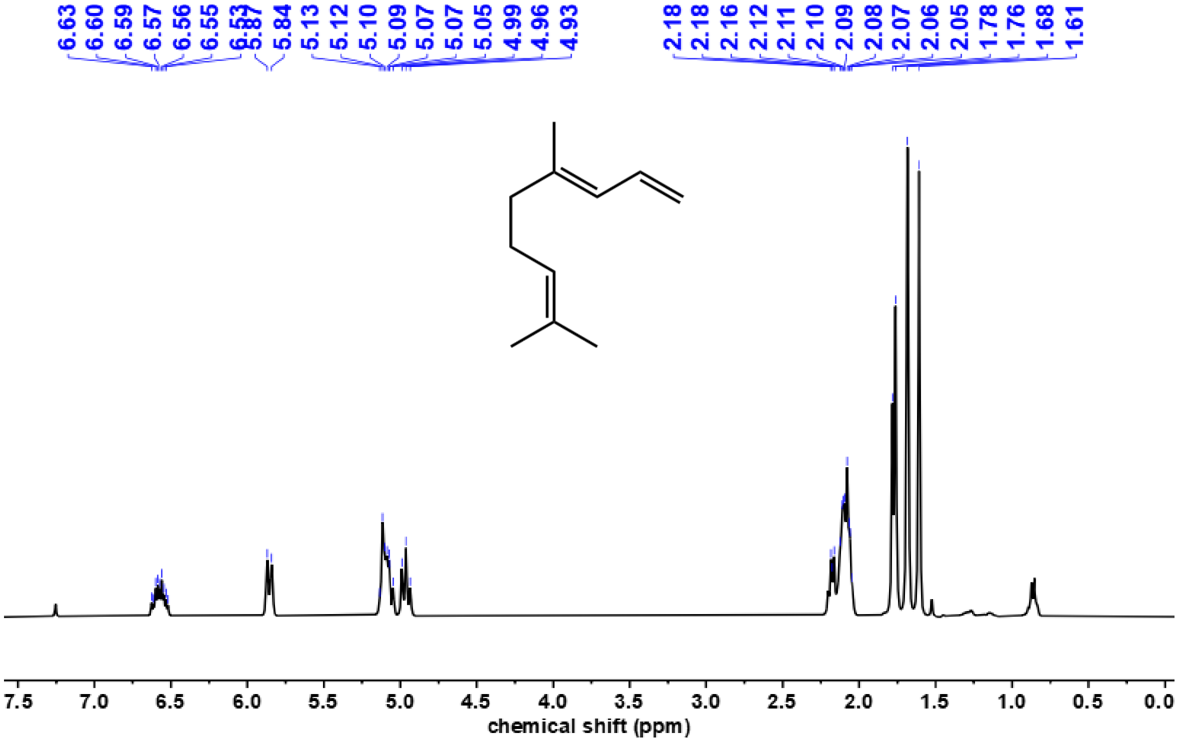

Figure S4.1. ^{1}H NMR spectrum of (E)-4,8-dimethyl-1,3,7-nonatriene (300 MHz, $CDCl_3$, 298 K).

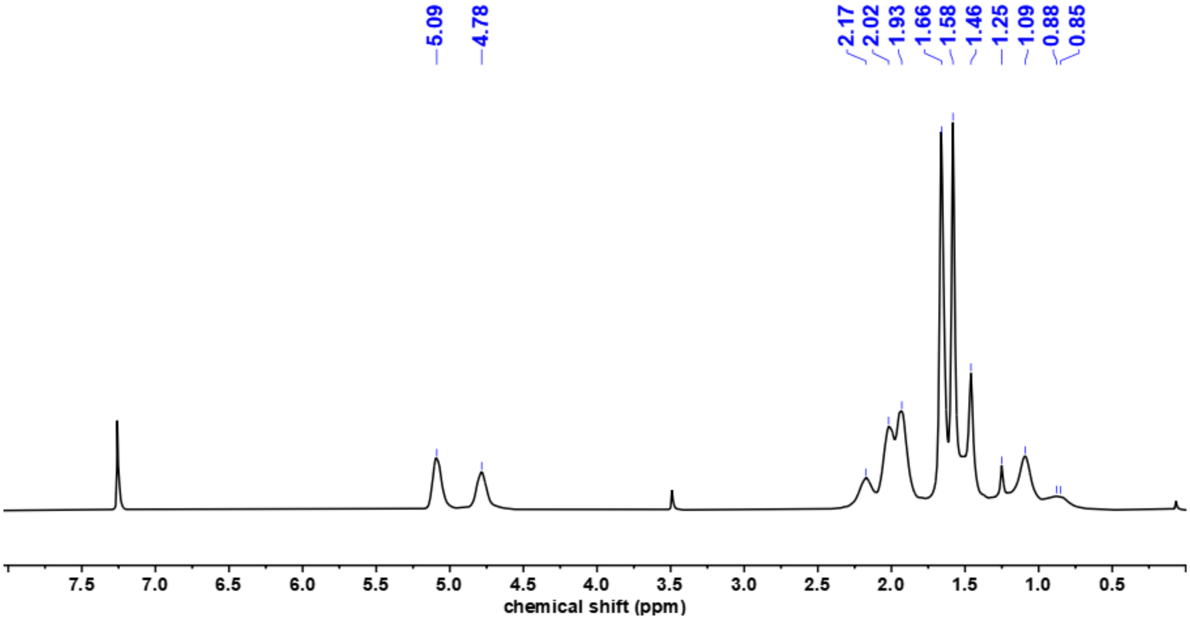

Figure S4.2. ^{1}H NMR (300 MHz, $CDCl_3$, 298 K) of PDMNT obtained with catalyst **1** (run **1**, Table 4.1).

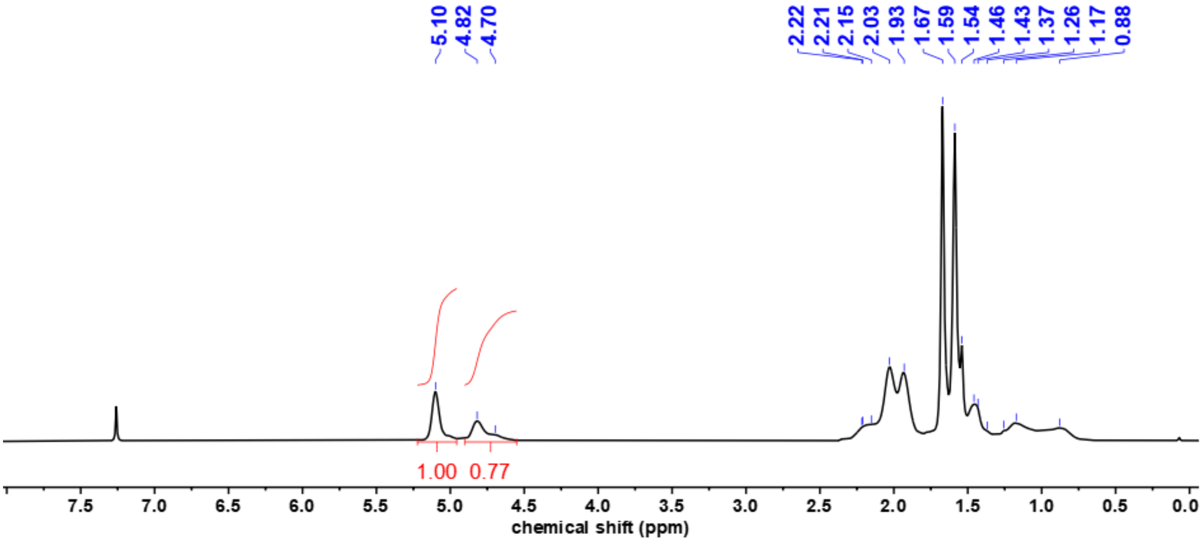

Figure S4.3. ^{1}H NMR (400 MHz, $CDCl_3$, 298 K) of DMNT-M copolymer from run **3**, Table 4.2.

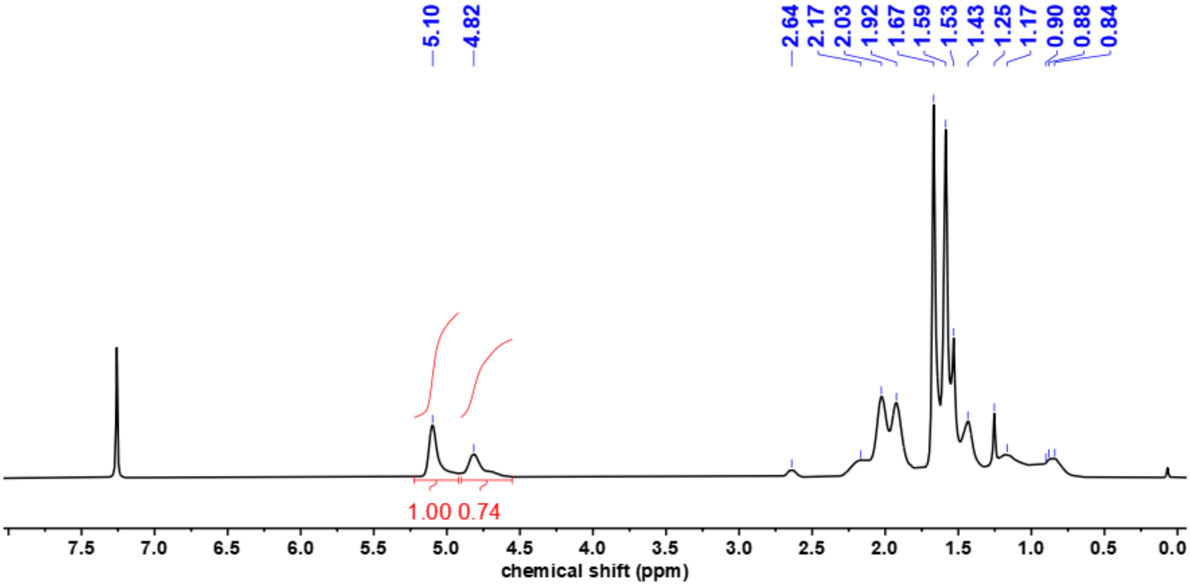

Figure S4.4. ^{1}H NMR (400 MHz, $CDCl_3$, 298 K) of DMNT-O copolymer from run **8**, Table 4.2.

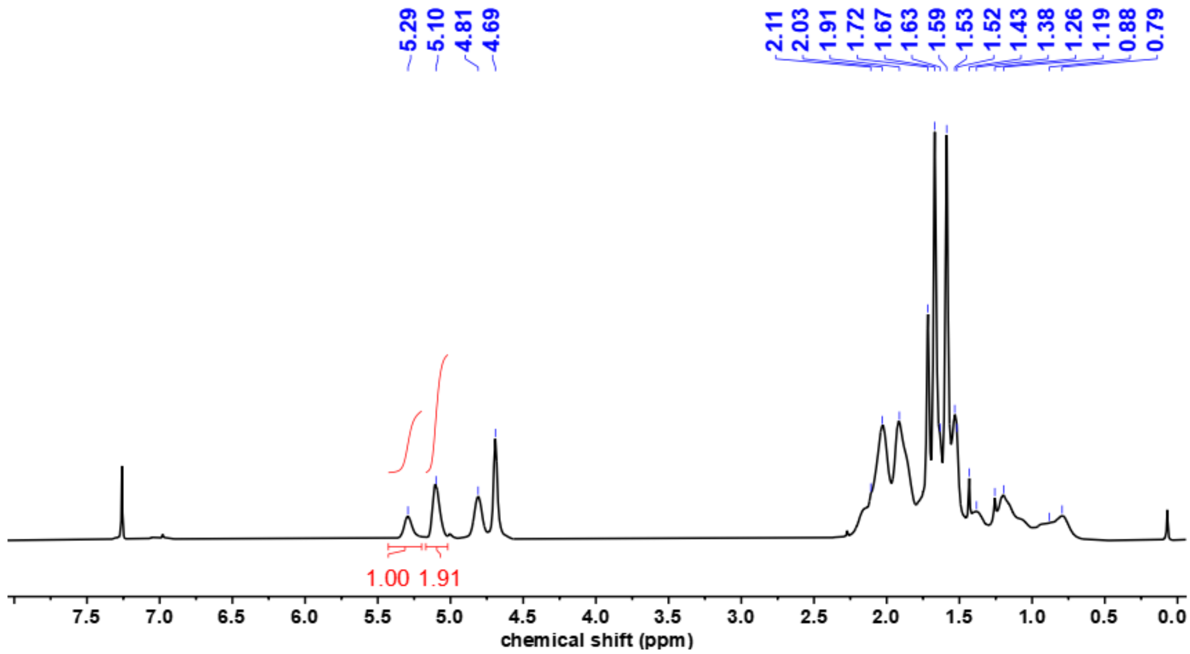

Figure S4.5. ^{1}H NMR (400 MHz, $CDCl_3$, 298 K) of DMNT-IVC copolymer from run **2**, Table 4.3.

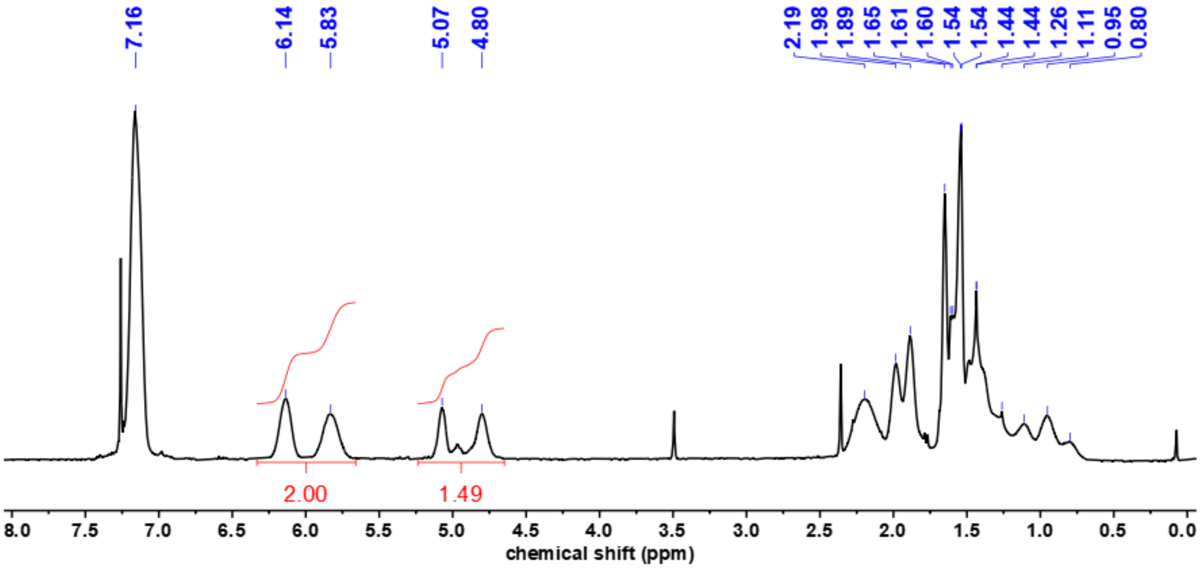

Figure S4.6. ^{1}H NMR (400 MHz, $CDCl_3$, 298 K) of DMNT-1PB copolymer from run **8**, Table 4.3.

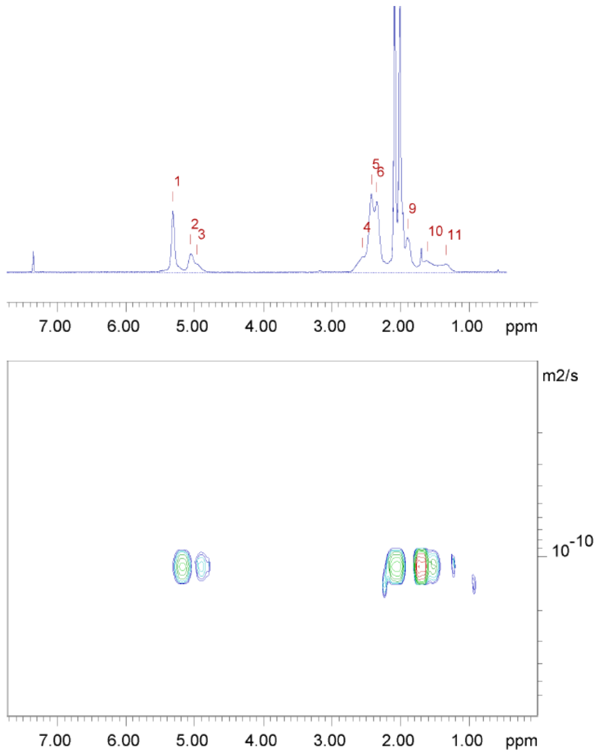

Figure S4.7. 2D DOSY NMR spectra (400 MHz, $CDCl_3$, 298 K) of DMNT-M copolymer from run **5**, Table 4.2.

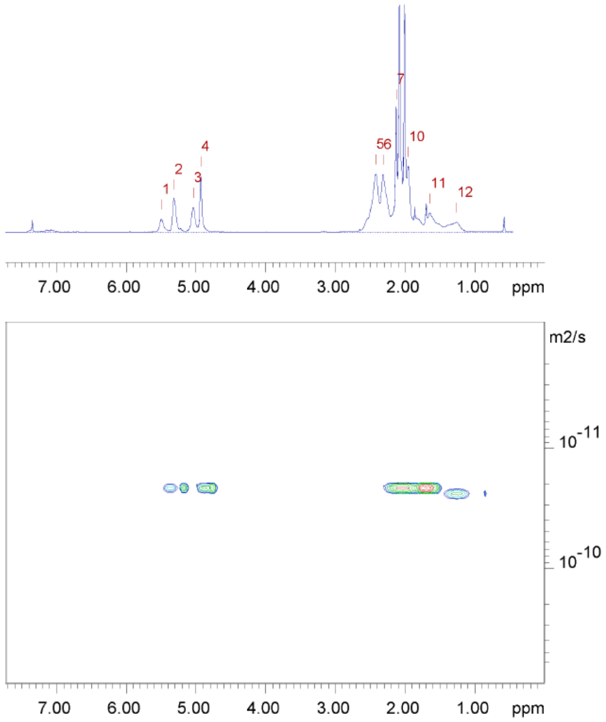

Figure S4.8. 2D DOSY NMR spectra (400 MHz, $CDCl_3$, 298 K) of DMNT-IVC copolymer from run **2**, Table 4.3.

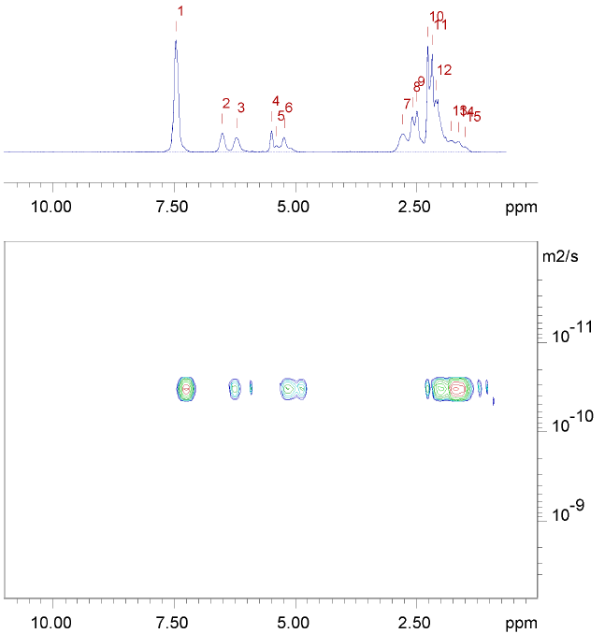

Figure S4.9. 2D DOSY NMR spectra (400 MHz, $CDCl_3$, 298 K) of DMNT-1PB copolymer from run **9**, Table 4.3.

4.2 Determination of Copolymer Compositions

- **Determination of DMNT and M contents in DMNT-M copolymers by ^1H NMR ($CDCl_3$, 298 K).**

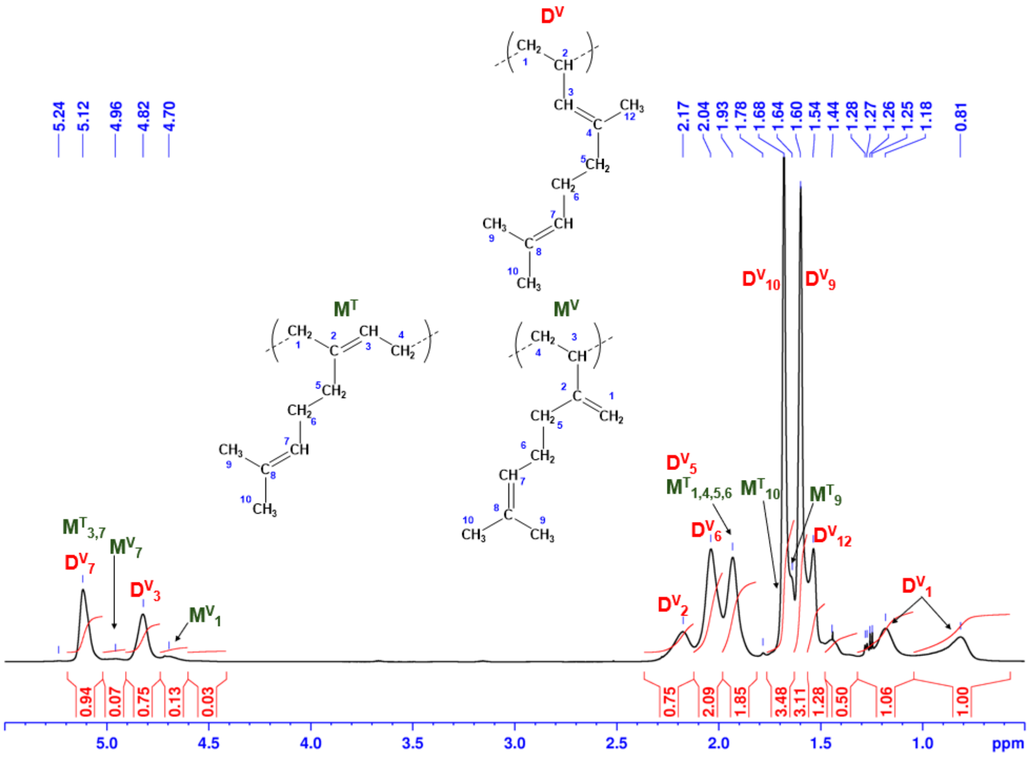

$$DMNT\ (mol\%) = \frac{A_{D_3^V}}{A_{TOT}} x\ 100$$

$$M^T\ (mol\%) = \frac{(A_{(D_7^V + M_{3,7}^T)} - A_{D_3^V})/2}{A_{TOT}} x\ 100$$

$$M^V\ (mol\%) = \frac{A_{M_1^V}/2}{A_{TOT}} x\ 100$$

where: $A_{D_3^V}$ is the area of the signals at δ = 4.82 ppm, $A_{(D_7^V + M_{3,7}^T)}$ is the area of the signals at δ = 5.24 ppm and $A_{M_1^V}$ is the area of the signal at δ = 4.70 ppm.

And:

$$A_{TOT} = \left[(A_{(D_7^V + M_{3,7}^T)} - A_{D_3^V})/2\right] + \left[A_{D_3^V}\right] + \left[A_{M_1^V}/2\right]$$

- **Determination of DMNT and O contents in DMNT-O copolymers by ^{1}H NMR (CDCl$_3$, 298 K).**

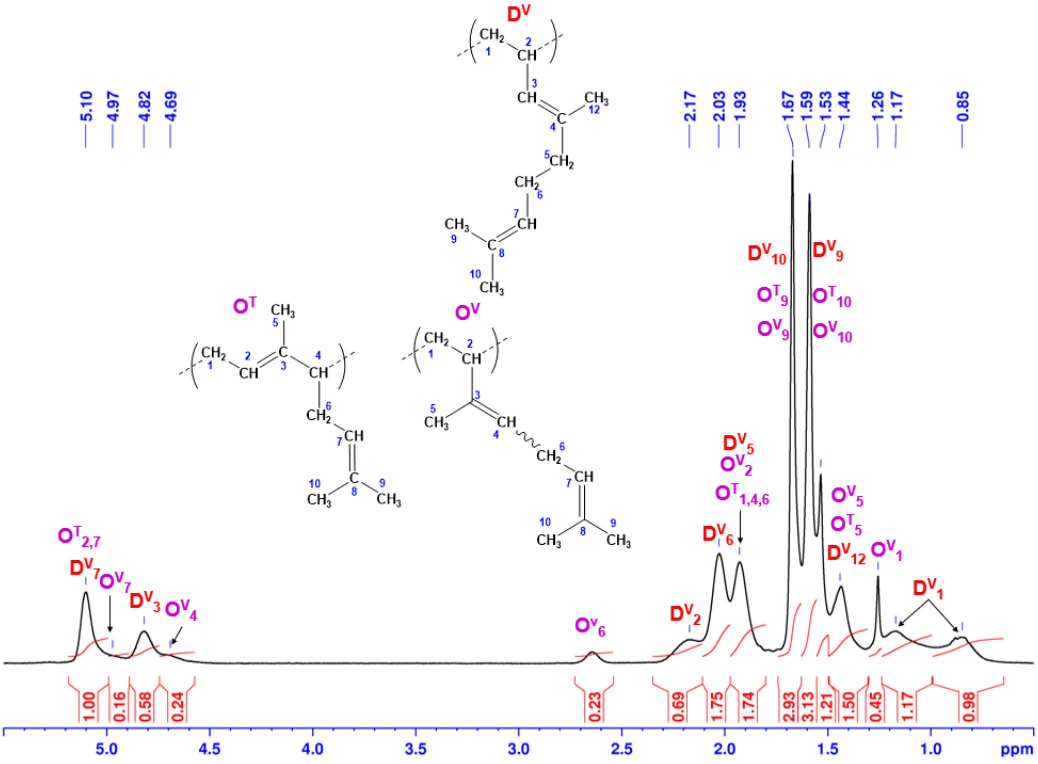

$$DMNT\ (mol\%) = \frac{A_{D_3^V}}{A_{TOT}} x\ 100$$

$$O^T\ (mol\%) = \frac{(A_{(D_7^V + O_{2,7}^T)} - A_{D_3^V})/2}{A_{TOT}} x\ 100$$

$$O^V\ (mol\%) = \frac{A_{O_4^V}}{A_{TOT}} x\ 100$$

where: $A_{D_3^V}$ is the area of the signals at δ = 4.82 ppm, $A_{(D_7^V+O_{2,7}^T)}$ is the area of the signals at δ = 5.10 ppm and $A_{O_4^V}$ is the area of the signal at δ = 4.69 ppm.

And:

$$A_{TOT} = \left[(A_{(D_7^V+O_{2,7}^T)} - A_{D_3^V})/2\right] + \left[A_{D_3^V}\right] + \left[A_{O_4^V}\right]$$

- **Determination of DMNT and IVC contents in DMNT-IVC copolymers by ^{1}H NMR ($CDCl_3$, 298 K).**

$$DMNT\ (mol\%) = \frac{A_D}{A_{TOT}} x\ 100$$

$$IVC\ (mol\%) = \frac{A_{IVC}}{A_{TOT}} x\ 100$$

where: A_D is the area of the signals at δ = 5.10 ppm and A_{IVC} is the area of the signal at δ = 5.29 ppm (Figure S4.5).

And:

$$A_{TOT} = [A_D] + [A_{IVC}]$$

- **Determination of DMNT and 1PB contents in DMNT-1PB copolymers by ^{1}H NMR ($CDCl_3$, 298 K).**

$$DMNT\ (mol\%) = \frac{A_D/2}{A_{TOT}} x\ 100$$

$$1PB\ (mol\%) = \frac{A_{1PB}/2}{A_{TOT}} x\ 100$$

where: A_D is the area of the signals at δ = 4.80-5.07 ppm and A_{1PB} is the area of the signal at δ = 5.83-6.14 ppm (Figure S4.6).

And:

$$A_{TOT} = [A_D/2] + [A_{1PB}/2]$$

4.3 DSC Thermal Analyses

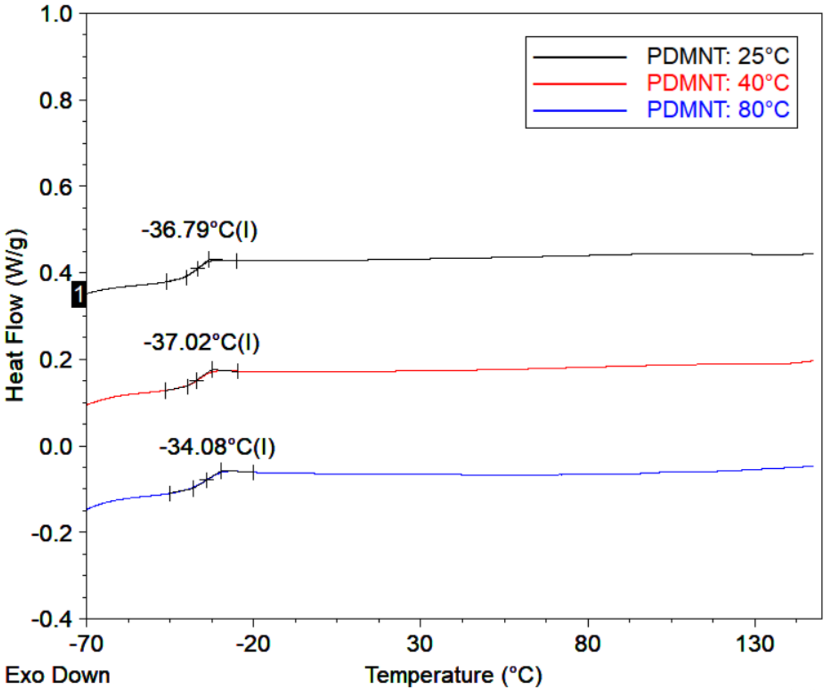

Figure S4.10. DSC thermograms of PDMNT obtained with catalyst **1** at different temperatures (runs **1, 2** and **3**, Table 4.1).

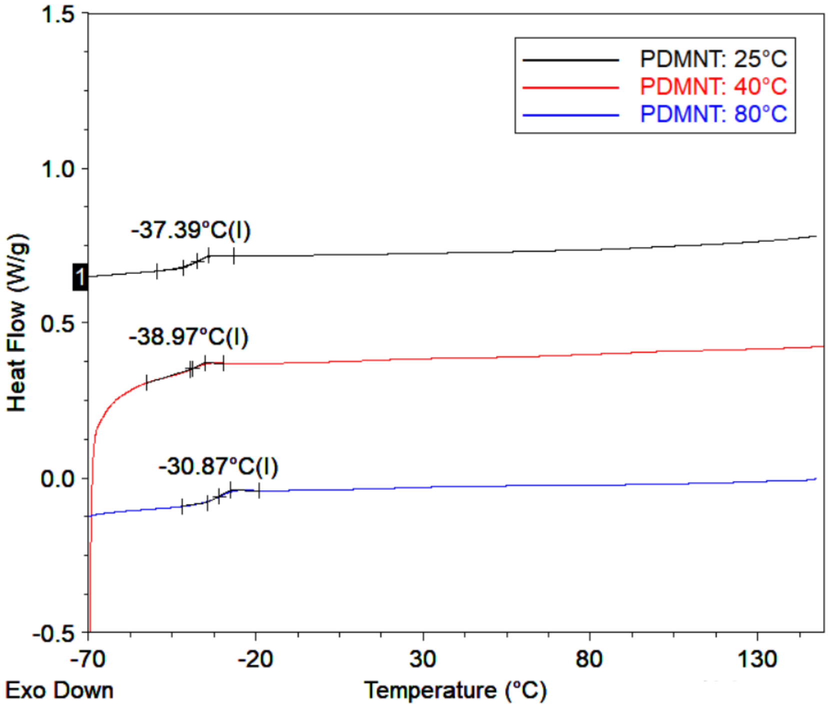

Figure S4.11. DSC thermograms of PDMNT obtained with catalyst **2** at different temperatures (runs **4, 5** and **6**, Table 4.1).

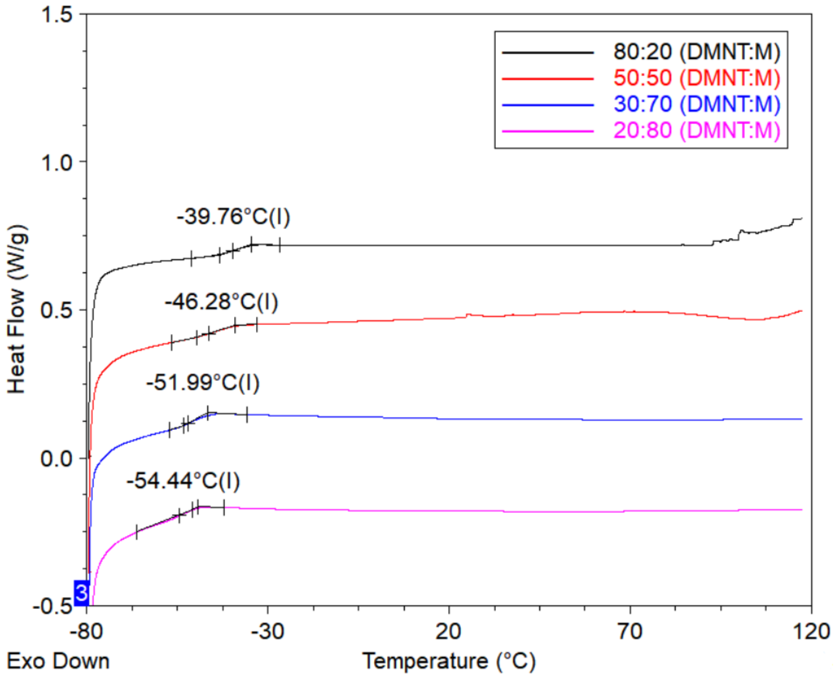

Figure S4.12. DSC thermograms of DMNT-M copolymers relative to the different compositions from runs **3-6**, Table 4.2.

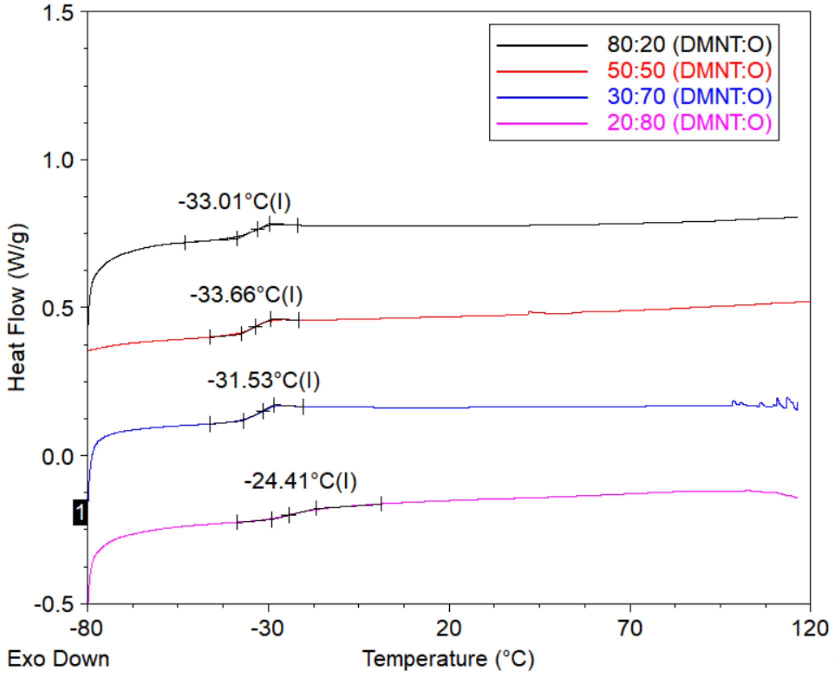

Figure S4.13. DSC thermograms of DMNT-O copolymers relative to the different compositions from runs **7-10**, Table 4.2.

4.4 GPC Analyses

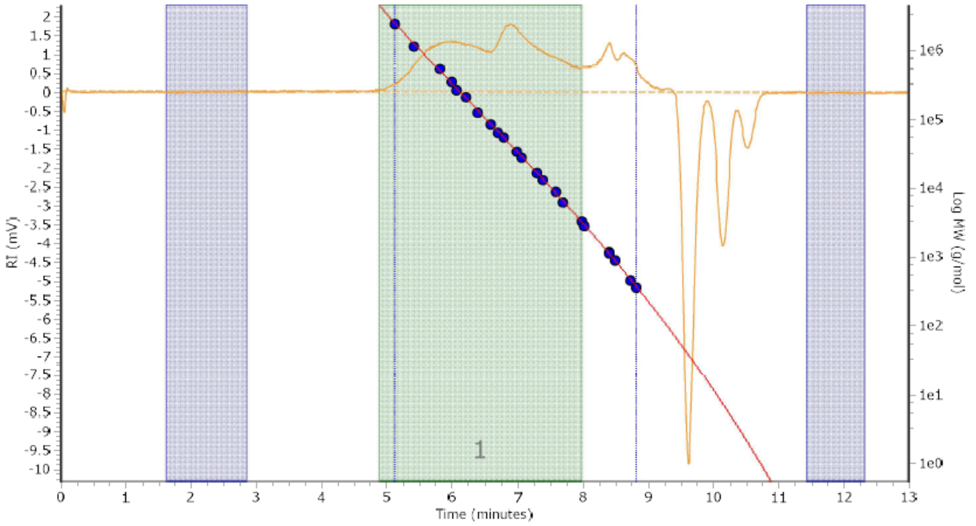

Molecular Weight Averages

Peak	Mp (g/mol)	Mn (g/mol)	Mw (g/mol)	Mz (g/mol)	Mz+1 (g/mol)	Mv (g/mol)
Peak **1**	41766	27580	298297	1137330	1936685	221352

PD
10.82

Figure S4.14. GPC curve of PDMNT obtained with catalyst **1**, from run **1**, Table 4.1.

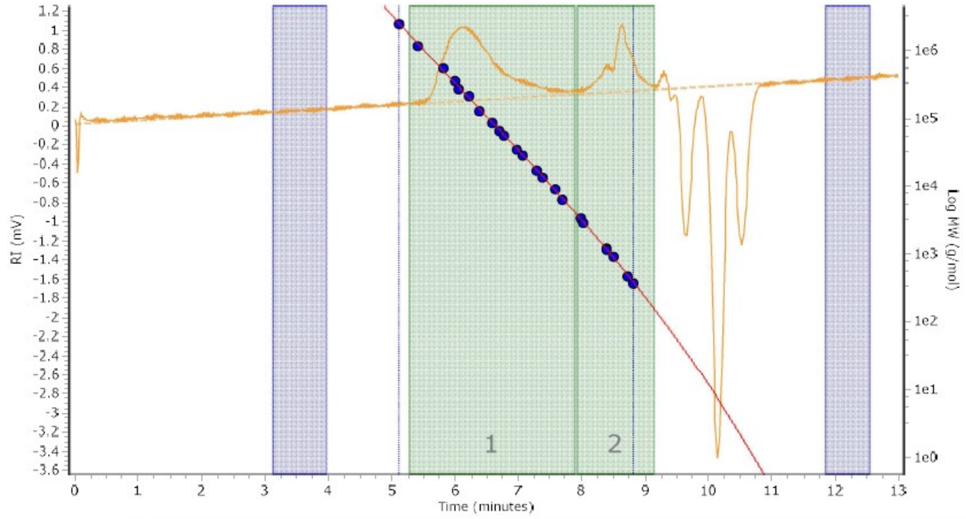

Molecular Weight Averages

Peak	Mp (g/mol)	Mn (g/mol)	Mw (g/mol)	Mz (g/mol)	Mz+1 (g/mol)	Mv (g/mol)
Peak **1**	221167	72446	230237	389546	554463	207941
Peak 2	635	585	842	1262	1815	793

PD
3.178
1.439

Figure S4.15. GPC curve of PDMNT obtained with catalyst **2,** from run **4**, Table 4.1.

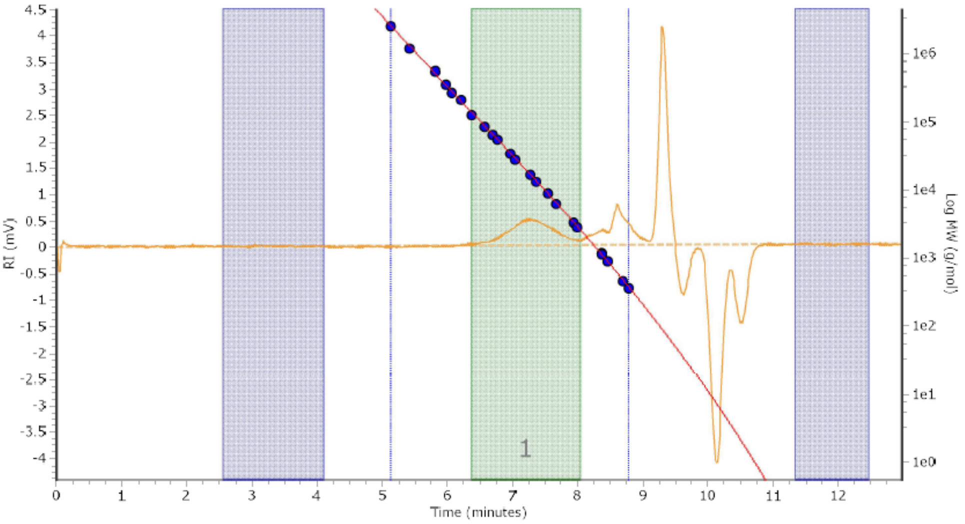

Molecular Weight Averages

Peak	Mp (g/mol)	Mn (g/mol)	Mw (g/mol)	Mz (g/mol)	Mz+1 (g/mol)	Mv (g/mol)
Peak **1**	16915	11980	22592	40772	63977	20552
PD						
1.886						

Figure S4.16. GPC curve of DMNT-M copolymer from run **3**, Table 4.2.

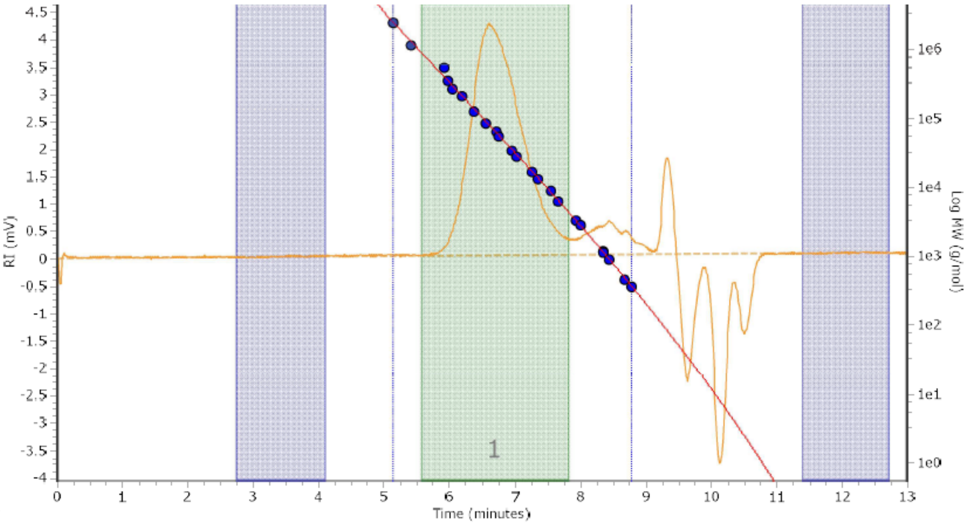

Molecular Weight Averages

Peak	Mp (g/mol)	Mn (g/mol)	Mw (g/mol)	Mz (g/mol)	Mz+1 (g/mol)	Mv (g/mol)
Peak **1**	80130	37403	80964	142074	227539	73619
PD						
2.165						

Figure S4.17. GPC curve of DMNT-O copolymer from run **8**, Table 4.2.

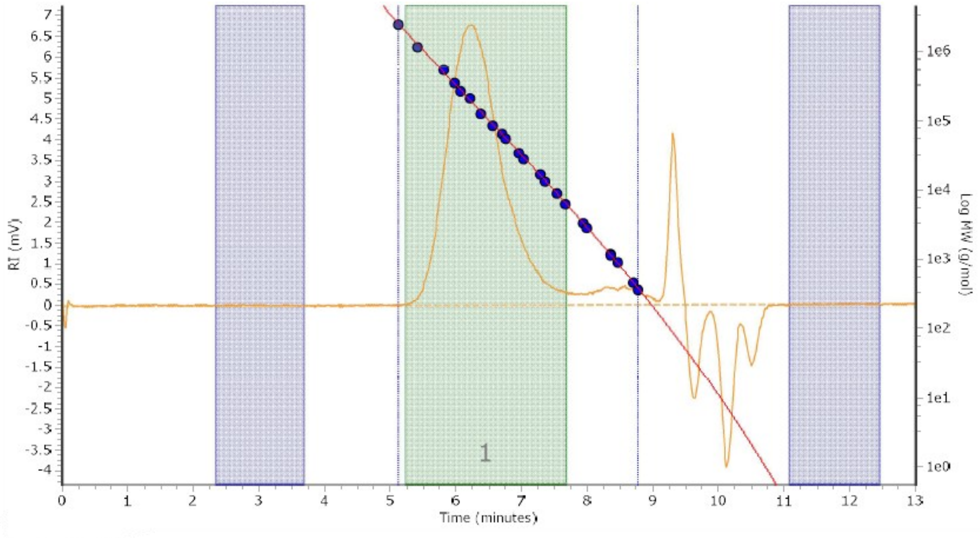

Molecular Weight Averages

Peak	Mp (g/mol)	Mn (g/mol)	Mw (g/mol)	Mz (g/mol)	Mz+1 (g/mol)	Mv (g/mol)
Peak **1**	194935	88890	226756	402951	601024	204577
PD						
2.551						

Figure S4.18. GPC curve of DMNT-IVC copolymer from run **2**, Table 4.3.

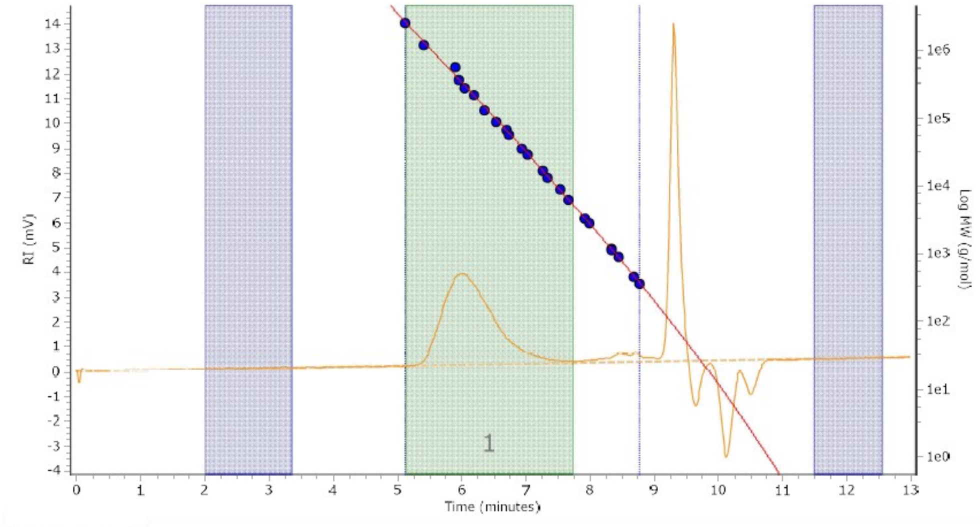

Molecular Weight Averages

Peak	Mp (g/mol)	Mn (g/mol)	Mw (g/mol)	Mz (g/mol)	Mz+1 (g/mol)	Mv (g/mol)
Peak **1**	324384	123105	318541	517982	702199	290601
PD						
2.588						

Figure S4.19. GPC curve of DMNT-1PB copolymer from run **8**, Table 4.3.

Appendix 5

5.1 NMR Spectra

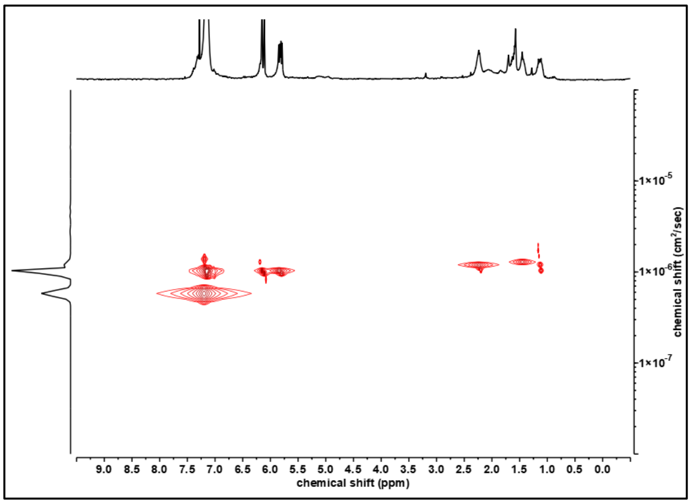

Figure S5.1. 2D DOSY NMR spectra (400 MHz, $CDCl_3$, 298 K) of 1PB-M copolymer.

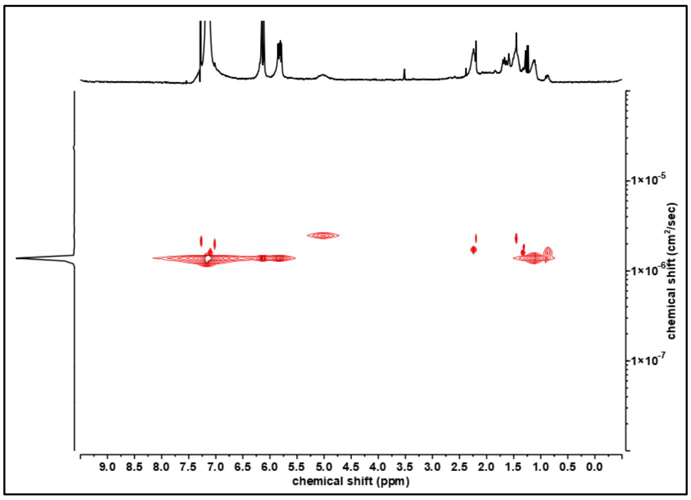

Figure S5.2. 2D DOSY NMR spectra (400 MHz, $CDCl_3$, 298 K) of 1PB-O copolymer.

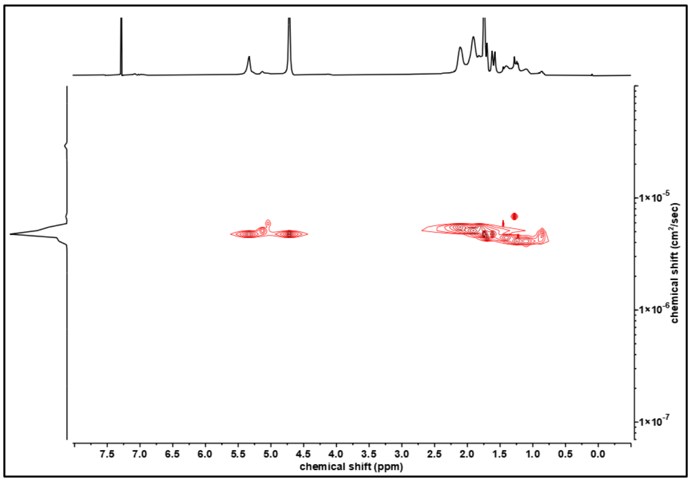

Figure S5.3. 2D DOSY NMR spectra (400 MHz, $CDCl_3$, 298 K) of IVC-M copolymer.

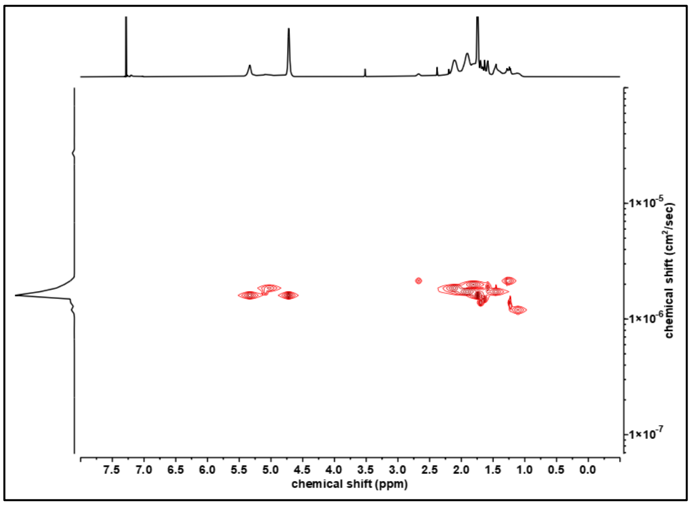

Figure S5.4. 2D DOSY NMR spectra (400 MHz, $CDCl_3$, 298 K) of IVC-O copolymer.

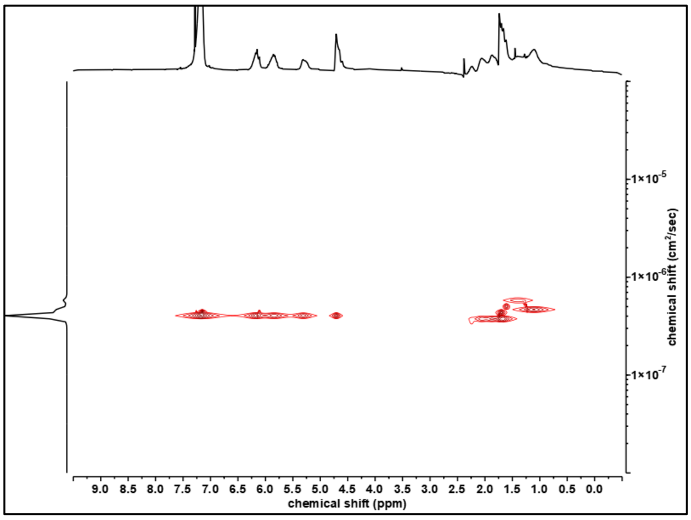

Figure S5.5. 2D DOSY NMR spectra (400 MHz, $CDCl_3$, 298 K) of IVC-1PB copolymer.

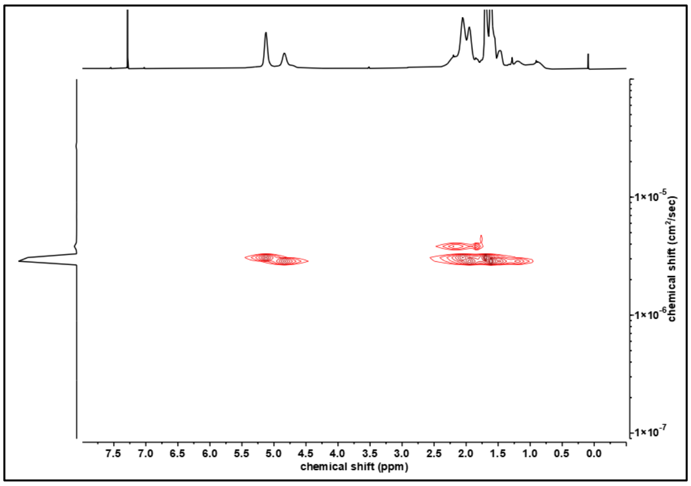

Figure S5.6. 2D DOSY NMR spectra (400 MHz, $CDCl_3$, 298 K) of DMNT-M copolymer.

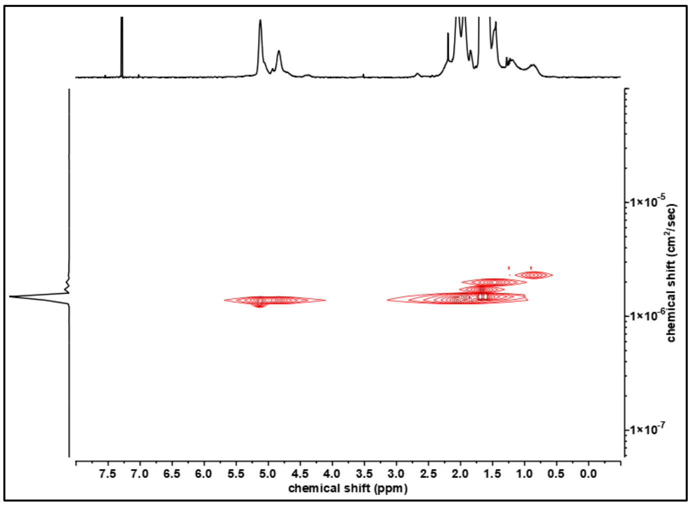

Figure S5.7. 2D DOSY NMR spectra (400 MHz, $CDCl_3$, 298 K) of DMNT-O copolymer.

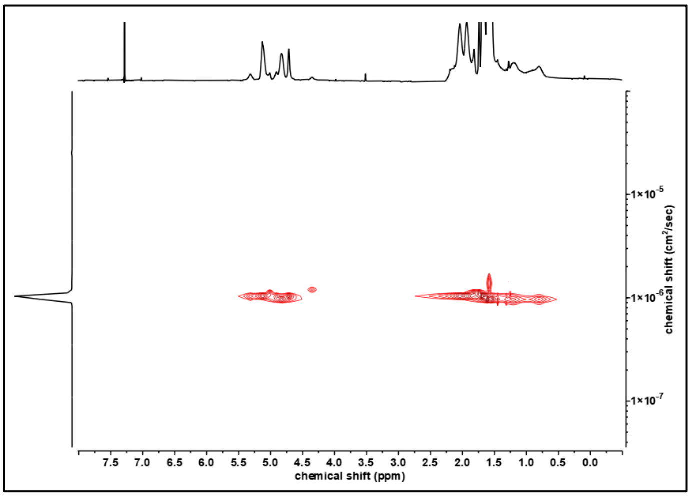

Figure S5.8. 2D DOSY NMR spectra (400 MHz, $CDCl_3$, 298 K) of DMNT-IVC copolymer.

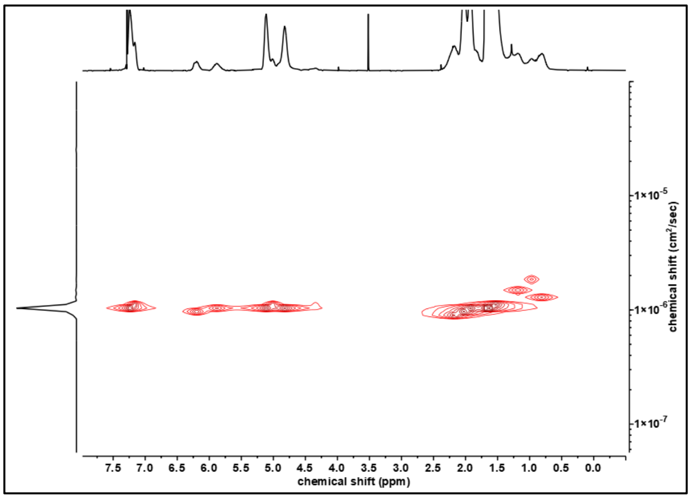

Figure S5.9. 2D DOSY NMR spectra (400 MHz, $CDCl_3$, 298 K) of DMNT-1PB copolymer.

5.2 DSC Thermal Analyses

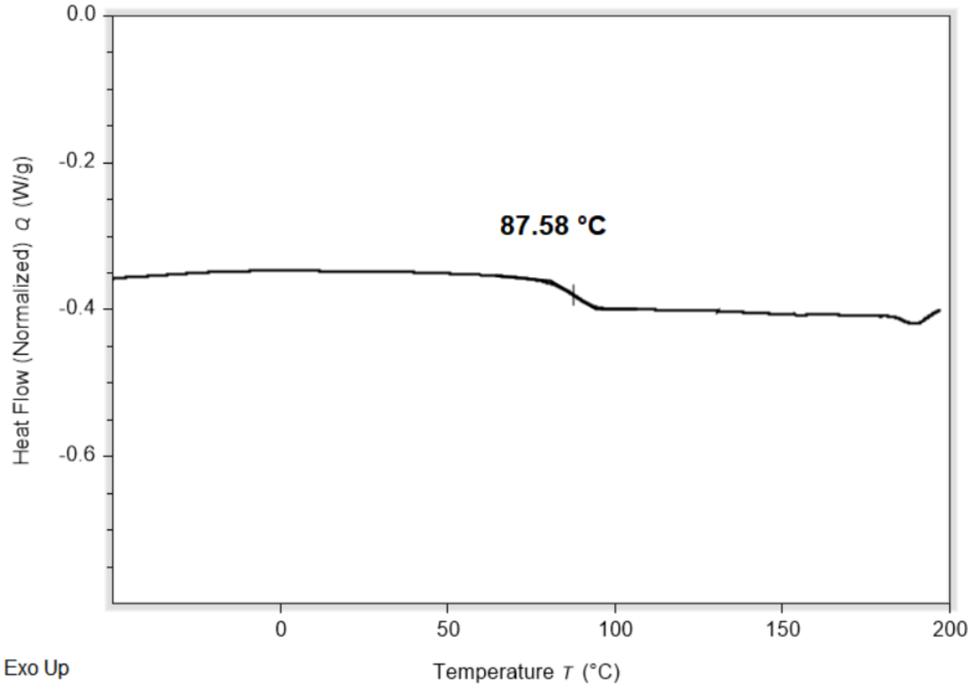

Figure S5.10. DSC thermograms of poly(1PB).

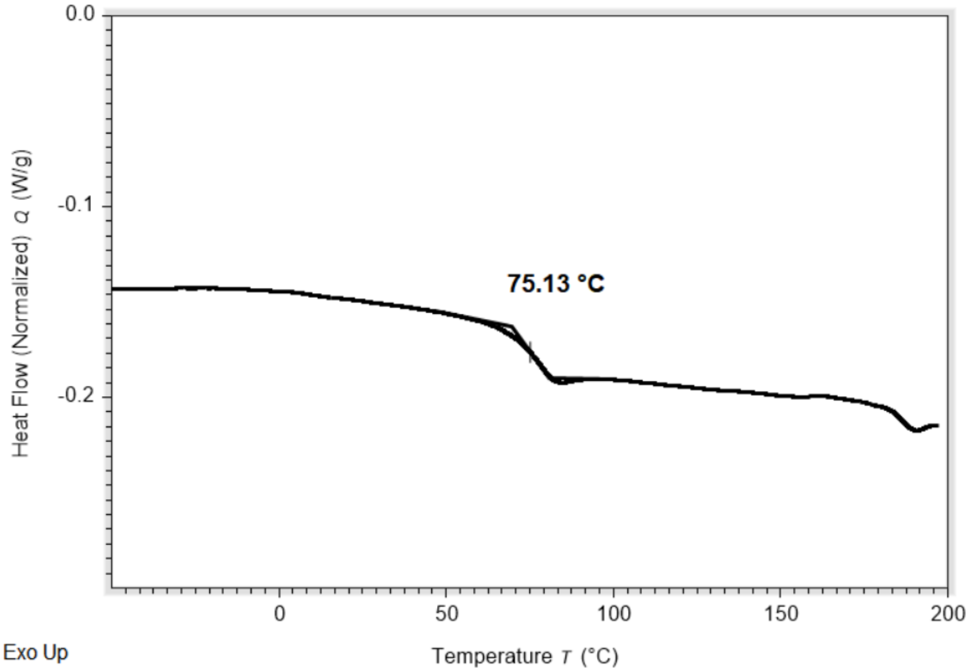

Figure S5.11. DSC thermograms of poly(IVC).

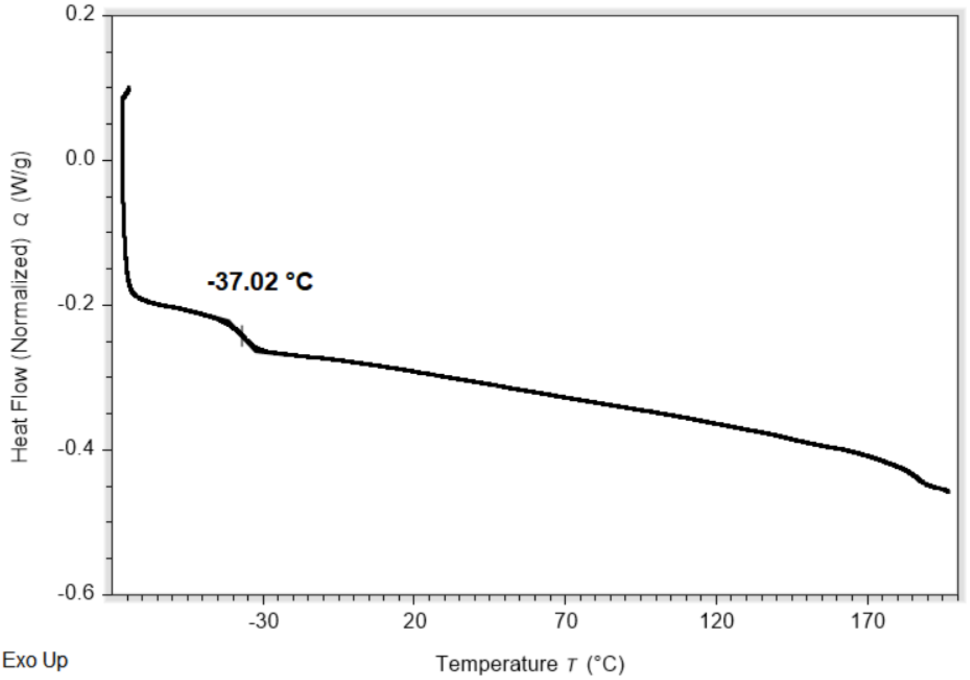

Figure S5.12. DSC thermograms of poly(DMNT).

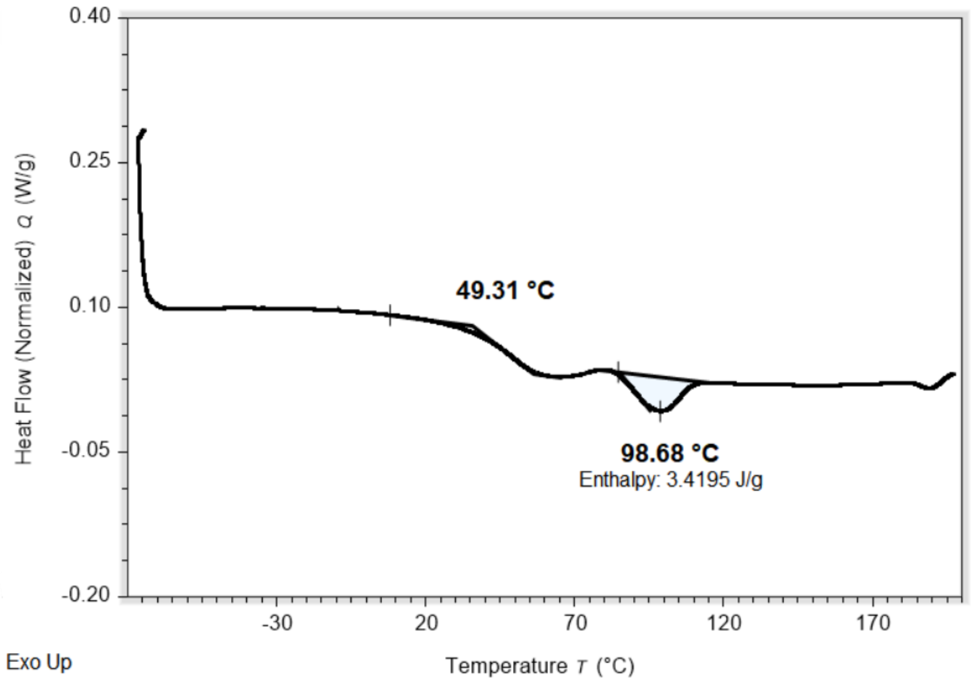

Figure S5.13. DSC thermograms of 1PB-M copolymer.

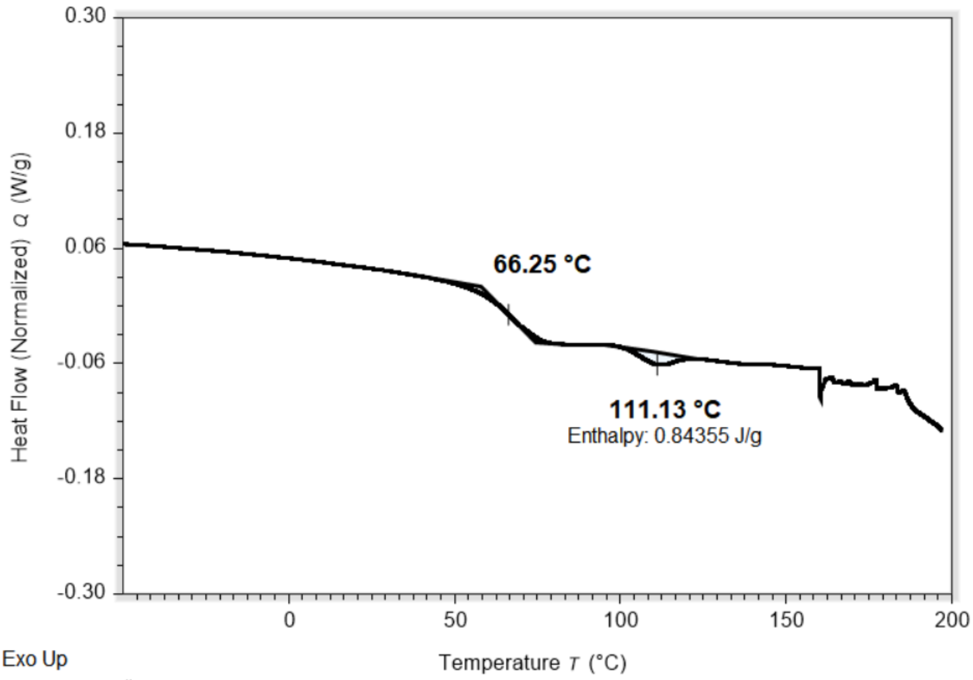

Figure S5.14. DSC thermograms of 1PB-O copolymer.

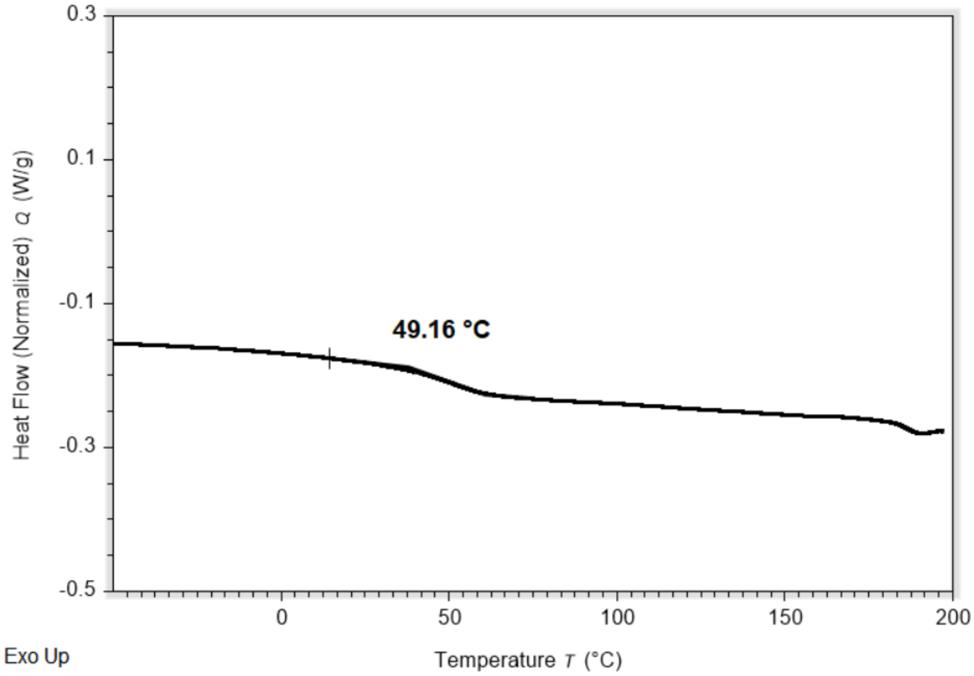

Figure S5.15. DSC thermograms of IVC-M copolymer.

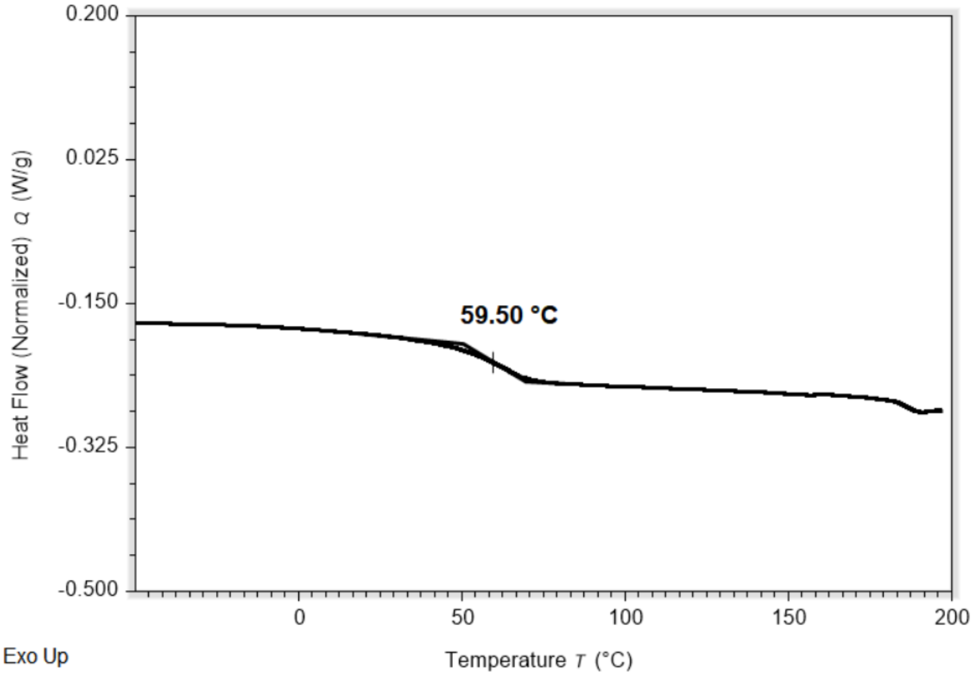

Figure S5.16. DSC thermograms of IVC-O copolymer.

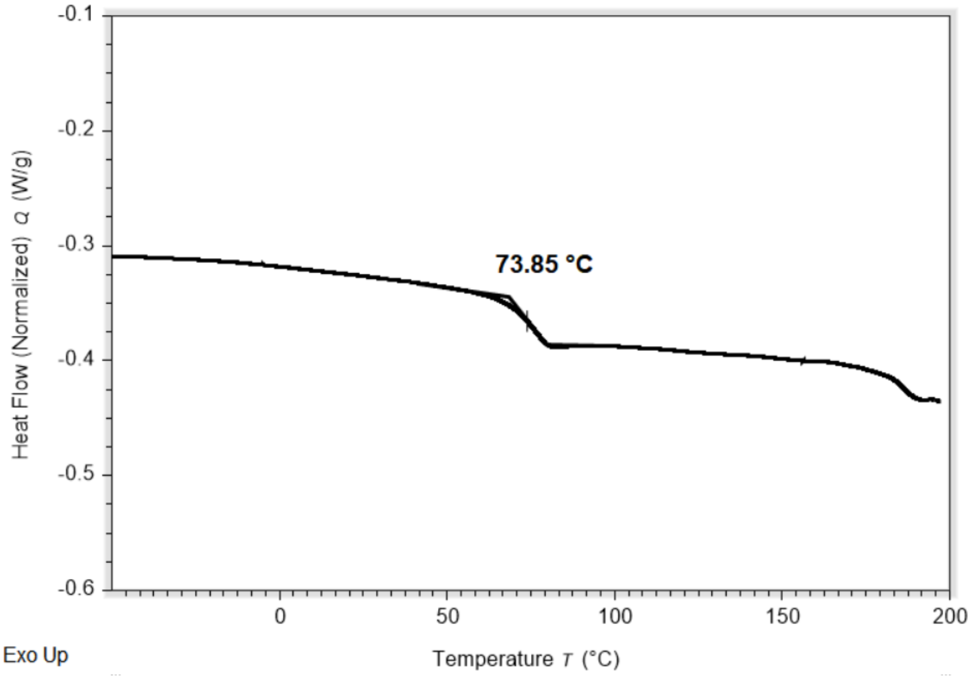

Figure S5.17. DSC thermograms of IVC-1PB copolymer.

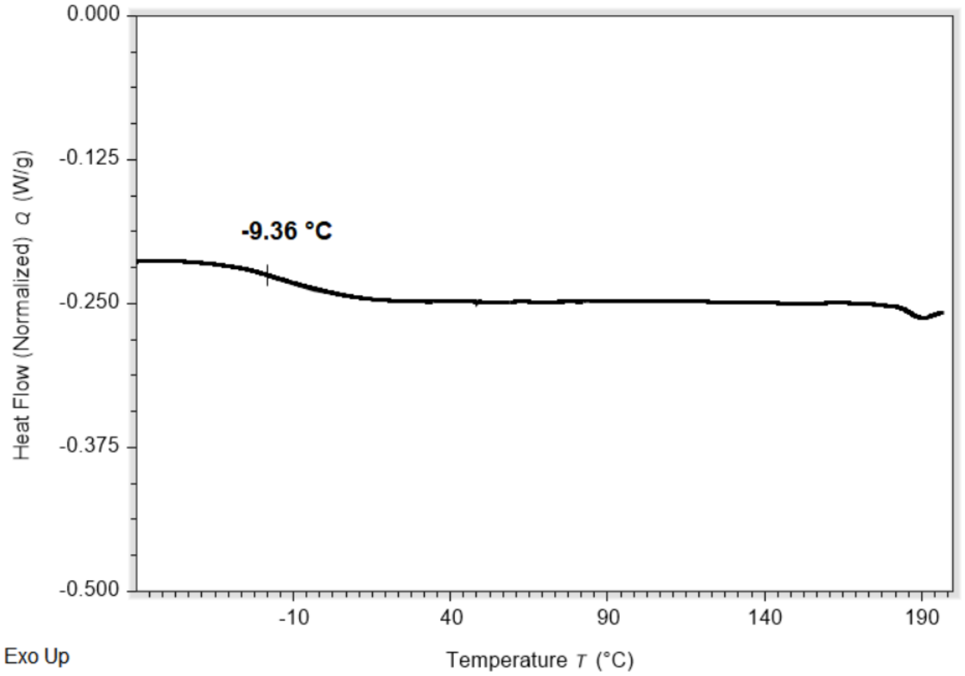

Figure S5.18. DSC thermograms of DMNT-M copolymer.

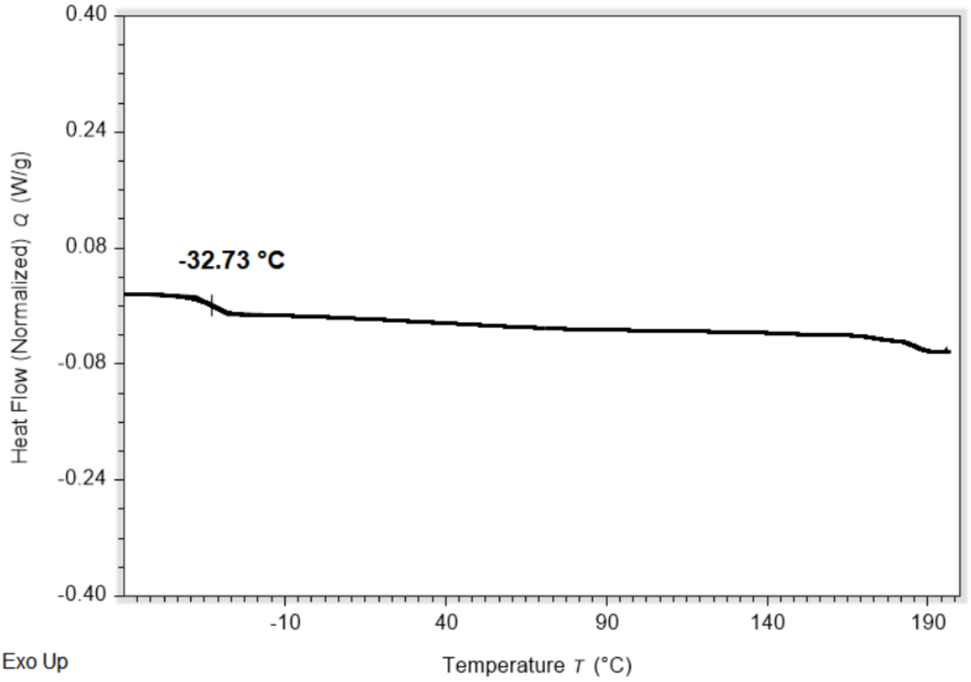

Figure S5.19. DSC thermograms of DMNT-O copolymer.

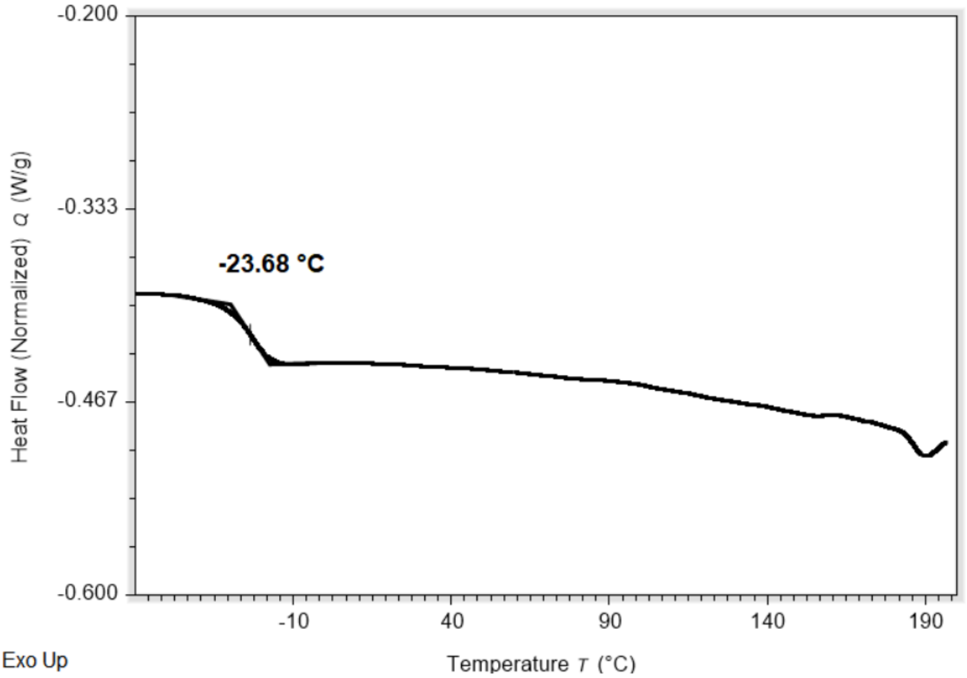

Figure S5.20. DSC thermograms of DMNT-IVC copolymer.

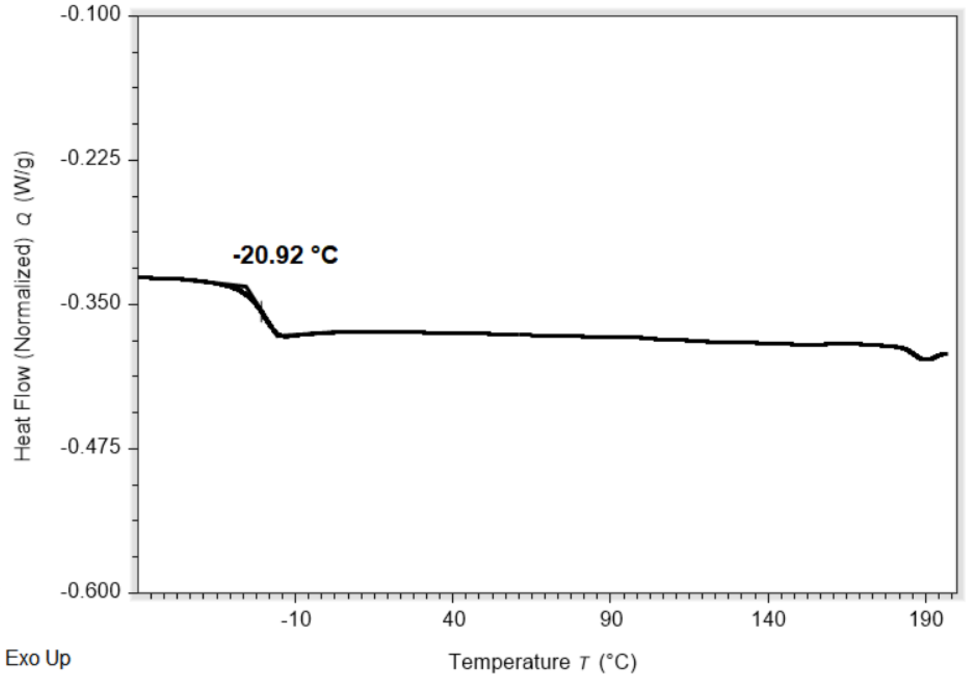

Figure S5.21. DSC thermograms of DMNT-1PB copolymer.

5.3 GPC Analyses

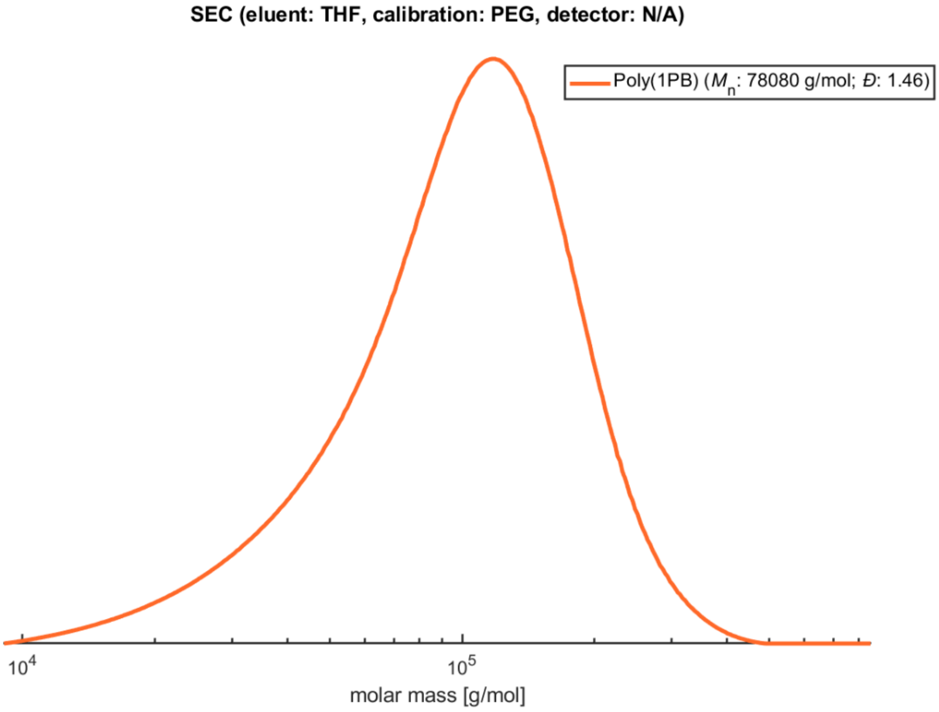

Figure S5.22. GPC curve of poly(1PB).

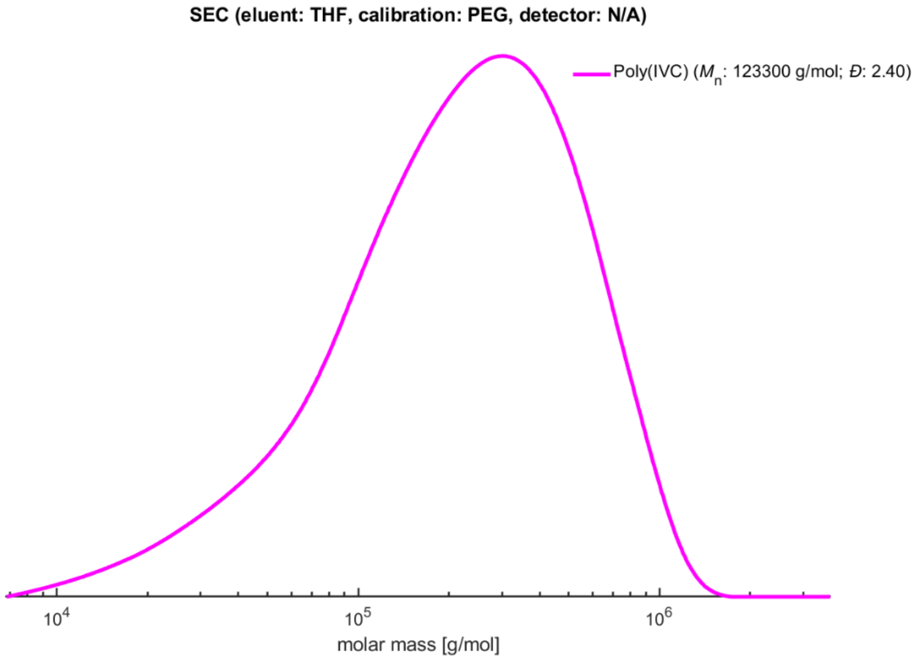

Figure S5.23. GPC curve of poly(IVC).

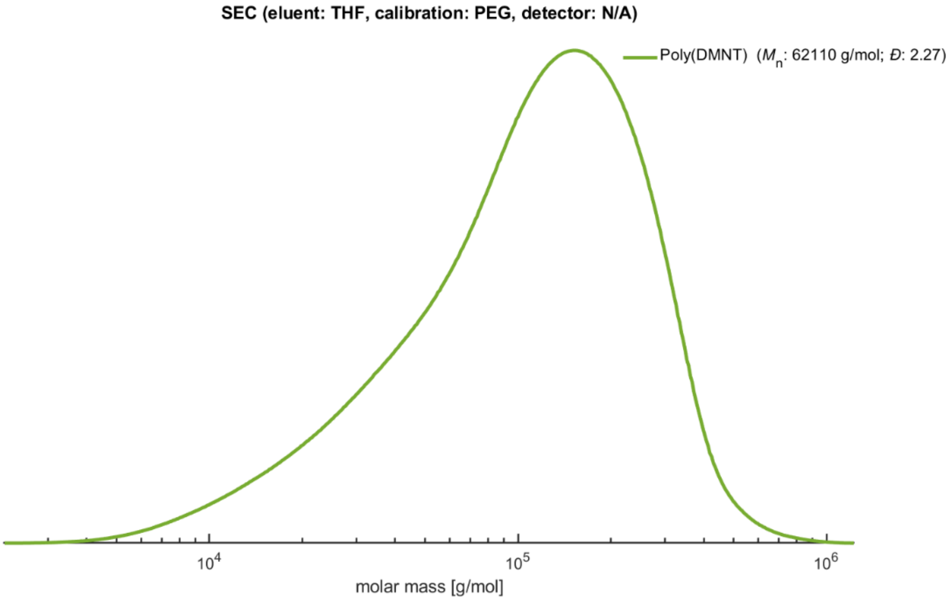

Figure S5.24. GPC curve of poly(DMNT).

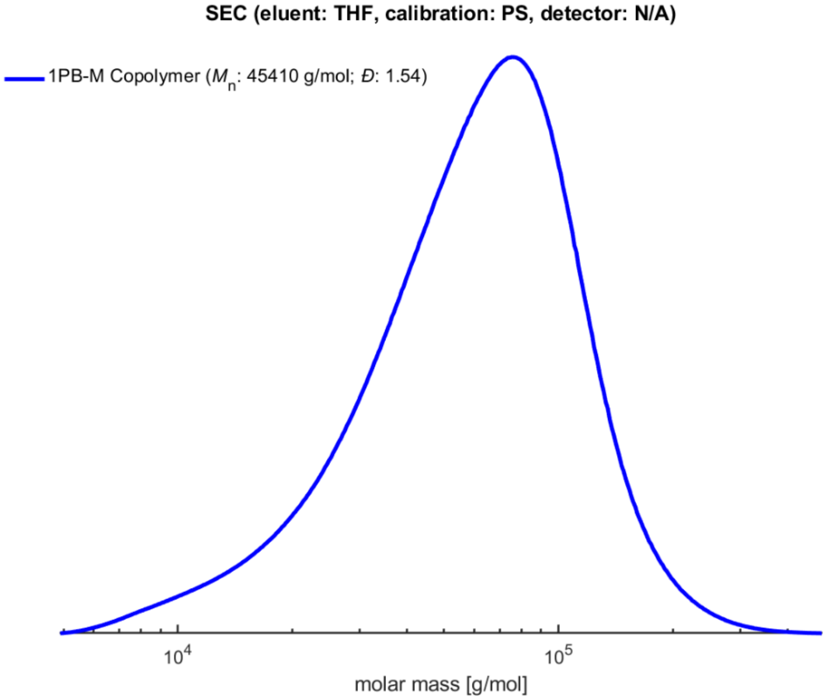

Figure S5.25. GPC curve of 1PB-M Copolymer.

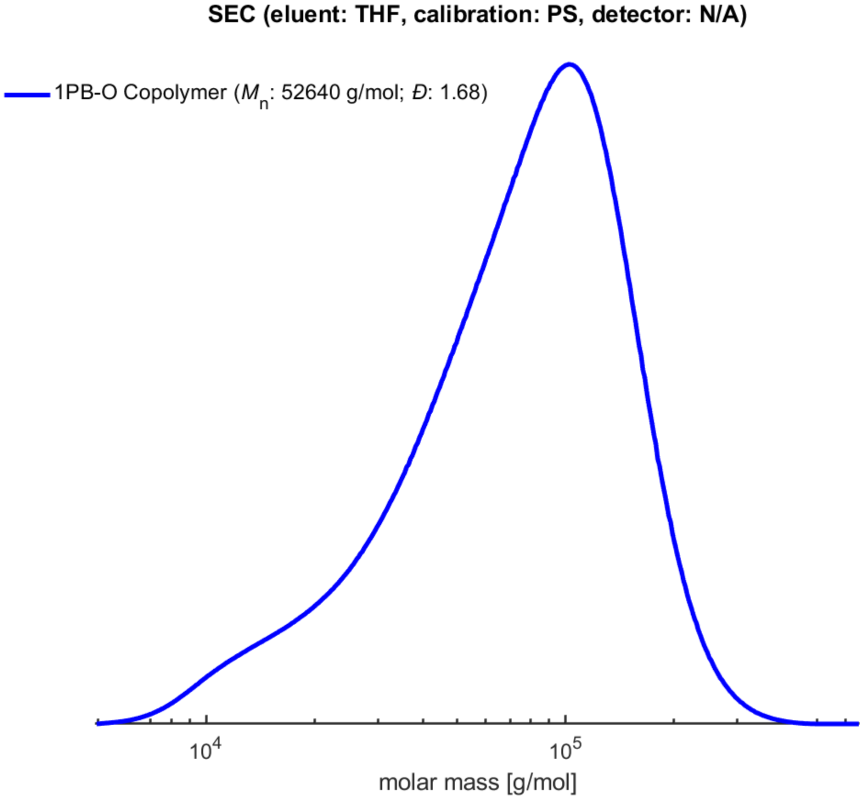

Figure S5.26. GPC curve of 1PB-O Copolymer.

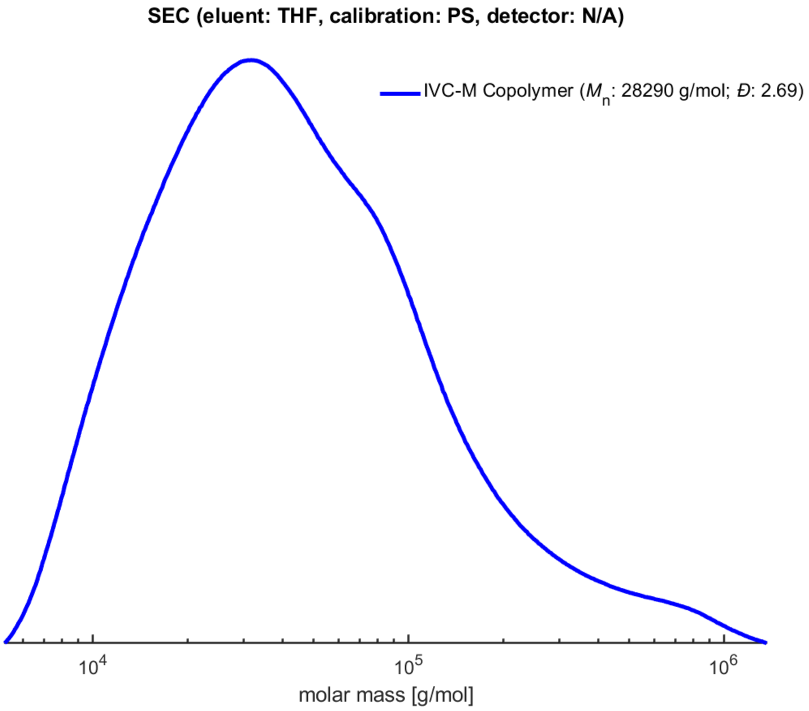

Figure S5.27. GPC curve of IVC-M Copolymer.

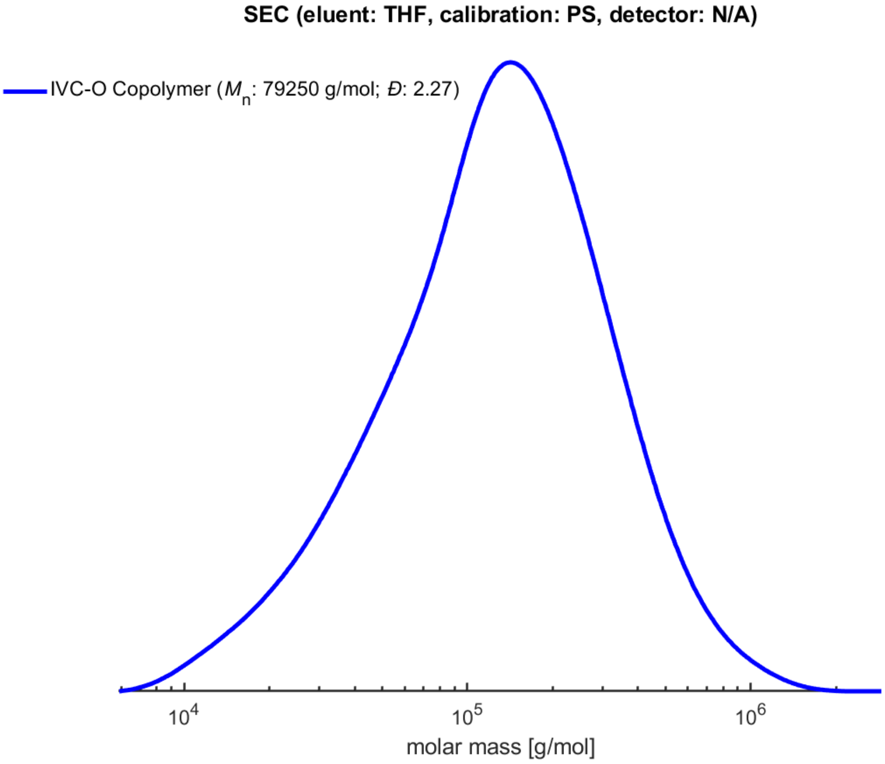

Figure S5.28. GPC curve of IVC-O Copolymer.

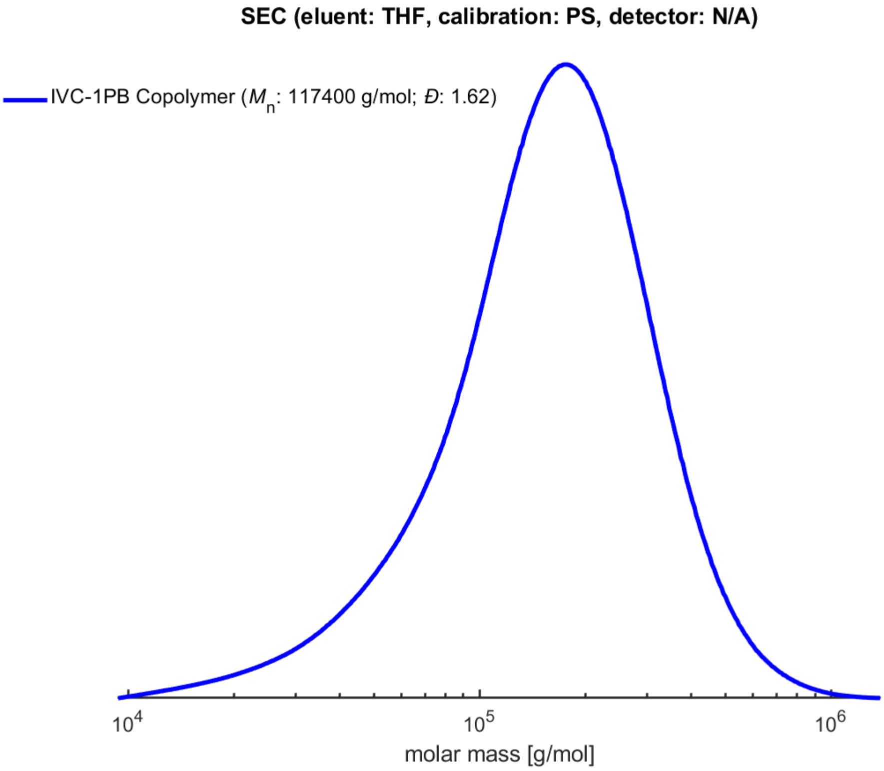

Figure S5.29. GPC curve of IVC-1PB Copolymer.

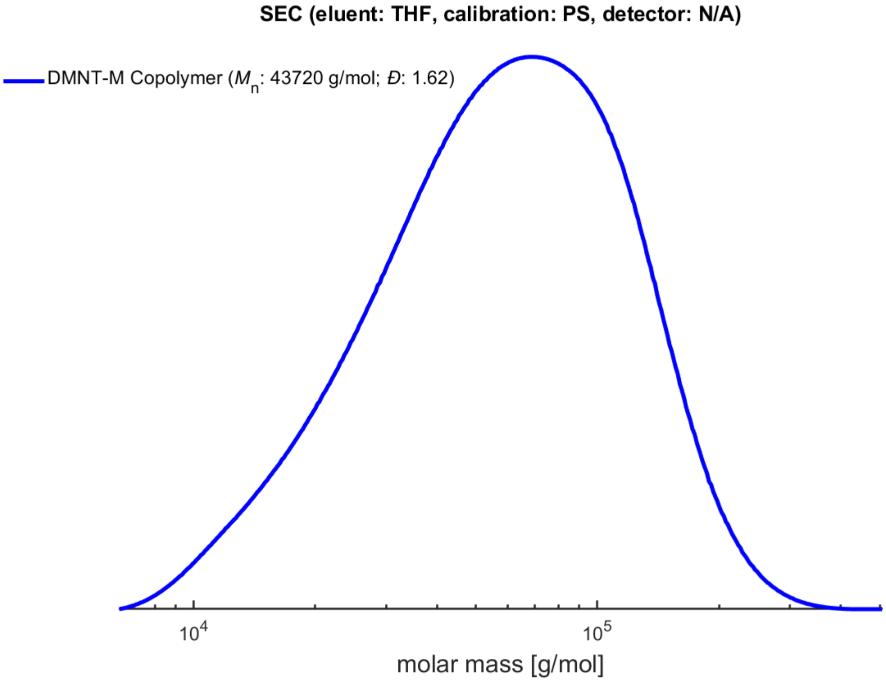

Figure S5.30. GPC curve of DMNT-M Copolymer.

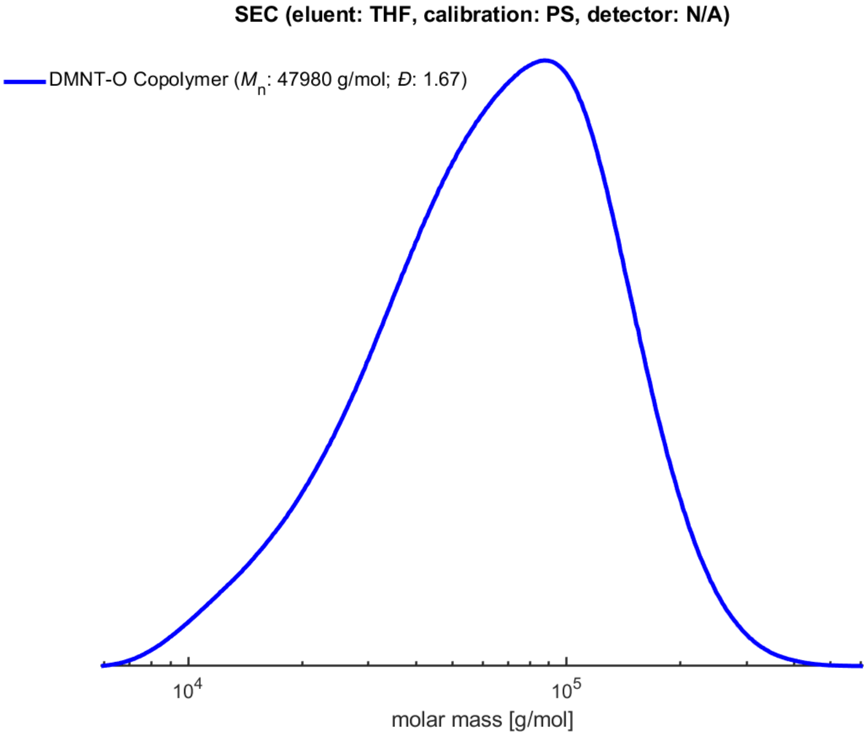

Figure S5.31. GPC curve of DMNT-O Copolymer.

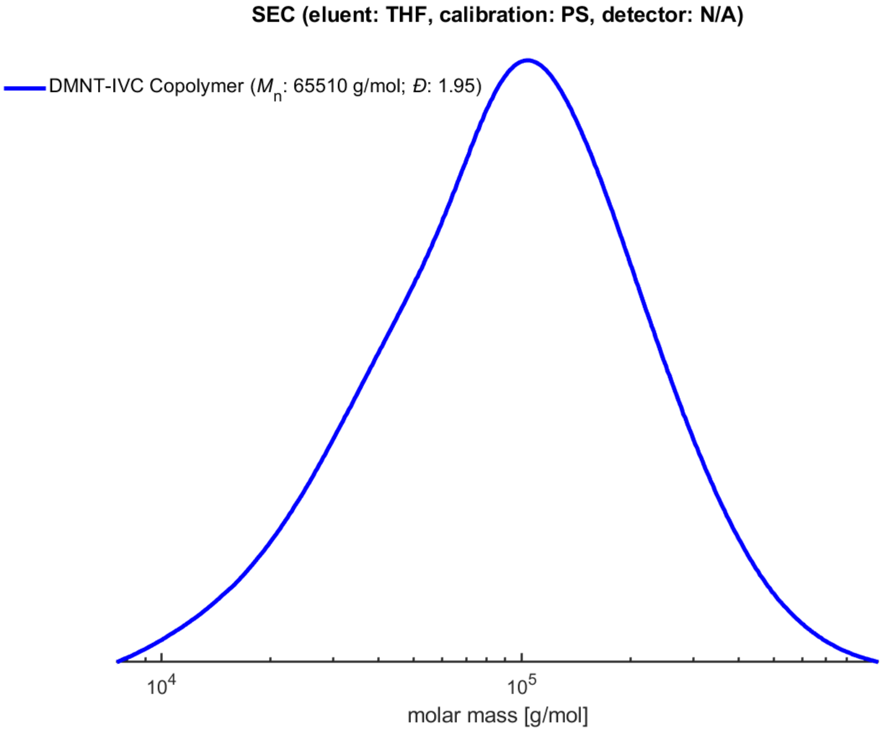

Figure S5.32. GPC curve of DMNT-IVC Copolymer.

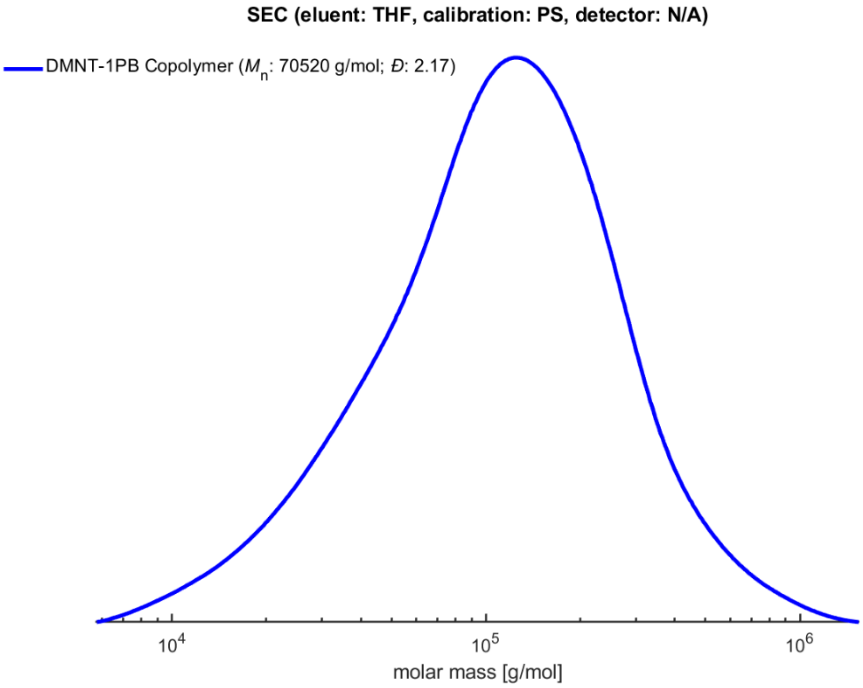

Figure S5.33. GPC curve of DMNT-1PB Copolymer.

List of Publications

1. *Isoselective Polymerization of 1-Vinylcyclohexene (VCH) and a Terpene Derived Monomer S-4-Isopropenyl-1-vinyl-1-cyclohexene (IVC), and Its Binary Copolymerization with Linear Terpenes*

Ilaria Grimaldi, Assunta D'Amato, Mariarosaria C. Gambardella, Antonio Buonerba, Raffaele Marzocchi, Finizia Auriemma,* and Carmine Capacchione*

Macromol. Rapid Commun. **2024**, 2400834

2. *Isospecific Polymerization of 1-Phenyl-1,3-butadiene and Its Copolymerization with Terpene-Derived Monomers*

Ilaria Grimaldi, Raffaele Marzocchi, Sara Esposito, Antonio Buonerba, Finizia Auriemma,* Giuseppe Femina, and Carmine Capacchione*

Macromolecules **2025**, 58, 15, 8344–8351

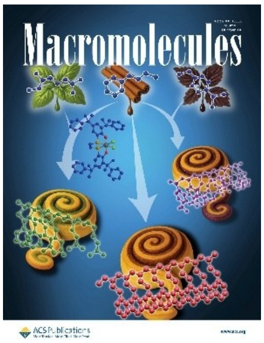

3. *Isospecific Polymerization of (E)-4,8-dimethyl-1,3,7-nonatriene (DMNT) and Its Binary Copolymerization with Ethylene and Styrene using Ti[OSSO]/MAO Catalysts*

Yulin Zheng[1], **Ilaria Grimaldi[1]**, Benoit Lacombe, Dirong Gong,* David Hermann Lamparelli, Carmine Capacchione*

[1]First shared author

European Polymer Journal, **2025**, 235, 114065

Other Publications:

4. *Synthesis and Characterization of* ***β****-Myrcene-Styrene and* ***β****-Ocimene-Styrene Copolymers*

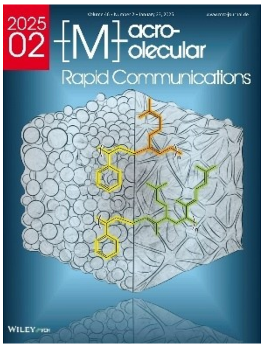

Raffaele Marzocchi, **Ilaria Grimaldi**, Odda Ruiz de Ballesteros, Giuseppe Femina, Adriano Guida, Rosa Ricciardi, Pasquale Morvillo, Carmine Capacchione,* and Finizia Auriemma*

Macromol. Rapid Commun. **2024**, 2400641

5. *Cyclopentadienyl–Silsesquioxane Titanium Complexes in the Polymerizations of Styrene and L-Lactide*

Joan Vinueza-Vaca, Shoaib Anwar, Salvatore Impemba, **Ilaria Grimaldi**, Gerardo Jiménez, Carmine Capacchione, Vanessa Tabernero,* and Stefano Milione*

Polymers, **2025**, 17, 2715

List of Conferences Attended

Conference	Title	Type of presentation
XX PhD Day 2024 April 18-19, 2024, Pisa (IT)	"Titanium Complex-Catalyzed Stereoselective Polymerization of Natural Precursors: Synthesis and Characterization of Biopolymers"	Oral
IUPAC MACRO 2024 - The 50th World Polymer Congress July 01-04, 2024, Warwick (UK)	"Stereoregular Polymerization of Molecules of Natural Origin Promoted by Titanium Complexes With OSSO-Type Ligands"	Oral
Il Contributo dei Giovani Chimici in Campania - Edizione 2024 July 19, 2024, Caserta (IT)	"Stereoselective Polymerization of 1-Vinylcyclohexene and (S)-4-Isopropenyl-1-Vinyl-1-Cyclohexene and their Copolymerization with Styrene and Terpenes"	Oral
SCI 2024 - XXVIII Congresso Nazionale della Società Chimica Italiana August 26-30, 2024, Milan (IT)	"Exploring Titanium-OSSO Complexes for Stereoselective Polymerization of 1-Vinylcyclohexene and (S)-4-Isopropenyl-1-Vinyl-1-Cyclohexene, along with Styrene Copolymerization"	Poster
SusChem'24 - Workshop on Sustainable Polymers and Circular Economy of Plastics September 01-04, 2024, Ischia (IT)	"Isospecific Polymerization of Bio-Based trans-1-phenyl-1,3-butadiene Promoted by Titanium-OSSO Complexes and Its Copolymerization with Linear Terpenes"	Poster
XI Workshop Gruppo Interdivisionale Green Chemistry – Chimica Sostenibile October 24-25, 2024, Turin (IT)	"Isoselective Polymerization of 1-Vinylcyclohexene and (S)-4-Isopropenyl-1-Vinylcyclohexene: Synthesis and Copolymerization with Styrene and Terpenes"	Oral
European Polymer Federation (EPF 2025) June 22-27, 2025, Groningen (NL)	"Stereoselective Polymerization and Copolymerization of Renewable (E)-4,8-Dimethyl-1,3,7-Nonatriene Using Titanium-Based OSSO Catalysts"	Poster

Polymerisation and depolymerisation chemistry: the second century Faraday Discussion September 08-10, 2025, Oxford (UK)	“Bio-Based Alternatives to Styrene and Butadiene for the Synthesis of Sustainable (Block) Copolymers”	Poster